université
PARIS-SACLAY

Radiative cooling
of a spin ensemble

Thèse de doctorat de l'Université Paris-Saclay

École doctorale n° 564, physique de l'Ile-de-France (PIF)
Spécialité de doctorat: Physique
Unité de recherche: Université Paris-Saclay, CEA, CNRS, SPEC,
91191, Gif-sur-Yvette, France.
Référent: : Faculté des sciences d'Orsay

**Thèse présentée et soutenue par visioconférence,
le 16 juin 2020, par**

Bartolo ALBANESE

Composition du jury:

Yann-Michel Niquet	Président
Directeur de recherche, CEA/INAC	
Yiwen Chu	Rapporteur
Professeure, ETH Zurich	
Stephen Lyon	Rapporteur
Professeur, Princeton University	
Marco Affronte	Examinateur
Professeur, CNR Modena	
Gunnar Jeschke	Examinateur
Professeur, ETH Zurich	
Nicolas Sangouard	Examinateur
Chargé de recherche, IPHT, CEA Saclay	
Patrice Bertet	Directeur
Directeur de recherche, SPEC, CEA Saclay	

A Giocs,
per tutti gli abbracci e i momenti felici

Acknowledgements

If I will smile while thinking of my four years of PhD, the merit goes to all the people with whom I shared my experience.

My first thanks are for Patrice, for the care and the passion he put in teaching me his rigorous scientific method and in making sure I was happy and satisfied while growing professionally. In this path, I would have been lost without the guide of Sebastian and Vishal, who taught me how to do everything in the lab, helping me whenever they had time, and even when they did not have any. A special thanks is owed to my predecessor Audray, for being always so kind and for her thesis manuscript that has been my precious bible for all these years.

Thanks to all the permanent members of the Quantronics group and close coworkers, who created in me an idea of work team that will be hard to equal: Daniel, Cristian, Hugues, Philippe, Denis, Marcelo, Fabien, Hélène, Rainier and Emmanuel. To all the students and postdocs of the lab, for making every small pause a funny moment, thank you: Ambroise, Anil, Nicolas, Daniel, Leandro, Marianne, Milos, Cyril, Eric and Léo. Thanks to my two office mates, Fernanda and Emanuele, for the loud joy they created even in the most stressful times. Thanks to all the people of SPEC that gave all sort of technical help, always with sympathy and friendliness, making it possible to realize and run the experiments on an everyday basis: Pascal, the nanofabrication team of Pief and Sébastien, the people of the mechanical workshop, Dominique, Jean-Claude and Vincent, the cryogenic group of Patrick, Philippe, Matthieu and Aurélia.

Many collaborators have been essential for the realization and understanding of the experiments. Thanks to John Morton and to the whole London group, Christoph and James particularly, for providing the bismuth-doped silicon sample and for all the help, the nice discussions and the precious suggestions. Thanks to Andreas Wallraff and Marek Pechal for the superconducting switch they developed, and to William Oliver for providing the Travelling Wave Parametric Amplifier. Thanks also to Bill Coish and Yinan Fang, for shining some light on the physical origin of the polarization transfer we observed.

Thanks to my family and to my old and new friends, for being close to me in so many wonderful ways. And thanks to Roberta, for whom I wish I found some pure words.

Contents

Rèsumé détaillé

La découverte de l'interaction des spins avec la radiation électromagnétique aux fréquences rf ou micro-ondes a conduit au développement de la résonance magnétique, dont les pionniers sont Rabi, Bloch et Purcell [1–3]. Dans les expériences habituelles de résonance magnétique, le couplage spin-photon est l'échelle d'énergie la plus faible du système. Le rayonnement électromagnétique des spins, qui permet la détection des spins, n'a pas d'impact mesurable sur la dynamique des spins. Cette dernière reste entièrement régie par le couplage à d'autres degrés de liberté de l'environnement, comme le mouvement atomique ou moléculaire, les phonons ou l'interaction dipolaire avec d'autres spins. La température du spin est donc fixée par le réseau hôte indépendamment du rayonnement thermique. Cependant, dejà dans les premier temps de la résonance magnétique, Purcell a prédit que la relaxation radiative des spins devrait être renforcé en insérant l'échantillon dans une cavité résonante de petit volume de mode et de facteur de qualité élevé. Les premières observations de cette prédiction de Purcell avec des spins ont été rapportées en 1985 par Sleator et al. [4] pour un ensemble de spins nucléaires de Cl. Le taux d'émission radiative a été accéléré de 11 ordres de grandeur, pour atteindre $10^{-16}\,\mathrm{s}^{-1}$. Le temps de relaxation d'environ 3000 ans était cependant toujours significativement plus important que les temps de relaxation non radiative dominants estimés à l'ordre de jours dans l'expérience, maintenant ainsi les spins bien thermalisés au réseau.

Le régime Purcell, dans lequel le rayonnement est le principal canal de relaxation du spin, n'a été atteint que récemment dans les expériences de Bienfait et al.[5], en utilisant des micro-résonateurs supraconducteurs développés pour des applications d'information quantique. L'amélioration obtenue du couplage spin-photon a été exploitée pour atteindre une sensibilité de la résonance paramagnétique électrique (RPE) record et présente un intérêt potentiel pour l'information quantique [6].

Le but de cette thèse est d'explorer les conséquences du régime de Purcell sur la thermalisation des spins. Notre idée principale est que, dans le régime Purcell, les spins devraient se thermaliser à la température des photons micro-onde dans la cavité, et devenir en quelque sorte découplés du réseau cristallin dans lequel ils sont insérés. Nous démontrons cette idée en prouvant que les spins peuvent être refroidis à une température inférieure à celle de l'échantillon, simplement par des processus radiatifs. De plus, cette approche de refroidissement des spins représente une nouvelle méthode générale pour hyperpolariser un ensemble de spins électroniques.

La première partie du manuscrit est consacrée aux outils conceptuels nécessaires à la compréhension des expériences. Nous fournissons des informations théoriques sur les circuits quantiques à la fréquence des micro-ondes et sur les spins. Nous introduisons la description quantique des modes des cavités et des lignes de transmission, en mettant l'accent sur leur état thermique et leurs propriétés de bruit. Nous abordons ensuite les spins électroniques et leur interaction avec le rayonnement électromagnétique, et nous

décrivons l'effet Purcell et les principes de la spectroscopie RPE pulsés. Enfin, nous introduisons le système de spin électronique étudié dans notre expérience : les donneurs de bismuth dans le silicium.

La deuxième partie de la thèse contient les principaux résultats expérimentaux, qui sont décrits dans les chapitres 5, 6 et 7. Le chapitre 5 décrit la mise en œuvre du spectromètre avec un résonateur supraconducteur et la spectroscopie des donneurs de bismuth. On observe une modulation de l'enveloppe de l'écho par les électrons, causée par le bain de ^{29}Si de spins nucléaires. En ce qui concerne la relaxation des spins, nous prouvons que les spins des donneurs de bismuth atteignent le régime de Purcell à un champ magnétique suffisamment important. À des champs plus faibles, les processus de transfert de polarisation non radiative rendus possibles par l'environnement des spins nucléaires prennent le relais de la relaxation de Purcell.

Le refroidissement radiatif des donneurs de bismuth dans le régime Purcell est démontré dans le sixième chapitre de la thèse. Il est d'abord démontré que les spins sont thermalisés au mode de la cavité à la température de l'échantillon de 850 mK. Le mode de la cavité est ensuite refroidi en connectant son entrée à une résistance froide à 15 mK. Une augmentation de polarisation des spins par un facteur supérieur à 2 révèle que la température des spins est réduite jusqu'à 350 mK, prouvant que les spins sont refroidis radiativement en dessous de la température de l'échantillon[7].

Dans le dernier chapitre de la thèse, nous étudions l'origine de la relaxation non radiative du spin observée à faible champ magnétique. Nous démontrons que le transfert de polarisation dans le spectre du donneur de bismuth est présent, probablement en raison des processus de flip-flops des spins.

Principe de refroidissement radiatif des spins

Pour introduire le principe du refroidissement radiatif des spins, considérons un système physique échangeant de l'énergie avec plusieurs bains à différentes températures. Le système va s'équilibrer à une température intermédiaire dont la valeur dépendra de la force Γ_j avec laquelle le système est couplé à chaque bain, définie comme la vitesse à laquelle le système se détend jusqu'à son état de base en émettant un quantum d'énergie dans le bain j s'il est à température zéro. Si un taux de relaxation Γ_{j0} est beaucoup plus important que tous les autres, le système se thermalisera à la température du bain $j0$, quelle que soit la température des autres.

Le principe du refroidissement radiatif de spin est illustré dans la Fig.0.1. Le système que nous visons à refroidir est un ensemble de spins électroniques interagissant avec deux bains : les phonons dans son réseau hôte de température T_{phon} et les photons micro-ondes dans son environnement électromagnétique de température T_{phot}. Comme indiqué précédemment, le taux d'émission radiative spontanée Γ_{phot}, dans les conditions habituelles de résonance magnétique, est bien inférieur au taux de relaxation spin-réseau cristallin Γ_{phon}, de sorte que la température du spin T_{spin} s'équilibre à T_{phon}.

Cependant, l'effet Purcell offre la possibilité d'inverser ce scénario : l'insertion des spins dans le petit volume de mode d'une cavité à facteur de qualité élevé peut accélérer le taux d'émission radiative spontanée jusqu'au point $\Gamma_{\mathrm{phot}} \gg \Gamma_{\mathrm{phon}}$, amenant ainsi les spins à l'équilibre thermique avec le mode de la cavité. La condition obtenue $T_{\mathrm{spin}} \approx T_{\mathrm{phot}}$ offre alors la possibilité de refroidir les spins à une température inférieure à celle du réseau, en contrôlant T_{phot}.
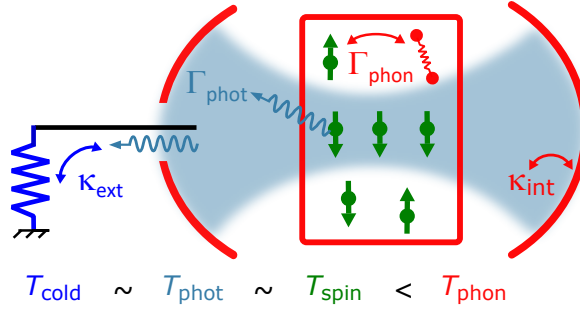
Figure 0.1: **Principe de refroidissement radiatif des spins.** Les spins (vert) d'un cristal (rouge) sont couplés à la fois à un bain de phonons à température T_{phon} avec un taux Γ_{phon} et à un bain de photons micro-ondes à température T_{phot} avec un taux Γ_{phot}, qui détermine leur température d'équilibre T_{spin}. La température des photons T_{phot} est déterminée par leur couplage avec le taux κ_{int} aux pertes internes de la cavité à T_{phon} et avec le taux κ_{ext} à la résistance connectée à l'entrée de la cavité. Lorsque cette charge est placée à basse température T_{froid}, le champ intracavité est refroidi radiativement à condition que $\kappa_{\text{ext}} \gg \kappa_{\text{int}}$ et les spins sont refroidis à leur tour si $\Gamma_{\text{phot}} \gg \Gamma_{\text{phon}}$.

Tout comme le système de spins, le mode de la cavité échange de l'énergie avec deux bains. Comme le montre la figure 0.1, il est couplé avec le taux κ_{int} aux pertes internes à T_{phon} et avec le taux κ_{ext} au rayonnement thermique émis par une résistance froide de température T_{froid} connectée à l'entrée de la cavité. En concevant le port d'entrée de telle sorte que $\kappa_{\text{ext}} \gg \kappa_{\text{int}}$, la température du mode cavité est alors thermisée à T_{cold}. En conséquence, les spins du régime Purcell sont censés être refroidis par rayonnement à T_{cold}, quelle que soit la température de l'échantillon.

Avant de décrire la réalisation expérimentale du refroidissement radiatif, dans la première partie de la thèse, nous fournissons le contexte théorique nécessaire pour discuter de tous les aspects pertinents de l'expérience. Dans le chapitre 2 nous introduisons la description quantique de notre circuit micro-ondes composé de la cavité supraconductrice, des lignes de transmission et de l'amplificateur. Comme nous sommes particulièrement intéressés par l'état thermique d'un tel circuit, nous nous concentrons sur le bruit thermique et sa détection.

Nous passons ensuite, dans le chapitre 3, à la description de la dynamique des spins couplés à une cavité micro-ondes. Deux grandeurs clés sont introduites : le taux de relaxation d'énergie du mode de la cavité $\kappa = \kappa_{\text{ext}} + \kappa_{\text{int}}$ et la force d'interaction spin-photon $\hbar g$, qui est le produit du moment dipolaire magnétique du spin et des fluctuations du vide du champ magnétique à l'endroit du spin. À la résonance, le taux de relaxation spontanée Purcell est de $\Gamma_{\text{phot}} = 4g^2/\kappa$. La relaxation de Purcell à température finie est également prise en compte car elle est d'une importance capitale dans notre expérience. Le taux de relaxation des spins vers l'équilibre thermique dans le régime Purcell est $\Gamma_1 = \Gamma_{\text{phot}}[2n_{\text{th}}(T_{\text{phot}}) + 1]$, où $n_{\text{th}}(T_{\text{phot}})$ est la population de photons thermiques dans la cavité à T_{phot}. La dernière partie du chapitre fournit une brève description des techniques et concepts standard de la spectroscopie RPE pulsée, et en particulier de la séquence d'écho de Hahn. Pour déduire la température de spins, nous utilisons en effet le fait que l'amplitude de l'écho de spin A_e est proportionnelle à la polarisation dépendant de la température $p(T_{\text{spin}})$. Il est intéressant de noter que $p(T_{\text{spin}})$ devrait avoir la même dépendance à la température que Γ_1 pour un ensemble de spins $1/2$, une prédiction simple que nous testons dans cette thèse.

Nos expériences sont réalisées avec un système de spin modèle, le spin électronique des donneurs de bismuth dans le silicium. Ils sont constitués d'atomes de bismuth de substitution dans le réseau du silicium à l'état neutre, où ils piègent un électron de conduction. Nous décrivons la structure et les propriétés des donneurs de bismuth dans le silicium dans le chapitre 4.

ESR spectroscopie du bismuth dans le silicium naturel

Dans le chapitre 5 nous décrivons la configuration du spectromètre RPE et rendons compte des expériences de spectroscopie des donneurs de bismuth réalisées à 15 mK avec B_0 entre 0 et 70 mT. La conception du spectromètre est basée sur les travaux de Bienfait et al. [6]. La cavité est un résonateur supraconducteur de fréquence ω_0 constitué d'une fine couche de niobium modelée sur le dessus de la puce de silicium implantée avec des donneurs de bismuth (voir Fig.0.2a). L'électron du donneur avec fréquence de Larmor ω_{spin} est accordée en résonance avec la cavité par l'application d'un champ magnétique externe B_0 parallèle au fil inducteur. Les spins proches du fil sont couplés avec force g au mode de la cavité (voir Fig.0.2b). L'échantillon est monté dans un support en Cu et couplé de manière capacitive à une antenne micro-onde qui règle le taux de couplage κ_{ext} de telle sorte que $\kappa_{\mathrm{ext}} \gg \kappa_{\mathrm{int}}$.
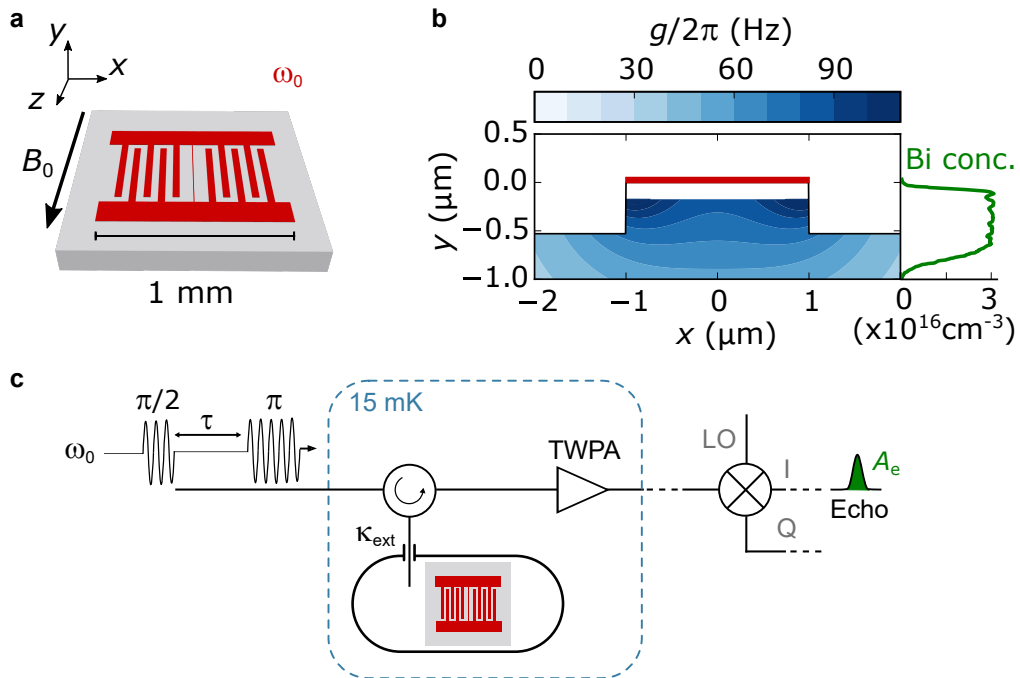
Figure 0.2: **Spectromètre RPE avec un résonateur supraconducteur. a,** Résonateur supraconducteur en niobium (rouge) placé sur une puce de silicium implantée avec des donneurs de bismuth. **b,** Section transversale du dispositif autour du fil inducteur (rouge). La constante de couplage spin-photon g (code couleur) est représentée dans la région Bi-dopée. **c,** Représentation schématique de la configuration du spectromètre avec la séquence d'impulsions de Hahn-écho illustrée sur la ligne d'entrée.

Nous détectons le signal de résonance magnétique au moyen de techniques de spectroscopie RPE pulsées. Nous utilisons en particulier la séquence d'écho de Hahn où une impulsion $\pi/2$ est suivie après un temps τ par une impulsion π induisant un rephasage

des spins et l'émission d'un écho après un délai supplémentaire τ. Après amplification, l'écho émis est démodulé et enregistré à température ambiante (voir Fig.0.2c).

La mesure de l'amplitude de l'écho A_e en fonction de B_0 montre un pic de signal chaque fois qu'une transition de spin d'un donneur de bismuth est en résonance avec la cavité (voir Fig.0.3a). Nous discutons le spectre dans Sc.5.4.1.
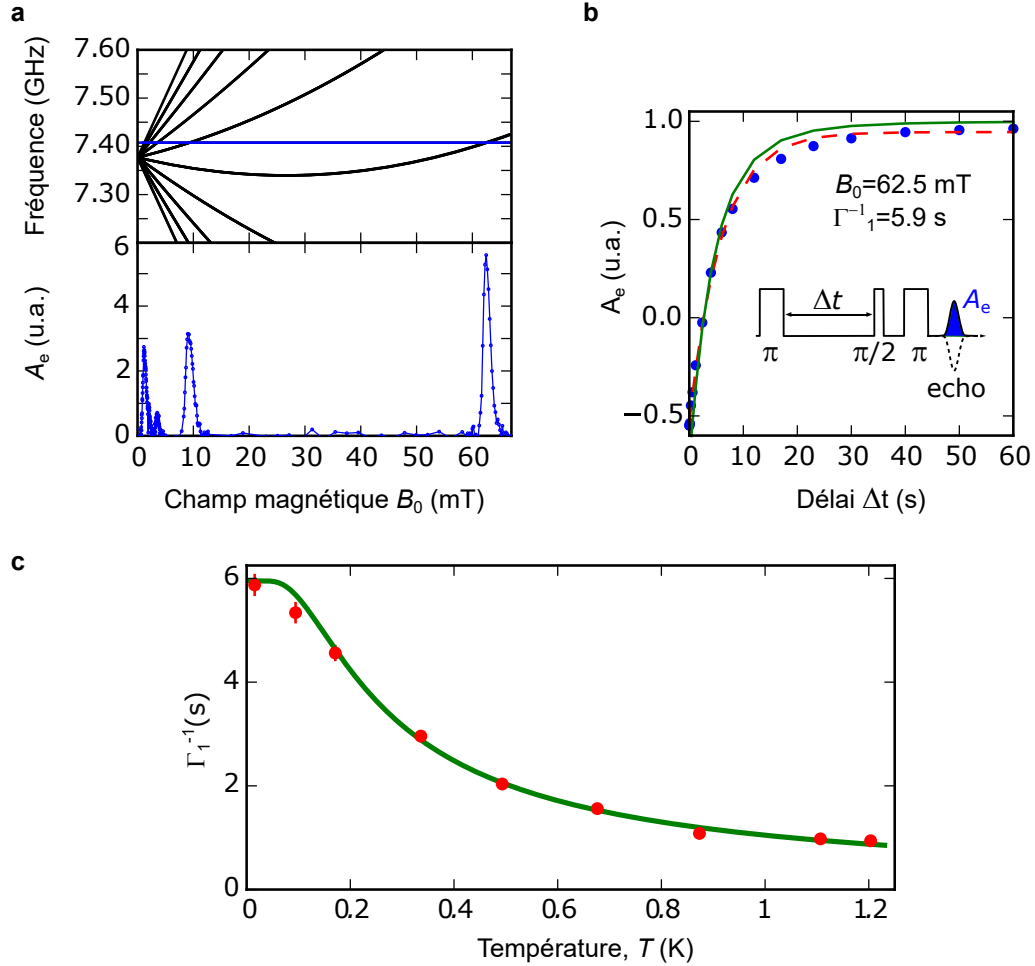
Figure 0.3: **Spectroscopie RPE du bismuth : principaux résultats. a,** En haut, fréquence des transitions RPE calculée en fonction de B_0. La fréquence du résonateur est indiquée en bleu. En bas, amplitude de l'écho mesurée en fonction de B_0. **b,** Relaxation de l'énergie de spins mesurée à $B_0 = 62,5\,\mathrm{mT}$ avec la séquence de *inversion recovery* illustrée dans l'encadré. La ligne rouge en pointillés est un fit exponentiel avec la constante de temps Γ_1^{-1}. La simulation numérique de la relaxation de Purcell est illustrée en vert. **c,** Temps de relaxation Γ_1^{-1} mesuré en fonction de la température (rouge). La dépendance prévue de la température pour la relaxation Purcell est indiquée en vert.

Dans la Sc.5.6 nous montrons qu'à $15\,\mathrm{mK}$ la transition de spin de champ la plus élevée se relax au taux d'émission radiative spontanée calculé Γ_{phot}, démontrant que les spins sont dans le régime Purcell (voir Fig.0.3b). La relaxation des spins est ensuite mesurée en fonction de la température. Le taux de relaxation des spins extrait Γ_1 suit la dépendance du taux Purcell par rapport à la température (voir Fig.0.3c), montrant que les spins restent dans le régime Purcell à des températures supérieures à $1\,\mathrm{K}$.

L'étude de la relaxation des spins à un champ magnétique inférieur révèle qu'un processus de relaxation non radiatif est présent. Nous attribuons cela au transfert de polarisation par des processus de flip-flops entre donneurs voisins, rendu possible par l'environnement de spin nucléaire du silicium. Nous étudions expérimentalement ce processus dans le dernier chapitre de la thèse.

Refroidissement radiatif d'un ensemble de spins électroniques

La démonstration de refroidissement radiatif est rapportée au chapitre 6. La configuration est représentée schématiquement dans la Fig.0.4a. L'échantillon est thermalisé à $T_{\mathrm{phon}} = 850\,\mathrm{mK}$, tandis que l'entrée de la cavité est connectée via un commutateur soit à une résistance chaude à T_{phon} soit à une résistance froide à $T_{\mathrm{froid}} = 15\,\mathrm{mK}$. Dans la configuration de l'interrupteur froid, les spins en régime Purcell devraient alors être refroidis à la température du mode de la cavité $T_{\mathrm{phot}} \approx T_{\mathrm{cold}}$, bien en dessous de T_{phon}. Le facteur de refroidissement η est défini comme le rapport de la polarisation du spin dans les deux configurations de commutation. Comme la polarisation de spin et le taux de relaxation Purcell ont la même dépendance à la température, η devrait également être égal au rapport entre le taux de relaxation de spin mesuré dans les deux configurations de commutateur.

Nous déterminons d'abord T_{phot} dans les deux configurations du commutateur avec un ensemble de mesure du bruit détaillé dans Sc.6.4. Nous constatons qu'en connectant l'entrée du résonateur à la résistance froide, la température du mode de la cavité est refroidie radiativement jusqu'à $T_{\mathrm{phot}}^{\mathrm{cold}} = 500 \pm 60\,\mathrm{mK}$. Nous attribuons le refroidissement partiel à la présence de pertes par micro-ondes entre le résonateur et la résistance froide.

Le signal Hahn-echo fait plus que doubler lorsqu'il est mesuré dans la configuration froide (voir Fig.0.4b), démontrant une hyperpolarisation radiative avec $\eta = 2.3 \pm 0.1$ (voir Sc.**??**). Nous mesurons également les taux de relaxation pour les deux réglages du commutateur et trouvons $\Gamma_1^{\mathrm{hot}}/\Gamma_1^{\mathrm{cold}} = \eta$, comme prévu (voir Fig.0.4c). Le η mesuré correspond à une température de spins $T_{\mathrm{spin}} = 350 \pm 10\,\mathrm{mK}$, qui est proche (ou même légèrement inférieure) de la température du champ $T_{\mathrm{phot}}^{\mathrm{cold}}$ estimée à partir des mesures de bruit. Cela prouve que la relaxation spin-reseau cristallin n'est pas le facteur limitant le refroidissement de spins, et que les spins se thermalisent à la température de leur environnement électromagnétique dans les limites de la précision de l'expérience.

Nous concluons ce chapitre par une brève discussion des applications possibles de cette nouvelle technique d'hyperpolarisation à la spectroscopie par résonance magnétique.

Transfert de polarisation chez les donneurs de bismuth

Comme nous l'avons vu plus haut, nous observons à bas champ un processus de relaxation qui entre en compétition avec la relaxation radiative Purcell. Dans le dernier chapitre Ch.7 nous étudions expérimentalement son origine.

Nous attribuons cet effet au transfert de polarisation entre différents niveaux hyperfins du spectre des donneurs de bismuth via des flip-flops entre des paires de donneurs couplées par l'interaction dipolaire. Un tel transfert de polarisation apparaît comme une relaxation plus rapide sur la transition sondée par la cavité micro-onde.
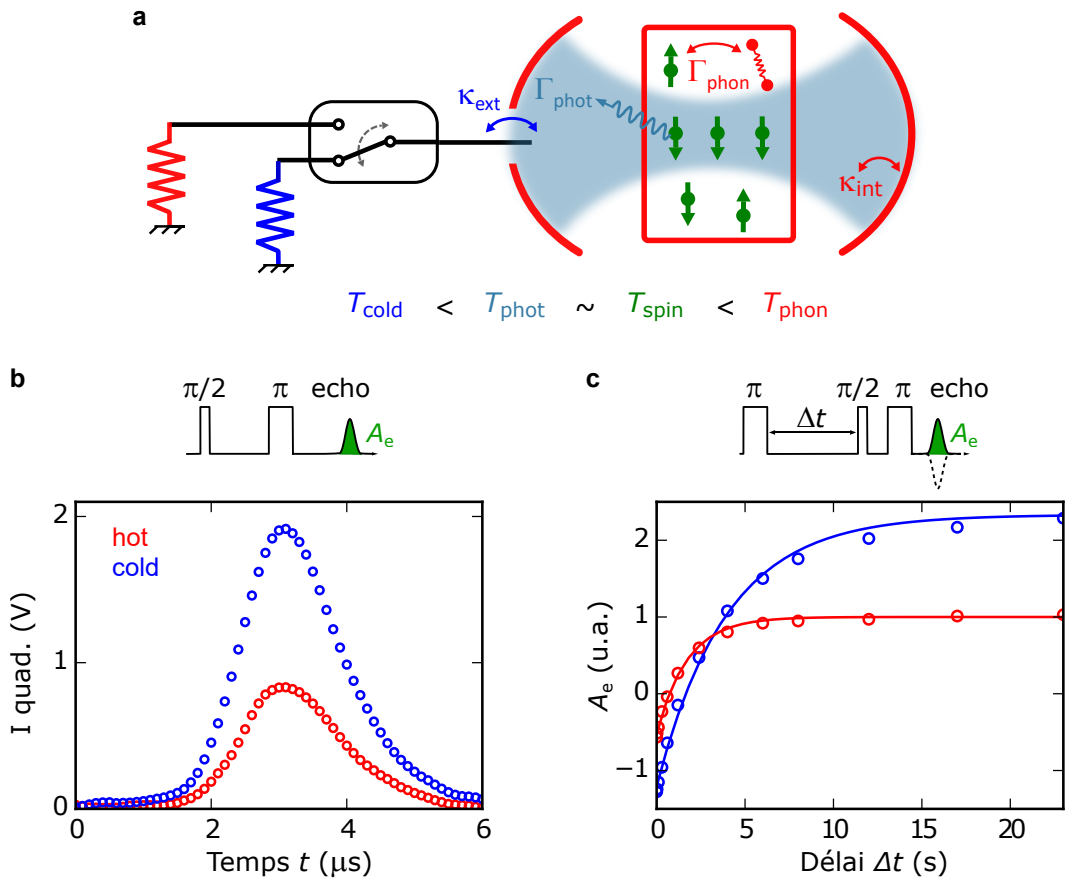
Figure 0.4: **Principe de refroidissement par rayonnement et principaux ré-sultats. a,** Représentation schématique de l'expérience. **b,** amplitude de l'écho de Hahn mesurée lorsque le commutateur est connecté à la résistance chaude (rouge) et froide (bleue). **c,** relaxation des spins mesurée lorsque l'interrupteur est réglé sur la résistance chaude (rouge) et froide (bleue). Les lignes solides sont des fits exponentiels avec constante de temps Γ_1^{-1}.
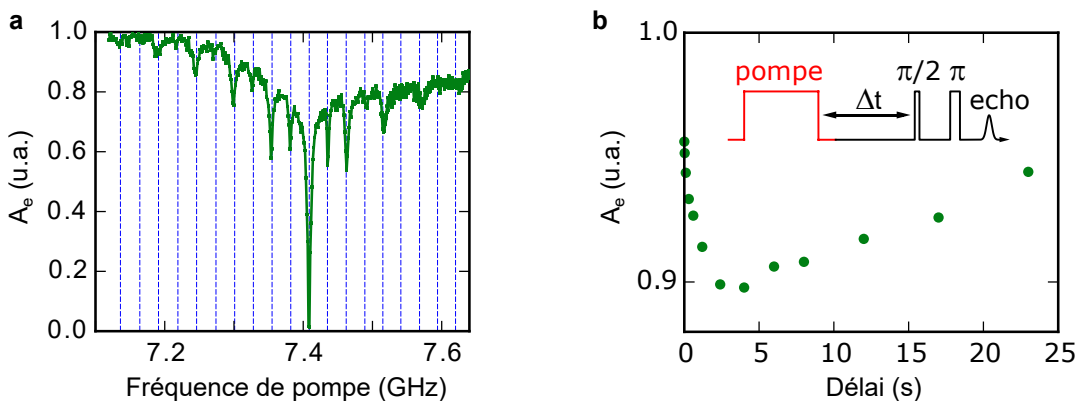
Figure 0.5: **Transfert de polarisation. a,** Amplitude de l'écho en fonction de la fréquence de la pompe à $B_0 = 10\,\mathrm{mT}$. La pompe est presque constamment en marche. Les lignes pointillées sont les fréquences de transition de spin à ce champ. **b,** Amplitude de l'écho mesurée pour $\omega_{\mathrm{pump}}/2\pi = 7.518\,\mathrm{GHz}$ en fonction du délai entre une impulsion de pompe de $10\,\mathrm{ms}$ et la détection de l'écho.

Pour étudier ce processus, nous réalisons une expérience de double résonance. Dans cette expérience, la polarisation d'une transition est surveillée tandis qu'une autre est saturée. En présence d'un transfert de polarisation, la polarisation de la transition surveillée devrait diminuer en conséquence de l'excitation de la seconde. Dans la Fig.0.5a, nous rapportons le résultat de l'amplitude de l'écho A_e mesurée en fonction de la fréquence d'une signal de pompe. Une baisse est observée chaque fois que la pompe est en résonance avec une autre transition, ce qui démontre le transfert de polarisation à faible champ. Ce processus n'est par contre pas observé à champ plus élevé, où la relaxation longitudinale de spins est constamment dans le régime de Purcell.

Dans une deuxième expérience, nous abordons la dynamique du processus en mesurant le temps nécessaire au transfert de polarisation entre deux transitions. Pour ce faire, nous mesurons l'amplitude de l'écho en fonction du délai après une courte impulsion de pompe saturant une transition différente. Comme le montre la Fig.0.5b, l'amplitude de l'écho atteint un minimum quelques secondes après l'impulsion, ce qui montre que le transfert de polarisation se fait sur des échelles de temps comparables à la relaxation de Purcell.

Même si une analyse quantitative est nécessaire, nous concluons que le transfert de polarisation est effectivement responsable du processus de relaxation non radiatif observé. Nous soutenons que l'origine physique du processus est constituée par les bascules entre les spins de donneurs voisins, dont nous parlons dans Sc.4.3.

Nous remarquons enfin qu'en présence d'une telle dynamique de population, le refroidissement radiatif d'une transition hyperpolariserait l'ensemble du spectre RPE des donneurs. Les preuves rapportées d'un refroidissement du spin à faible champ (voir Sc.6.5.2) indiquent qu'il s'agit d'un scénario réaliste. Cependant, nous ne disposons d'aucune preuve expérimentale de cet effet.

Chapter 1

Introduction

The discovery of the interaction of spins with electromagnetic radiation at rf or microwave frequencies lead to the development of magnetic resonance, pioneered by Rabi, Bloch and Purcell [1–3]. In usual magnetic resonance experiments, the spin-photon coupling is the weakest energy scale in the system. Electromagnetic radiation by the spins, which enables spin detection, has no measurable impact on spin dynamics. The latter remains entirely governed by the coupling to other environmental degrees of freedom, such as atomic or molecular motion, phonons, or dipolar interaction with other spins. The spin temperature is thus set by the host lattice independently of the thermal radiation. However, already in the early days of magnetic resonance, Purcell predicted that spin radiative relaxation should be enhanced by inserting the sample in a resonant cavity of small mode volume and high quality factor [8]. First observations of Purcell-enhancement with spins were reported in 1985 by Sleator et al. [4] for an ensemble of Cl nuclear spins. The radiative emission rate was accelerated by 11 order of magnitudes, reaching $10^{-16}\,\mathrm{s}^{-1}$. The relaxation time of about 3000 years was however still significantly larger than the dominant non-radiative relaxation times estimated to be on the order of days in the experiment, keeping the spins well thermalized to the lattice.

The Purcell regime, in which radiation is the dominant spin relaxation channel, was reached only recently in experiments by Bienfait et al. [5], using superconducting micro-resonators developed for quantum information applications. The obtained enhancement of the spin-photon coupling has been exploited to reach record ESR sensitivity and has potential interest for quantum information [6].

The focus of this thesis is to explore the consequences of the Purcell regime on spin thermalization. Our main idea is that, in the Purcell regime, spins should thermalize to the temperature of the microwave photons in the cavity, and become in a sense decoupled from the host lattice. We demonstrate this idea by proving that spins can be cooled at a temperature lower than the sample, simply by radiative processes. Moreover, this spin cooling approach represents a new general method to hyperpolarize an ensemble of electron spins.

The first part of the manuscript is dedicated to the conceptual tools necessary to understand the experiments. We provide theoretical background on quantum circuits at microwave frequency, and on spins. We introduce the quantum description of the modes of cavities and transmission lines, with a focus on their thermal state and noise properties. We then turn to electron spins and their interaction with the electromagnetic radiation, and we describe the Purcell effect and the principles of pulsed Electron Spin Resonance (ESR) spectroscopy. Finally, we introduce the electron spin system studied

in our experiment: bismuth donors in silicon.

The second part of the thesis contains the main experimental results, which are described in chapters 5, 6 and 7. Chapter 5 describes the implementation of the spectrometer with a superconducting resonator and the spectroscopy of the bismuth donors. Electron-Spin-Echo Envelope Modulation is observed, caused by the bath of ^{29}Si nuclear spins. As regards spin relaxation, we prove that bismuth donor spins reach the Purcell regime at sufficiently large magnetic field. At lower fields, non-radiative polarization transfer processes enabled by the nuclear spin environment take over Purcell relaxation.

The radiative cooling of the bismuth donors in the Purcell regime is demonstrated in the sixth chapter of the thesis. Spins are first shown to be thermalized to the cavity mode at the sample temperature of 850 mK. The cavity mode is then cooled by connecting its input to a cold resistor at 15 mK. A twofold increase of the spin polarization reveals that the spin temperature is reduced down to 350 mK, proving that spins are radiatively cooled below the sample temperature [7].

In the last chapter of the thesis we investigate the origin of the non-radiative spin relaxation observed at low magnetic field. We demonstrate that polarization transfer within the bismuth donor spectrum is present, probably due to spin flip-flop processes.

1.1   Principle of spin radiative cooling

To introduce the principle of spin radiative cooling, let us consider a physical system exchanging energy with several baths at different temperatures. The system will equilibrate at an intermediate temperature whose value will depend on the strength Γ_j with which the system is coupled to each bath, defined as the rate at which the system relaxes to its ground state by emitting a quantum of energy into bath j if it is at zero temperature. If one relaxation rate Γ_{j0} is much larger than all the others, the system will thermalize to bath $j0$, regardless of the temperature of the others.
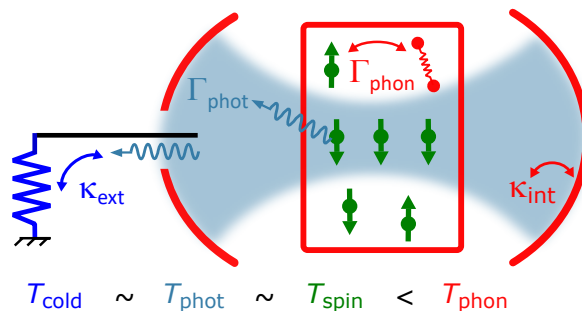
Figure 1.1: **Spin radiative cooling principle.** Spins (green) in a crystal (red) are coupled both to a bath of phonons at temperature T_{phon} with a rate Γ_{phon} and to a bath of microwave photons at a temperature T_{phot} with a rate Γ_{phot}, which determines their equilibrium temperature T_{spin}. The temperature of the photons T_{phot} is determined by their coupling with rate κ_{int} to the cavity internal losses at T_{phon} and with rate κ_{ext} to the load located at the cavity input. When this load is placed at low temperature T_{cold}, the intra-cavity field is radiatively cooled provided that $\kappa_{\text{ext}} \gg \kappa_{\text{int}}$ and the spins are cooled in turn if $\Gamma_{\text{phot}} \gg \Gamma_{\text{phon}}$.

The principle of spin radiative cooling is illustrated in Fig.1.1. The system we aim to

cool down is an ensemble of electron spins interacting with two baths: the phonons in its host lattice of temperature T_{phon} and the microwave photons in its electromagnetic environment of temperature T_{phot}. As said earlier, the radiative spontaneous emission rate Γ_{phot}, in usual magnetic resonance conditions, is much lower than the spin-lattice relaxation rate Γ_{phon}, so that the spin temperature T_{spin} equilibrates at T_{phon}.

However, the Purcell effect offers the possibility to reverse this scenario: inserting the spins in the small mode volume of a high-quality-factor cavity can accelerate the radiative spontaneous emission rate up to the point $\Gamma_{\mathrm{phot}} \gg \Gamma_{\mathrm{phon}}$, thus bringing the spins at thermal equilibrium with the cavity mode. The obtained condition $T_{\mathrm{spin}} \approx T_{\mathrm{phot}}$ offers then the possibility to cool the spins at a temperature lower than the lattice, by controlling T_{phot}.

Similarly to the spin system, the cavity mode exchanges energy with two baths. As seen in Fig.1.1, it is coupled with rate κ_{int} to the internal losses at T_{phon} and with rate κ_{ext} to the thermal radiation emitted by a cold resistor of temperature T_{cold} connected to the cavity input. By engineering the input port so that $\kappa_{\mathrm{ext}} \gg \kappa_{\mathrm{int}}$, the cavity mode temperature is then thermalized at T_{cold}. As a consequence, spins in the Purcell regime are expected to be radiatively cooled to T_{cold}, regardless of the sample temperature.

Before describing the experimental realization of radiative cooling, in the first part of the thesis we provide the theoretical background necessary to discuss all the relevant aspects of the experiment. In Chapter 2 we introduce the quantum description of our microwave circuit consisting in the superconducting cavity, transmission lines and amplifier. Since we are particularly interested in the thermal state of such a circuit, we focus on thermal noise and its detection.

We then move, in Chapter 3, to the description of the dynamics of spins coupled to a microwave cavity. Two key quantities are introduced: the cavity mode energy relaxation rate $\kappa = \kappa_{\mathrm{ext}} + \kappa_{\mathrm{int}}$ and the spin-photon interaction strength $\hbar g$, which is the product of the spin magnetic dipole moment and the magnetic field vacuum fluctuations at the spin location. At resonance, the Purcell spontaneous relaxation rate is $\Gamma_{\mathrm{phot}} = 4g^2/\kappa$. Purcell relaxation at finite temperature is also considered since it is of key importance in our experiment. The rate at which spins relax to thermal equilibrium in Purcell regime is shown to be $\Gamma_1 = \Gamma_{\mathrm{phot}}[2n_{\mathrm{th}}(T_{\mathrm{phot}}) + 1]$, where $n_{\mathrm{th}}(T_{\mathrm{phot}})$ is the thermal photon population in the cavity at T_{phot}. The last part of the chapter provides a brief description of standard pulse ESR spectroscopy techniques and concepts, and in particular of the Hahn echo sequence. To infer the spin temperature, we indeed use the fact that the spin echo amplitude A_e is proportional to the temperature-dependent polarization $p(T_{\mathrm{spin}})$. Interestingly, $p(T_{\mathrm{spin}})$ is expected to have the same temperature dependence as Γ_1 for an ensemble of spins 1/2, a simple prediction we test in this thesis.

Our experiments are performed with a model spin system, the electron spin of bismuth donors in silicon. They consist of substitutional bismuth atoms in the silicon lattice in their neutral state, where they trap a conduction electron. We describe the structure and properties of bismuth donors in silicon in Chapter 4.

1.2 ESR spectroscopy of bismuth in natural silicon

In Chapter 5 we describe the setup of the ESR spectrometer and report on bismuth donor spectroscopy experiments performed at $15\,\mathrm{mK}$ with B_0 between 0 and $70\,\mathrm{mT}$. The spectrometer design is based on the work of Bienfait et al. [6]. The cavity is a superconducting resonator of frequency ω_0 made of a thin film of niobium patterned

on top of the silicon chip implanted with bismuth donors (see Fig.1.2a). The donor electron spins Larmor frequency ω_{spin} is tuned at resonance with the cavity by the application of an external magnetic field B_0 parallel to the inductor wire. Spins close to the wire are coupled with strength g to the cavity mode (see Fig.1.2b). The sample is mounted in a Cu holder and coupled capacitively to a microwave antenna that sets the coupling rate κ_{ext} such that $\kappa_{\text{ext}} \gg \kappa_{\text{int}}$.
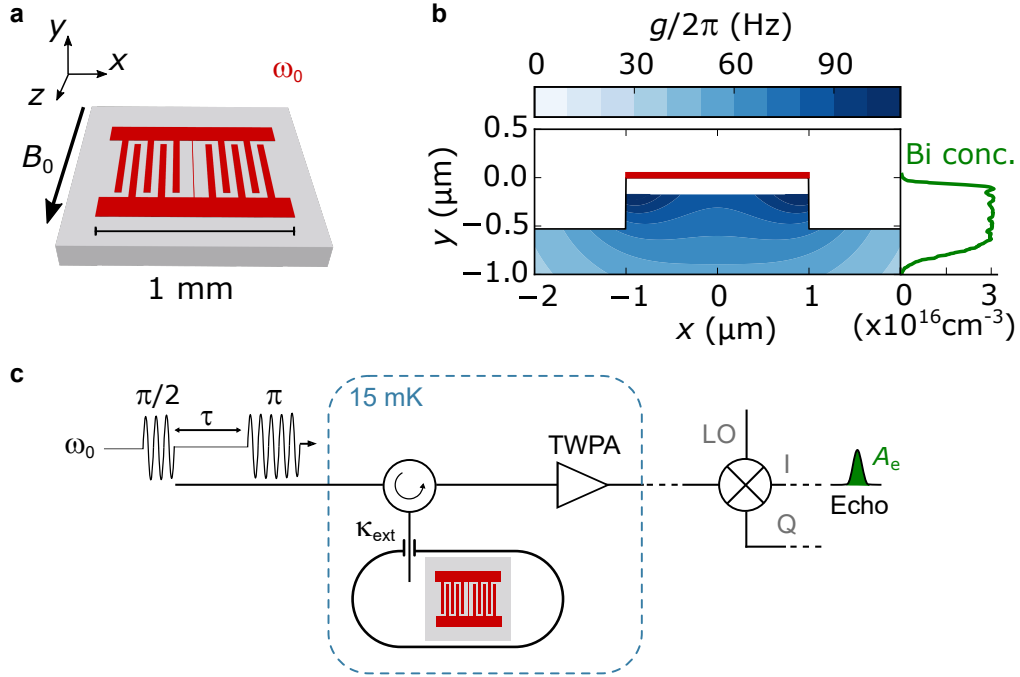
Figure 1.2: **ESR spectrometer with a superconducting resonator. a,** Niobium superconducting resonator (red) patterned on top of a silicon chip implanted with bismuth donors. **b,** Device cross section around the inductor wire (red). The spin-photon coupling constant g (color code) is represented in the Bi-doped region. **c,** Schematic representation of the spectrometer setup with the Hahn-echo pulse sequence illustrated on the input line.

We detect the magnetic resonance signal by means of pulsed ESR spectroscopy techniques. We use in particular the Hahn echo sequence where a $\pi/2$ pulse is followed after a time τ by a π pulse inducing rephasing of the spins and the echo emission after a further delay τ. After amplification, the emitted echo is demodulated and recorded at room temperature (see Fig.1.2c).

Measurement of the echo amplitude A_{e} as a function of B_0 shows a peak of signal whenever a bismuth donor spin transition is resonant with the cavity (see Fig.1.3a). We discuss the spectrum in Sc.5.4.1.

In Sc.5.6 we show that at 15 mK the highest field spin transition relaxes at the calculated radiative spontaneous emission rate Γ_{phot}, demonstrating that spins are in the Purcell regime (see Fig.1.3b). The spin relaxation is then measured as a function of temperature. The extracted spin relaxation rate Γ_1 follows the expected temperature dependence of the Purcell rate (see Fig.1.3c), showing that spins stay in the Purcell regime at temperatures above 1 K.

The study of spin relaxation at lower magnetic field reveals that a non-radiative relaxation process is present. We attribute this to polarization transfer by flip-flop processes
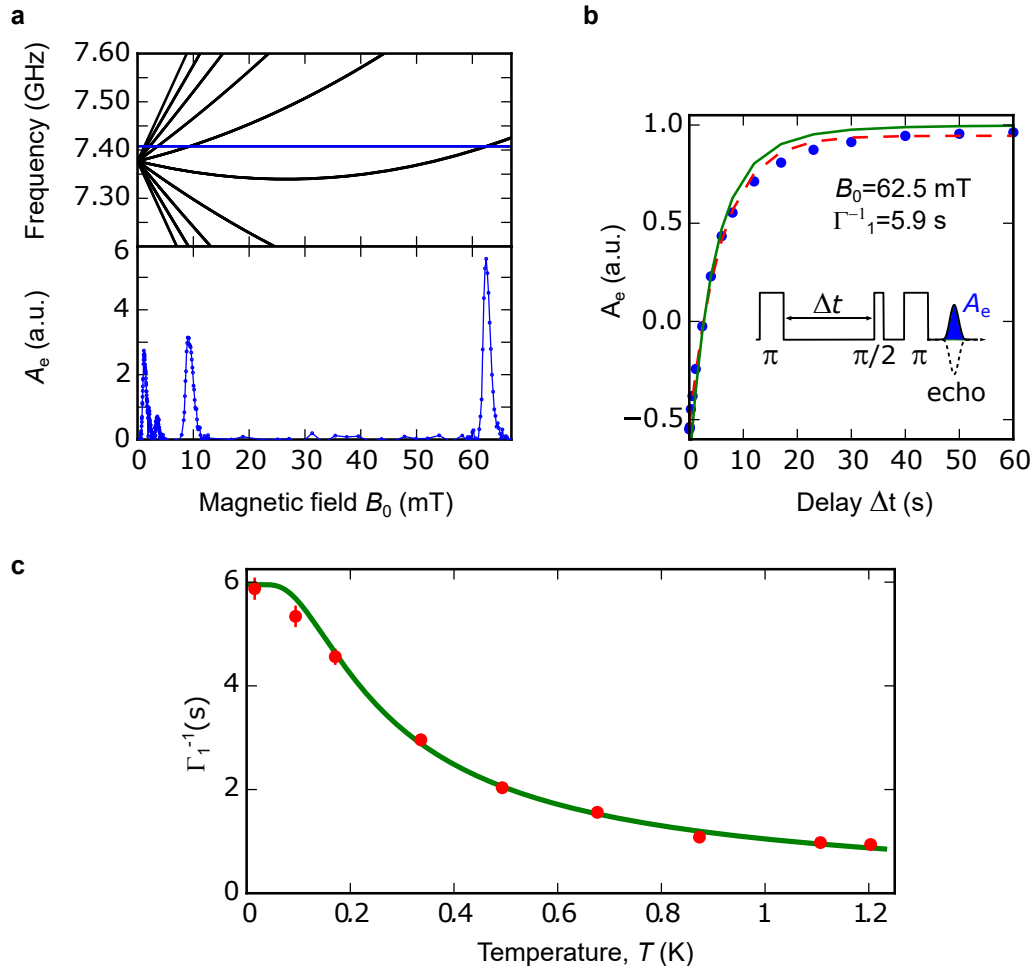
Figure 1.3: **ESR spectroscopy of bismuth: main results. a,** Top, calculated ESR transitions frequency as a function of B_0. The resonator frequency is reported in blue. Bottom, measured echo amplitude as a function of B_0. **b,** Spin longitudinal relaxation measured with the inversion recovery sequence illustrated in the inset at $B_0 = 62.5\,\text{mT}$. Dashed red line is an exponential fit with time constant Γ_1^{-1}. Numerical simulation of the Purcell relaxation is shown in green. **c,** Relaxation time Γ_1^{-1} measured as a function of temperature (red). The expected temperature dependence for Purcell relaxation is shown in green.

between neighbouring donors, enabled by the silicon nuclear spin environment. We experimentally investigate this process in the last chapter 7 of the thesis.

1.3 Radiative cooling of an electron spin ensemble

The radiative cooling demonstration is reported in Chapter 6. The setup is schematically represented in Fig.1.4a. The sample is thermalized at $T_{\mathrm{phon}} = 850\,\mathrm{mK}$, while the cavity input is connected via a switch either to a hot resistor at T_{phon} or to a cold one at $T_{\mathrm{cold}} = 15\,\mathrm{mK}$. In the cold switch configuration, spins in the Purcell regime are then expected be cooled at the cavity mode temperature $T_{\mathrm{phot}} \approx T_{\mathrm{cold}}$, well below T_{phon}. The cooling factor η is defined as the ratio of spin polarization in the two switch configurations. Since spin polarization and Purcell relaxation rate have the same temperature dependence, η is also expected to be equal to the ratio between the spin relaxation rate measured in the two switch settings.
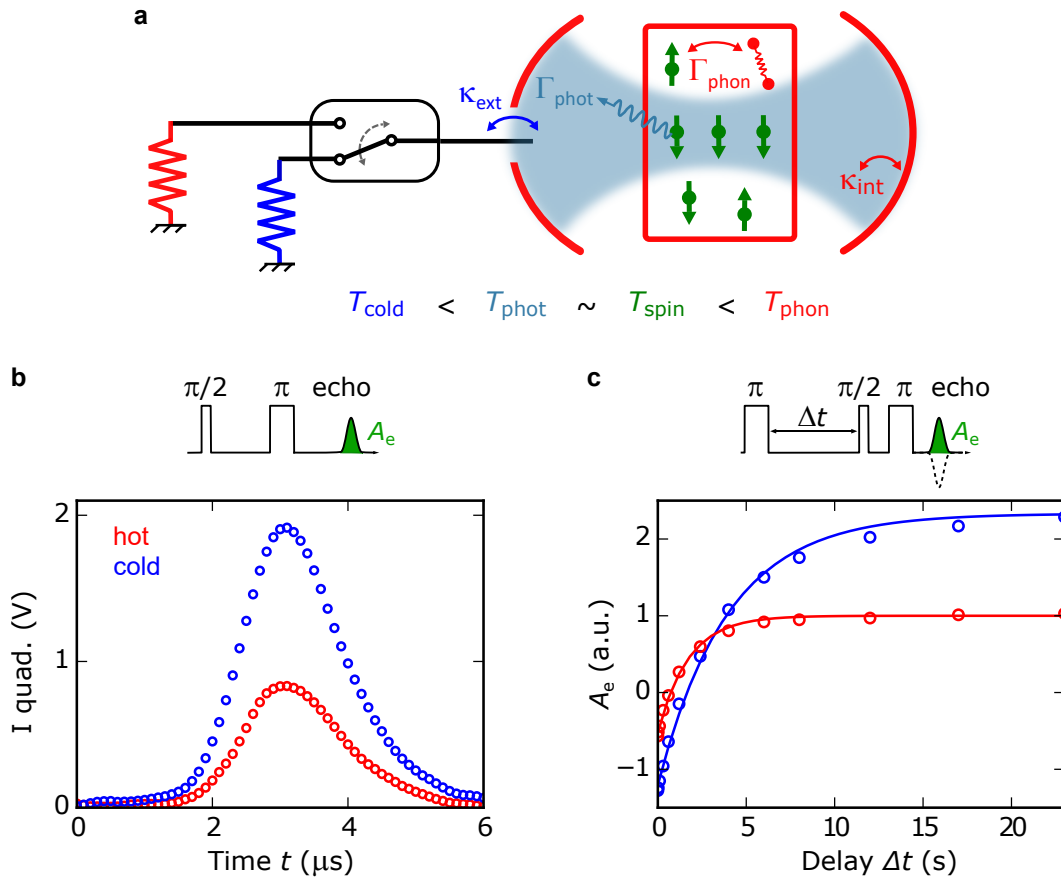
Figure 1.4: **Radiative cooling principle and main results. a,** Schematic representation of the experiment. **b,** Hahn echo amplitude measured when the switch is connected to the hot (red) and cold (blue) resistor. **c,** Spin relaxation measured in the hot (red) and cold (blue) switch setting. Solid lines are exponential fit with time constant Γ_1^{-1}.

We first determine T_{phot} in the two switch configurations with a set of noise measurement detailed in Sc.6.4. We find that connecting the resonator input to the cold resistor, the cavity mode temperature is radiatively cooled down to $T_{\mathrm{phot}}^{\mathrm{cold}} = 500 \pm 60\,\mathrm{mK}$. We

attribute the only partial cooling to the presence of microwave losses in between the resonator and the cold resistor.

The Hahn-echo signal more than doubles when measured in the cold configuration (see Fig.1.4b), demonstrating radiative hyperpolarization with $\eta = 2.3\pm0.1$ (see Sc.6.5). We also measure the relaxation rates for the two switch settings and find $\Gamma_1^{\text{hot}}/\Gamma_1^{\text{cold}} = \eta$, as expected (see Fig.1.4c). The measured η corresponds to a spin temperature $T_{\text{spin}} = 350 \pm 10\,\text{mK}$, which is close to (or even slightly lower than) the field temperature $T_{\text{phot}}^{\text{cold}}$ estimated from noise measurements. This proves that spin-lattice relaxation is not the factor limiting the spin cooling, and that the spins thermalize to the temperature of their electromagnetic environment within the accuracy of the experiment.

We conclude the chapter with a brief discussion of possible applications of this new hyperpolarization technique to magnetic resonance spectroscopy.

1.4 Polarization transfer in bismuth donors

As discussed earlier, we observe at low field a relaxation process competing with the radiative Purcell relaxation. In the last chapter Ch.7 we experimentally investigate its origin.

We attribute this effect to polarization transfer between different hyperfine levels of the bismuth donor spectrum via flip-flops between pairs of donors coupled by the dipolar interaction. Such polarization transfer appears as a faster relaxation on the transition probed by the microwave cavity.
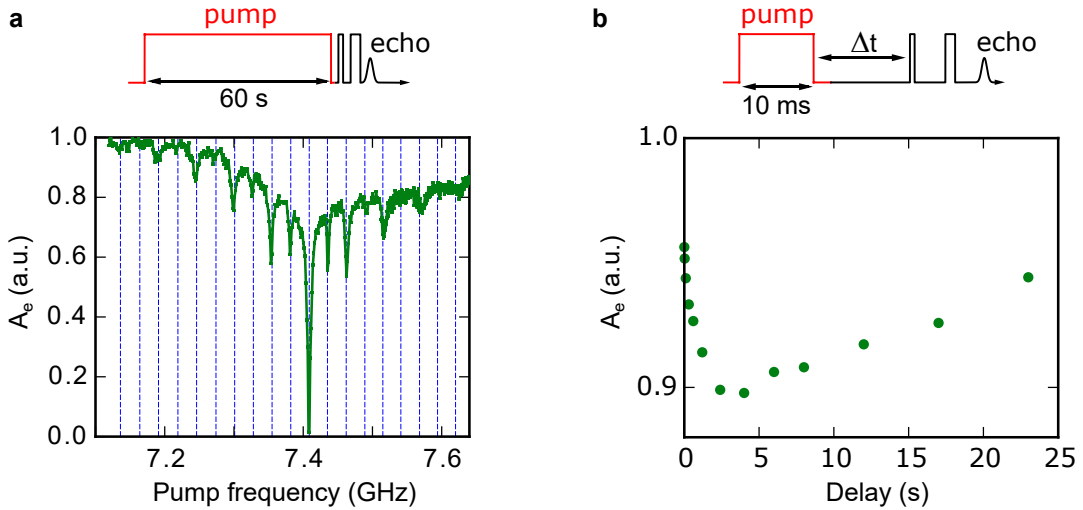
Figure 1.5: **Polarization transfer. a,** Echo amplitude as a function of the pump frequency at $B_0 = 10\,\text{mT}$. The pump is almost constantly on. Dashed lines are the spin transition frequencies at this field. **b,** Echo amplitude measured for $\omega_{\text{pump}}/2\pi = 7.518\,\text{GHz}$ as a function of the delay between a 10 ms pump pulse and echo detection.

In order to study this process, we perform a double resonance experiment. In such experiment, the polarization of one transition is monitored while another one is saturated. In the presence of polarization transfer, the polarization of the monitored transition is expected to decrease as a consequence of the excitation of the second one. In Fig.1.5a we report the result of the echo amplitude A_e measured as a function of the frequency of a pump tone. A dip is observed whenever the pump is resonant with another transition,

demonstrating polarization transfer at low field. This process is instead not observed at higher field, where spin longitudinal relaxation is consistently in the Purcell regime.

In a second experiment we address the dynamics of the process by measuring how long it takes for polarization to be transferred between two transitions. To do so, we measure the echo amplitude as a function of the delay after a short pump pulse saturating a different transition. As seen in Fig.1.5b, the echo amplitude reaches a minimum a few seconds after the pulse, showing that polarization transfer takes place on timescales comparable to the Purcell relaxation.

Even if a quantitative analysis is needed, we conclude that the polarization transfer is indeed responsible for the observed non-radiative relaxation process. We argue that the physical origin of the process are flip-flops between neighbouring donor spins, that we discuss in Sc.4.3.

We finally notice that in the presence of such population dynamics, the radiative cooling of one transition would hyperpolarize the whole donor ESR spectrum. The reported evidence of spin cooling at low field (see Sc.6.5.2) indicates that this is a realistic scenario. However, we have no experimental evidence of this effect.

Chapter 2

Quantum circuits

In the spin radiative cooling experiment, a central role is played by the microwave cavity to which spins are coupled and by the circuit to which it is connected. In this chapter we provide a quantum description of this microwave environment, forming the framework of the experiments reported in this thesis.

Before that, we address a simple physical question that we are going to encounter all along this thesis, that is how to determine the equilibrium temperature T_{sys} of a physical system coupled to N baths of different temperature T_j. As we derive in Appendix A, T_{sys} will be an intermediate temperature dependent on the strength Γ_j with which the system is coupled to each bath, defined as the rate at which the system would spontaneously relax from its first excited to its ground state by emitting a quantum of energy into this bath at zero temperature. For a system coupled to N bosonic reservoirs, T_{sys} is obtained by

$$n_{\text{th}}(T_{\text{sys}}) = \sum_{j=1}^{N} \frac{\Gamma_j}{\Gamma} n_{\text{th}}(T_j), \tag{2.1}$$

where

$$n_{\text{th}}(T) = \frac{1}{e^{\hbar \omega_{\text{sys}}/kT} - 1} \tag{2.2}$$

is the occupation number of a bosonic mode of frequency ω_0, and $\Gamma = \sum_{j=1}^{N} \Gamma_j$ the total system-bath coupling. If the system is dominantly coupled to one bath $j0$ ($\Gamma_{j0} \gg \Gamma_{j \neq 0}$), the system therefore equilibrates close to T_{j0} regardless of the temperature of the other reservoirs.

In this chapter, we apply this insight to the thermalization of the mode of a microwave cavity coupled to several reservoirs. We first describe the main properties of quantum microwave fields as well as the principal quantum states used later on. We then recall the quantization of a LC resonator as well as of the propagating modes in a transmission line. We continue by giving elements of input output theory, which describes how the intra-cavity field of a resonator is related to the propagating modes of the transmission lines to which it is coupled. At the end of this part we use the obtained results to calculate the thermal state of the circuit we use in the radiative cooling experiment. In the second part of the chapter we introduce the quantum theory of linear amplifiers to discuss the quantum limits on amplification and introduce the Josephson Travelling Wave Amplifier used in this work. We end this chapter presenting the superconduct-

ing microwave switch used in the radiative cooling experiment to study the cooling dynamics.

2.1   Quantum description of an electromagnetic mode

In classical electrodynamics, an electromagnetic mode of frequency ω is characterized by its complex amplitude $A = |A| e^{i\phi}$. An equivalent practical representation consists in the in-phase and out-of-phase quadratures $X = \mathrm{Re}(A)$ and $Y = \mathrm{Im}(A)$, as shown in Fig.2.1a. The quantum mechanical description of the mode is obtained promoting the canonical conjugate quadratures to the corresponding quantum operators $\hat{X}$ and $\hat{Y}$ obeying the commutation relation $[\hat{X}, \hat{Y}] = i/2$. The variance of the two quadratures is then bounded by the Heisemberg uncertainty principle $\langle \Delta \hat{X}^2 \rangle \langle \Delta \hat{Y}^2 \rangle \geqslant 1/16$. It is also possible to describe the field by the annihilation and creation operators defined as:

$$\hat{a} = \hat{X} + i\hat{Y}$$
$$\hat{a}^\dagger = \hat{X} - i\hat{Y}$$

(2.3)

obeying the commutation relation $[\hat{a}, \hat{a}^\dagger] = 1$. The eigenvalue n of the number operator $\hat{n} = \hat{a}^\dagger \hat{a}$ represents the number of photons populating the mode. The mode state can then be also defined in the Fock basis of the $\hat{n}$ operator eigenstates.
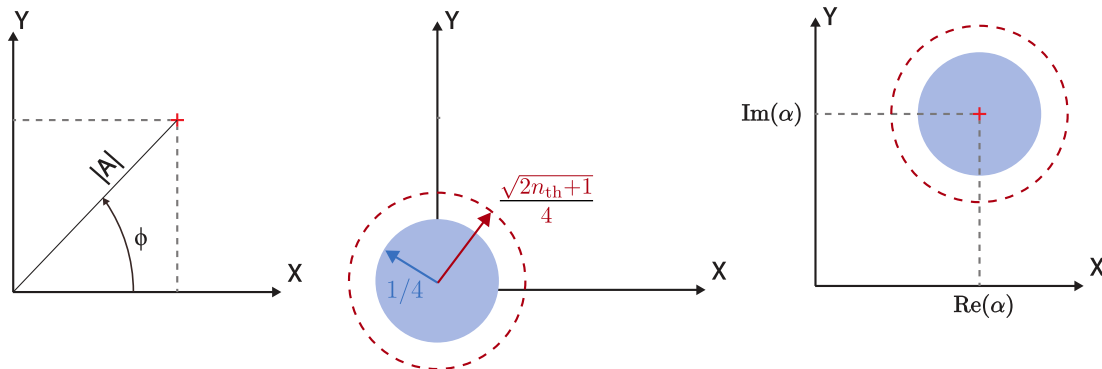
Figure 2.1: **Electromagnetic field state phase-space representation. a** Classical picture. **b** Vacuum (solid fill) and thermal (red dashed) states. **c** Coherent (blue fill) and coherent thermal (dashed red line) states.

We now briefly go through three states of an electromagnetic mode that are used in the following of this thesis. We focus on their representation and particularly on their noise properties, relevant for the discussions on the modes thermalization.

2.1.1   Vacuum state

The lowest energy state $|n = 0\rangle$ in the Fock basis is called the vacuum state. It contains zero photons and the expectation value of the two quadratures is also fixed to zero, $\langle \hat{X} \rangle = \langle \hat{Y} \rangle = 0$. However, the quadratures variance satisfies:

$$\langle \Delta \hat{X}^2 \rangle = \langle \Delta \hat{Y}^2 \rangle = \frac{1}{4}.$$

(2.4)

The field fluctuations are therefore non-zero even in the vacuum state and coincide with the minimal variance authorized by the Heisenberg principle for two quadratures verifying $\langle \Delta \hat{X}^2 \rangle = \langle \Delta \hat{Y}^2 \rangle$ (see Fig.2.1b). The finite value of these zero point fluctuations (ZPF) determines the coupling strength of a two level system (TLS), such a spin 1/2, to the electromagnetic radiation. Moreover, it fixes the quantum limits to amplification and noise.

2.1.2 Thermal state

In an electromagnetic mode at thermal equilibrium with a bath of temperature T a thermal state is established. It is a statistical mixture of Fock states $|n\rangle$ given by the Boltzmann distribution, and the mean-value and variance of the two quadratures (see Fig.2.1b) can be shown to be:

$$\langle \Delta \hat{X} \rangle = \langle \Delta \hat{Y} \rangle = 0 \tag{2.5}$$

$$\langle \Delta \hat{X}^2 \rangle = \langle \Delta \hat{Y}^2 \rangle = \frac{2n_{th} + 1}{4}. \tag{2.6}$$

The noise is therefore an indicator of the mode temperature via the mean number of thermal photons $n_{\text{th}}(T)$.

   In the high temperature limit $kT \gg \hbar\omega$, the quadrature thermal fluctuations in Eq.2.6 reduce to $kT/2\hbar\omega$, thus showing a linear dependence on T. On the opposite side, in the low temperature limit $kT \ll \hbar\omega$, the thermal state tends to the vacuum state and the noise approaches the quantum limit $\langle \Delta \hat{X}^2 \rangle = 1/4$.

2.1.3 Coherent states

The electromagnetic classical signals that are here used as drives for both spins and cavity are well described by the eigenstates $|\alpha\rangle$ of the annihilation operator $\hat{a}$, called coherent states. The number of photons populating such states obeys Poissonian statistics and its mean value is $\langle \alpha | \hat{a}^\dagger \hat{a} | \alpha \rangle = |\alpha|^2$. The coherent state for $\alpha = 0$ thus coincides with the vacuum state. Concerning the field quadratures, they show the same variance of vacuum $\langle \Delta \hat{X}^2 \rangle = 1/4$, while the mean value is given by α: $\langle \Delta \hat{X} \rangle = \text{Re}(\alpha)$, $\langle \Delta \hat{Y} \rangle = \text{Im}(\alpha)$, as shown in Fig.2.1c. If the variance is instead given by the thermal fluctuations of Eq.2.6, we speak of coherent thermal states.

2.2 The cavity and the propagating modes

2.2.1 The cavity: an LC resonator

The electromagnetic environment for the spins in the course of this thesis will be the resonant mode of an LC circuit, whose quantum description and relevant characteristics are addressed hereafter. We consider a resonator consisting in an inductance L in parallel with a capacitance C. The magnetic flux Φ in the inductor and the charge q in the capacitor are conjugate variables represented by the operators $\hat{\Phi}$ and $\hat{q}$ obeying the commutation relation $[\hat{\Phi}, \hat{q}] = i\hbar$. The LC harmonic oscillator Hamiltonian is then:

$$\hat{H}(\hat{\Phi}, \hat{q}) = \frac{\hat{\Phi}^2}{2L} + \frac{\hat{q}^2}{2C}, \tag{2.7}$$
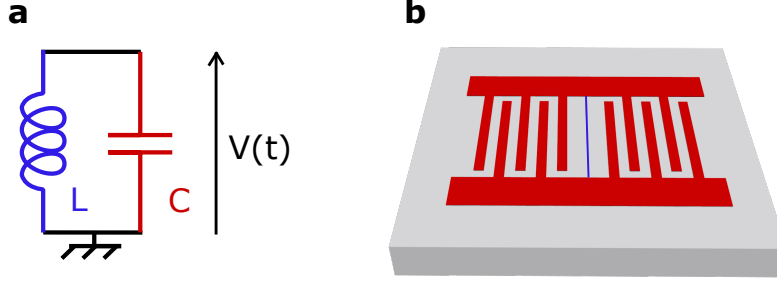
Figure 2.2: **LC oscillator. a,** Schematic **b,** Example of implementation: a superconducting planar resonator comprising a interdigitated capacitance (red) in parallel with an inductor wire (blue).

which can be expressed in the occupation number representation as:

$$\hat{H} = \hbar\omega_0(\hat{a}^\dagger\hat{a} + \frac{1}{2}), \tag{2.8}$$

with $\hat{a}$ and $\hat{a}^\dagger$ related to $\hat{\Phi}$ and $\hat{q}$ by:

$$\hat{a} = \frac{1}{\sqrt{2\hbar Z_0}}(\hat{\Phi} + iZ_0\hat{q}) \tag{2.9}$$

$$\hat{a}^\dagger = \frac{1}{\sqrt{2\hbar Z_0}}(\hat{\Phi} - iZ_0\hat{q}), \tag{2.10}$$

where $\omega_0 = 1/\sqrt{LC}$ is the resonator frequency and $Z_0 = \sqrt{L/C}$ the resonator impedance. We then express the voltage $\hat{V}$ across the capacitor and the current $\hat{I}$ in the inductor as a function of the bosonic operators:

$$\hat{V} = \frac{\hat{q}}{C} = i\omega_0\sqrt{\frac{\hbar Z_0}{2}}(\hat{a}^\dagger - \hat{a}) \tag{2.11}$$

$$\hat{I} = \frac{\hat{\Phi}}{L} = \omega_0\sqrt{\frac{\hbar}{2Z_0}}(\hat{a}^\dagger + \hat{a}). \tag{2.12}$$

Fock states $|n\rangle$ are eigenstates of $\hat{H}$ and verify $\hat{H}|n\rangle = \hbar\omega_0(n + \frac{1}{2})$. The resonator ground state is the vacuum state $|0\rangle$ and thus voltage and current zero point fluctuations are given by:

$$\delta I^2 = \langle 0|\hat{I}^2|0\rangle = \frac{\hbar\omega_0^2}{2Z_0} \tag{2.13}$$

$$\delta V^2 = \langle 0|\hat{V}^2|0\rangle = \frac{\hbar Z_0\omega_0^2}{2}. \tag{2.14}$$

The LC circuit current and voltage vacuum fluctuations generate, respectively, a magnetic field $\hat{B}(r) = \delta B(r)(\hat{a} + \hat{a}^\dagger)$ around the inductor wire and an electric field $\hat{E}(r) = i\delta E(r)(\hat{a} - \hat{a}^\dagger)$ in between capacitor plates, where $\delta B(r)$ and $\delta E(r)$ are the fields rms vacuum fluctuations at position r. The amplitude of magnetic field fluctuations δB at

the spin locations determines the coupling of the spins to the resonator mode and thus their ability to thermalize to it.

2.2.2 The propagating modes: lossless transmission lines
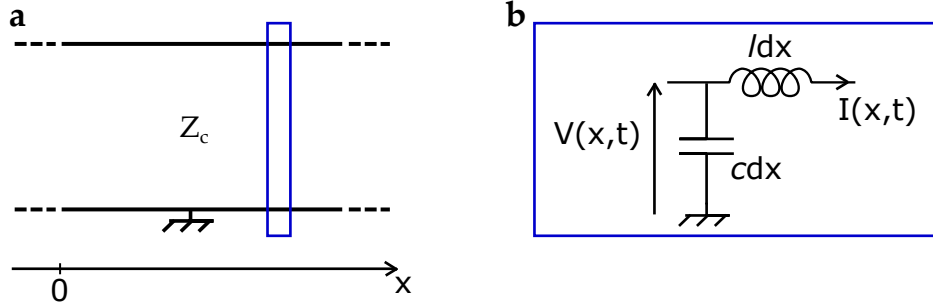
Figure 2.3: **Transmission line. a** Two wire representation. **b** Each infinitesimal part of a transmission line can be modeled as an LC.

The second kind of electromagnetic modes we encounter all along this work are propagating waves in coaxial lines, realizing the main environment to which the LC cavity is coupled. Propagating modes in coaxial cables and planar waveguides are described in classical electromagnetism by transmission line theory [9]. A transmission line can be modeled as a chain of infinitesimal lumped element LC circuits, with series inductance l and parallel capacitance c per unit length, as shown in Fig.2.3. The solution of the resulting wave equation describing the circuits are a left and a right propagating wave whose sum gives the voltage across the capacitance c for each location x and time t, $V(x, t)$:

$$V(x, t) = V^{\rightharpoonup}(x, t) + V^{\leftharpoonup}(x, t), \tag{2.15}$$

where $V^{\leftrightharpoons}(x, t) = V_0^{\leftrightharpoons} \cos \left[\omega(t \pm x/v_{ph}) + \phi_0^{\leftrightharpoons} \right]$, with $v_{ph} = 1/\sqrt{lc}$ the phase velocity and $\phi_0^{\leftrightharpoons}$ the initial phase. The current $I(x, t)$ in the infinitesimally short inductance l is related to $V(x, t)$ by the characteristic impedance $Z_{\rm c} = \sqrt{l/c}$:

$$I(x, t) = Z_{\rm c}^{-1}[V^{\rightharpoonup}(x, t) - V^{\leftharpoonup}(x, t)]. \tag{2.16}$$

In an infinite transmission line, right and left propagating modes are independent. If instead the line is terminated at $x = 0$ by a load of impedance Z_l, this couples the two counter-propagating modes:

$$V^{\rightharpoonup}(t) + V^{\leftharpoonup}(t) = \frac{Z_l}{Z_{\rm c}}(V^{\rightharpoonup}(t) - V^{\leftharpoonup}(t)). \tag{2.17}$$

This leads to the definition of the reflection coefficient R relating the left and right mode amplitudes to the load-line impedance mismatch:

$$R = \frac{V^{\leftharpoonup}(t)}{V^{\rightharpoonup}(t)} = -\frac{Z_l - Z_{\rm c}}{Z_l + Z_{\rm c}}. \tag{2.18}$$

We now move to the quantum description. A review on quantization of transmission lines is given in [10]; here we go through some useful results for subsequent discussions.

The transmission line can be described by left and right frequency-resolved mode associated to as many left and right annihilation and creation operators, $\hat{a}^{\leftleftarrows}(\omega)$ and $\hat{a}^{\leftleftarrows\dagger}(\omega)$, verifying $[\hat{a}^{\leftleftarrows}(\omega), \hat{a}^{\leftleftarrows\dagger}(\omega')] = 2\pi\delta(\omega - \omega')$. Since we are here generally interested in narrow-band signals of central frequency ω_a, it is convenient to work in the time-domain in the rotating frame at ω_a. Neglecting contributions from frequencies far from ω_a, the rotating wave approximation leads to the following expression for the propagating field operator at $x = 0$:

$$\hat{V}^{\leftleftarrows}(t) = \sqrt{\frac{\hbar\omega_a Z_\mathrm{c}}{4\pi}}(\hat{a}^{\leftleftarrows}(t) + \hat{a}^{\leftleftarrows\dagger}(t)), \qquad (2.19)$$

where $\hat{a}^{\leftleftarrows}(t)$ is the Fourier transform of $\hat{a}^{\leftleftarrows}(\omega)$ satisfying $[\hat{a}^{\leftleftarrows}(t), \hat{a}^{\leftleftarrows\dagger}(t')] = 2\pi\delta(t - t')$ (performing a Markov approximation). We stress here that $\hat{a}^{\leftleftarrows}(t)$ are propagating mode operators describing a field flux, thus the expectation value for the number of bosons in the mode gives access to the power carried by the quasi monochromatic wave of frequency ω_a:

$$P^{\leftleftarrows}(t) = \hbar\omega_a \langle \hat{a}^{\leftleftarrows\dagger}(t)\hat{a}^{\leftleftarrows}(t)\rangle. \qquad (2.20)$$

A further simplification of the notation is obtained introducing a new operator defining propagating spatio-temporal modes of finite temporal and spectral extension, at variance with the 'infinite bandwidth' operators $\hat{a}^{\leftleftarrows}(t)$. We thus define:

$$\hat{a}^{\leftleftarrows} = \int \hat{a}^{\leftleftarrows}(t)u(t)dt, \qquad (2.21)$$

where $u(t)$ is the envelope of the propagating signal mode of bandwidth $\Delta\omega$, obeying the normalization $\int [u(t)]^2 dt = 1$. The commutation relation $[\hat{a}^{\leftleftarrows}, \hat{a}^{\leftleftarrows\dagger}] = 1$ being satisfied, these spatio-temporal modes are equivalent to the bosonic annihilation and creation operators and the results of section Sc.2.1 can be used.

2.3 Cavity coupled to a transmission line

The cavity is in our experiment coupled to the modes propagating in a transmission line in order to read out its field, to drive it coherently and to achieve control over its thermal state. The LC resonator is then connected via a coupling capacitance C_c to a transmission line of characteristic impedance Z_c, as shown in Fig.2.4. A resistor R in parallel to the LC circuit models the internal losses. In this paragraph we introduce the relevant quantities characterizing the circuit before giving a quantum optics description of this system.

2.3.1 Equivalent circuit and cavity damping rates

By coupling the RLC resonator to the transmission line, its resonance frequency ω_0 and its characteristic impedance Z_0 are slightly modified. The resonator impedance $Z_{RLC} = 1/R + i(C\omega - 1/L\omega)$ seen from A (see Fig.2.4) is now connected in parallel with $Z_\mathrm{ext} = Z_\mathrm{c} + 1/iC_c\omega$. In the low coupling limit $Z_\mathrm{c}C_c\omega_0 \ll 1$ and close to resonance $\omega \sim \omega_0$, an approximate equivalent $R'L'C'$ circuit can be built (see Fig.2.4), with $L' = L$ and $C' \approx C + C_c$. The slightly renormalized frequency and characteristic
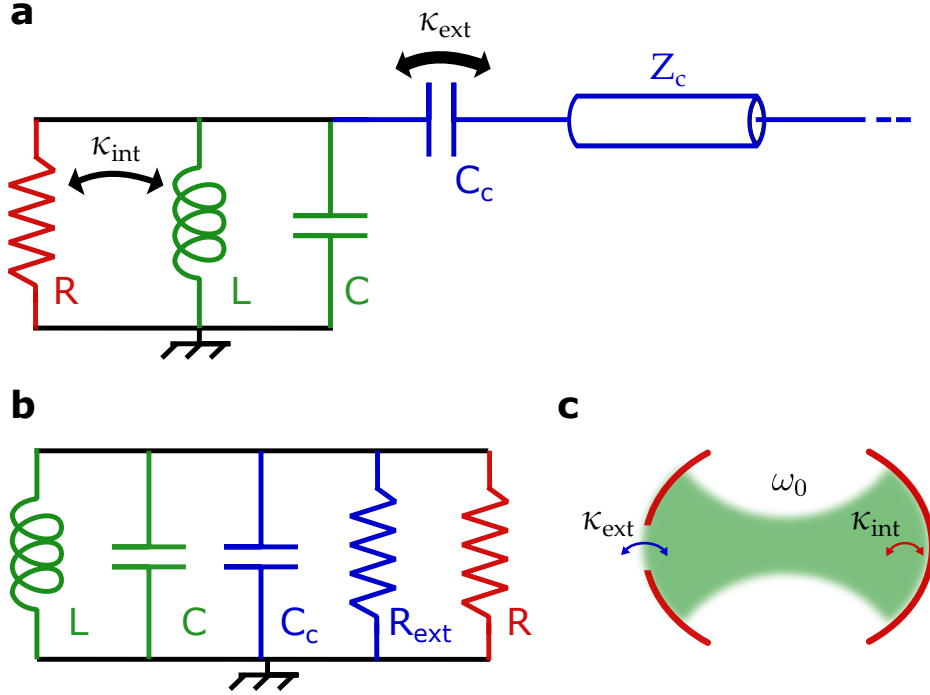
Figure 2.4: **Cavity coupled to a transmission line. a** The energy stored in the mode of the LC resonator is dissipated into the internal resistance at rate κ_{int} and leaks out into the capacitively coupled transmission line with rate κ_{ext} **b** Norton equivalent circuit. **c** Quantum optics equivalent representation.

impedance are therefore $\omega_0' = 1/\sqrt{LC'}$ and $Z_0' = \sqrt{L/C'}$. For the sake of clarity, in the following we keep the notations ω_0 and Z_0 for the renormalized values. More relevantly, the equivalent circuit enables to link the dissipation rates of the cavity to the circuit parameters. The ohmic environment modeled by R' is:

$$\frac{1}{R'} = \frac{1}{R} + \frac{1}{R_{\text{ext}}}, \quad \text{with} \quad \frac{R_{\text{ext}}}{Z_c} \approx 1/Z_c^2 C_c^2 \omega_0^2. \tag{2.22}$$

The resonator damping is then obtained from the quality factor of a *RLC* parallel circuit $Q^{-1} = R^{-1}\sqrt{L/C}$. We identify two contributions to the total quality factor $Q^{-1} = Q_{\text{ext}}^{-1} + Q_{\text{int}}^{-1}$: the external losses described by $Q_{\text{ext}}^{-1} = R_{\text{ext}}^{-1}\sqrt{L/C'}$ and the internal losses described by $Q_{\text{int}}^{-1} = R^{-1}\sqrt{L/C'}$. The energy dissipation rate into the two baths is thus defined as $\kappa_{\text{ext,int}} = \omega_0/Q_{\text{ext,int}}$.

The above results are valid in the limit of high external quality factor Q_{ext}, where $Z_c C_c \omega_0 \ll 1$. By analogy with optical cavities, the necessary high impedance of the coupling capacitance corresponds to high reflectivity of the output coupler mirror, realizing therefore a field mode well confined in the resonator.

2.3.2 Input-output theory for a driven damped cavity

The cavity mode we want to control and measure is coupled to two baths: it exchanges energy at rates κ_{int} and κ_{ext} with the internal dissipations and with the transmission line modes, respectively. Since we are interested in the field entering and leaking out from the cavity, we need here a quantum description of the full system that includes the bath modes. Such a description is obtained extending to the quantum case the

classical theory relating the cavity mode, the incoming and the outcoming waves. This quantum input-output theory is valid for the general case of a system of Hamiltonian $\hat{H}$ coupled to many continuum of modes with coupling rates κ_i.

Our system is an *LC* resonator whose Hamiltonian and field operator $\hat{a}$ have been introduced in Eqs.2.8-2.10. The transmission line constitutes a bath for the resonator and is described by the propagating operators introduced in Eq.2.19, here called $\hat{a}_{in}(t)$ for the mode propagating toward the cavity port and $\hat{a}_{out}(t)$ for outcoming mode. The coupling strength κ_i can be identified with the energy relaxation rate κ_{ext} if a Markov approximation is performed in the validity limit of coupling to a continuum of modes. The second bath consisting in internal losses is coupled with strength κ_{int} and can be treated in the exact same way as a terminated transmission line connected to a second port, defining the two other propagating operators $\hat{a}_{in,int}$ and $\hat{a}_{out,int}$. The evolution of $\hat{a}(t)$ in the Heisenberg picture is then given by the following master equation:

$$\partial_t \hat{a}(t) = \frac{[\hat{a}, \hat{H}]}{i\hbar} - \frac{1}{2}\kappa \hat{a}(t) + \sqrt{\kappa_{int}}\hat{a}_{in,int}(t) + \sqrt{\kappa_{ext}}\hat{a}_{in}(t), \quad (2.23)$$

where $[\hat{a}, \hat{H}]/i\hbar = -i\omega_0$ for a *LC* oscillator and $\kappa = \kappa_{int} + \kappa_{ext} = \omega_0/Q$ is the total cavity damping rate. The $(1/2)\kappa \hat{a}(t)$ is a damping term, while the terms $\sqrt{\kappa_i}\hat{a}_{in,i}(t)$ are the source terms. A continuity equation holds at the interface between the cavity and the transmission line, imposing that the sum of the right and left propagating fields must be equal to the field radiated by the cavity:

$$\hat{a}_{in,i}(t) + \hat{a}_{out,i}(t) = \sqrt{\kappa_i}\hat{a}. \quad (2.24)$$

2.3.3 Cavity under coherent driving

The classical fields we send to the cavity in our experiments are described by the coherent states $|\alpha\rangle$ introduced in Sec.2.1.3. Under classical drive the cavity input mode is in the eigenstate α_{in} of the propagating operator $\hat{a}_{in}$, carrying the power $P_{in} = \hbar\omega|\alpha_{in}|^2$ as given by Eq.2.20. The expectation value of the intra-cavity field $\langle \hat{a}\rangle(t) = \alpha(t)$ is then obtained from Eq.2.23:

$$\partial_t \alpha(t) = -i\omega_0\alpha(t) - \frac{\kappa_{ext} + \kappa_{int}}{2}\alpha(t) + \sqrt{\kappa_{ext}}\alpha_{in}(t). \quad (2.25)$$

After Fourier transformation we thus find the steady-state solution for α:

$$\alpha(\omega) = \frac{2\sqrt{\kappa_{ext}}}{\kappa_{int} + \kappa_{ext} - 2i(\omega - \omega_0)}\alpha_{in}(\omega). \quad (2.26)$$

At resonance, a drive of power P_{in} will stabilize a mean number of intra-cavity photons $\bar{n} = |\alpha|^2$ given by:

$$\bar{n} = \frac{4\kappa_{ext}}{\hbar\omega_0(\kappa_{ext} + \kappa_{int})^2}. \quad (2.27)$$

The amplitude of the coherent cavity field is for us of particular relevance since it determines the transverse magnetic field driving the spins through the coherent oscillation of the current in the resonator inductor wire. For an incident drive power P_{in}, the average current and magnetic field are:

$$\langle \hat{I} \rangle (t) = 2\delta I \sqrt{\bar{n}} \cos(\omega_0 t) \tag{2.28}$$

$$\langle \hat{B}(r) \rangle (t) = 2\delta B(r) \sqrt{\bar{n}} \cos(\omega_0 t). \tag{2.29}$$

2.3.4 Scattering matrix measurement
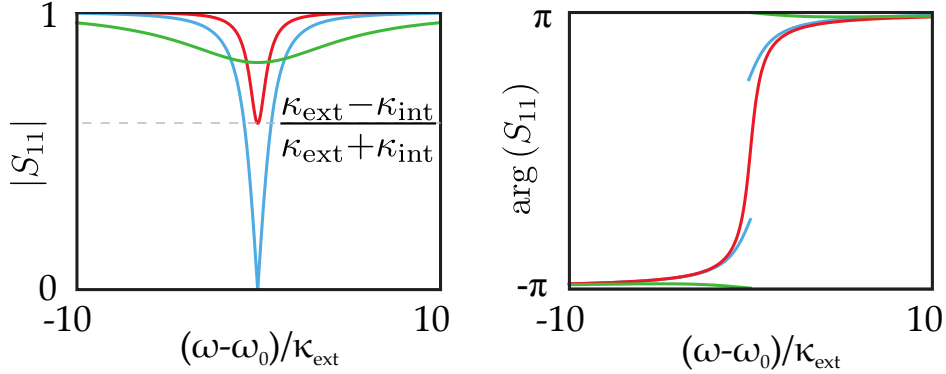
Figure 2.5: **Cavity reflection measurement.** Reflection coefficient $S_{11}(\omega)$ calculated for $\kappa_{\text{int}} = 10\kappa_{\text{ext}}$ (green), $\kappa_{\text{int}} = \kappa_{\text{ext}}$ (blue) and $\kappa_{\text{int}} = \kappa_{\text{ext}}/4$ (red). Left and right panel represent the modulus and phase of $S_{11}(\omega)$, respectively.

The behavior of a n-port linear device connected to n transmission lines is fully described by the $n \times n$ scattering matrix consisting in the reflection and transmission coefficients $S_{i,j}$ for the propagating fields defined as:

$$\hat{S}_{i,j}(\omega) = \frac{\hat{a}_{out,i}}{\hat{a}_{in,j}}, \quad \text{with} \quad \hat{a}_{in,k} = 0 \ \forall k \neq j. \tag{2.30}$$

The scattering coefficients $S_{i,j}$ are in general measured using classical coherent input drives, using typically a Vector Network Analyzer (VNA). The propagating field operators can then be replaced by the coherent signals $\alpha_{\text{in,i}}$ and $\alpha_{\text{out,i}}$. Eq.2.24 relating the output to input and intra-cavity fields gives $\alpha_{\text{in,i}} + \alpha_{\text{out,i}} = \sqrt{\kappa_i}\alpha(\omega)$. Using then the expression for the intra cavity field Eq.2.26 we obtain the reflection coefficient S_{11} for our LC resonator coupled to a single transmission line:

$$S_{11}(\omega) = \frac{\sqrt{\kappa_{\text{ext}}}\alpha(\omega) - \alpha_{\text{in}}}{\alpha_{\text{in}}} = \frac{\kappa_{\text{ext}} - \kappa_{\text{int}} + 2i(\omega - \omega_0)}{\kappa_{\text{ext}} + \kappa_{\text{int}} - 2i(\omega - \omega_0)}. \tag{2.31}$$

The relative strength of the external coupling rate κ_{ext} with respect to the internal losses damping rate κ_{int} defines three different regimes, as illustrated in Fig 2.5:

- **The under-coupled regime, where $\kappa_{\text{int}} \gg \kappa_{\text{ext}}$**, see green curves. Only a small dip in amplitude and a small phase shift are expected. Under-coupled cavities only weakly perturb the incident field.

- **The critical coupling regime, where $\kappa_{\text{int}} \approx \kappa_{\text{ext}}$**, see blue curves. The reflected amplitude goes to zero at resonance, where the cavity behaves as an impedance matched load absorbing all the power.

- **The over-coupled regime, where $\kappa_{\text{int}} \ll \kappa_{\text{ext}}$**, see red curves. The amplitude
  dip is small but the phase rotates by 2π across resonance. In the over-coupled
  regime most of the field is reflected but a large phase shift is caused.

A fit of $S_{11}(\omega)$ provides access to ω_0, κ_{int} and κ_{ext} without need of calibration of the
line, since $|S_{11}| = 1$ far from resonance. We notice here that the S-parameters are
defined as the complex conjugate $S_{i,j}(\omega)^\star$ of what is derived here.

In section 2.3.2 we have pointed out that the cavity internal dissipation can be described
in terms of a second port connected to a transmission line terminated by an impedance
matched load. For the following discussion it is then useful to introduce the transmission
from this second port toward the output port 1, S_{12}, as it determines how the incoming
thermal noise from the internal losses via $\hat{a}_{\text{in,int}}$ is transmitted to the output mode $\hat{a}_{\text{out}}$.
Following the same procedure as for S_{11}, we get:

$$S_{12}(\omega) = \frac{2\sqrt{\kappa_{\text{ext}}\kappa_{\text{int}}}}{\kappa_{\text{ext}} + \kappa_{\text{int}} - 2i(\omega - \omega_0)}. \tag{2.32}$$

2.3.5   Thermal population and noise in the cavity-transmission line system

In addition to the coherent control of the cavity, a fundamental requirement in our
spin radiative cooling experiment is the possibility to establish and measure a cavity
mode thermal state. In this section we first look at the thermal state in a semi-infinite
transmission line terminated by different loads and then we move to the the case in
which the cavity is connected to such a circuit.

We consider a semi-infinite transmission line connected to an impedance-matched load
at temperature T_{load}, as depicted in Fig.2.6a. The reflection coefficient given by Eq.2.18
being zero, the left propagating modes $\hat{a}^\leftarrow(\omega)$ are independent from the right propagat-
ing modes incoming to the load and they are populated only by the thermal radiation
emitted by the load. Such a perfectly absorbing load thus behaves as a black body
emitting according to Planck's law Eq.2.2, and thus realizes a thermal state in the left
propagating modes satisfying:

$$\langle \hat{a}^{\leftarrow\dagger}\hat{a}^\leftarrow \rangle (\omega) = n_{\text{th}}(\omega, T_{\text{load}}). \tag{2.33}$$

A second case of interest illustrated in Fig.2.6b is a terminated transmission line con-
nected to an attenuator at temperature T_β: a two port impedance matched lossy ele-
ment therefore characterized by $S_{11} = S_{22} = 0$ and $S_{21} = S_{12} = \sqrt{1-\beta}$, with β the
attenuation factor commonly expressed in dB. The left propagating mode is thus cou-
pled with relative strength β to the bath at T_β and with relative strength $1 - \beta$ to the
load bath at T_{load}. According to Eq.A.8, the left modes thermalize at an intermediate
effective temperature T_{left} defined as:

$$\langle \hat{a}^{\leftarrow\dagger}\hat{a}^\leftarrow \rangle = n_{\text{th}}(T_{\text{left}}) = \beta n_{\text{th}}(T_\beta) + (1 - \beta)n_{\text{th}}(T_{\text{load}}). \tag{2.34}$$

Before moving to the analysis of the circuit illustrated in Fig.2.6c, we introduce the
device named circulator, commonly represented by a circle with arrow inside. It is a
lossless non reciprocal three port device that decouples the counter-propagating modes
in a transmission lines [9]. For a clockwise circulator $|S_{21}| = |S_{32}| = |S_{13}| = 1$, while
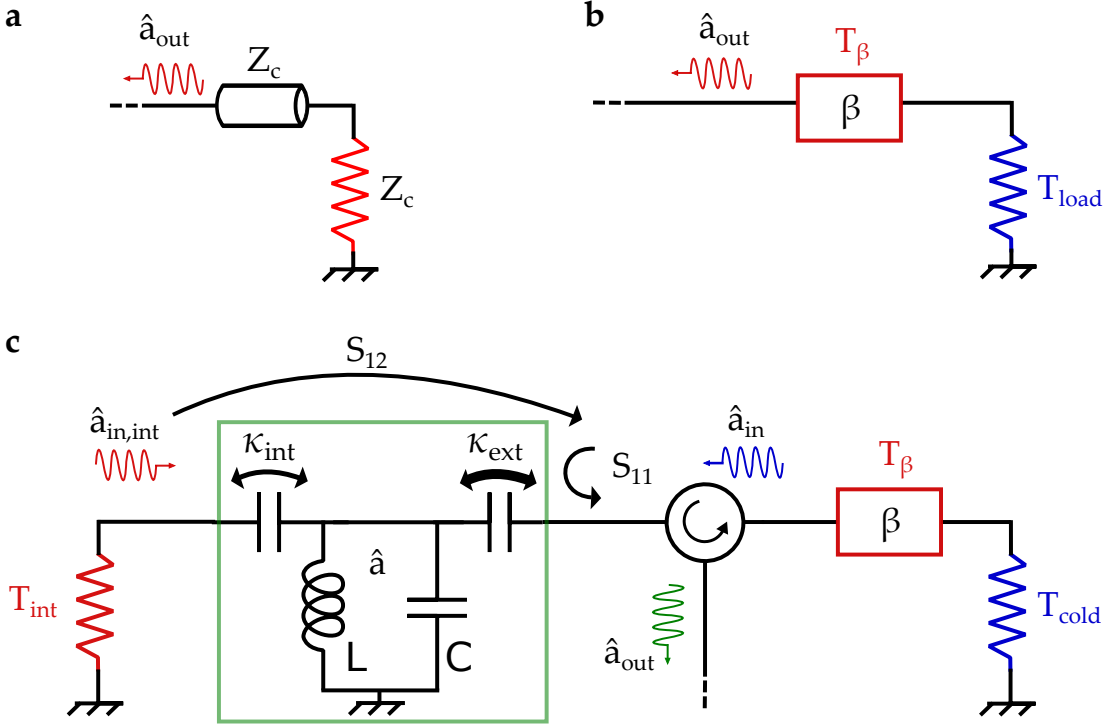
Figure 2.6: **Thermalization of electromagnetic modes in a microwave circuit.**
a, A transmission line terminated by an impedence mateched load. The reflection coefficient at the load is zero so that the left propagating mode consists in the thermal radiation from the load, independently of the incoming state. **b,** Thermal radiation emitted by an impedance matched load is partially thermalized by an attenuator with transmission coefficient $S_{21} = \sqrt{\beta}$ and no reflection. **c,** The cavity mode $\hat{a}$ is coupled with strength κ_{int} to the thermal radiation at T_{int} and with strength κ_{ext} to the bath consisting in the incoming modes $\hat{a}_{\text{in}}$. The output modes $\hat{a}_{\text{out}}$ are the sum of the transmitted $\hat{a}_{\text{in,int}}$ and the reflected $\hat{a}_{\text{in}}$.

$|S_{12}| = |S_{23}| = |S_{31}| = 0$ prevents transmission in the opposite direction. As a result the right propagating modes in the line connected to port 1 of the circulator is transmitted on port 2, while the left propagating mode on the same line is given by the input on port 3. Circulators allow thus to separate input and output lines in microwave experiments and to isolate a device from part of the circuit.

The circuit represented in Fig.2.6c describes in a simplified manner the setup used in the spin radiative cooling experiment. The aim of this circuit is to cool the resonator mode at the temperature T_{cold}, lower than its internal losses temperature T_{int}. As detailed in section Sc.2.3.4, the cavity can be described as a two port device, whose port 2 models its coupling to the internal losses at rate κ_{int} while port 1 realizes the coupling at rate κ_{ext} to the rest of the circuit. Cavity input and output modes on port 1 propagate on two different transmission lines as they are routed by a circulator. From the circuit point of view, the cavity is fully described by its scattering matrix coefficients S_{11} and S_{12} introduced in Eqs.2.31-2.32, while its internal degree of freedom $\hat{a}$ evolves according to Eq.2.23. We first look at the thermal state in the three relevant propagating modes: $\hat{a}_{\text{in,int}}$, $\hat{a}_{\text{in}}$ and $\hat{a}_{\text{out}}$. The internal loss input mode on port 2 $\hat{a}_{\text{in,int}}$ is at thermal equilibrium with the load at T_{int} and obeys Eq.2.33: $\langle \hat{a}_{\text{in,int}}^{\dagger} \hat{a}_{\text{in,int}} \rangle (\omega) = n_{th}(\omega, T_{\text{int}})$. The input mode on port 1 $\hat{a}_{\text{in}}$ is the mode routed by the circulator from

the transmission line terminated by the load at T_{cold} and attenuated by a factor β at T_β, due to unwanted losses. It is therefore at thermal equilibrium at a temperature T_{ext} given by Eq.2.34:

$$\langle \hat{a}_{\text{in}}^\dagger \hat{a}_{\text{in}} \rangle = n_{th}(T_{\text{ext}}) = \beta n_{th}(T_\beta) + (1 - \beta)n_{th}(T_{\text{cold}}). \tag{2.35}$$

Once the two input modes state is known, the outgoing field $\hat{a}_{\text{out}}$ is directly obtained from the cavity scattering parameters: $\hat{a}_{\text{out}}(\omega) = S_{12}(\omega)\hat{a}_{\text{in,int}} + S_{11}(\omega)\hat{a}_{\text{in}}$. The output mode thermal equilibrium population $n_{\text{th}}(T_{out}) = \langle \hat{a}_{\text{out}}^\dagger \hat{a}_{\text{out}} \rangle$ is thus given by:

$$\langle \hat{a}_{\text{out}}^\dagger \hat{a}_{\text{out}} \rangle (\omega) = |S_{11}(\omega)|^2 \, n_{\text{th}}(T_{\text{ext}}) + (1 - |S_{11}(\omega)|^2)n_{\text{th}}(T_{\text{int}}). \tag{2.36}$$

Far from resonance, the output mode is equal to the reflected input mode and is therefore at the intermediate temperature T_{ext} in between T_{cold} and T_β. On the other hand, close to resonance the cavity couples the output mode to the thermal radiation of the cavity internal losses at T_{int}. The outcoming modes are routed to the output transmission line by the circulator. Their thermal state can be characterized by measuring the noise power spectral density:

$$S(\omega) = \langle \Delta \hat{X}^2 \rangle + \langle \Delta \hat{Y}^2 \rangle = n_{\text{th}}(T_{\text{out}}(\omega)) + 1/2 \tag{2.37}$$

with a spectrum analyzer connected to the output line. Such a measurement will provide information on the cavity and circuit modes temperatures.
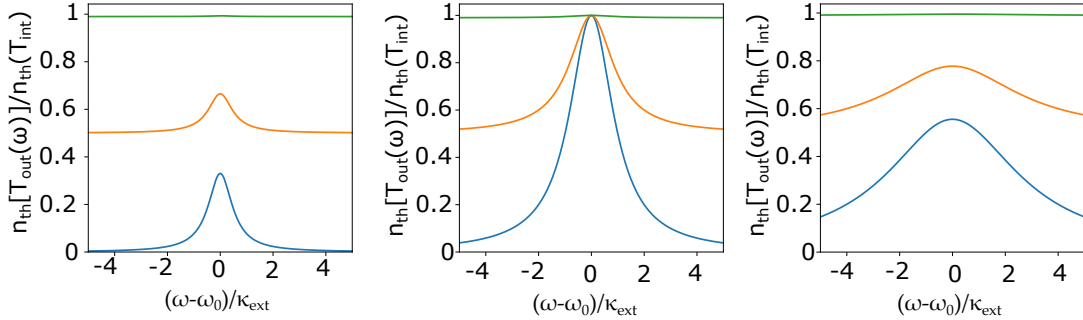
Figure 2.7: **Output mode thermal equilibrium population $n_{\textbf{th}}[T_{out}(\omega)]$.** The mean number of thermal photons in the output modes is calculated with Eq.2.36 taking $T_\beta = T_{\text{int}} = 1\,\text{K}$, $T_{\text{cold}} = 20\,\text{mK}$ and $\omega_0/2\pi = 7.4\,\text{GHz}$ for three different values of attenuation: $\beta = 0$ (blue), $\beta = 3\,\text{dB}$ (orange) and $\beta = 20\,\text{dB}$ (green). Left, $\kappa_{\text{int}} = \kappa_{\text{ext}}/10$: the cavity is in the overcoupled regime and at resonance the output mode is only partially thermalized to the hot losses. Middle, $\kappa_{\text{int}} = \kappa_{\text{ext}}$: the cavity is critically coupled to the output mode that at resonance is perfectly thermalized to the internal losses at $1\,\text{K}$. Right, $\kappa_{\text{int}} = 5\kappa_{\text{ext}}$: the cavity is in the undercoupled regime.

Now that we have determined the thermal equilibrium of the circuit, we focus on the intra-cavity field $\hat{a}$. It is coupled to the internal loss bath at temperature T_{int} with strength κ_{int} and to the continuum of input modes at temperature T_{ext} with strength κ_{ext}. Once again, according to Eq.A.8 the system consisting in the cavity mode thermalizes to an effective bath at the intermediate temperature T_{phot}:

$$\langle \hat{a}^\dagger \hat{a} \rangle = n_{\text{th}}(T_{\text{phot}}) = \frac{\kappa_{\text{ext}}}{\kappa} n_{\text{th}}(T_{\text{ext}}) + \frac{\kappa_{\text{int}}}{\kappa} n_{\text{th}}(T_{\text{int}}), \tag{2.38}$$

where $n_{\text{th}}(T_{\text{ext}})$ is given by Eq.2.35. If the cavity is in the over-coupled regime $\kappa_{\text{ext}} \gg \kappa_{\text{int}}$ and the circuit losses are negligible $\beta \ll 1$, then the cavity thermalizes to the cold load rather than to its internal loss bath and thus $T_{\text{phot}} \approx T_{\text{cold}}$.

2.4 Thermal noise and amplification

To detect small changes in the thermal noise of the output field, it is essential to have a low-noise amplification chain. A first commonly used solution for measuring weak microwave signals at low temperature are semiconductor High Electron Mobility Transistor (HEMT) that can add an equivalent thermal noise of temperature T_{N} on the order of a few Kelvin. We refer to T_{N} as the amplifier noise temperature. Even lower level of added noise is desirable but it has to be considered that quantum mechanics fixes the limits on the minimum noise that an amplifier adds to the input signal, as shown by Haus and Mullen[11] and Caves[12]. Microwave amplifiers reaching this quantum limit of added noise have been developed in the context of CQED and go under the name of Josephson Parametric Amplifiers (JPA). In the following we introduce the quantum limits on amplification and we present the working principle and main characteristics of the Josephson Travelling Wave Parametric Amplifier (JTWPA) used in our experiments.

2.4.1 Quantum limits on amplification
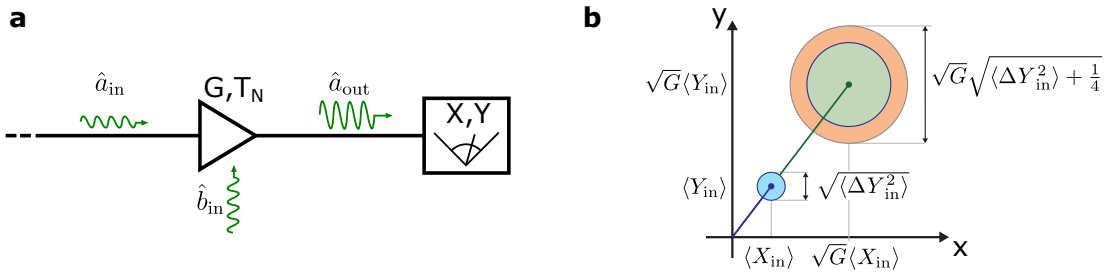
Figure 2.8: **Linear amplifiers. a** A linear amplifier of gain G and noise temperature T_{N} is used to detect a narrow band signal. **b,** Phase-space representation in the limit of high gain. The disks indicate the standard deviation of the quadratures before and after amplification. A phase-preserving amplifier degrades the SNR, with the added noise represented in red.

A microwave amplifier of gain G is a two-port device connected to an input and an output transmission lines (see Fig.2.8). Input and output signals of frequency ω and of narrow bandwidth $\Delta\omega$ are conveniently described by the right propagating spatio-temporal modes $\hat{a}_{\text{in}}$ and $\hat{a}_{\text{out}}$ introduced in Eq.2.21.

The amplified signal is measured at the end of the output transmission line either by a homodyne demodulation, yielding the quadratures I and Q, or by a frequency spectrum analyzer giving the spectral power density S. The I and Q quadratures obtained by the homodyne demodulation are proportional to the $\hat{X}$ and $\hat{Y}$ operators, with arbitrary rotation in the XY plane tuned via the local oscillator phase. The average signal in one quadrature is then proportional to $\langle \hat{X} \rangle$ and the variance to $\langle \Delta \hat{X}^2 \rangle$. The outcome of the spectrum analyzer measurement is instead $\langle \hat{X}^2 + \hat{Y}^2 \rangle$, which, in the absence of a signal coincides with the noise power $\langle \Delta \hat{X}^2 \rangle + \langle \Delta \hat{Y}^2 \rangle$.

We consider here only phase-preserving amplification. If we naively applied the classical relations between input and output quadratures of a linear amplifier to the quantum case, we would define $\hat{X}_{\text{out}} = \sqrt{G}\hat{X}_{\text{in}}$ and $\hat{Y}_{\text{out}} = \sqrt{G}\hat{Y}_{\text{in}}$. This definition however does not satisfy the commutation relation for the operators $\hat{a}_{\text{out}}$ and $\hat{a}_{\text{in}}$, besides the trivial case $G = 1$. Following Caves [12], an internal mode $\hat{b}_{\text{in}}$ of the amplifier, commuting with $\hat{a}_{\text{in}}$, needs to be introduced to describe the amplification:

$$\hat{a}_{\text{out}} = \sqrt{G}\hat{a}_{\text{in}} + \sqrt{G-1}\hat{b}_{\text{in}}^{\dagger}, \tag{2.39}$$

with $\hat{b}_{\text{in}}$ satisfying $[\hat{b}_{\text{in}}, \hat{b}_{\text{in}}^{\dagger}] = 1$ and $[\hat{b}_{\text{in}}, \hat{a}_{\text{in}}] = 0$. By assuming $\langle \hat{b}_{\text{in}} \rangle = 0$, one finds:

$$\langle \hat{X}_{\text{out}} \rangle = \sqrt{G} \langle \hat{X}_{\text{in}} \rangle \tag{2.40}$$

$$\langle \hat{Y}_{\text{out}} \rangle = \sqrt{G} \langle \hat{Y}_{\text{in}} \rangle, \tag{2.41}$$

in analogy to classical description. However, when deriving the quantum version of the input-output equations for the noise, the amplifier internal mode plays an essential role in causing a deviation from the classical limit. When no signal is present, then the outcoming noise referred to the input obeys:

$$\frac{\langle \Delta \hat{X}_{\text{out}}^2 \rangle + \langle \Delta \hat{Y}_{\text{out}}^2 \rangle}{G} = \langle \Delta \hat{X}_{\text{in}}^2 \rangle + \langle \Delta \hat{Y}_{\text{in}}^2 \rangle + \left(1 - \frac{1}{G}\right)(\langle \Delta \hat{X}_{\text{b}}^2 \rangle + \langle \Delta \hat{Y}_{\text{b}}^2 \rangle), \tag{2.42}$$

where $\langle \Delta \hat{X}_{\text{b}}^2 \rangle$ are the internal mode fluctuations. We thus identify two distinct contribution to the output noise: the input noise and the noise added by the amplifier that originates from the internal mode fluctuations. We thus find it convenient to define $S_{\text{out}} = \langle \Delta \hat{X}_{\text{out}}^2 \rangle + \langle \Delta \hat{Y}_{\text{out}}^2 \rangle$ the noise detected, and $S_{\text{in}} = \langle \Delta \hat{X}_{\text{in}}^2 \rangle + \langle \Delta \hat{Y}_{\text{in}}^2 \rangle$ and $S_{\text{amp}} = \langle \Delta \hat{X}_{\text{b}}^2 \rangle + \langle \Delta \hat{Y}_{\text{b}}^2 \rangle$ its two contributions so that, for large gain, $S_{\text{out}}/G = S_{\text{in}} + S_{\text{amp}}$.

If the incoming mode $\hat{a}_{\text{in}}$ is in a thermal state, the input noise is found from Eq.2.6 to be $S_{\text{in}} = n_{\text{th}}(T_{\text{in}}) + 1/2$. In the limit $k_{\text{B}}T_{\text{in}} \ll \hbar\omega$, thermal fluctuations are negligible and the detected noise $S_{\text{in}} = 1/2$ is of quantum origin due to the minimum variance admitted by the Heisenberg principle.

Like the input modes, the amplifier internal mode fluctuations are also bounded by the Heisenberg principle giving $\langle \Delta \hat{X}_{\text{b}}^2 \rangle \langle \Delta \hat{Y}_{\text{b}}^2 \rangle \geqslant 1/16$. By further imposing that the added noise is phase-insensitive $\langle \Delta \hat{X}_{\text{b}}^2 \rangle = \langle \Delta \hat{Y}_{\text{b}}^2 \rangle \geqslant 1/4$ [12], the quantum-limit on the amplifier output noise is obtained:

$$\frac{\langle \Delta \hat{X}_{\text{out}}^2 \rangle + \langle \Delta \hat{Y}_{\text{out}}^2 \rangle}{G} \geqslant \langle \Delta \hat{X}_{\text{in}}^2 \rangle + \langle \Delta \hat{Y}_{\text{in}}^2 \rangle + 1/2. \tag{2.43}$$

This results shows that in case of large gain the minimum noise added by a phase-preserving amplifier is equivalent to half a photon more ($S_{\text{amp}} \geqslant 1/2$) in the effective input noise power S_{out}/G, as stated by the Haus-Caves theorem. Equivalently, the quantum limits on the amplifier noise temperature reads:

$$k_{\text{B}}T_{\text{N}} \geqslant \frac{\hbar\omega}{2}. \tag{2.44}$$
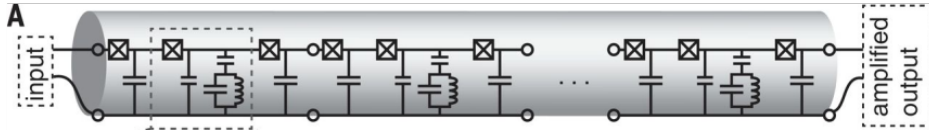
Figure 2.9: **JTWPA equivalent circuit.** A nonlinear transmission line is realized with a series of Josephson junctions. Some unit cells, like the one contoured by a dashed line, include a parallel LC resonator guaranteeing the phase matching condition. Extracted from [13].

2.4.2 The Josephson Travelling Wave Parametric Amplifier

Amplification at the quantum limit has been reached in the microwave domain exploiting the inductance nonlinearity of Josephson junctions embedded in an almost dissipationless superconducting resonator of frequency ω_0. As demonstrated in the pioneering work by Yurke et al. [14], such a circuit enables parametric amplification of signals at frequency $\omega_s \approx \omega_0$, by transferring the energy of a pump at frequency ω_p to the signal and to a complementary idler of frequency ω_I. Two limitations of such devices are the bandwidth typically bounded to a few tens of Megahertz and the low saturation power in general smaller than $-110\,\text{dBm}$.

Overcoming these limits has been demonstrated by moving from resonators to transmission lines, where the field is amplified while propagating in the nonlinear medium. In the device used in this thesis, the distributed nonlinearity in the transmission line is realized with a chain of Josephson junctions, as shown in Fig.2.9, from which the name of Josephson Travelling Wave Parametric Amplifier (JTWPA). Here the pump tone propagating in the line together with the signal enables a four-wave mixing process satisfying energy conservation $2\omega_p = \omega_s + \omega_i$ by generation of the idler. Conservation of momentum imposes the phase matching condition $2k_p = k_s + k_i$ that needs engineering of the dispersion relation $k(\omega)$ to compensate for pump-induced phase shifts. For this purpose a series of lumped-element resonators is realized along the transmission line, opening a stop-band in the dispersion relation and allowing to reach the phase matching for different pump powers. For more details refer to ref.[13], while a characterization of the similar device used in this thesis is provided in the next chapters.

2.5 Superconducting microwave switch

Another superconducting device that will be of interest in this thesis is a superconducting microwave switch developed by Pechal et al. [15]. We use this device in the radiative cooling experiment to investigate the dynamics of the cooling process. Its interest in our experiment lies in the fact that it is able to switch in a few nanoseconds without heating. It consists of two hybrid couplers connected in a Mach-Zehnder-like configuration, where the two arms are two independently tunable coplanar waveguide resonators (see Fig.6.16a). Tunability is obtained with a series of 5 quantum-interference-device (SQUID) loops placed in the center of the two resonators. The inductance of these SQUID arrays is controlled by changing the applied magnetic flux with two superconducting coils. When both resonators are detuned, the input signal split by the first coupler is reflected by the resonators and, because of the phase relation between the two outputs of the coupler, recombines in port 2. Conversely, in the resonant configuration the signal is transmitted in the two arms toward the second hybrid coupler,

recombining in port 3.
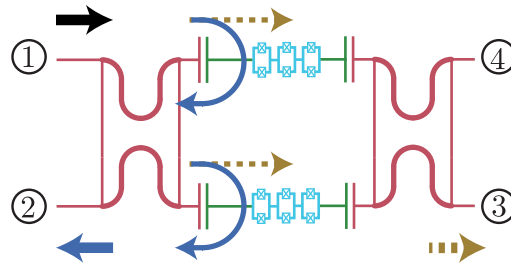
Figure 2.10:   **Superconducting switch circuit.** Schematic diagram of the super-conducting switch showing the input signal path for the two switch states. In the off-resonant case (solid arrows), the signal is reflected by the resonators and directed to port 2, while in the resonant case (dashed arrows) it is transmitted and reaches port 3. Extracted from ref. [15].

Chapter 3

Spins in a cavity

In this chapter, we first model the dynamics of a spin coupled to a single electromagnetic mode, such as the resonant mode of an LC circuit. We focus in particular on the so-called "weak coupling" regime. We show how the cavity field acts as a reservoir for the spins, enabling spin cooling. After presenting the equation of motion of the spin ensemble, we discuss magnetic resonance detection methods used in our experiments.

We restrict our study in this chapter to electronic spins $1/2$. Our discussion also applies without any change to nuclear spins $1/2$; for multilevel systems, our treatment applies to a two-level restriction of the full energy spectrum, while effects of the multilevel structure are discussed in the next chapters.

3.1 Spin dynamics in the Purcell regime

We discuss in this section the spin radiative relaxation enhancement by a resonant cavity before studying spin thermalization and dynamics.

3.1.1 Cavity-induced relaxation

Consider the system depicted in Fig.3.1, where a spin is in the mode volume of a damped cavity realized by an LC circuit. As discussed in Ch.2, the Hamiltonian of such a resonator is $\hat{H}_{\mathrm{phot}} = \hbar\omega_0(\hat{a}\hat{a}^\dagger + \frac{1}{2})$ and its damping rate is the sum of internal losses and coupling to the measurement line: $\kappa = \kappa_{\mathrm{int}} + \kappa_{\mathrm{ext}}$. The current in the inductor wire, $\hat{I} = \delta I(\hat{a} + \hat{a}^\dagger)$, generates a magnetic field $\hat{\boldsymbol{B}}_1(\boldsymbol{r}) = \delta\boldsymbol{B}(\boldsymbol{r})(\hat{a} + \hat{a}^\dagger)$ at the spin location $\boldsymbol{r}$, determining the magnitude of spin-photon coupling g.

Spin-cavity interaction Hamiltonian

We first consider a single spin at location $\boldsymbol{r}$, described by the dimensionless vectorial spin operator $\hat{\boldsymbol{S}} = (\hat{S}_x, \hat{S}_y, \hat{S}_z)$. A static magnetic field B_0 is applied along z. We isolate a two-level system from the spin energy levels, the ground state $|\mathfrak{g}\rangle$ and the excited state $|\mathfrak{e}\rangle$, whose field-dependent transition frequency is $\omega_s(B_0) = (E_\mathfrak{e} - E_\mathfrak{g})/\hbar$. We introduce the Pauli matrices $(\hat{\sigma}_x, \hat{\sigma}_y, \hat{\sigma}_z)$, where:

$$\hat{\sigma}_x = \begin{pmatrix} 0 & 1 \\ 1 & 0 \end{pmatrix}, \quad \hat{\sigma}_y = \begin{pmatrix} 0 & -i \\ i & 0 \end{pmatrix} \text{ and } \quad \hat{\sigma}_z = \begin{pmatrix} 1 & 0 \\ 0 & -1 \end{pmatrix} \tag{3.1}$$
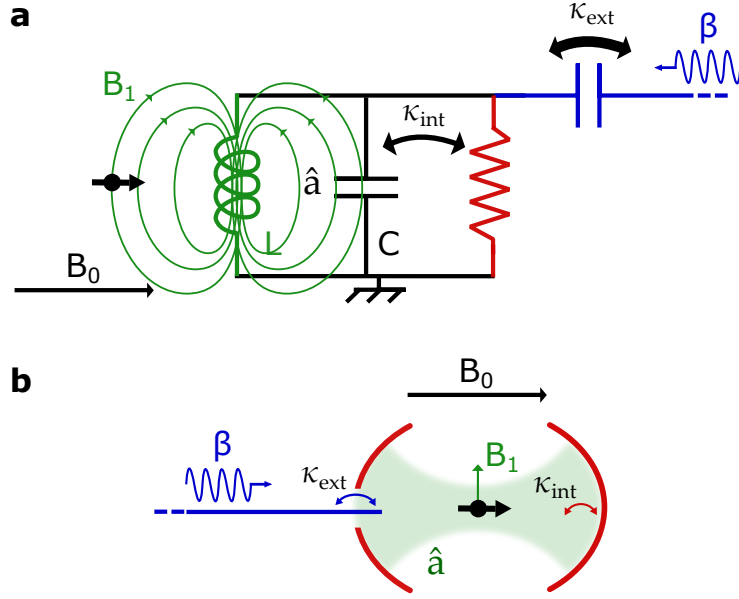
Figure 3.1:   **Spin-cavity coupling.** **a** A spin polarized by a static magnetic field B_0 is coupled to an LC resonator by the transverse field B_1 generated by the inductor current. The resonator is damped by internal and external losses while it is driven by the input signal of amplitude β. **b** The quantum optics equivalent representation.

One can also define the spin rising ($\hat{\sigma}_+$) and lowering ($\hat{\sigma}_-$) operators as $\hat{\sigma}_\pm = \frac{1}{2}(\hat{\sigma}_x \pm i\hat{\sigma}_y)$, whose matrix form are:

$$\hat{\sigma}_+ = \begin{pmatrix} 0 & 1 \\ 0 & 0 \end{pmatrix} \quad \text{and} \quad \hat{\sigma}_- = \begin{pmatrix} 0 & 0 \\ 1 & 0 \end{pmatrix}. \tag{3.2}$$

In the basis $\{|\mathfrak{e}\rangle, |\mathfrak{g}\rangle\}$, the spin Hamiltonian reads:

$$\hat{H}_s(B_0) = \frac{\hbar\omega_s(B_0)}{2}\hat{\sigma}_z. \tag{3.3}$$

The spin interaction with the resonator field results in a magnetic coupling described by the interaction Hamiltonian:

$$\hat{H}_{\text{int}} = -\hbar\gamma_e \hat{\mathbf{S}} \cdot \hat{\mathbf{B}}_1 = -\hbar\gamma_e \hat{\mathbf{S}} \cdot \delta\mathbf{B}(\mathbf{r})(\hat{a} + \hat{a}^\dagger), \tag{3.4}$$

where $\gamma_e = 28\,\text{GHz/T}$ is the so-called gyromagnetic ratio of the free electron spin. In the $\{|\mathfrak{e}\rangle, |\mathfrak{g}\rangle\}$ restriced spin-basis, treating $\hat{H}_{\text{int}}$ as a perturbation of the uncoupled Hamiltonian $\hat{H}_0 = \hat{H}_{\text{phot}} + \hat{H}_{\text{spin}}$ and performing the rotating wave approximation yields the Jaynes-Cummings Hamiltonian [16]:

$$\hat{H}_{\text{int}} = \hbar g(\hat{\sigma}_+ \hat{a} + \hat{\sigma}_- \hat{a}^\dagger), \tag{3.5}$$

where $g = -\gamma_e \langle\mathfrak{e}| \hat{\mathbf{S}} \cdot \delta\mathbf{B}(\mathbf{r}) |\mathfrak{g}\rangle$. The two terms in the Hamiltonian describe respectively absorption and emission of photons by the spins. In a perfectly isolated spin-cavity system, the Jaynes-Cummings Hamiltonian predicts the phenomenon known as vacuum

Rabi oscillation [17]: a spin initially in its excited state will emit and re-absorb reversibly a single photon into an empty cavity at a frequency $2g$.

In the presence of interaction with the environment of both the spins and the resonator, the duration of these coherent exchange is limited by two phenomena: the resonator damping rate κ gives a characteristic intra-cavity photon lifetime of $1/\kappa$, while spins lose their coherence at a rate $\gamma = 1/T_2$, where T_2 is the so called spin coherence time that we describe in the following of this chapter. Two regimes can then be distinguished, as shown in Fig.3.2:
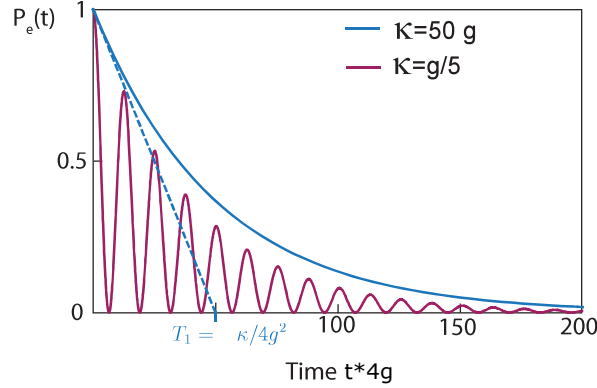
Figure 3.2: **Weak and strong coupling regime for a single spin.** The population of the spin excited state $|\mathfrak{e}\rangle$ is calculated solving Eq.3.7 in absence of drive ($\beta = 0$), neglecting non-radiative processes ($\Gamma_{\mathrm{phon}} = \gamma = 0$) and at resonance ($\omega_s = \omega_0$). In the strong coupling regime ($g > \kappa$) it shows oscillations while in the weak coupling regime it decays exponentially at rate $4g^2/\kappa$.

- **The strong coupling regime**, when $g \gg \kappa, \gamma$ (see red curve): excitation lifetimes are long compared to the Rabi period and Rabi oscillations may be observed [17].

- **The weak coupling regime**, when $g \ll \kappa, \gamma$ (see blue curve): excitations decay faster than the coherent exchange time, thus Rabi oscillation are replaced by an irreversible decay.

In the following, we will focus on the weak coupling that, if other conditions are satisfied, is the relevant regime for realizing radiative cooling of the spins.

Master equation for the open spin-cavity system

Before going to the approximation allowed by the weak coupling regime, let's consider the complete description at zero temperature of the spin-cavity system interacting with the environment (see Fig.3.3). The spin is coupled to the lattice bath with strength Γ_{phon} while the cavity dissipates into the environment via its internal and external loss channels. Such an open system can be described by the Lindblad master equation Eq.A.1. A microwave drive of amplitude β (linked to the input power by $P_{\mathrm{in}} = \hbar\omega_{\mathrm{d}} |\beta|^2$) is described by $\hat{H}_d/\hbar = i\sqrt{\kappa_{\mathrm{ext}}}(\beta\hat{a}^\dagger e^{-i\omega_d t} + \beta^*\hat{a}e^{i\omega_d t})$. The Hamiltonian of the system in the frame rotating at ω_d is then:

$$\hat{H} = \Delta_0\hat{a}^\dagger\hat{a} + \frac{\Delta_s}{2}\hat{\sigma}_z + g(\hat{\sigma}_+\hat{a} + \hat{\sigma}_-\hat{a}^\dagger) + i\sqrt{\kappa_{\mathrm{ext}}}(\beta\hat{a}^\dagger - \beta^*\hat{a}), \qquad (3.6)$$
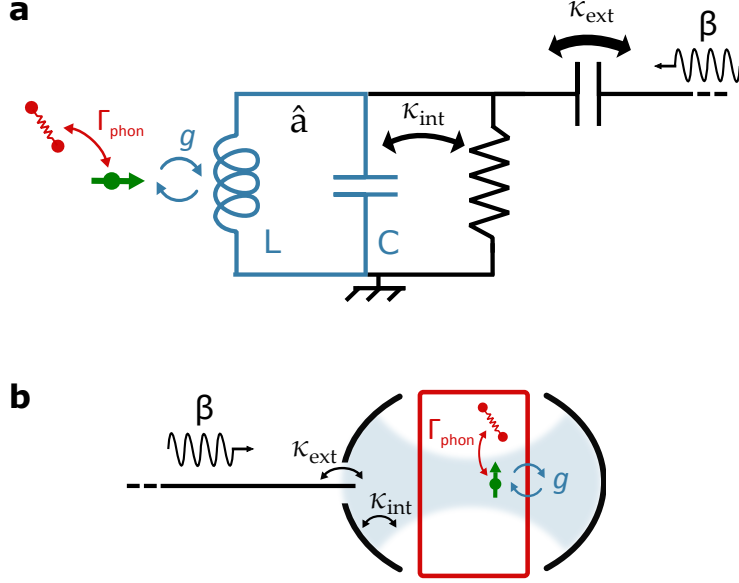
Figure 3.3:   **Spin-cavity open system. a** The spin is coupled to the lattice bath and coherently exchanges energy with the resonator which is damped by losses and driven by the input signal β. **b** Quantum optics equivalent representation including the sample (red).

where $\Delta_0 = \omega_0 - \omega_d$ and $\Delta_s = \omega_s - \omega_d$. Three Lindblad operators describe the non-unitary processes at zero temperature. The cavity relaxation via external and internal losses is described by $\hat{\mathcal{L}}_{\text{phot}} = \sqrt{\kappa}\hat{a}$. The spin-lattice energy relaxation is described by $\hat{\mathcal{L}}_{\text{phon}} = \sqrt{\Gamma_{\text{phon}}}\hat{\sigma}_-$ and spin decoherence by $\hat{\mathcal{L}}_2 = \sqrt{\gamma/2}\hat{\sigma}_z$. Such a master equation fully describes the system and is valid in the strong and weak coupling regime. Using the density matrix ρ to describe the spin-cavity system, it reads:

$$
\begin{aligned}
\frac{\mathrm{d}\rho}{\mathrm{d}t} &= -\frac{i}{\hbar}[\hat{H}, \rho] \\
&+ (\hat{\mathcal{L}}_{\text{phon}}\rho\hat{\mathcal{L}}_{\text{phon}}^\dagger - \frac{1}{2}\hat{\mathcal{L}}_{\text{phon}}^\dagger\hat{\mathcal{L}}_{\text{phon}}\rho - \frac{1}{2}\rho\hat{\mathcal{L}}_{\text{phon}}^\dagger\hat{\mathcal{L}}_{\text{phon}}) \\
&+ (\hat{\mathcal{L}}_{\text{phot}}\rho\hat{\mathcal{L}}_{\text{phot}}^\dagger - \frac{1}{2}\hat{\mathcal{L}}_{\text{phot}}^\dagger\hat{\mathcal{L}}_{\text{phot}}\rho - \frac{1}{2}\rho\hat{\mathcal{L}}_{\text{phot}}^\dagger\hat{\mathcal{L}}_{\text{phot}}) \\
&+ (\hat{\mathcal{L}}_2\rho\hat{\mathcal{L}}_2^\dagger - \frac{1}{2}\hat{\mathcal{L}}_2^\dagger\hat{\mathcal{L}}_2\rho - \frac{1}{2}\rho\hat{\mathcal{L}}_2^\dagger\hat{\mathcal{L}}_2),
\end{aligned}
\tag{3.7}
$$

Enhanced spontaneous emission in the weak coupling regime: the Purcell Effect

In the weak coupling regime, the large resonator damping κ compared to the coherent exchange rate g makes it possible to treat the resonator mode as an effective Markovian bath for the spin. Here we report the main results of a procedure based on the resonator adiabatic elimination that gets rid of the resonator operators while taking into account the drive [18–20]. A new master equation in the drive rotating frame is thus obtained for the reduced spin density matrix $\tilde{\rho}$:

$$\frac{\mathrm{d}\tilde{\rho}}{\mathrm{d}t} = -\frac{i}{\hbar}[\hat{H}_{\mathrm{eff}}, \tilde{\rho}]$$

$$+(\hat{\mathcal{L}}_{\mathrm{phon}}\tilde{\rho}\hat{\mathcal{L}}_{\mathrm{phon}}^\dagger - \frac{1}{2}\hat{\mathcal{L}}_{\mathrm{phon}}^\dagger\hat{\mathcal{L}}_{\mathrm{phon}}\tilde{\rho} - \frac{1}{2}\rho\hat{\mathcal{L}}_{\mathrm{phon}}^\dagger\hat{\mathcal{L}}_{\mathrm{phon}})$$

$$+(\hat{\mathcal{L}}_{\mathrm{phot}}\tilde{\rho}\hat{\mathcal{L}}_{\mathrm{phot}}^\dagger - \frac{1}{2}\hat{\mathcal{L}}_{\mathrm{phot}}^\dagger\hat{\mathcal{L}}_{\mathrm{phot}}\tilde{\rho} - \frac{1}{2}\tilde{\rho}\hat{\mathcal{L}}_{\mathrm{phot}}^\dagger\hat{\mathcal{L}}_{\mathrm{phot}})$$

$$+(\hat{\mathcal{L}}_2\tilde{\rho}\hat{\mathcal{L}}_2^\dagger - \frac{1}{2}\hat{\mathcal{L}}_2^\dagger\hat{\mathcal{L}}_2\tilde{\rho} - \frac{1}{2}\tilde{\rho}\hat{\mathcal{L}}_2^\dagger\hat{\mathcal{L}}_2), \tag{3.8}$$

with $\hat{H}_{\mathrm{eff}}$ being the new effective spin Hamiltonian:

$$\hat{H}_{\mathrm{eff}} = \frac{\Delta_s - \xi}{2}\hat{\sigma}_z + g(\alpha\hat{\sigma}_+ + \alpha^*\hat{\sigma}_-), \tag{3.9}$$

where $\alpha = 2\sqrt{\kappa_{\mathrm{ext}}}\beta/(\kappa + 2i\Delta_0)$ is the steady state intra-resonator field amplitude calculated in absence of spins with the input-output relations (see Eq.2.26), and $\xi = \frac{g^2\Delta}{\Delta^2 + \kappa^2/4}$ with $\Delta = \Delta_0 - \Delta_s = \omega_0 - \omega_s$ being the spin-cavity detuning. The ξ term is renormalization of the spin frequency that we neglect in the following since it is of order g^2/κ.

As a consequence of the resonator adiabatic elimination, the Lindblad operator $\hat{\mathcal{L}}_{\mathrm{phot}}$ describing the resonator losses is replaced by the operator $\hat{\mathcal{L}}_{\mathrm{phot}} = \sqrt{\Gamma_{\mathrm{phot}}(\Delta)}\hat{\sigma}_-$ acting on the spins. This new operator describes spin radiative relaxation into the effective resonator bath. This cavity-induced spontaneous radiative relaxation was predicted in 1946 by Purcell[8] for spins and is known as the Purcell effect. The rate Γ_{phot} can be shown to be:

$$\Gamma_{\mathrm{phot}} = \frac{\kappa g^2}{\kappa^2/4 + \Delta^2}. \tag{3.10}$$

This exponential relaxation of a spin in a damped cavity is shown in Fig. 3.2, where the numerical solution of Eq.3.7 is reported for $\Delta_s = \Delta_0 = 0$, in the absence of drive ($\beta = 0$) and neglecting non radiative processes ($\gamma = \Gamma_{\mathrm{phon}} = 0$) for both strong (red) and weak (blue) coupling regimes. The coupling to the cavity induces therefore a new radiative relaxation channel for the spins, which competes with the relaxation by spin-lattice interaction.

3.1.2 Spin equilibrium and dynamics

We now describe in more details spin dynamics in the Purcell regime.

Equation of motion and mapping to Bloch equations

The master equation and effective Hamiltonian obtained from resonator adiabatic elimination (Eqs.3.8-3.9) yield the following semi-classical equations of motion for the spin observables and for the intra-cavity field, calculated in the drive rotating frame and at zero temperature:

$$\frac{\mathrm{d}\langle\hat{\sigma}_x\rangle}{\mathrm{d}t} = \Delta_s\langle\hat{\sigma}_y\rangle - \gamma_\perp\langle\hat{\sigma}_x\rangle \tag{3.11}$$

$$\frac{\mathrm{d}\langle\hat{\sigma}_y\rangle}{\mathrm{d}t} = -\Delta_s\langle\hat{\sigma}_x\rangle - \omega_1\langle\hat{\sigma}_z\rangle - \gamma_\perp\langle\hat{\sigma}_y\rangle \tag{3.12}$$

$$\frac{\mathrm{d}\langle\hat{\sigma}_z\rangle}{\mathrm{d}t} = \omega_1\langle\hat{\sigma}_y\rangle - \Gamma_1(0)\left[\langle\hat{\sigma}_z\rangle + 1\right] \tag{3.13}$$

$$\langle\hat{a}\rangle = \alpha - \frac{i2g}{\kappa + 2i\Delta}\langle\hat{\sigma}_-\rangle\,, \tag{3.14}$$

with $\gamma_\perp = \gamma + \frac{\Gamma_{\mathrm{phon}}}{2} + \frac{\Gamma_{\mathrm{phot}}}{2}$, $\Gamma_1(0) = \Gamma_{\mathrm{phon}} + \Gamma_{\mathrm{phot}}$ and, considering α to be a real number, $\omega_1 = -2g\alpha$. We note here that Eqs.3.11-3.13 are identical to the Bloch equations derived with fully classical description of the field, except for the new energy relaxation term given by the Purcell effect.
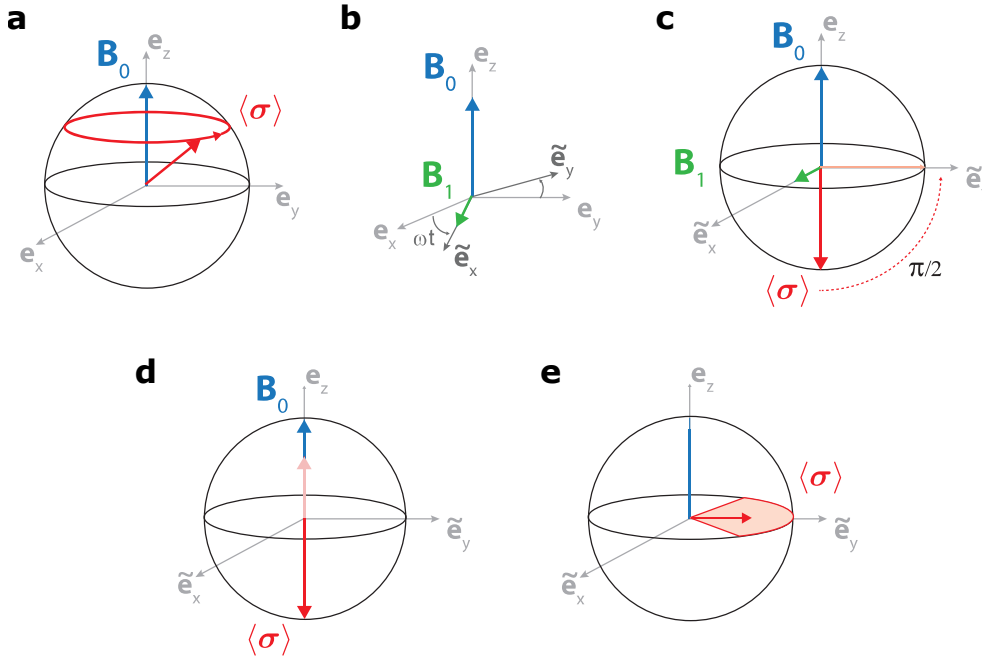
Figure 3.4: **Spin coherent dynamics and relaxation. a** Under a static magnetic field, the spin vector $\langle\hat{\boldsymbol{\sigma}}\rangle$ precesses at frequency ω_s in the laboratory frame. **b** Rotating frame of an oscillating magnetic field B_1. **c** In such a rotating frame, the application of a short microwave pulse allows to rotate the spin. **d** Longitudinal relaxation process bringing the spin vector to thermal equilibrium. **e** Decoherence process leading to a fan-out of the spin transverse component.

We now recall basic features of spin dynamics on the Bloch sphere. The spin vector $\langle\hat{\boldsymbol{\sigma}}\rangle$ is conveniently represented in the Bloch sphere of radius one: the south pole indicates the ground state with the spin aligned along z while the equator on the $x - y$ plane is where the vector points in case of full transverse magnetization. Neglecting relaxation and decoherence processes ($\Gamma_{\mathrm{phot}} = \Gamma_{\mathrm{phon}} = \gamma = 0$), the spin ensemble explores the surface of the sphere. Under a static magnetic field applied along $\tilde{\boldsymbol{e}}_z$, the spin precesses in the laboratory frame at the Larmor frequency ω_s. In the rotating frame at ω_d, it is static in absence of drive. When turning on the drive, it starts rotating around the vector $\omega_1\tilde{\boldsymbol{e}}_x + \Delta_s\tilde{\boldsymbol{e}}_z$ at an angular speed called the Rabi frequency:

$$\Omega_{\mathrm{R}} = \sqrt{\Delta_s^2 + \omega_1^2}. \tag{3.15}$$

When the applied drive is resonant with the spins ($\Delta_s = 0$), the magnetization vector precesses at speed ω_1 around $\tilde{\boldsymbol{e}}_x$. Such rotation axis depend on the phase of the applied drive α and can thus be arbitrarly chosen within the $x - y$ plane. By realizing a microwave pulse of duration τ_{p}, we can perform a rotation of angle $\theta_{\mathrm{p}} = \omega_1 \tau_{\mathrm{p}}$ around the chosen axis. Rotations around $\tilde{\boldsymbol{e}}_z$ can be also realized combining two rotations in the $x - y$ plane. Magnetization can be thus brought to any point on the Bloch sphere. In our experiments we will mainly use π and $\pi/2$ pulses around x and y axes.

The effect of the environment gives rise to two relaxation processes described by Eqs.3.11-3.13:

- **Energy relaxation**, As we have previously discussed, the term proportional to $\Gamma_1(0)$ describes the energy loss from the spin and emitted into the environment at zero temperature in an irreversible process whose characteristic time is generally denoted as $T_1 = 1/\Gamma_1$. The effect of energy relaxation is an exponential decay at rate $\Gamma_1(0)$ of the spin polarization $p \equiv -\langle \hat{\sigma}_z \rangle$ to its thermal equilibrium state, $p(0) = 1$ at zero temperature. We discuss in detail the finite temperature case in the next section.

- **Decoherence**, The terms proportional to $\gamma_\perp$ are responsible for the decay of the transverse components $\langle \hat{\sigma}_x \rangle$ and $\langle \hat{\sigma}_y \rangle$ whose charecteristic time is commonly denoted as the coherence time T_2 and its maximum value is $2T_1$. Note that for spins, as will be seen in the next chapter Ch.4, decoherence is in general due to a local, slowly evolving source of noise. The Markov approximation is then not satisfied, and the decay of $\sigma_{x,y}$ not exponential.

The steady-state solutions of the Bloch equations are well-known:

$$\langle \hat{\sigma} \rangle_x^{(s)} = \frac{\Delta_s \omega_1 / \gamma_\perp^2}{1 + (\Delta_s/\gamma_\perp)^2 + \omega_1^2/\Gamma_1 \gamma_\perp} \tag{3.16}$$

$$\langle \hat{\sigma} \rangle_y^{(s)} = \frac{\omega_1 / \gamma_\perp}{1 + (\Delta_s/\gamma_\perp)^2 + \omega_1^2/\Gamma_1 \gamma_\perp} \tag{3.17}$$

$$\langle \hat{\sigma} \rangle_z^{(s)} = \frac{1 + (\Delta_s/\gamma_\perp)^2}{1 + (\Delta_s/\gamma_\perp)^2 + \omega_1^2/\Gamma_1 \gamma_\perp}. \tag{3.18}$$

The transverse component of the spin shows a maximum for $\omega_1^2/\Gamma_1 \gamma_\perp = 1$ before the overall spin vector expectation value vanishes when $\omega_1 \gg \Gamma_1 \gamma_\perp$. This saturation condition reached at large drive power corresponds to the two spin levels being populated with equal probability and therefore effectively not any more interacting with the microwave radiation.

Besides providing the spin coherent evolution and relaxation in the presence of a drive, Eqs.3.11-3.14 also provide the signal emitted from the spin. The transverse spin component changes the intra-cavity field by $2ig/(\kappa + 2i\Delta) \langle \hat{\sigma}_- \rangle$ leading to a signal leaking from the cavity that can be found using the input output theory relation $\langle \hat{a}_{\mathrm{out}} \rangle = \sqrt{\kappa_{\mathrm{ext}}} \langle \hat{a} \rangle$ (see Eq.2.24). At resonance ($\Delta = 0$) the signal emitted from the spin into the output transmission line is thus roughly $2g \langle \hat{\sigma}_- \rangle / \sqrt{\kappa}$. It is proportional to the spin-photon coupling g, to $1/\sqrt{\kappa}$, and to the transverse spin component $\langle \hat{\sigma}_- \rangle$.

Homogeneous and inhomogeneous broadening

The decoherence process of a spin corresponds in the frequency domain to a finite spectral linewidth $1/T_2$ named 'homogeneous' broadening. In the presence of an ensemble of spins, the linewidth is in general much larger because of the inhomogeneity of the spin environment, resulting in a distribution of Larmor frequencies $\rho(\omega_s)$.

This 'inhomogeneous' broadening can be modeled as resulting from a sum of contributions of homogeneously broadened subsets, each of them described by the semiclassical Bloch equations Eqs.3.11-3.13. Such a sum results in a decay of the ensemble transverse magnetization $\hat{\sigma}_{x,y}^{(ens)}$ at a rate $1/T_2^* = \Gamma_{inh}$, with Γ_{inh} the width of $\rho(\omega_s)$ typically much larger than $1/T_2$.

Thermal equilibrium for a spin coupled to two baths
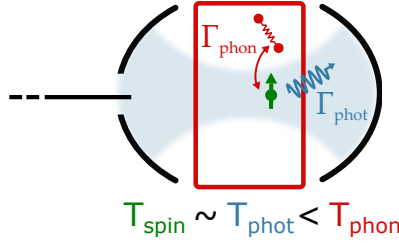
Figure 3.5: **Spin thermalization in the Purcell regime.** Quantum optics representation of the spin coupled to the lattice bath with strength Γ_{phon} and to the resonator effective bath with strength Γ_{phot}. In the Purcell regime ($\Gamma_{phot} \gg \Gamma_{phon}$) spins thermalize to the resonator mode temperature T_{phot}.

The master equation Eq.3.8, valid in the weak spin-cavity coupling regime, describes a spin coupled to two baths: the damped resonator mode and the lattice. Neglecting decoherence terms, Eq.3.8 at finite temperature then reads (see Appendix A):

$$\frac{d\tilde{\rho}}{dt} = -\frac{i}{\hbar}[\hat{H}_{eff}, \tilde{\rho}] - \frac{\Gamma_1(0)[n_{th}(T_{spin}) + 1]}{2}(\hat{\sigma}_+\hat{\sigma}_-\tilde{\rho} + \tilde{\rho}\hat{\sigma}_+\hat{\sigma}_- - 2\hat{\sigma}_-\tilde{\rho}\hat{\sigma}_+)$$
$$- \frac{\Gamma_1(0)n_{th}(T_{spin})}{2}(\hat{\sigma}_-\hat{\sigma}_+\tilde{\rho} + \tilde{\rho}\hat{\sigma}_-\hat{\sigma}_+ - 2\hat{\sigma}_+\tilde{\rho}\hat{\sigma}_-), \tag{3.19}$$

with $\hat{H}_{eff} = \frac{\Delta_s}{2}\langle\hat{\sigma}_z\rangle g(\alpha\hat{\sigma}_+ + \alpha^*\hat{\sigma}_-)$ and n_{th} given by Eq.2.1:

$$n_{th}(T_{spin}) = \frac{\Gamma_{phot}}{\Gamma_1(0)}n_{th}(T_{phot}) + \frac{\Gamma_{phon}}{\Gamma_1(0)}n_{th}(T_{phon}). \tag{3.20}$$

If the spin is in the Purcell regime where $\Gamma_{phot} \gg \Gamma_{phon}$, it is expected to thermalize to the resonator mode, $T_{spin} \approx T_{phot}$ independently on the lattice temperature. This opens the possibility to cool the spin below the host lattice temperature, as we demonstrate in the experiments reported in the next chapters.

From Eq.3.13, we derive the evolution of $\hat{\sigma}_z$:

$$\frac{d\langle\hat{\sigma}_z\rangle}{dt} = \omega_1\langle\hat{\sigma}_y\rangle - \Gamma_1(0)[2n_{th}(T_{spin}) + 1]\left[\langle\hat{\sigma}_z\rangle + \frac{1}{2n_{th}(T_{spin}) + 1}\right]. \tag{3.21}$$

Two changes are observed in the $\hat{\sigma}_z$ equation of motion with respect to the zero temperature case. First, the relaxation rate towards thermal equilibrium $\Gamma_1(T_{\text{spin}})$ is accelerated:

$$\Gamma_1(T_{\text{spin}}) = \Gamma_1(0)[2n_{\text{th}}(T_{\text{spin}}) + 1] \tag{3.22}$$

This is a consequence of the fact that, in addition to the spontaneous emission, absorption and stimulated emission processes become possible thus enhancing the relaxation rate by the factor $2n_{\text{th}}(T_{\text{spin}}) + 1$. Second, the thermal equilibrium value of the spin polarization $p(T_{\text{spin}})$ is reduced with respect to the zero temperature value of 1 to:

$$p(T_{\text{spin}}) = \frac{1}{2n_{\text{th}}(T_{\text{spin}}) + 1} = \tanh\left(\frac{\hbar\omega_{\text{s}}}{2k_{\text{B}}T_{\text{spin}}}\right) \tag{3.23}$$

The temperature dependence of spin polarization is thus given by the Curie law, resulting from the Boltzmann distribution of spin population between ground and excited state. We note here that both the energy relaxation rate and the polarization show the same temperature behaviour, as we have $\Gamma_1(T_{\text{spin}})/\Gamma_1(0) = p(0)/p(T_{\text{spin}}) = 2n_{\text{th}}(T_{\text{spin}}) + 1$.

By substituting Eq.3.20 into the expressions of both the relaxation rate (Eq.3.22) and the polarization (Eq.3.23), we get:

$$\Gamma_1(T_{\text{spin}}) = \Gamma_{\text{phot}}[2n_{\text{th}}(T_{\text{phot}}) + 1] + \Gamma_{\text{phon}}[2n_{\text{th}}(T_{\text{phon}}) + 1] \tag{3.24}$$

$$p(T_{\text{spin}}) = \frac{\Gamma_{\text{phot}}[2n_{\text{th}}(T_{\text{phot}}) + 1]}{\Gamma_1(T_{\text{spin}})}p(T_{\text{phot}}) + \frac{\Gamma_{\text{phon}}[2n_{\text{th}}(T_{\text{phon}}) + 1]}{\Gamma_1(T_{\text{spin}})}p(T_{\text{phon}}). \tag{3.25}$$

From Eq.3.24 we see that the total relaxation rate is still the sum of the radiative and spin-lattice relaxation rates, now enhanced by the thermal processes. On the other hand, the polarization of the spin at T_{spin} in Eq.3.25 is an average of the equilibrium polarization at the two bath temperatures weighted by the corresponding thermal relaxation rates.

Ensemble dynamics and equations for numerical simulation

The experiments presented in this thesis involve a large ensemble of spins coupled to the cavity. Due to inhomogeneous broadening and non-unique coupling, simulations of an N-spins ensemble evolution are necessary to reproduce and predict the measurements. More details on the numerical simulations presented here are found in ref.[21]. The ensemble is divided in M sub-ensembles with coupling g_m and spin resonance frequency $\omega_d + \Delta_s^{(m)}$, each of it regarded as homogeneous and hence described by the semiclassical Bloch equations Eqs.3.11-3.14. The decoherence rate γ is assumed equal for all sub-ensembles. On the other hand, since we're interested in the Purcell regime, the relaxation rate of each sub-ensemble $\Gamma_1^{(m)}(g_m, \Delta_m)$ is calculated with the Purcell formula Eq.3.10. The equations describing the evolution of the sub-ensemble m together with the intra-cavity field are then:

$$\frac{\mathrm{d}\langle\hat{\sigma}_x^{(m)}\rangle}{\mathrm{d}t} = \Delta_s^{(m)}\langle\hat{\sigma}_y^{(m)}\rangle + 2g_k\langle\hat{Y}\rangle\langle\hat{\sigma}_z^{(m)}\rangle - \gamma\langle\hat{\sigma}_x^{(m)}\rangle \tag{3.26}$$

$$\frac{\mathrm{d}\langle\hat{\sigma}_y^{(m)}\rangle}{\mathrm{d}t} = \Delta_s^{(m)}\langle\hat{\sigma}_x^{(m)}\rangle - 2g_k\langle\hat{X}\rangle\langle\hat{\sigma}_z^{(m)}\rangle - \gamma\langle\hat{\sigma}_y^{(m)}\rangle \tag{3.27}$$

$$\frac{\mathrm{d}\langle\hat{\sigma}_z^{(m)}\rangle}{\mathrm{d}t} = 2g_k\langle\hat{X}\rangle\langle\hat{\sigma}_y^{(m)}\rangle - 2g_k\langle\hat{Y}\rangle\langle\hat{\sigma}_x^{(m)}\rangle - \Gamma_1^{(m)}\left[\langle\hat{\sigma}_z^{(m)}\rangle + p^{(m)}\right] \tag{3.28}$$

$$\frac{\mathrm{d}\langle\hat{X}\rangle}{\mathrm{d}t} = \sqrt{\kappa_{\mathrm{ext}}}\beta_X - \frac{\kappa}{2}\langle\hat{X}\rangle - \sum_{j=1}^{M}g_j\langle\hat{\sigma}_y^{(j)}\rangle \tag{3.29}$$

$$\frac{\mathrm{d}\langle\hat{Y}\rangle}{\mathrm{d}t} = \sqrt{\kappa_{\mathrm{ext}}}\beta_Y - \frac{\kappa}{2}\langle\hat{Y}\rangle + \sum_{j=1}^{M}g_j\langle\hat{\sigma}_x^{(j)}\rangle, \tag{3.30}$$

where $\beta_{X,Y}$ are the in-phase and out of phase parts of the input drive and $p^{(m)}$ is the initial polarization. We note that the last term in equation Eqs.3.29-3.30 couples all the M differential equations by including all feedback effects of the field radiated by the spins on their dynamics. However, in the experiments discussed in this thesis the spin ensemble cooperativity defined as $C = 2Ng^2/\kappa\gamma$ verifies $C \ll 1$, making it possible to further simplify the solution of the system of M differential equations. In this regime the field generated by the spins is too small to affect significantly their own dynamics and can thus be neglected for most of the experimental time. The numerical solution of all the sub-ensembles is then obtained independently and finally all contributions are summed with the weights given by $\rho(\omega_\mathrm{s})$ and the coupling distribution $\rho(g)$. We use this simplified approach for the simulation of our experiments that are presented in the following of this thesis.

3.2   Inductive detection of magnetic resonance

In the previous section we have seen how the spin transverse magnetization $\langle\hat{\sigma}_{x,y}\rangle$ generates a field in the LC resonator that is proportional to the magnetic coupling g realized by the inductive part of the resonant circuit. The field leaking out of the resonator allows then spin detection. Such 'inductive detection' is the most widely used magnetic resonance measurement technique.

The transverse magnetization can be produced by either a continuous or a pulsed excitation. In the case of continuous drive, the precessing magnetization can result in an absorption or phase shift of the incoming microwave, which can typically be detected with lock-in techniques. Sequences of drive pulses can instead produce transient transverse magnetization on the time-scale of the relevant relaxation times of the system. Since the latter is the main technique we have used in our experiments, we detail it hereafter for an inhomogeneous ensemble in the simplified case of large cavity bandwidth ($\kappa \gg 1/T_2^*$). Throughout the remaining of this thesis, for the sake of simplicity, we refer to the spin ensemble magnetization normalized to 1 with the same symbol used for the single spin vector operator $\hat{\boldsymbol{\sigma}}$.
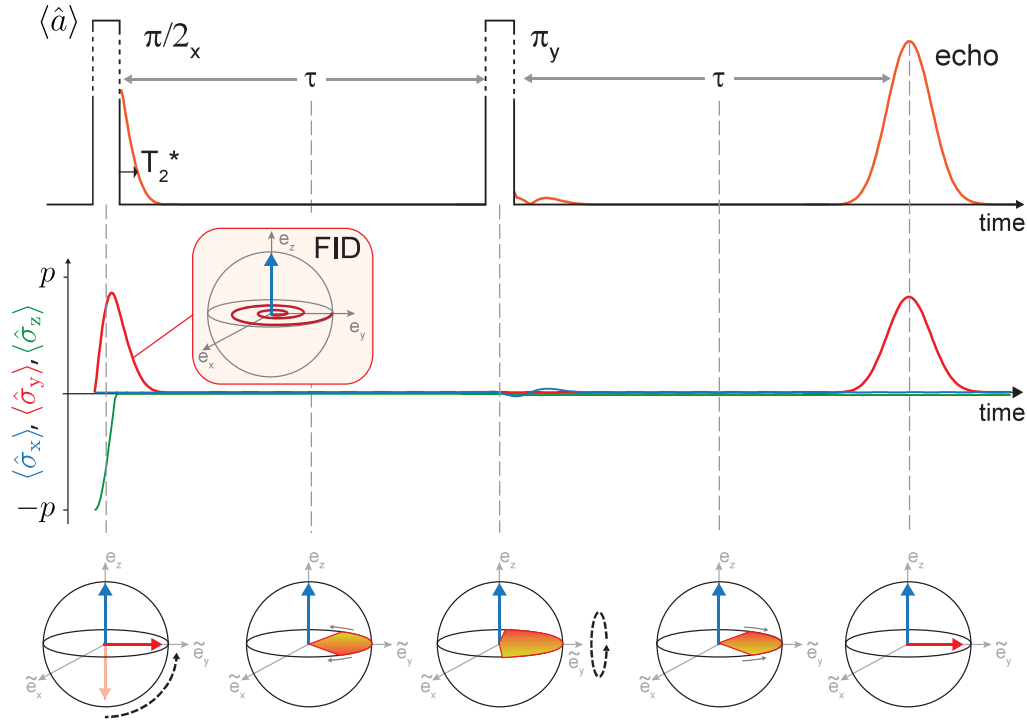
Figure 3.6: **Free induction decay and echo.** Starting from thermal equilibrium, the application of a first microwave pulse around $\tilde{\boldsymbol{e}}_x$ rotates the ensemble magnetization to the equatorial plane of the Bloch sphere, inducing the emission of a coherent signal (the FID) before decoherence takes place. After a delay time τ a second pulse rotates the magnetization around $\tilde{\boldsymbol{e}}_y$ by a angle of π yielding a magnetization refocusing after another delay τ with consequent emission of the echo signal. The effects of the finite cavity bandwidth are neglected. Top graph: The resonator field $\langle \hat{a} \rangle$. In black the field originated by the drive; the coloured line is the field emitted by the spins. Middle graph: The three components of the ensemble magnetization (extracted from numerical simulation for typical ESR parameters). Bottom: Bloch sphere representation of the collective spin evolution with the effect of the pulses illustrated by the black arrows.

3.2.1 Pulsed electron spin resonance

Free induction decay

The application of a pulse of tipping angle $\theta_{\mathrm{p}} = \pi/2$ brings the equilibrium longitudinal magnetization of an inhomogeneous ensemble of N spins on the equatorial plane realizing the transverse polarization $\langle \hat{\sigma}_- \rangle = Np(T_{\mathrm{spin}})$. Immediately after the pulse, the magnetization vector precesses around $\boldsymbol{e}_z$ at the Larmor frequency ω_{s} while the transverse and longitudinal components are decaying exponentially at rates $1/T_2^*$ and Γ_1, respectively (Eqs.3.11-3.13, see Fig.3.6). This oscillating magnetization generates a damped coherent intra-cavity field (see Eq.3.14) named free induction decay (FID):

$$\langle \hat{a} \rangle_{\mathrm{FID}}(t) \sim \frac{Ng}{\kappa} p(T_{\mathrm{spin}}) e^{i\omega_{\mathrm{s}}t} e^{-t/T_2^*} \tag{3.31}$$

Spin echo

The fast decay of the spin ensemble coherence due to inhomogeneous broadening can be made reversible by the pulse sequence named Hahn Echo [22], which is used in most of our experiments (see Fig.3.6). A first $\pi/2$ pulse induces the transverse magnetization $\langle \hat{\sigma}_- \rangle = Np(T_{\text{spin}})$ decaying in the characteristic time T_2^* while emitting the FID signal. After a delay time $\tau \gg T_2^*$ a π pulse $90°$-rotated with respect to the $\pi/2$ pulse is applied, effectively reverting the time evolution of the ensemble. As a result, after a second delay of duration τ the magnetization refocuses and reaches its initial value. The time reversal of FID is observed before the coherence decays again in the same T_2^* time. The signal emitted by the refocused magnetization is known as 'spin echo' and, being a revival of the FID, its amplitude is also proportional to the initial ensemble polarization $p(T_{\text{spin}})$. For this reason the echo signal is the spin thermometer we use in our radiative cooling experiments. If no relaxation processes were present, echo amplitude would stay constant as a function of τ. Instead, it decays due to decoherence at the rate $\gamma_\perp$.

A major advantage of spin echo is its time separation from the applied pulses compared to FID. The decay of the intra-cavity field generated by the input pulses overlaps with the FID, possibly preventing the spin signal detection. This effect becomes particularly relevant for small cavity bandwidth with respect to the inhomogeneous spin linewidth, as it is the case in our experiments.

Rabi oscillations in the presence of inhomogeneous broadening

The drive pulse calibration is performed by measuring the Rabi oscillations with the Hahn-echo sequence. For that, the echo is detected as a function of the tipping angle θ_p of the refocusing pulse, varied by sweeping the pulse power P_{in}. This results in oscillations of the echo signal, as we detail hereafter.

Consider an ensemble spins with identical coupling g and initial polarization p, divided in N subsets of detuning Δ_j, distributed according to $\rho(\Delta)$. An ideal $\pi/2$ pulse applied around the $x-$axis at time -2τ creates a transversal magnetization state aligned on the $y-$axis. The evolution of each spin subset j at of detuning Δ_j at times $-2 \leqslant t < -\tau$ is:

$$\begin{cases} \langle \hat{\sigma}_x^{(j)}(t) \rangle & = p\sin\left(\Delta_j(t + 2\tau)\right) \\ \langle \hat{\sigma}_y^{(j)}(t) \rangle & = p\cos\left(\Delta_j(t + 2\tau)\right) \\ \langle \hat{\sigma}_z^{(j)}(t) \rangle & = 0 \end{cases} \tag{3.32}$$

Applying a pulse of tipping angle θ_p around the y-axis at time $t = -\tau$ leads to the following evolution at times $t \geqslant -\tau$ for each subset j:

$$\begin{cases} \langle \hat{\sigma}_x^{(j)}(t) \rangle & = p\sin\left(\Delta_j(t + 2\tau)\right)\cos\theta_p \\ \langle \hat{\sigma}_y^{(j)}(t) \rangle & = p\cos\left(\Delta_j(t + 2\tau)\right) \\ \langle \hat{\sigma}_z^{(j)}(t) \rangle & = p\sin\left(\Delta_j(t + 2\tau)\right)\sin\theta_p \end{cases} \tag{3.33}$$

Assuming that the tipping angle is identical for all spin subsets, one can show that the transverse magnetization at time $t = 0$ is:

$$\begin{cases} \langle \hat{\sigma}_x(0) \rangle & = \frac{p}{2}(1 + \cos\theta_p) \sum_j \sin\left(2\Delta_j\tau\right) \\ \langle \hat{\sigma}_y(0) \rangle & = \frac{p}{2}(1 - \cos\theta_p) + \frac{p}{2}(1 + \cos\theta_p) \sum_j \cos\left(2\Delta_j\tau\right) \end{cases} \tag{3.34}$$

If $2\tau \gg T_2^*$, the sums $\sum_j \sin(2\Delta_j\tau)$ and $\sum_j \cos(2\Delta_j\tau)$ average to zero and as a result the spin integrated echo signal A_e is proportional only to:

$$A_e \propto \frac{p}{2}(1 - \cos\theta_p), \tag{3.35}$$

allowing to determine P_{in} corresponding to a π pulse.

CPMG sequence
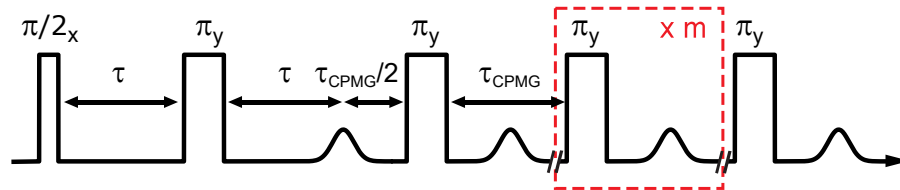
Figure 3.7: **CPMG sequence.** The spin echo generated by the Hahn echo sequence can be refocused m times by a series of equally spaced π pulses applied along the echo phase direction.

After the echo detection, waiting a time of about $1/\Gamma_1$ to let the spins come back to equilibrium is necessary before repeating the Hahn Echo sequence and detect a second echo. This limit can be overcome by the Carr-Purcell-Meiboom-Gill (CPMG) sequence that allows to refocus the magnetization several times before decoherence occurs (see Fig.3.7). The first part of CPMG is the Hahn echo sequence. A delay time $\tau_{CPMG}/2$ (generally different from τ) after the echo, a train of m π pulses equally spaced by τ_{CPMG} is applied. Each π pulse causes an additional magnetization refocusing and therefore emission of an extra echo. As a result, in a single experimental sequence m extra echoes are detected in the same measurement time. Averaging all the echoes would lead to an ideal $\sqrt{m}$-fold improvement of the signal-to-noise ratio (SNR), that is however limited at high m by the residual decoherence rate. In many experiments we use the CPMG sequence to increase the SNR and perform faster measurements.

Chapter 4

Bismuth donors in Silicon

This last chapter of the Background part is dedicated to the spin system we use in our experiments: bismuth donors in silicon (Si:Bi). The first in-depth study of group-V donors in silicon is due to the works from Honig and Feher [23, 24] performed in the 1950s, particularly focused on phosphorus and arsenic. Renewed attention to these systems has emerged in the last twenty years after the Kane's proposal of a quantum computer based on phosphorus donors in silicon [25].

Silicon as a host material for donor spins is of great interest because its main isotope ^{28}Si has zero nuclear spin so that an enriched ^{28}Si crystal would realize a very quiet magnetic environment. And indeed, ultra-long coherence times were measured for donor electron spins in silicon, which makes them suitable candidates for quantum information processing and storage. Due to its simple energy spectrum and widespread use in CMOS technology, phosphorus is the most studied silicon donor. Other group-V donors include ^{31}P, ^{33}As, ^{121,123}Sb and ^{209}Bi(see 4.1). Bismuth is the heaviest atom and shows the largest electron confinement, consistently with the largest hyperfine interaction and ionization energy. It recently gained new attention due to its optimal working point at which its spin transition frequency is at first order independent on magnetic field and thus insensitive to magnetic field noise, leading to the longest measured coherence time for an electron spin in the solid state [26].

Table 4.1: **Group V donors characteristics:** ionization energy (E_D), apparent Bohr radius (a_0), nuclear spin and hyperfine coupling constant (A) and the energy difference between the first excited valley state and the ground state (ΔE). Extracted from [27–31].

Donor		^{31}P	^{33}As	^{123}Sb	^{121}Sb	^{209}Bi
E_D	(meV)	45.6	53.8	42.8	42.8	71
a_0	(nm)	1.82	1.66	1.86	1.86	1.45
ΔE	(meV)	13	22.5	12.3	12.3	41
I		1/2	3/2	5/2	7/2	9/2
A	(MHz)	118	198	186	101	1475.4

In this chapter we aim at providing the main information on bismuth donors in silicon needed to describe our experiments. We first present the electronic structure before concentrating on the spin Hamiltonian to illustrate the spin energy levels and microwave transitions in the relevant limits. We then move to the decoherence and energy relaxation processes with particular focus on the role of the environment of ^{29}Si

nuclear spins. We briefly discuss the effect of strain before analyzing the phenomena induced by optical illumination. We conclude with some details on the fabrication and characterization of the sample used in our experiments.

4.1   A substitutional donor in silicon
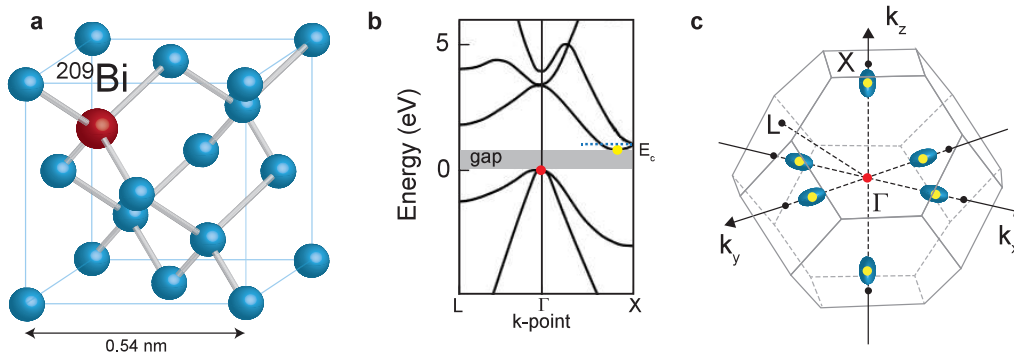
Figure 4.1: **Bismuth donor in silicon. a** A single bismuth substitutional impurity in silicon diamond lattice. **b** Silicon energy band diagram; valence band maximum and conduction band minimum highlighted in red and yellow, respectively. **c** First Brillouin Zone, with the six degenerate valleys of the conduction band indicated in yellow. Blue ellipsoids symbolize isoenergy surfaces.

Silicon is an element of the IV-group crystallizing in a diamond structure, where each silicon atom is at the center of a tetrahedron whose vertices are occupied by its four first neighbours to which is covalently bound (see Fig.4.1a). The corresponding Brillouin zone in the reciprocal space is shown in Fig.4.1c. The band structure represented in Fig.4.1b, shows an indirect band-gap of energy $E_{\mathrm{g}} = 1.1\,\mathrm{eV}$ at $300\,\mathrm{K}$. While the valence band maximum is at the center Γ of the Brillouin zone, the six-fold degenerate conduction band minimum takes place at a distance $0.85\ 2\pi/a$ from Γ along the six vectors $\pm\boldsymbol{k}_{\mathrm{x}}$, $\pm\boldsymbol{k}_{\mathrm{x}}$ and $\pm\boldsymbol{k}_{\mathrm{z}}$, $a = 0.543\,\mathrm{nm}$ being the silicon lattice parameter. These six degenerate conduction band minima are called silicon valleys.

A bismuth donor is an impurity substituting a silicon atom in the lattice. Four of its valence electrons form a covalent bond with the four neighbouring silicon atoms, keeping almost unaltered the local geometry (see Fig.4.1). The fifth electron is either bound to the bismuth nucleus Coulomb potential forming the 'neutral donor' (state D^0) or ionized to the conduction band (state D^+). The ionization energy is $E_{\mathrm{D}} =71\,\mathrm{meV}$ [29].

4.1.1   Electronic state

The V-group donors in silicon are called shallow impurities because $E_{\mathrm{D}} \ll E_{\mathrm{g}}$. Since the donor electron wavefunction of such impurities extends over many lattice sites (see Fig.4.2a), it is naturally written as a linear combination of wavefunctions of electrons in the silicon conduction band, and inherits some of their characteristics. Moreover, the dielectric properties of silicon affects the Coulomb interaction with the central ion. We first consider the approximate solution for the electronic structure obtained applying the method developed by Kohn and Luttinger [32] (see also [33]), based on the effective mass theory (EMT). Here the electrostatic potential of the nucleus binding

Figure 4.2: **Bismuth electronic states. a** Illustrative schematic of the donor wave function and of the Coulomb potential compared to the lattice parameter. **b** Six-fold degenerate ground states predicted by effective mass theory with an additional valley-orbit interaction perturbation.

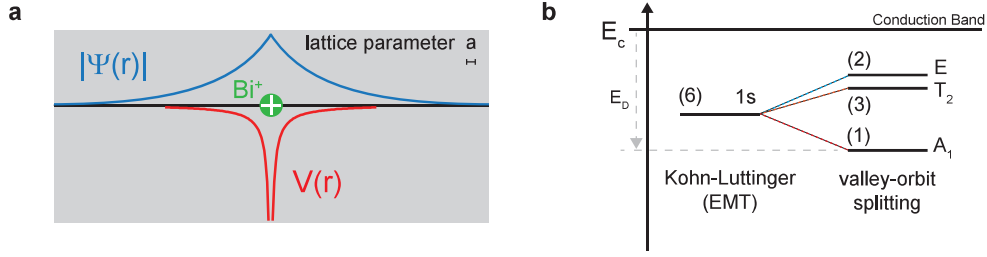the electron is modeled by the Coulomb potential $V(r) = -e^2/(\epsilon_{\text{Si}}r)$, where ϵ_{Si} is the silicon dielectric constant. The EMT predicts a 1s ground state in the form of a superposition of six degenerate valley wavefunctions consisting of the product of the conduction band function $\phi_{\boldsymbol{k}_\mu}(\boldsymbol{r})$ with a hydrogen-like envelope function $F_\mu(\boldsymbol{r})$ at the μ-th conduction-band valley [34]:

$$\Psi(\boldsymbol{r}) = \sum_\mu \alpha_\mu F_\mu(\boldsymbol{r})\phi_{\boldsymbol{k}_\mu}(\boldsymbol{r}). \tag{4.1}$$

The Bohr radius a_0 reported in Table 4.1 is here the parameter indicating the spatial extension of the hydrogenic envelope function $F_\mu(\boldsymbol{r})$. The coefficients $|\alpha_\mu|$ represent instead the probability for the donor electron to occupy the μ valley state and are called valley populations. The approximations of EMT lead to the same solutions for all the donors, giving the same a_0 and an ionization energy $E_{\text{D}} = -31.3\,\text{meV}$.

These results are in contradiction with the differences observed between the donors as evidenced in Table 4.1. Moreover, the prediction of a single degenerate state is in contradiction with experimental results [28]. Such discrepancies are attributable to the EMT failing in taking into account the environment in the proximity of the donor nucleus. An improved model takes into account the tetrahedric unit cell surrounding the donor together with the core and valence electron screening the the Bi nucleus attractive potential, by adding a phenomenological interaction called 'valley-orbit' [34]. This more accurate model catches the observed ground state degeneracy lifting, predicting three distinct 1s states labeled by their tetrahedral symmetry group designation: a symmetrical ground-state A_1, a three-fold degenerate level T_2 and a two-fold degenerate level E (see Fig. 4.2b).

The valley-orbit interaction yields the different ionization energy, Bohr radius and hyperfine coupling constant for the various donors in agreement with measurements, as reported in Table 4.1. Bismuth emerges as the most strongly bound donor with $E_{\text{D}} = 71\,\text{meV}$ and consistently with the smallest Bohr radius $a_0 = 1.45\,\text{nm}$ and largest hyperfine constant $A/2\pi = 1.4754\,\text{GHz}$. In the following, we are mainly interested in the spin properties of the donor in its neutral ground state A_1. Nonetheless, an important role is played by the higher energy states in various phenomena we discuss in this thesis.
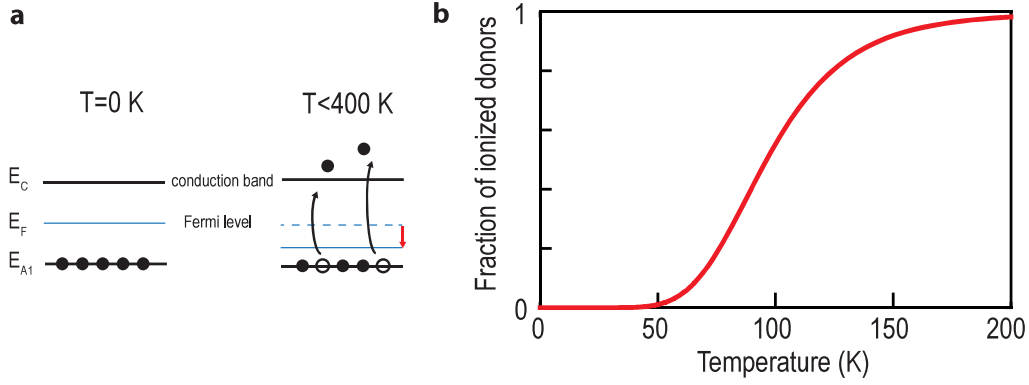
Figure 4.3:   **Bismuth charge state. a** At non-zero temperature, electrons bound to donors are excited to the conduction band, resulting in a partial ionization of the donors and a lowering of the Fermi energy level. **b** Fraction of ionized donors $N_{\mathrm{D}}^{+}/N_{\mathrm{D}}$ as a function of temperature in the case of bismuth, evaluated with $E_{\mathrm{D}} = 71\,\mathrm{meV}$ and $N_{\mathrm{D}} = 10^{16}\ \mathrm{cm}^{-3}$.

4.1.2   Charge state

The probability for a donor to be in the neutral or ionized state depends not only on the ionization energy and temperature, but also on the density of implanted atoms N_{D} and the density of states close to the conduction band minimum N_{c}. By calculating the position of the Fermi-level in between the conduction band and the donor ground state A_1, the equation for the number of ionized donors N_{D}^{+} in a non-degenerate semiconductor is found to be:

$$N_{\mathrm{D}}^{+} = \frac{N_{\mathrm{D}}}{1 + (2N_{\mathrm{D}}^{+}/N_{\mathrm{c}})e^{E_{\mathrm{D}}/k_{\mathrm{B}}T}}, \tag{4.2}$$

where $T < 400\,\mathrm{K}$ is assumed to neglect the contribution of free carriers excitation from the valence band. Solving Eq.4.2 for a concentration of bismuth donors $N_{\mathrm{D}} = 10^{16}\,\mathrm{cm}^{-3}$ and an ionization energy $E_{\mathrm{D}} = 71\,\mathrm{meV}$ (see Fig.4.3), bismuth donors are found in their neutral state for temperatures up to 40 K. In our experiments performed at $T < 1.2\,\mathrm{K}$, all donors are expected to be in their neutral state. However, even at low temperatures, donors can also be ionized by externally applied electric field [35, 36] or internal electric field associated to the formation of Schottky barriers [37].

4.2   Spin levels and ESR-allowed transitions

We now consider the spin properties of a neutral bismuth donor, arising from the electron spin $S = 1/2$ and the nuclear spin $I = 9/2$ coupled by the hyperfine constant $A/2\pi = 1.4754\,\mathrm{GHz}$. In the presence of an applied magnetic field $\boldsymbol{B}$, the spin Hamiltonian reads [38]:

$$\hat{H}/\hbar = \boldsymbol{B} \cdot \left(\gamma_{\mathrm{e}} \hat{\boldsymbol{S}} \otimes \mathbb{1} - \gamma_{\mathrm{n}} \mathbb{1} \otimes \hat{\boldsymbol{I}} \right) + A \hat{\boldsymbol{S}} \cdot \hat{\boldsymbol{I}}, \tag{4.3}$$

where $\gamma_{\mathrm{e}}/2\pi = 27.997\,\mathrm{GHz/T}$ and $\gamma_{\mathrm{n}}/2\pi = 6.962\,\mathrm{MHz/T}$ are the electronic and nuclear gyromagnetic ratios, respectively. The first term describes the Zeeman effect and the

second the isotropic hyperfine coupling [38]. We now follow the analysis made by Mohammady et al. in ref.[39] to discuss the properties of the eigen-states and of the ESR transitions, with particular focus on the limit of low magnetic field. First, we rewrite Eq.4.3 assuming a static magnetic field $\boldsymbol{B}_0 = B_0 \boldsymbol{e}_z$ applied along z:

$$\hat{H}_0/\hbar = A\hat{S}_z\hat{I}_z + \frac{A}{2}(\hat{S}_+\hat{I}_- + \hat{S}_-\hat{I}_+) + \omega_0(\hat{S}_z - \delta\hat{I}_z), \tag{4.4}$$

where $\omega_0 = B_0\gamma_e$ and $\delta = \gamma_n/\gamma_e = 10^{-3}$. The twenty states defining the Zeeman basis $\{|m_{\mathrm{s}}, m_{\mathrm{i}}\rangle\}$, with $m_{\mathrm{s}} = \pm 1/2$ and $m_{\mathrm{i}} = -9/2...9/2$, do not diagonalize the Hamiltonian due to the hyperfine coupling. The eigenstates are therefore hybridized electro-nuclear states we detail hereafter. The energy spectrum as a function of B_0 obtained from diagonalization of the Hamiltonian Eq.4.4 is shown in Fig4.4.

4.2.1 Eigenstates

To introduce the spin system eigenstates, we first consider the application of the Hamiltonian Eq.4.4 on a state of the Zeeman basis:

$$\hat{H}_0/\hbar\,|\pm\tfrac{1}{2}, m_{\mathrm{i}}\rangle = \left(\pm\frac{A}{2}m_{\mathrm{i}} \pm \frac{\omega_0}{2} + \omega_0\delta m_{\mathrm{i}}\right)|\pm\tfrac{1}{2}, m_{\mathrm{i}}\rangle + \frac{A}{2}\hat{I}_\pm\,|\mp\tfrac{1}{2}, m_{\mathrm{i}}\rangle. \tag{4.5}$$

As expected, Zeeman states are mixed by the hyperfine interaction. However, it is evident that the $|\tfrac{1}{2}, \tfrac{9}{2}\rangle$ and $|-\tfrac{1}{2}, -\tfrac{9}{2}\rangle$ are unmixed eigenstates of the Hamiltonian since $\hat{I}_\pm\,|\mp\tfrac{1}{2}, \pm\tfrac{9}{2}\rangle = 0$. Their energy is:

$$E_{|\pm\frac{1}{2},\pm\frac{9}{2}\rangle} = \frac{9}{2}A \pm \frac{\omega_0}{2}(1 + 9\delta). \tag{4.6}$$

In the bismuth spectrum (see Fig.4.4), these two unmixed states are the only ones showing a linear energy dependence on magnetic field.

In the presence of the hyperfine coupling term, the projection of the total angular momentum $\hat{\boldsymbol{F}} = \hat{\boldsymbol{I}} + \hat{\boldsymbol{S}}$ onto $\boldsymbol{e}_z$ is still commuting with the Hamiltonian, $[\hat{H}_0, \hat{S}_z + \hat{I}_z] = 0$, and its eigenvalue $m = m_{\mathrm{i}} + m_{\mathrm{s}}$ is thus a good quantum number. From Eq.4.5 it appears that for $|m| < 5$, $|\pm\tfrac{1}{2}, m_{\mathrm{i}}\rangle = |\pm\tfrac{1}{2}, m \mp \tfrac{1}{2}\rangle$ hybridizes with $|\mp\tfrac{1}{2}, m_{\mathrm{i}} \pm 1\rangle = |\mp\tfrac{1}{2}, m \pm \tfrac{1}{2}\rangle$. As shown in ref.[39], the expression for the eigenstates exact for any field and value of m is then:

$$|\pm, m\rangle = a_m^\pm\,|\pm\tfrac{1}{2}, m \mp \tfrac{1}{2}\rangle + b_m^\pm\,|\mp\tfrac{1}{2}, m \pm \tfrac{1}{2}\rangle, \tag{4.7}$$

where

$$a_m^\pm = \cos\frac{\theta_m}{2} \tag{4.8}$$

$$b_m^\pm = \pm\sin\frac{\theta_m}{2}, \tag{4.9}$$

with the value of θ_m given by:

$$\tan\theta_m = \frac{(25 - m^2)^{1/2}}{m + \frac{\omega_0}{A}(1 + \delta)}. \tag{4.10}$$
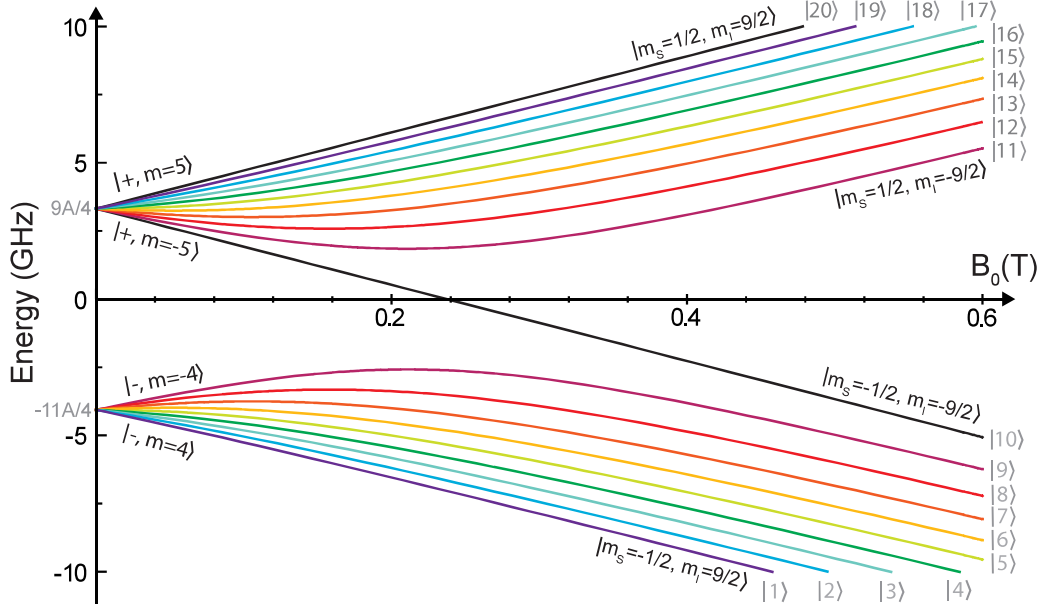
Figure 4.4:   **Bismuth energy spectrum. a** Energy-levels computed from the diagonalisation of the Si:Bi Hamiltonian as a function of B_0 (Eq.4.4). The coupled energy-levels $E_m^\pm$ are color-coded from purple to red, the uncoupled energy-levels are in black. Figure adapted from [39, 40]

The corresponding eigen-energies are:

$$E_m^\pm = \frac{A}{2}(-\epsilon \pm R_m), \tag{4.11}$$

where:

$$R_m^2 = \left[m + \frac{\omega_0}{A}(1+\delta)\right]^2 + (25 - m^2) \tag{4.12}$$

$$\epsilon = \frac{1}{2} + 2\omega_0 m\delta. \tag{4.13}$$

We notice that in the high-field limit the Zeeman basis is recovered as the eigen-basis of the Hamiltonian, as expected from the fact that the hyperfine coupling becomes negligible compared to the Zeeman term that is linearly increasing with B_0. Indeed $\tan\theta_m \to 0$, thus $a_m^\pm \to 1$ and $b_m^\pm \to 0$, leading the $|\pm, m\rangle$ state to converge respectively to the Zeeman eigenstates $|m_\mathrm{s} = \pm\frac{1}{2}, m_\mathrm{i} = m \mp \frac{1}{2}\rangle$. Coherently with this analysis, it is apparent that the eigenstates can be labeled in various ways (see Fig.4.1): by order of increasing energy $\{|i\rangle, i = 1, ...20\}$, by the coupled basis $\{|\pm, m\rangle\}$ and in the high field limit by the electron and nuclear spin quantum numbers in the Zeeman basis $\left\{|m_\mathrm{s}, m_\mathrm{i}\rangle, m_\mathrm{s} = \pm\frac{1}{2}, m_\mathrm{i} = -\frac{9}{2}...\frac{9}{2}\right\}$.

Low-field limit

At $B_0 = 0$ nine degenerate ground states ('+' in the coupled basis notation) are separated from 11 excited states ('−') by $5A/2\pi \approx 7.37$ GHz, often called zero-field splitting. In our experiments we are in the 'low field limit' where $\omega_0 = B_0\gamma_\mathrm{e} \ll A$, or close to it. The following approximation for the '+' and '−' eigen-energies is then obtained:

$$E_m^+ = +\frac{9}{4}A + \frac{m}{10}\omega_0(1 + \delta \mp 10\delta) \quad \text{with} \quad m \in -5, 5 \tag{4.14}$$

$$E_m^- = +\frac{11}{4}A - \frac{m}{10}\omega_0(1 + \delta \mp 10\delta) \quad \text{with} \quad m \in -4, 4. \tag{4.15}$$

In this limit, the effect of B_0 is to linearly lift the degeneracy within the two multiplets. The magnetic field dependence of all the energies, and the coefficients $a_m^\pm$ and $b_m^\pm$ describing the mixing of the Zeeman states, are strongly dependent on m in this regime.
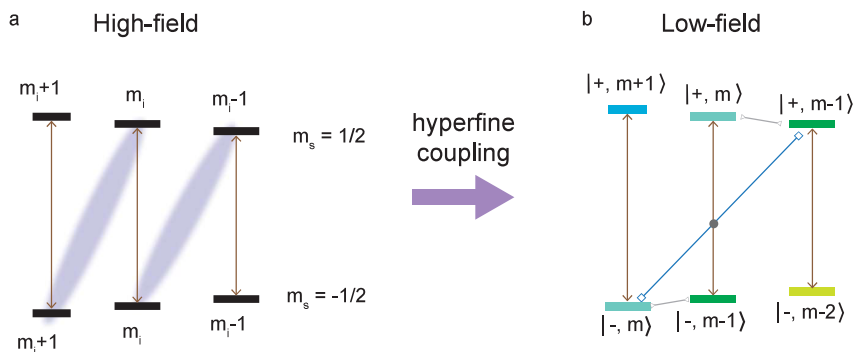
Figure 4.5: **Transition schematics. a** At high field, the usual ESR transition between levels $|m_s = \frac{1}{2}, m_i\rangle \leftrightarrow |m_s = -\frac{1}{2}, m_i\rangle$ are allowed (brown arrows). At lower fields, the hyperfine coupling renders the Zeeman basis invalid to describe the hybridized electron-nuclear states (symbolized by the blue ellipses) **b** In the low-field limit an accurate description is given by the coupled basis $|\pm, m\rangle$. The high field transitions are now labeled $|+, m\rangle \leftrightarrow |-, m-1\rangle$. The hyperfine-induced mixing allows in addition the transitions $|-, m\rangle \leftrightarrow |+, m-1\rangle$ (blue arrow), as well as $|+, m\rangle \leftrightarrow |+, m-1\rangle$ and $|-, m\rangle \leftrightarrow |-, m-1\rangle$ in the MHz range (grey arrows).

4.2.2 ESR-allowed transitions

As discussed in ch.3, in a magnetic resonance experiment the Rabi frequency induced by the drive and the signal emitted by the spin are proportional to the matrix element $\langle i |\hat{\boldsymbol{S}}| j\rangle$. In the following we estimate it for Si:Bi in the relevant limits.

S_x transitions allowed at large magnetic field

In the high-field limit, electron and nuclear spins are decoupled and the eigenstates of Si:Bi converge to the Zeeman basis, leading to the usual selection rules for electron spin transitions: $|\Delta m_s| = 1$. The transitions with non-zero matrix element are the ten $|m_s = \frac{1}{2}, m_i\rangle \leftrightarrow |m_s = -\frac{1}{2}, m_i\rangle$ with the associated $\langle 1/2, m_i |\hat{S}_x| - 1/2, m_i\rangle = 1/2$, as expected for an electronic spin $1/2$.

S_x transitions allowed at low magnetic field

At lower field, the states $|\frac{1}{2}, m_i\rangle$ and $|-\frac{1}{2}, m_i\rangle$ are changed in the hybrid states $|+, m\rangle$ and $|-, m-1\rangle$ as illustrated in Fig.4.5. The same transition at lower field does not
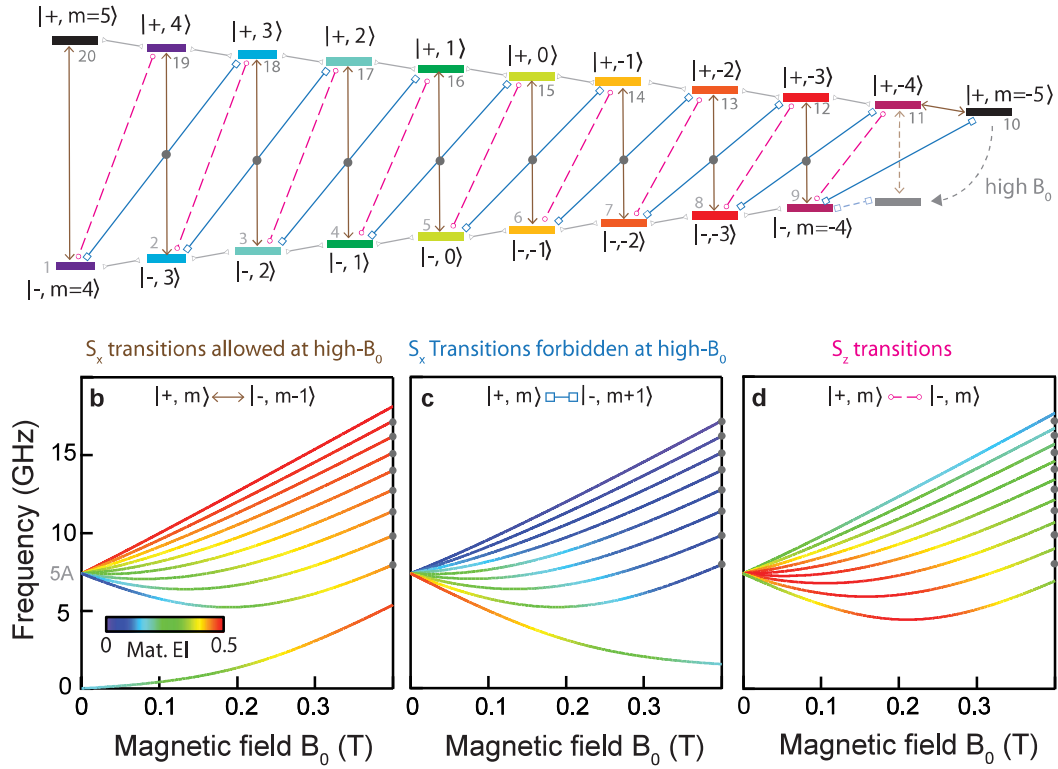
Figure 4.6:   **Bismuth ESR transitions.**   **a** Energy levels diagram with ESR allowed transitions symbolized with arrows: S_x transitions allowed at large B_0 $|+, m\rangle \leftrightarrow |-, m-1\rangle$ (brown arrows, panel **b**), S_x transitions forbidden at large B_0 $|+, m\rangle \leftrightarrow |-, m+1\rangle$ (blue square arrows, panel **c**) and S_z transitions forbidden at large B_0 $|+, m\rangle \leftrightarrow |-, m\rangle$ (pink circle arrows, panel **d**). NMR-like transitions are shown with grey triangle arrows. The additional grey level shows the position of the $|+, -5\rangle$ level at large B_0. **b-d** Frequencies of ESR allowed transitions as a function of B_0. The curves coloring indicates the transition matrix element value. The color scale is identical for all panels and given in inset of panel **b**. The grey circles in **a** and on the right-side of panels **b-d** frames indicate degenerate transitions (see main text). Figure extracted from [37].

correspond anymore to a pure electron spin flip and the the S_x matrix element becomes smaller than $1/2$ and dependent on m:

$$\langle +, m \left| \hat{S}_x \right| -, m-1 \rangle = \frac{1}{2} a_m^+ a_{m-1}^- = \frac{1}{2} \cos \frac{\theta_m}{2} \cos \frac{\theta_{m-1}}{2}. \tag{4.16}$$

Beside reducing the matrix element of these 10 transitions, hybridization enables at low field 9 extra transitions between $|-, m\rangle$ and $|+, m-1\rangle$. The frequency and matrix elements of these 9 transitions forbidden at high field are plotted in Fig.4.6. Their matrix elements, tending to zero at high field, are:

$$\langle -, m \left| \hat{S}_x \right| +, m-1 \rangle = \frac{1}{2} b_m^+ b_{m-1}^- = -\frac{1}{2} \sin \frac{\theta_m}{2} \sin \frac{\theta_{m-1}}{2}. \tag{4.17}$$

A new weaker selection rule for the S_x transitions thus appears due to the hyperfine interaction, fixing $|\Delta m| = 1$.

We notice here that the transitions $|+, m\rangle \leftrightarrow |-, m-1\rangle$ and $|+, m-1\rangle \leftrightarrow |-, m\rangle$ are quasi degenerate in frequency for $|m| \leqslant 4$, especially if compared to typical values of inhomogeneous broadening, and that their matrix elements are complementary: $\left|b_m^- b_{m-1}^+\right|/2 + \left|a_m^+ a_{m-1}^-\right|/2 \approx 1/2$.

NMR-like S_x transitions

In addition to the transitions in the GHz range discussed above, the electro-nuclear hybridization allows S_x transitions between $|\pm, m\rangle$ and $|\pm, m-1\rangle$. These transitions in the MHz range corresponds in the high field limit to pure nuclear spin flips that can only be driven by the nuclear spin matrix element I_x. These sizeable S_x matrix elements acquired at low field are:

$$\langle +, m \left|\hat{S}_x\right| +, m-1\rangle = \frac{1}{2}a_m^+ b_{m-1}^+ = \frac{1}{2}\cos\frac{\theta_m}{2}\sin\frac{\theta_{m-1}}{2} \qquad (4.18)$$

$$\langle -, m \left|\hat{S}_x\right| -, m-1\rangle = \frac{1}{2}a_{m-1}^- b_m^- = -\frac{1}{2}\cos\frac{\theta_{m-1}}{2}\sin\frac{\theta_m}{2}. \qquad (4.19)$$

Consequently, these transition can be driven faster than the usual nuclear spin transitions, as demonstrated in [41]. Moreover, their electronic character lead to a stronger spin-spin interaction as we will see in the following.

S_z transitions

Another property of Si:Bi caused by the hyperfine coupling is the existence at low field of 9 transitions with sizeable S_z matrix element. A microwave field $\boldsymbol{B}_1$ parallel to be zero can thus excite these transitions connecting the levels $|+, m\rangle$ and $|-, m\rangle$, whose matrix element is given by:

$$\langle +, m \left|\hat{S}_z\right| -, m\rangle = \sin\frac{\theta_m}{2}. \qquad (4.20)$$

Their field dependence of these matrix elements and of the corresponding transition frequency is shown in Fig.4.6. We notice that their frequency is in-between two S_x transitions.

Clock-transitions

In the Si:Bi spectrum shown in Fig.4.6 exist 8 minima. These $df/dB = 0$ sweet-spots predicted by Mohamady et al. [39, 42] for V-group donors in silicon are called clock transitions and originates from the interplay of the Zeeman and the hyperfine terms in the Hamiltonian. Observed experimentally by Wolfowicz et al. [26], clock transitions are of particular interest for quantum information applications since their coupling to magnetic noise is strongly suppressed and substantial increase of coherence time is observed. Among the V-group donors, bismuth is the only one presenting clock transitions in the gigahertz range, thus suitable for quantum information processing in combination with circuit-QED.

4.2.3   Effective spin 1/2 approximation

We discuss here the possibility to describe the twenty-level bismuth spin system as an effective spin $1/2$ in a magnetic resonance experiment. The two transitions $|+, m\rangle \leftrightarrow |-, m-1\rangle$ and $|+, m-1\rangle \leftrightarrow |-, m\rangle$ are quasi degenerate in the $|m| \leqslant 4$ manifold so they are simultaneously resonant with the drive field B_1. As long as interaction with the environment is negligible, the corresponding four spin states are isolated from the other 16 and the two resonant transitions are well described as two species of spin $1/2$ with slightly different Larmor frequency and S_x matrix element.
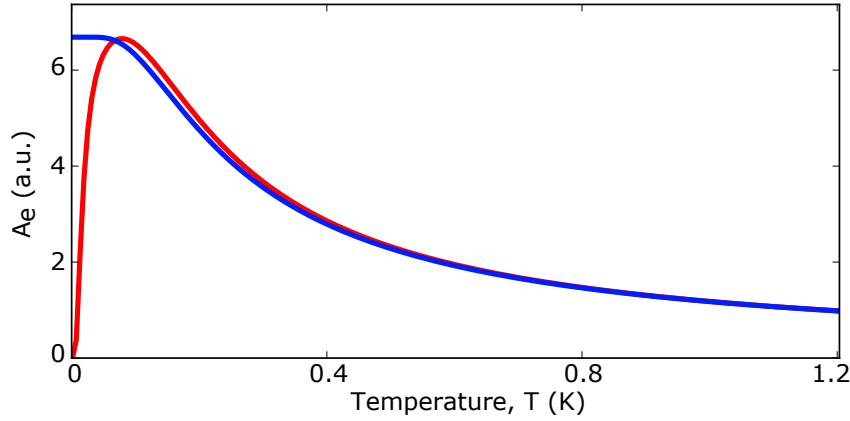
Figure 4.7: **Polarization dependence on temperature.** Polarization $p_{\mathrm{Bi}}(T)$ (red) of the two quasi-degenerate transitions $|+, 0\rangle \leftrightarrow |-, -1\rangle$ and $|+, -1\rangle \leftrightarrow |-, 0\rangle$ at $B_0 = 62.5\,\mathrm{mT}$ as a function of temperature compared to the polarization $p_{1/2}(T)$ (blue) of a spin $1/2$ having the same transition frequency. The two curves are normalized to assume the value of 1 at $1.2\,\mathrm{K}$.

One major deviation from the spin $1/2$ approximation is expected for the temperature dependence of the polarization $p(T)$ of the probed transitions and therefore of the magnetic resonance signal proportional to it. For a spin $1/2$, we have seen that $p_{1/2} = \langle \sigma_z \rangle (T) = \tanh(\hbar \omega / 2kT)$. The polarization of the two resonant transitions is instead the population distribution unbalance between the two excited and the two ground states: $p_{\mathrm{Bi}}(T) = (p_{|-,m\rangle} + p_{|-,m-1\rangle} - p_{|+,m\rangle} - p_{|+,m-1\rangle})$, where $p_{|\pm,m\rangle} = e^{-E_{\pm,m}/kT}/Z$ is the occupation probability of $|\pm, m\rangle$, with $Z = \sum_{\pm,m} e^{-E_{\pm,m}/kT}$ the partition function. The red line in Fig.4.7 shows $p_{\mathrm{Bi}}(T)$ for the quasi degenerate transitions $|+, 0\rangle \leftrightarrow |-, -1\rangle$ and $|+, -1\rangle \leftrightarrow |-, 0\rangle$ at $B_0 = 62.5\,\mathrm{mT}$ compared to the $p_{1/2}(T)$ of a spin $1/2$ with the same transition frequency $\omega_0/2\pi = 7.41\,\mathrm{GHz}$.

As long as $T > 100\,\mathrm{mK}$ and $B_0 < 70\,\mathrm{mT}$, the thermal energy is much larger than the energy difference between hyperfine states of both $+$ and $-$ manifolds $E_{|\pm,m\rangle} - E_{|\pm,m-1\rangle}$. In that case, one can show that $p_{\mathrm{Bi}}(T) \simeq \frac{1}{9} \frac{1 + e^{-\hbar\omega_0/kT}}{1 + 11/9 e^{-\hbar\omega_0/kT}} \tanh(\hbar\omega_0/2kT)$, which can be approxmiated by $\frac{1}{10} \tanh(\hbar\omega_0/2kT)$ especially when $kT > \hbar\omega_0$, which happens in our case for $T > 300\,\mathrm{mK}$. This is visible in Fig.4.7, where the computed $p_{\mathrm{Bi}}(T)$ (red curve) indeed coincides well with the result for a spin-1/2 $p_{1/2}(T)$ (blue curve) for $T > 300\,\mathrm{mK}$ (by proper choice of the scale for A_{e}).

4.3 Bismuth donor interactions with the spin bath

Each bismuth donor interacts with two different kinds of neighbouring spins: other bismuth donors and ^{29}Si nuclear spins. We address in the following the details of these interactions and their effects. The quantitative analysis is based on the parameters of the sample used in our experiments: bismuth donor concentration $C = 3 \times 10^{16}\,\mathrm{cm}^{-3}$ and 4.9% natural abundance of ^{29}Si. In Table 4.2 we report relevant energy and length scale of the spin baths in our sample.

Table 4.2: **Length and energy scales of the donor and ^{29}Si spin baths in our sample:** Average bismuth electron spin Larmor frequency ω_S, average ^{29}Si nuclear spin Larmor frequency ω_I, the average distance between neighbouring ^{29}Si nuclear spins $d_{^{29}\mathrm{Si}}$, the average distance between neighbouring Bi donor spins d_{Bi}, the dipolar coupling between two ^{29}Si spins $H_{\mathrm{dip}}^{\mathrm{Si\text{-}Si}}$, the dipolar coupling $H_{\mathrm{dip}}^{\mathrm{Bi\text{-}Bi}}$ between two Bi spins separated by d_{Bi}, the dipolar coupling $H_{\mathrm{dip}}^{\mathrm{Si\text{-}Si}}$ between two ^{29}Si spins separated by d_{Si}, the hyperfine coupling $H_{\mathrm{hf}}^{\mathrm{Bi\text{-}Si}}$ between a Bi donor spin and the closer ^{29}Si spins, homogeneous Bi donor linewidth γ_2 given by the measured decoherence rate of bismuth ESR transition at $10\,\mathrm{mT}$. The energy values are estimated in the field range 0-70 mT.

Bi $\omega_S/2\pi$	$\sim 7.4\,\mathrm{GHz}$
^{29}Si $\omega_I/2\pi$	$0 - 0.5\,\mathrm{MHz}$
$d_{^{29}\mathrm{Si}}$	$\sim 0.7\,\mathrm{nm}$
d_{Bi}	$\sim 20\,\mathrm{nm}$
$H_{\mathrm{dip}}^{\mathrm{Si\text{-}Si}}/h$	$\sim 50\,\mathrm{Hz}$
$H_{\mathrm{dip}}^{\mathrm{Bi\text{-}Bi}}/h$	$\sim 10\,\mathrm{kHz}$
$H_{\mathrm{hf}}^{\mathrm{Bi\text{-}Si}}/h$	$\lesssim 1\,\mathrm{MHz}$
γ_2	$2\,\mathrm{kHz}$

4.3.1 Nuclear spin bath

The ^{29}Si isotope has a spin 1/2 and constitutes the most relevant magnetic impurity in the otherwise spinless ^{28}Si environment.

Hamiltonian

In the following we describe a single ESR transition of the bismuth spectrum as an effective spin $S = 1/2$ of frequency ω_S. The interaction of the donor spin with a ^{29}Si nuclear spin $I = 1/2$ of frequency ω_I is described by the hyperfine hamiltonian $\hat{H}_{\mathrm{hf}} = \hat{\boldsymbol{S}}\boldsymbol{A}\hat{\boldsymbol{I}}$, where $\boldsymbol{A}$ is the hyperfine tensor accounting for both isotropic Fermi contact and dipolar interaction. Since $\omega_S \gg \omega_I, |A|$ (see Table 4.2) the donor spin quantization axis is unaffected by the nuclear spin and electro-nuclear spin flip-flop are highly forbidden. The non-secular terms proportional to the S_x operators are thus neglected and the Hamiltonian of a donor interacting with a ^{29}Si nucler spin in a static magnetic field B_0 applied along z is [43]:

$$\hat{H} = \omega_S S_z - \omega_I I_z + B S_z I_z + C S_z I_x, \tag{4.21}$$

where the hyperfine couplings B and C are proportional to the bismuth transition energy sensitivity to the magnetic field df/dB. Each bismuth ESR transition thus interacts with different strength with the nuclear spin bath.

The effective spin-$1/2$ approximation is valid in the high field limit where the hyperfine coupling $|A|$ is much smaller than the energy difference between two hyperfine states of bismuth $E_m^{+-} - E_m^{+-} \approx \gamma_e B_0/10$. Given that the maximum value of $|A|$ is of the order of $1\,\mathrm{MHz}$, at $B_0 < 1\,mT$ the donor spin interaction to the most coupled $^{29}\mathrm{Si}$ nuclear spins causes mixing of the donor eigenstates and Eq.4.21 is not anymore valid.

Inhomogeneous broadening

The static inhomogeneity of the silicon nuclear spin bath causes via the secular terms in Eq.4.21 the local magnetic field along z seen by each donor to be different and thus contributes to the inhomogeneuos broadening of the ESR spin linewidths. This $^{29}\mathrm{Si}$-induced broadening has been measured for phosphorus and bismuth donors in silicon to be $2.5\,\mathrm{G}$ [44] and $4\,\mathrm{G}$ [45, 46], respectively. The difference being caused by the more confined bismuth electron wavefunction that yields larger Fermi contact hyperfine coupling to the closer nuclei. The ESR linewidth can be estimated as $\Delta B = \sqrt{2ln2f \sum_i A_i^2}$ [44], where f is the fraction of $^{29}\mathrm{Si}$ and A_i is the Fermi contact hyperfine coupling to the nuclear spin at site i. The relevant Fermi contact hyperfine couplings of bismuth have been estimated by Y. M. Niquet from CEA-INAC, by calculating the donor electron wavefunction at the lattice sites with a tight-binding model [47]. Using the calculated A_i, the estimated linewidth is $\Delta B = 4.2\,\mathrm{G}$ [38], close to the experimental value. Notice that the frequency linewidth $\Gamma_{\mathrm{inh}} = \frac{df}{dB}\Delta B$ originated by the $^{29}\mathrm{Si}$ static field $\Delta B = 4\,\mathrm{G}$ is expected to be different for each bismuth ESR transition due to their different magnetic field sensitivity $df/dB(B_0)$.

Decoherence by spectral diffusion

We consider now the effect of silicon nuclear spin bath fluctuations on the donor spin. As reported in Table 4.2, the average distance of $0.7\,\mathrm{nm}$ between nuclear spins gives a nuclear dipolar coupling of the order of $\sim 50\,\mathrm{Hz}$ that induces nuclear spin flip-flops. As a consequence, the donor is subjected to a fluctuating magnetic field perturbing its Larmor frequency and causing the loss of the phase information during its coherent evolution.

In Ch.3 we have seen that this relaxation of the spin transverse component to zero is known as decoherence. In this process the phase of the two spin states superposition is lost due to interaction with the environment. The Hahn echo sequence suppresses dephasing caused from static inhomogeneity of the magnetic field but is sensitive to the magnetic field fluctuations during the spin evolution time 2τ. This process can be seen as a random walk of the spin frequency within the spin spectral line, and for this reason take the name of spectral diffusion. Increasing the delay time τ the spin-echo amplitudes then disappears in a characteristic time called coherence time T_2.

When dephasing processes are negligible, T_2 is equal to its maximum value of $2T_1$. This is the case for bismuth in silicon at temperatures $T > 14\,\mathrm{K}$ [45]. Our experiments are performed at $T < 1.5\,\mathrm{K}$ where the spin-lattice T_1 exceeds hours and T_2 is limited by the fluctuations of the nuclear spin bath. At such low temperatures the nuclear spin T_1 is negligibly long and the bath dynamics is dominated by nuclear spin flip-flops.

The nuclear spins closest to the donor cannot easily exchange energy with other spins in the bath, due to their large detuning induced by the strong spatial dependence of the contact hyperfine coupling to the electron and constitute the so called "frozen-core" [38]. On the other hand, spins too far away negligibly affect the donor spin energy. It is therefore the "active shell" in the intermediate region that causes donor decoherence. This nuclear-induced spectral diffusion results in a stretched exponential decay of the transverse magnetization [38, 48].
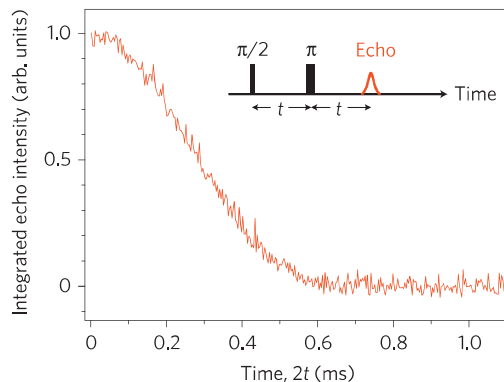

Figure 4.8: **Coherence time of bismuth in natural silicon.** Spin echo decay measured in natural silicon for bismuth concentration of $3 \times 10^{15} \, \text{cm}^{-3}$ at $10 \, \text{K}$ and at $8.81 \, \text{T}$ with field aligned along [100]. A spectral diffusion coherence time of $400 \, \mu\text{s}$ is extracted from fit with a stretched exponential function. Adapted from [45].

Coherence time of bismuth in natural silicon has been extensively studied [38, 45, 46]. A spectral diffusion coherence time T_2 ranging from $0.3 \, \text{ms}$ to $0.8 \, \text{ms}$ is observed at 9.7 GHz and $B_0 = 0.57 \, \text{T}$ depending on the B_0 orientation [38], in agreement with the model of nuclear flip-flop by dipolar coupling. The angular dependence arises from the expression of the nuclear dipolar coupling being strongly affected by the alignment of the nuclei with respect to the field. Due to the different df/dB of the various bismuth transitions at low field, $T_{2\,\text{SD}}$ depends on the measured transitions [38]. As expected from the dynamics of the nuclear bath, the temperature dependence of T_2 reported in refs. [45, 46] shows no change below $14 \, \text{K}$, thus a similar value for T_2 in between $0.3 \, \text{ms}$ and $0.8 \, \text{ms}$ is foreseen in our experiment.

As previously discussed, at the clock transitions $df/dB = 0$ and consequently all the decoherence processes presented above are strongly suppressed. Wolfowicz et. al [26] showed an enhancement of T_2 from $0.8 \, \text{ms}$ to $90 \, \text{ms}$ in natural silicon. In isotopically purified ^{28}Si samples the contribution of the ^{29}Si nuclear bath is eliminated and the record value of $2.6 \, \text{s}$ has been reported [26].

4.3.2 Electron spin echo envelope modulation

Another effect of the silicon nuclear spins coupled to the donor is the modulation of the echo amplitude at frequencies related to the nuclear transition frequencies. This effect arises from the rotation of the nuclear quantization axis after an electron spin flip. The consequent nuclear precession affects coherently the electron spin motion leading to the electron spin echo modulation (ESEEM) phenomenon. We follow here the approach of references [43, 49] to introduce it.
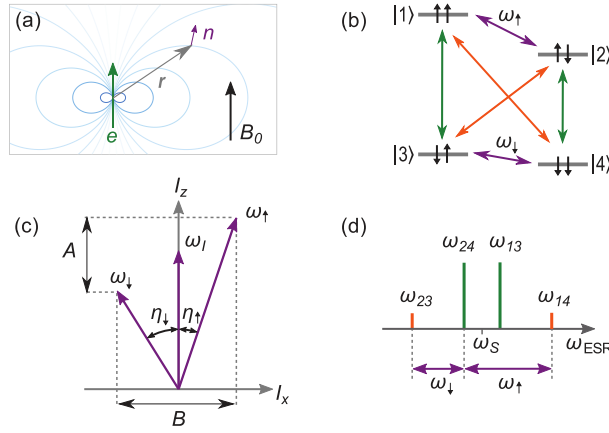
Figure 4.9: **ESEEM model system for electron spin S=1/2 and nuclear spin I=1/2. a** Nuclear spin (purple) subject to external field B_0 and dipole field (blue) of a nearby electron spin (green) located at relative position r. **b** Energy diagram showing the electron transitions (green), the nuclear transitions (purple), and the (normally forbidden) electron-nuclear transitions (orange). The energy levels $|1\rangle, ..., |4\rangle$ are labeled according to the eigenstate of the Zeeman basis. **c** Quantization axes $\omega_\uparrow$ and $\omega_\downarrow$ due to mixing of the nuclear states, which results in inclination of the axis from z by the angles $\eta_\uparrow$ and $\eta_\downarrow$, respectively. **d** EPR spectrum showing the electron transitions (green) and the electro-nuclear transitions (orange) as well as the relation of these transitions to the nuclear frequencies $\omega_\uparrow$ and $\omega_\downarrow$ (purple). Figure taken from [49]

The system of an electron spin S=1/2 coupled to a nuclear spin I=1/2 and subjected to a B_0 field applied along z is described by the Hamiltonian in Eq.4.21.

The term $C\hat{S}_z\hat{I}_x$ is responsible for the dependence of the nuclear spin quantization axis on the electron spin state. The angle of this axis with respect to the z direction when the electron spin is in the $|\uparrow\rangle$ or $|\downarrow\rangle$ state is:

$$\eta_\uparrow = \arctan \frac{C}{B + 2\omega_I} \tag{4.22}$$

$$\eta_\downarrow = \arctan \frac{C}{B - 2\omega_I} \tag{4.23}$$

The nuclear state thus now depend on the electron state, and the two corresponding new nuclear transition frequencies are:

$$\omega_\uparrow = (\omega_I + \frac{B}{2}) \cos \eta_\uparrow - \frac{C}{2} \sin \eta_\uparrow \tag{4.24}$$

$$\omega_\downarrow = (\omega_I - \frac{B}{2}) \cos \eta_\downarrow - \frac{C}{2} \sin \eta_\downarrow. \tag{4.25}$$

The hybridization of the eigenstates originated by this rotation of the effective field seen by the nuclear spin leads to new allowed nuclear-spin-non-preserving transitions illustrated in Fig.4.9 together with the states energies. These transitions changing simultaneously the electron and spin states have a matrix element equal to $\sin \eta$, where $\eta = (\eta_\uparrow - \eta_\downarrow)/2$. In the trivial case of $C = 0$, $\eta_{\uparrow,\downarrow} = 0$ and only the nuclear-spin-preserving transition having matrix element equal to $\cos \eta$ are allowed.

The new transitions in the hybridized four level system lead to the appearance of ES-EEM in the Hahn echo measurement as a function of the delay time τ. The application of pulses resonant with the uncoupled electron spin transition ω_S and having bandwidth larger than $\omega_{\uparrow,\downarrow}$, results in the excitation of the four possible transitions. After the π pulse the coherence of one transition is redistributed on all the four transitions, each of it with its own frequency. The different phase acquired by the four coherences in the time τ after the refocusing pulse yields a periodic modulation of the echo amplitude $A_e(\tau)$ that neglecting decoherence and assuming ideal pulses is found to be [43]:

$$A_e(\tau) = 1 - \frac{k}{4}[2 - 2\cos(\omega_\uparrow \tau) - 2\cos(\omega_\downarrow \tau) + \cos((\omega_\uparrow - \omega_\downarrow)\tau) + \cos((\omega_\uparrow + \omega_\downarrow)\tau)],$$

$$(4.26)$$

where the modulation visibility k is given by:

$$k = \sin^2(2\eta) = \left(\frac{C\omega_I}{\omega_\uparrow \omega_\downarrow}\right)^2.$$

$$(4.27)$$

The frequency spectrum of this modulation contains information on the hyperfine coupling and Larmor frequency of neighboring nuclear spins, and thus constitutes a powerful tool of pulsed ESR. In the two extreme limits of very weak coupling ($\omega_I \gg B, C$) and very strong coupling ($\omega_I \ll B, C$) there is a vanishing electron-spin dependent quantization axis for the nuclear spin and the visibility tends to zero. In the weak coupling regime $k = (C/\omega_I)^2$ and is thus proportional to $1/B_0^2$. In this limit the modulation spectrum simplifies including only the Larmor frequency ω_I and its double. The maximum of visibility is instead reached when $\eta = \pi/4$, corresponding to $\omega_I \approx \pm B/2$. When the electron is coupled to many nuclear spins, the resulting echo amplitude is a product of the modulation factors given by Eq.4.26 for each nucleus. Decoherence is taken into account by an extra exponential factor describing the transverse relaxation as a function of τ.
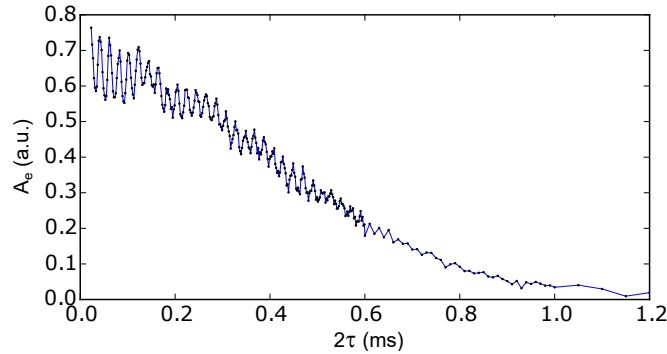
Figure 4.10: **ESEEM oscillation in Si:Bi at 96 G.** Hahn echo decay measured at 15 mK and $\omega_0/2\pi = 7.409$ GHz.

ESEEM oscillations have been studied in natural silicon [44, 50] at high field ($B_0 \approx 0.57$ T) and more recently in an isotopically purified sample [49] at very low field ($B_0 < 0.4$ mT). The ESEEM measurements reported in this thesis fall in a third different regime, beeing measured in a natural silicon sample at low field ($1 < B_0 < 10$ mT). In Fig.4.10 it is shown the echo decay we measured at 10 mT, where ESEEM oscillation at about 100 kHz are clearly visible.

In the presence of ESEEM, the electron spin frequency oscillates in a range γ_{eff} that may be much larger than the homogeneous linewidth given by the decoherence rate γ_2. We now give an estimate of this effective linewidth for the measurement shown in Fig.4.10, as it will be used in the next section. In a semi-classical picture, after the application of the π pulse, the magnetic field seen by the nuclear spin changes its axis triggering a Larmor nutation of the nuclear spins around this new axis at frequency ω_I'. In turn, this nutation feeds back onto the electron spin, modulating its Larmor frequency with periodicity $\tau_I' = 2\pi/\omega_I'$. The amplitude of this modulation can be roughly estimated from the visibility of the ESEEM oscillations k. When the pulse delay is a multiple of the ESEEM period $\tau = m\tau_I'$, no phase is acquired by the electron spin during the pulse sequence time 2τ and the echo amplitude is maximum. When instead the pulse delay is an odd multiple of half the ESEEM period $\tau = (2m+1)\tau_I'/2$, the electron spin acquires a random phase $\phi \leqslant \pi\gamma_{\text{eff}}\tau_I'$. When the maximum value of ϕ approaches π, the echo amplitudes reaches zero, $k = 1$ and $\gamma_{\text{eff}} = \omega_I'/2\pi$. The effective linewidth for a small value of k is then approximately $\gamma_{\text{eff}} = (\omega_I'/\pi^2)\arccos(1-k)$.

The ESEEM oscillations in the echo decay of Fig.4.10 show a modulation at about $\omega_I'/2\pi = 100\,\text{kHz}$ and a visibility $k \sim 0.3$, thus resulting in an effective electron spin linewidth $\gamma_{\text{eff}} \sim 25\,\text{kHz}$. This value is about one order of magnitude larger than the spectral diffusion linewidth $\gamma_2 = 1/T_2 \sim 2\,\text{kHz}$.

4.3.3 Donor spin bath

Hamiltonian

We now turn to the interaction of a bismuth donor with the surrounding spin bath realized by the other donors. As reported in Table 4.2, the average distance between bismuth dopants in our sample is $d_{\text{Bi}} = (3/4\pi C)^{1/3} = 20\,nm$, where $C = 3 \times 10^{16}\,\text{cm}^{-3}$ is the peak doping concentration. Given that d_{Bi} is much larger than the $1.45\,\text{nm}$ bismuth electron wavefunction radius, the hyperfine Fermi contact coupling between neighbouring donor is negligible and a purely dipolar interaction Hamiltonian $\hat{H}_{dip}$ can be assumed. Considering two electron spins $\hat{\boldsymbol{S}}_1$ and $\hat{\boldsymbol{S}}_2$ separated by $\boldsymbol{r}$, $\hat{H}_{dip}$ reads:

$$\hat{H}_{\text{dip}} = \frac{2\pi\mu_0\gamma_e^2\hbar^2}{r^3}(A + B + C + D + E + F) \tag{4.28}$$

$$A = \hat{S}_{1z}\hat{S}_{2z}(1 - 3\cos^2\theta) \tag{4.29}$$

$$B = -\frac{1}{4}(\hat{S}_{1+}\hat{S}_{2-} + \hat{S}_{1-}\hat{S}_{2+})(1 - 3\cos^2\theta) \tag{4.30}$$

$$C = -\frac{3}{2}(\hat{S}_{1+}\hat{S}_{2z} + \hat{S}_{1z}\hat{S}_{2+})\sin\theta\cos\theta e^{-i\phi} \tag{4.31}$$

$$D = -\frac{3}{2}(\hat{S}_{1-}\hat{S}_{2z} + \hat{S}_{1z}\hat{S}_{2-})\sin\theta\cos\theta e^{i\phi} \tag{4.32}$$

$$E = -\frac{3}{4}\hat{S}_{1+}\hat{S}_{2+}\sin^2\theta e^{-2i\phi} \tag{4.33}$$

$$F = -\frac{3}{4}\hat{S}_{1-}\hat{S}_{2-}\sin^2\theta e^{+2i\phi} \tag{4.34}$$

$$\tag{4.35}$$

where $\boldsymbol{r} = r(\sin\theta\cos\phi\boldsymbol{e}_x + \sin\theta\sin\phi\boldsymbol{e}_y + \cos\theta\boldsymbol{e}_z)$ in the polar coordinates system. The value of $2\pi\mu_0\gamma_e^2\hbar/(d_{\text{Bi}}^3) \approx 10\,\text{kHz}$ gives the order of magnitude of the dipolar coupling for two electron spins separated by $d_{\text{Bi}} = (3/4\pi C)^{1/3} = 20\,nm$. This coupling is reduced

for most of bismuth transitions, which have a smaller magnetic dipole with respect to a pure electron spin transition.

As we have seen for the interaction with silicon nuclear spins, terms proportional to S_z lead to broadening of the ESR linewidth. However, in our sample the $\sim 10\,\mathrm{kHz}$ dipolar coupling to neighbouring donors contributes negligibly to the inhomogeneous broadening, which is instead determined by the $^{29}\mathrm{Si}$ environment (see 3.1.2). Similarly, the dynamics of the bismuth donor bath is expected not to contribute to the decoherence of the central bismuth spin compared to the $^{29}\mathrm{Si}$ bath. As a consequence, the terms A, C and D are neglected hereafter. Contrary to the description of the donors interaction to the $^{29}\mathrm{Si}$ bath, we are interested in the non-secular terms proportional to $S_{+,-}$ of Eq.4.28 yielding to polarization transfer via flip-flop processes.

Flip flop rate

A flip-flop process can be described as an incoherent transfer of energy from the center donor to a neighbouring spin. Consider two bismuth donors separated by a distance r initially in the state $|E, m\rangle \otimes |G, n\rangle$ and flip-flopping to the final state $|E', m'\rangle \otimes |G', n'\rangle$ via the transitions $|E, m\rangle \rightarrow |E', m'\rangle$ and $|G, n\rangle \rightarrow |G', n'\rangle$. The flip-flop rate can be estimated as:

$$\Gamma_{n \rightarrow n'}^{m \rightarrow m'}(\Delta_f) = \frac{2\pi}{\hbar} \left| \langle E', m'| \otimes \langle G', n'| \hat{H}_{\mathrm{dip}}(r) |E, m\rangle \otimes |G, n\rangle \right|^2 \frac{1}{\hbar \gamma_{\mathrm{Bi}}} \frac{\gamma_{\mathrm{Bi}}^2}{\gamma_{\mathrm{Bi}}^2 + \Delta f^2},$$

(4.36)

where γ_{Bi} is the donor transition linewidth and Δ_f is the frequency detuning between the two spin transitions. In the simple case of exponential coherence decay, the linewidth γ_{Bi} coincides with the decoherence rate γ_2. However, in our experiment at magnetic fields of $10\,\mathrm{mT}$ or lower, ESEEM oscillations attest that the spin frequency undergoes larger fluctuations. One can thus model the transition linewidth as being given by $\gamma_{\mathrm{Bi}} \approx \gamma_{\mathrm{eff}}$, as discussed in the previous section.

By defining d_{eff} as the average distance between two resonant spins satisfying $\Delta f \approx \gamma_{\mathrm{eff}}$, Eq.4.36 can be rewritten as:

$$\Gamma_{n \rightarrow n'}^{m \rightarrow m'} = \frac{2\pi}{\hbar} \left| \langle E', m'| \otimes \langle G', n'| \hat{H}_{\mathrm{dip}}(d_{\mathrm{eff}}) |E, m\rangle \otimes |G, n\rangle \right|^2 \frac{1}{\hbar \gamma_{\mathrm{eff}}}. \qquad (4.37)$$

The B, E and F terms in Eq.4.28 allows a number of different flip-flop processes for neighbouring bismuth donors. Their rate is too slow to be relevant for decoherence processes. However, as we detail in the following, a subset of the allowed flip-flops can lead to polarization transfer within the hyperfine level manifold.

Polarization transfer

Consider the bismuth energy level scheme in Fig.4.11a. The two quasi-degenerate transitions $|16\rangle \leftrightarrow |5\rangle$ and $|15\rangle \leftrightarrow |4\rangle$ are resonant with the drive signal used to measure the electron spin resonance. The echo amplitude is then proportional to the population unbalance $\Delta N = N_{|16\rangle} + N_{|15\rangle} - N_{|5\rangle} - N_{|4\rangle}$. After excitation, spin longitudinal relaxation is measured by recording $\Delta N(t)$ via the echo. Transfer of polarization from the

probed transition to other non-resonant transitions via flip-flop processes at time scales comparable with the relevant Γ_1 processes can contribute to the observed longitudinal relaxation.

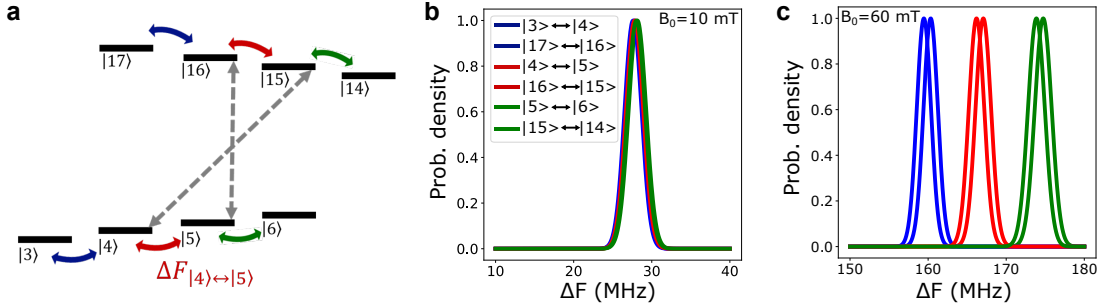Figure 4.11: **Hyperfine transitions spectrum. a** Sketch of a subensemble of Si:Bi spin energy levels. The quasi-degenerate ESR transitions $|16\rangle \leftrightarrow |5\rangle$ and $|15\rangle \leftrightarrow |4\rangle$ (grey arrows) are resonant with the detection cavity. The small arrows of the same colour represent the pairs of quasi-degenerate hyperfine transitions of frequency ΔF. **b** Spectrum of the 6 considered hyperfine transitions at $B_0 = 10\,\text{mT}$. **c** Spectrum of the hyperfine transitions at $B_0 = 60\,\text{mT}$.

Flip-flops between neighbouring donors, in which the resonant ESR transition relaxes to its ground state while a non-resonant transition is excited, are highly suppressed by energy conservation. Indeed, the detuning Δ_f in Eq.4.36 is of tens of MHz at the typical applied field B_0, much larger than the ESR linewidth of a few MHz. Such electron-spin flip-flop rate does not thus play any role in the longitudinal relaxation process. Other flip-flop processes involving the hyperfine transitions are however possible.

The hyperfine NMR-like transitions are degenerate in couples, as depicted in Fig.4.11a. However, at field as low as 10 mT, the inhomogeneous broadening induced by ^{29}Si magnetic field causes all the hyperfine transition lines to highly overlap (see Fig.4.11b). As for the ESR transitions, this broadening can be calculated as $\Gamma_{\text{inh}} = 4\,\text{G} \cdot df/dB$. df/dB is different for all transitions but leads to an average broadening of 1 MHz, much larger than the detuning between the hyperfine transitions at $10\,\text{mT}$ (see Fig.4.11b). As a result, resonant flip-flops where the donor spins change their quantum number m are possible. Such processes redistribute the population within the two $+$ and $-$ manifolds leading to a reduction of the measured ΔN at the resonant transitions.

At magnetic field as high as $B_0 \approx 60\,\text{mT}$, the detuning between the couples of quasi-degenerate hyperfine transitions increases up to a few MHz, larger than the line broadening (see Fig.4.11). Energy conservation thus inhibits most of flip-flop processes. The only flip-flops still allowed are between the couples of quasi-degenerate transitions, that however do not change ΔN or redistribute the population, and have then no effect on spin relaxation.

We now try to estimate the rate at which the flip-flop processes between hyperfine transitions takes place at $10\,\text{mT}$, leading to transfer of polarization outside of the probed transition $|16\rangle \leftrightarrow |5\rangle$ and $|15\rangle \leftrightarrow |4\rangle$. Two different flip-flop processes can be distinguished, the first caused by the B term and the second by the E and F terms in Eq.4.28.

The B term of the dipolar coupling proportional to $\hat{S}_{1+}\hat{S}_{2-}$ has a non-zero matrix element only for flip-flops satisfying $\Delta_m = 0$ (see Fig.4.12a). This selection rule together with the resonance condition imposed by energy conservation implies that only donors
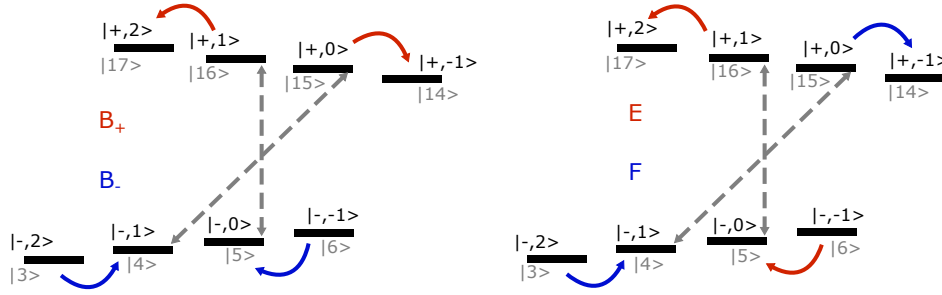
Figure 4.12: **Flip-flop processes at 10 mT. a** Example of flip-flops induced by the B term in Eq.4.28 between two spin in the + excited state manifold (red) and two spins in the ground state manifold (blue). In both cases ΔN is reduced by 2. **b** Example of flip-flops induced by the E (red) and F (blue) term between two spins sitting one in the + and the other in the − manifold. Both examples correspond to a decrease of ΔN by 2. In the two panels spin states are labeled by index of increasing energy (grey) and by the coupled basis (black).

Table 4.3: **Mixing coefficients of bismuth donor eigenstate.** Calculated for $B_0 = 9.6$ mT.

m	-5	-4	-3	-2	-1	0	1	2	3	4	5
a_m	0	0.327	0.461	0.562	0.646	0.720	0.786	0.846	0.901	0.952	1
b_m	1	0.945	0.888	0.827	0.763	0.694	0.619	0.534	0.434	0.306	0

in the same manifold can flip-flop in a B-term process: $|\pm, m\rangle \rightarrow |\pm, m+1\rangle$ with $|\pm, n\rangle \rightarrow |\pm, n-1\rangle$ or viceversa. For example, in the ground manifold a spin in $|3\rangle$ state can flip to $|4\rangle$ reducing ΔN while the neighbouring donor in the $|8\rangle$ can flop to the lower energy state $|7\rangle$. In order to give a rough estimate for a B-term flip-flop rate, we need to evaluate the effective average distance d_{eff} between two donors able to flip-flop. We focus on the ground state manifold at 10 mT and at a temperature for which all the − states are equally populated and the + manifold is empty. The central donor can then flip-flop with almost any neighbour, the only exception being for the $m = \pm 4$ states that can change m uniquely in one sense. However, due to inhomogeneous broadening the fraction of resonant spins is about $\gamma_{\text{eff}}/\Gamma_{\text{inh}}$. As previously discussed, the transition effective linewidth at 10 mT due to ESEEM oscillations is $\gamma_{\text{eff}} \sim 25$ kHz. The ^{29}Si-induced inhomogeneous broadening is $\Gamma_{\text{inh}} = 4\,\text{G} \cdot df/dB \approx 1$ MHz. The effective resonant donor concentration is thus $C_{\text{eff}} = C\gamma_{\text{eff}}/\Gamma_{\text{inh}} \approx 8 \times 10^{14}$, corresponding to an effective average distance $d_{\text{eff}} = (3/4\pi C_{\text{eff}})^{1/3} \approx 70$ nm. We can then write the B-term flip-flop rate for the − manifold using Eq.4.37 as:

$$\Gamma_{n \rightarrow n-1}^{m \rightarrow m+1} = \frac{2\pi}{\hbar^2} \left(\frac{2\pi \mu_0 \gamma_e^2 \hbar^2}{r^3} \right)^2 \frac{1}{16} (1 - 3\cos^2\theta)^2 b_n^2 a_{n-1}^2 a_m^2 b_{m+1}^2 \frac{1}{\gamma_{\text{eff}}}, \quad (4.38)$$

where $a_{m,n}$ and $b_{m,n}$ are the bismuth spin eigenstate mixing coefficients given by Eqs.4.8-4.9, whose values at 10 mT are listed in Table 4.3. The rate for $r = d_{\text{eff}}$ is then found to be of the order of $10^{-2}\,\text{s}^{-1}$. This value is however much larger for the couples of resonant donors separated by less probable distances $r < d_{\text{eff}}$ due to the $1/r^6$ dependence of the rate.

The E (F) term of Eq.4.28 proportional to $\hat{S}_{1+}\hat{S}_{2+}$ ($\hat{S}_{1-}\hat{S}_{2-}$) yield the $\Delta m = +2$ ($\Delta m = -2$) selection rule. The corresponding resonant flip flop processes are illustrated in Fig.4.12b. Donors in one manifold can flip-flop with neighbours occupying any state of the other manifold: $|\pm, m\rangle \rightarrow |\pm, m+1\rangle$ while $|\mp, n\rangle \rightarrow |\mp, n+1\rangle$ ($|\pm, m\rangle \rightarrow |\pm, m-1\rangle$ while $|\mp, n\rangle \rightarrow |\mp, n-1\rangle$). For example a spin in the excited manifold state $|16\rangle$ can flip to the higher energy state $|17\rangle$ reducing ΔN while a neighbouring spin in the ground state manifold flop from state $|3\rangle$ to state $|2\rangle$. Similarly to the case of B-term processes, the flip-flop rate of the the E and F terms are obtained from Eq.4.37:

$$\Gamma^{m\rightarrow m+1}_{n\rightarrow n+1} = \frac{2\pi}{\hbar^2}\left(\frac{2\pi\mu_0\gamma_e^2\hbar^2}{r^3}\right)^2 \frac{9}{16}\sin^4\theta\, a_n^2 b_{n+1}^2 b_m^2 a_{m+1}^2 \frac{1}{\gamma_{\text{eff}}} \tag{4.39}$$

$$\Gamma^{m\rightarrow m-1}_{n\rightarrow n-1} = \frac{2\pi}{\hbar^2}\left(\frac{2\pi\mu_0\gamma_e^2\hbar^2}{r^3}\right)^2 \frac{9}{16}\sin^4\theta\, b_n^2 a_{n-1}^2 a_m^2 b_{m-1}^2 \frac{1}{\gamma_{\text{eff}}}. \tag{4.40}$$

The flip-flop rate for the E and F processes is thus one order of magnitude faster, corresponding to a rate of about $10^{-1}\,\text{s}^{-1}$ for $r \approx d_{\text{eff}}$.

The evolution of $\Delta N(t)$ after the excitation is described by a rate equation including all relevant flip-flop and relaxation processes. The contributions of donors at different relative positions must be taken into account by averaging over the probability distribution for the spatial coordinates r and θ. In Chapter 7 we report evidences of such polarization transfer taking place at fields B_0 ranging from 0 to $10\,\text{mT}$.

4.4 Bismuth donor interaction with the lattice

4.4.1 Spin-lattice relaxation

The spin of bismuth donors in silicon can relax by exchanging energy with the lattice via phonon emission and absorption. As depicted in Fig4.13, two processes can be distinguished: relaxation with conservation of the nuclear spin ($\Delta m_s = \pm 1, \Delta m_i = 0$) with characteristic time T_s, and diagonal relaxation with an additional nuclear spin flip ($\Delta m_s = \pm 1, \Delta m_i = \mp 1$) with a characteristic time labeled T_x (see Fig.4.13). Diagonal relaxation labeled $T_{x'}$ involving a double spin flip ($\Delta m_s = \pm 1, \Delta m_i = \pm 1$) is instead highly forbidden [51].

In the following we isolate a two-level system $\{|\mathfrak{e}\rangle, |\mathfrak{g}\rangle\}$ in the bismuth spectrum having transition frequency ω_s. We describe it as an effective spin 1/2 coupled to the phonon radiation bath of temperature T_{latt} and thermal occupation number $n_{\text{th}}(\omega, T_{\text{latt}})$ given by Eq.2.2.

Direct-phonon process

We first consider the case in which the spin exchanges energy with the resonant phonon modes of frequency ω_s. The effective spin 1/2 polarization is then given by Eq.3.21 with $T_{\text{spin}} = T_{\text{latt}}$. From Eq.3.22, the temperature dependence of spin lattice relaxation in the direct-phonon case is then:

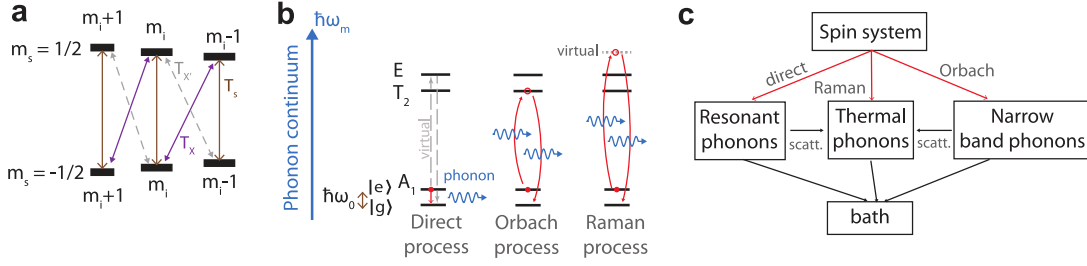$$\Gamma_{\text{dir}}(T_{\text{latt}}) = \Gamma_{\text{dir}}(0)[2n_{\text{th}}(T_{\text{latt}}) + 1] \tag{4.41}$$

Figure 4.13: **Spin-lattice relaxation processes. a** Subset of Si:Bi level schemes with the various spin-lattice relaxation processes. **b** Direct, Orbach and Raman phonon relaxation mechanisms. **c** Relaxation paths available for the spin system.

where $\Gamma_{\mathrm{dir}}(0)$ is the relaxation rate when the coupled resonant phonon modes are in their ground state and depends on the spin and material properties. In the case of shallow donors in silicon, $\Gamma_{\mathrm{dir}}(0)$ has been estimated theoretically by Roth [52] and Hasegawa [53] based on two different models where the spin-lattice coupling originates from the modulation of the spin-orbit coupling by crystal strain. From the formula derived by Hasagawa [53, 54], it is possible to extract the following expression for $\Gamma_{\mathrm{dir}}(0)$ in the case of T_s-type process:

$$\Gamma_{\mathrm{dir}}(0) = c(\Delta E)^{-2}\omega_s^5, \tag{4.42}$$

where ΔE is the energy difference between the first excited valley state and the ground state, and c is a coefficient expected to be similar for all shallow donors in silicon in the derivation of Hasegawa [53]. Its value can be estimated from the measurements reported by Morello et al.[54] for phosphorus donors at 40 mK. They found the expected ω_s^5-dependence: $\Gamma_{\mathrm{dir}} = 0.015(\omega_s/\gamma_{\mathrm{e}})^5 s^{-1}T^{-5}$, where γ_{e} is the gyromagnetic ratio for phosphorus. The correspondent value of c would then be $c \approx 1.5 - 3.2 \times 10^{-13}\,\mathrm{s}^{-1}\mathrm{GHz}^{-5}\mathrm{eV}^2$. We can then obtain a rough estimate for the direct phonon relaxation of bismuth in silicon, yielding at zero temperature and $\omega_s/2\pi = 7\,\mathrm{GHz}$, $\Gamma_{\mathrm{dir}}^{-1}(0) \approx 2 \times 10^5\,\mathrm{s}$

Two-phonon processes

At sufficiently high temperature, other processes involving two phonons start competing with the single phonon regime. These processes are schematically illustrated in Fig.4.13. In the Orbach process, the relaxation is mediated by the first excited valley state. The spin relaxes by absorbing a phonon of energy ΔE and emitting a phonon of energy $\Delta E - \hbar\omega_s$. In the case of Raman process, the excited state is replaced by a virtual state. Any phonon can thus be absorbed or emitted, the only matching condition being $|\hbar\omega_1 - \hbar\omega_2| = \hbar\omega_s$. In the high temperature limit $k_{\mathrm{B}}T \gg \hbar\omega_s$ when these processes are relevant, their temperature and frequency dependence is:

$$\text{Orbach process}\,[55]: \quad \Gamma_{\mathrm{latt}} \propto a\exp(-\Delta E/k_{\mathrm{b}}T) \tag{4.43}$$

$$\text{Raman process}\,[55]: \quad \Gamma_{\mathrm{latt}} \propto bT^9 + b'\omega_s^2 T^7, \tag{4.44}$$

where a, b, b' are temperature and frequency independent coefficients that are expected to be different for T_s and T_x processes [56].

The three different processes illustrated above are predominant in three different temperature ranges depending on the values of the a, b, b', c coefficients, and consequently
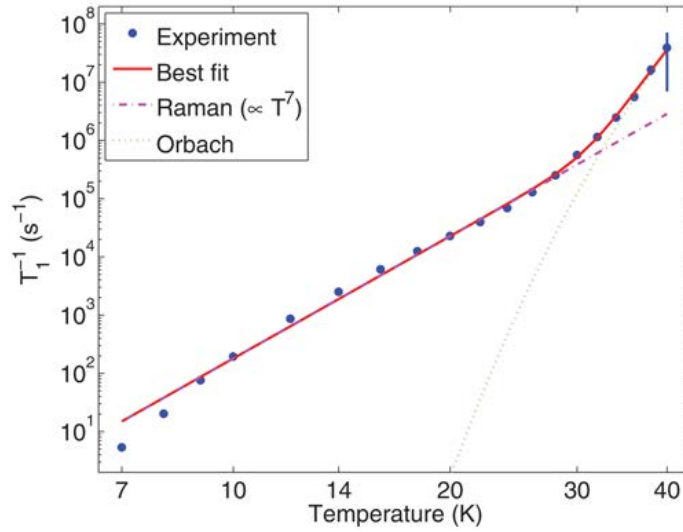
Figure 4.14: T_1 **dependences as a function of temperature.** Above $T = 25$ K an Orbach process dominates, whereas for lower temperature a Raman process is observed. The experiment is realized at $B_0 = 0.57$ T on the highest frequency transition at $f = 9.76$ GHz with a sample of concentration $[Bi] = 5 \times 10^{14}$ cm^{-3}. Extracted from [46].

changing for all the donors. In the case of bismuth, it has been experimentally determined that for T_s relaxation Orbach process is dominant above 25 K [45, 46, 57]. At lower temperatures Raman process overcomes, with experiments showing T^7 [38, 45, 46, 57] and T^9 [26, 58] dependence. At 4.2 K, $\Gamma_1^{-1} = 9$ s is for example reported by Wolfowicz et al [26]. The only measurement of bismuth non-radiative energy relaxation at temperatures where direct phonon process is expected to be dominant has been reported by Bienfait et al. [5]. In their work they measure $\Gamma_1^{-1} = 1500$ s at 20 mK using a superconducting resonator similar to the one of our experiments, a value somewhat smaller than the predicted direct-phonon relaxation time of the order of 10^5 s, indicating that other relaxation processes such as spatial spin diffusion and/or charge hopping might contribute as well.

The estimation of the spin-lattice relaxation rate for our radiative cooling experiment performed at about 1 K is thus not straightforward. From the $\Gamma_1^{-1} = 9$ s at 4.2 K reported by Wolfowicz et al [26], we can then estimate the lower bound on the two-phonon process at 1 K to be roughly $\Gamma_1^{-1} = 10^4$ s assuming a T^7-dependence of the Raman process. On the other hand, given the lower concentration of bismuth donors in our sample compared to ref. [5], we can assume $\Gamma_1^{-1} = 1500$ s as the minimum expected non-radiative relaxation time for our case.

4.4.2   Effect of strained silicon lattice

The effect of strain in the silicon lattice on the donor spin spectrum has been first observed in ref. [34] and had since then attracted a lot of interest [34, 59–62], recently motivated by the perspective of controlling the spin properties for quantum computing applications [61, 63].

The usual model to describe the effect of strain on the donor spin is the valley repopulation model. Strain lifts the degeneracy between the valley states, which leads to

changes in the ground state wavefunction, no longer described by the symmetric combination of Eq.4.1. This model predicts that the hyperfine coupling A should decrease quadratically with strain.

However, this is in contradiction with experimental data, which observe a linear dependence of A on strain for all donors in silicon [64]. This was attributed to the dependence of the central cell correction on the hydrostatic component of the strain ϵ_{hs}. For Bismuth, $dA/d\epsilon_{\text{hs}} = 28.2\,\text{GHz}$.
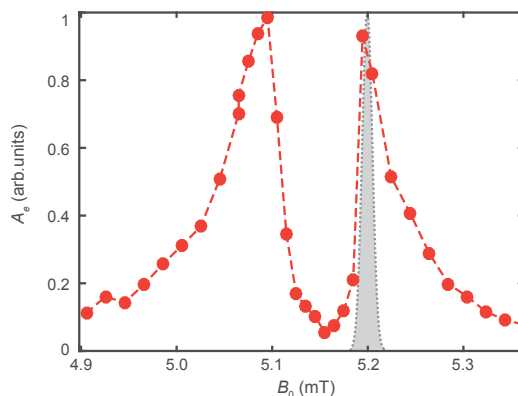

Figure 4.15: **Spectrum of bismuth donors in strained silicon.** The echo amplitude A_e as a function of magnetic field (red) shows two peaks with opposite sign of frequency shift with respect to the expected ESR spectrum (grey). The positive and negative resonance frequency shifts corresponds to different regions of the sample with opposite sign of the hydrostatic strain, that is linearly proportional to the hyperfine coupling change. Extracted from [65].

Pla et al.[65] explains the broadening of Si:Bi spectral lines measured in refs.[5, 6] as an effect of this hydrostatic strain linearly changing the hyperfine coupling A. The spectra of refs.[5, 6] are measured with an aluminum superconducting resonator very similar to the niobium resonator used in our experiments, fabricated on top of an isotopically purified ^{28}Si sample. The strain induces a line broadening of more than one order of magnitude with respect to Si:Bi line in bulk ^{28}Si, leading to a FWHM linewidth of about $2\,\text{G}$ (see Fig.4.15). The origin of this strain is attributed to differential thermal contraction between the aluminum film of the resonator and the silicon substrate while cooling the sample from ambient to cryogenic temperatures. In Chapter 5 we report the observation of the same phenomenon due to the thermal contraction of the resonator niobium film. In our case the strain broadening is however competing with the comparable ^{29}Si-induced broadening.

4.5 Optical illumination

4.5.1 Above-gap light

The irradiation of silicon with light at frequency larger than the band-gap generates conduction electrons interacting with the donors. The interaction of the carriers with the donor spins gives rise to a shortening of the spin lifetime, via a variety of processes whose detail is not yet fully understood.

Transfer of the conduction electron spin polarization to the donor

One possible effect of above-gap light is an effective transfer of polarization from the photo-excited conduction electrons spins to the donors. Feher and Gere [30] attribute to such a spin-exchange process the observation of a faster electron spin relaxation under illumination.

The transfer of polarization can result from trapping of conduction electrons by the neutral donor to form either negative charged donor state D^- in Si:P [66, 67] or bound exciton D^0X in Si:Bi when an electron-hole pair is trapped [68]. In the case of D^- formation, the random re-emission of one of the two electrons yield the donor spin polarization to relax to the free electron equilibrium polarization value [67]. In the case of donor bound-exciton D^0X formation the transfer of polarization happens via donor ionization. The D^0X state decay by recombination of the electron-hole pair and Auger emission of the second electron to the positive charged donor state D^+ (see Fig.4.16). The subsequent capture of a conduction electron to form the stable neutral D^0 state equilibrate the donor polarization to the conduction electron spins. Any other donor ionization process in the presence of conduction electron would lead to the same polarization transfer effect.

Donor nuclear spin hyperpolarization

The above-gap illumination has been observed to cause donor nuclear spin hyperpolarization under different experimental conditions. The mechanism underlying this effect is still debated.

Build-up of negative nuclear polarization of phosphorus donor has been observed at high field and low temperature, where the electron spins are highly polarized, under white light illumination [69]. The proposed mechanism is an Overhauser-like effect where phonon-induced cross-relaxation of the donor spin to a higher temperature bath compete with the pure electron-spin relaxation induced by capture and re-emission process [67].

In very similar experimental conditions, Morley et al.[45] have instead observed for bismuth donors the build-up of positive nuclear polarization. The authors attribute the process to photo-excited conduction electron spin relaxing to the equilibrium high polarization state by flip-flopping with the bismuth nuclear spin.

Negative nuclear polarization for bismuth in silicon is instead observed at $2\,\mathrm{T}$ and $1.4\,\mathrm{K}$ (high electron spin polarization) illuminating the sample with infrared light from a $1047\,\mathrm{nm}$ laser and thus only slightly above-gap [68]. The authors propose a cross-relaxation process mediated by the donor electro-nuclear hyperfine interaction. In their model the capture of a conduction electron and a hole by the donor lead the formation of a D^0X with parallel electron spins. This triplet state rapidly relax to a singlet state by flipping the donor nuclear spin due to the hyperfine coupling. The process stops when all donors are in the $m_i = -9/2$ state.

4.5.2   Donor bound-exciton transitions

Due to the silicon indirect band gap, D^0X relaxation is dominated by the non-radiative Auger recombination preventing coherent optical manipulation of Si:Bi spin. However, resonant excitation of D^0X by spin-dependent optical transition can be used to polarize and readout the donor nuclear and electronic spin state [70]. With phosphorus donors,
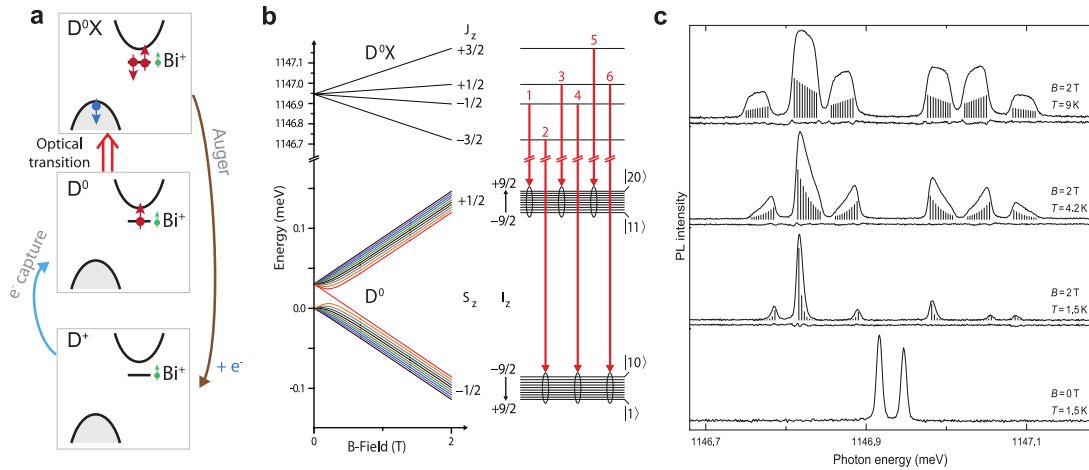
Figure 4.16: **Bound-exciton optical transitions. a** Sketch of the spins for states D^0X, D^0 and D^+ together with the transitions in between. **b** Zeeman splitting for D^0 and D^0X along with the dipole allowed optical transitions. **c** Observed stimulated photoluminescence spectrum for Si:Bi in a natural sample. **a** is extracted from [37], **b** and **c** from [68].

Yang et al. achieved electronic polarization of 90% and nuclear polarization of 76% at 1.4 K and 42.5 mT in an isotopically purified ^{28}Si sample where the optical transitions are well resolved [71]. A few years later Steger et al. [72] reach the even higher electronic polarization of 97% and nuclear polarization of 90% at 4.2 K and 84.5 mT. Moreover, the detection of the Auger electron by photo-conductivity measurements leads to very sensitive NMR experiment at low donor concentration [72]. We note here that at field lower than 100 mT and temperature higher than 1 K, above-gap light at 1047 nm is observed to depolarize both electron and nuclear spin transitions [71–73].

The same bound-exciton transitions between D^0 and D^0X as Si:P appears in Si:Bi (see Fig.4.16). Sekiguchi et al. [68] observed them by photoluminescence spectroscopy with above-gap laser illumination at 1047 nm. They resolve the zero-field hyperfine splitting but the natural abundance of ^{29}Si prevented them to resolve the nuclear states. Repeating the experiment with a ^{28}Si sample could provide a new way to hyperpolarize Si:Bi electron and nuclear spin.

4.6 Fabrication
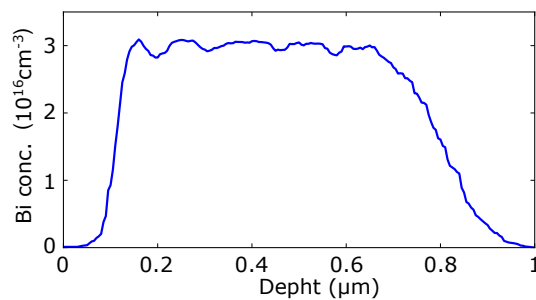
Figure 4.17: **Implantation profile.** Calculated from implantation parameters.

Bismuth impurities can be introduced during silicon crystal growth to provide bulk-doped natural silicon wafers or can be implanted in existing substrates. Due to the high atomic mass of bismuth (atomic weight=209), the implantation process creates many lattice defects. An annealing step above $600\,^{\circ}$C is required to heal the implantation damage and ensure that the implanted bismuth atoms are converted into substitutional impurities. Studer et al.[74] reported a conversion yield of $\approx 100\%$ with a two-step annealing ($3\,$min at $650\,^{\circ}$C followed by $10\,$min at $900\,^{\circ}$C).

The sample used in this work is a silicon chip with natural isotopic abundance of 4.7% of ^{29}Si nuclear spins. It was implanted with bismuth atoms in an energy range of $500-3000\,$keV, resulting in an estimated implantation profile shown in Fig.4.17. The sample was then annealed at a temperature of $900\,^{\circ}$C, for 5 minutes, under nitrogen flow. Based on [75], we expect an activation yield of 60%. The total number of dopants was confirmed by standard EPR spectroscopy as well as conductance measurements.

Chapter 5

ESR spectroscopy of bismuth donors in natural silicon

Despite its versatility, conventional inductive-detected ESR spectroscopy has a limited sensitivity that prevent its use to study nanoscale samples. Several alternative techniques such as STM tips [76], mechanical resonators [77, 78] or NV centers [79] have been developed to overcome this limit, reaching even single spin detection [54, 78, 80, 81]. However, effort has been still put on increasing the sensitivity of spectrometers based on inductive detection due to its universal applicability [82–85]. One promising direction is the use of superconducting resonators at low temperature, that allows to reduce the magnetic mode volume while keeping high quality factors [6, 83, 84, 86–88]. Sensitivity of 12 spins$/\sqrt{\text{Hz}}$ has been recently reached using a superconducting resonator with femtoliter detection volume together with a quantum limited amplifier [89].

The use of small-mode-volume and high-quality-factor superconducting resonators can also allow to reach the Purcell regime, where the cavity induced relaxation is the fastest spin relaxation process [5, 88]. One benefit of the Purcell-enhanced relaxation is the possibility to repeat the measurements much faster than what the intrinsic slow relaxation rate would impose, especially at low temperature, increasing the spectrometer sensitivity.

In this chapter we report the ESR spectroscopy of bismuth donors in natural silicon performed with a spectrometer based on a superconducting resonator very similar to the one described in refs [5, 6]. The donors more coupled to the resonator are thus expected to be in the Purcell regime. Rapid Purcell relaxation allows us to measure the ESR spectroscopy of bismuth at magnetic field lower than $70\,\text{mT}$ in the $10\,\text{mK}$-$1\,\text{K}$ temperature range, whereas intrinsic relaxation time is expected to be longer than tens of minutes. Recently, spectroscopy of bismuth donors implanted in an isotopically purified silicon sample has been performed with superconducting resonators in similar field and temperature regimes [6, 49, 89]. The Si:Bi spectroscopy reported hereafter differs for being measured in a silicon sample with natural abundance of ^{29}Si isotope carrying a nuclear spin $I = 1/2$.

73

5.1 Superconducting ESR resonator of high quality factor and small mode volume

For our purpose of realizing a sensitive spectrometer in the Purcell regime, two distinct figures of merit are required for the resonator. As detailed in ch.3, the spin signal emitted in the output line is roughly proportional to the ratio $g/\sqrt{\kappa}$ while the Purcell relaxation rate is $\Gamma_{\text{rad}} = 4g^2/\kappa$. A strong space confinement of the mode magnetic energy is thus needed for a large value of g, together with a low loss-rate κ. The design of such a small-mode-volume and high-quality-factor resonator is based on the previous work of Bienfait et al.[6, 37]. We report here the main motivations of the design and implementation choices.

5.1.1 Design

Small mode volume

The spin-photon coupling g is given by $g = -\gamma_e \langle \mathfrak{e}| \hat{\mathbf{S}} \cdot \delta\mathbf{B}(\mathbf{r}) |\mathfrak{g}\rangle$, where δB_1 is the magnetic field at the spin location generated by the vacuum fluctuations of the resonator current δI. From Eq.2.14, we have that one must minimize the resonator impedance Z_0 in order to maximize the current fluctuations. A small resonator inductance and a short distance between the spins and the flowing current are thus targeted.

The above criteria are well satisfied by a planar lumped-element geometry implemented by a small inductor wire in parallel with a large interdigitated capacitance. This structure is realized by a thin superconducting film patterned on top of the chip hosting the spins. The spins closer to the superconducting wire are the most coupled and constitute the probed ensemble.

High quality factor

The total resonator damping rate $\kappa = \kappa_{\text{int}} + \kappa_{\text{ext}}$ is limited by the minimum reachable internal loss rate κ_{int}. The coupling rate κ_{ext} to the measurement line can be freely designed in a large range of values and is determined by κ_{int}. As we discuss in the next chapter on radiative cooling, we aim in our experiment at the overcoupled regime, where $\kappa_{\text{ext}} \gg \kappa_{\text{int}}$. However, in order to keep the total damping rate κ sufficiently low, we target $\kappa_{\text{ext}} \approx 10\kappa_{\text{int}}$.

The internal losses of superconducting lumped-element resonator have been intensively studied, especially in the frame of quantum computing research, and internal quality factors in the range of 10^6 have been demonstrated [90]. The sources of internal losses can be grouped according to the four different physical phenomena that cause them: the motion of magnetic vortices trapped in the superconducting thin films [91], the presence of out of equilibrium quasi particles (i.e. non-superconducting quasi particles) [92], dielectric losses [93], originating mostly from dirty interfaces and in particular from the substrate-metal interface [94], and finally radiation from the resonator electric dipole [95]. While the first three can be optimized by material choices, fabrication procedures and geometry, the latter can be made negligible by enclosing the sample in a leak-tight metallic box, as shown in Fig.5.1a [96]. The box is designed so that all its modes have frequencies well above the planar LC resonator frequency. Despite the fact that superconducting boxes lead to better quality factors [97], we use an oxygen-

free high-conductivity copper box to be able to apply magnetic fields for our ESR measurements.

The coupling of the *LC* resonator to the measurement line is realized via capacitive coupling to an antenna that is entering the box through a drilled hole (see Fig.5.1a). The antenna is soldered to the inner conductor of a SMA connector screwed in the cavity wall. The insertion-depth of the SMA in the box wall determine the length of the antenna inside the box that can thus be tuned by several millimeters. The resulting coupling rate κ_{ext} is the sum of two contributions. The first one is a direct capacitive coupling to the antenna while the second one is an evanescent coupling mediated by the first mode of the copper box.

The copper box mode frequency and quality factor thus have to be designed to reach the target resonator κ_{ext}. The box must have the total quality factor smaller than its internal quality factor in order to couple the resonator to the antenna rather than to an additional loss channel. The box internal quality factor being of the order of several thousands, we aim at $Q_{\text{box}} \leqslant 1000$. The more the frequency of the first box mode is detuned with respect to the resonator, the lower κ_{ext}. We find that $\omega_{\text{box}}/2\pi = 8.5\,\text{GHz}$

The resonator is made of a 50 nm film of niobium. The choice of this material is due to the known possibility to reach high quality factor at temperatures higher than 1 K, that is the desired working point for the radiative cooling experiment. While aluminum would then be incompatible to the operating temperature too close to its superconducting critical temperature, another suitable superconducting material would be NbTiN. In the future the use of NbTiN could enable operation above 4 K and at even higher magnetic field. In our experiment however the maximum applicable magnetic field of about 140 mT parallel to the Nb surface is limited by the setup and not by the induced losses in the resonator.

The resonator frequency is chosen to be sufficiently close to the Si:Bi zero-field splitting of about 7.4 GHz. In the 0-100 mT range of applied B_0, several ESR transitions cross the resonator frequency provided that it is only a few hundreds of MHz detuned from the zero-field splitting.

5.1.2 Electromagnetic simulations

The resonator frequency and coupling to the measurement line via the copper box and the antenna are designed using 3D electromagnetic simulations realized with CST microwave studio. The real device is shown in Fig.5.1a. The CST model reproduces the geometry of the inside of the copper box (assuming perfect conductivity of the walls), the antenna, the silicon sample holder and chip (with relative dielectric constant $\epsilon_{\text{r}} = 11.5$) as well as the superconducting resonator (a perfect electrical conductor of zero-thickness). The copper sample holder and the resonator eigenmode frequencies can be determined in the software by exciting the port placed on the antenna and analyzing the frequency response, given as a S-parameters matrix.

The resonator geometry reported in Fig.5.1a consists in a 2-μm-wide inductive wire of lenght 705 μm in parallel with an interdigitated capacitance of 10 50-μm-wide fingers spaced by 50 μm. The whole structure fits in a rectangle of 1 mm by 1.4 mm and is fabricated on a silicon sample of 3.5 mm times 4 mm.

The simulated reflection parameter S_{11} is shown in Fig.5.1b. Since no losses are included, the sample holder and resonator modes results only in a 2π phase shift across the two resonances while the reflected amplitude is not affected. By fitting the two

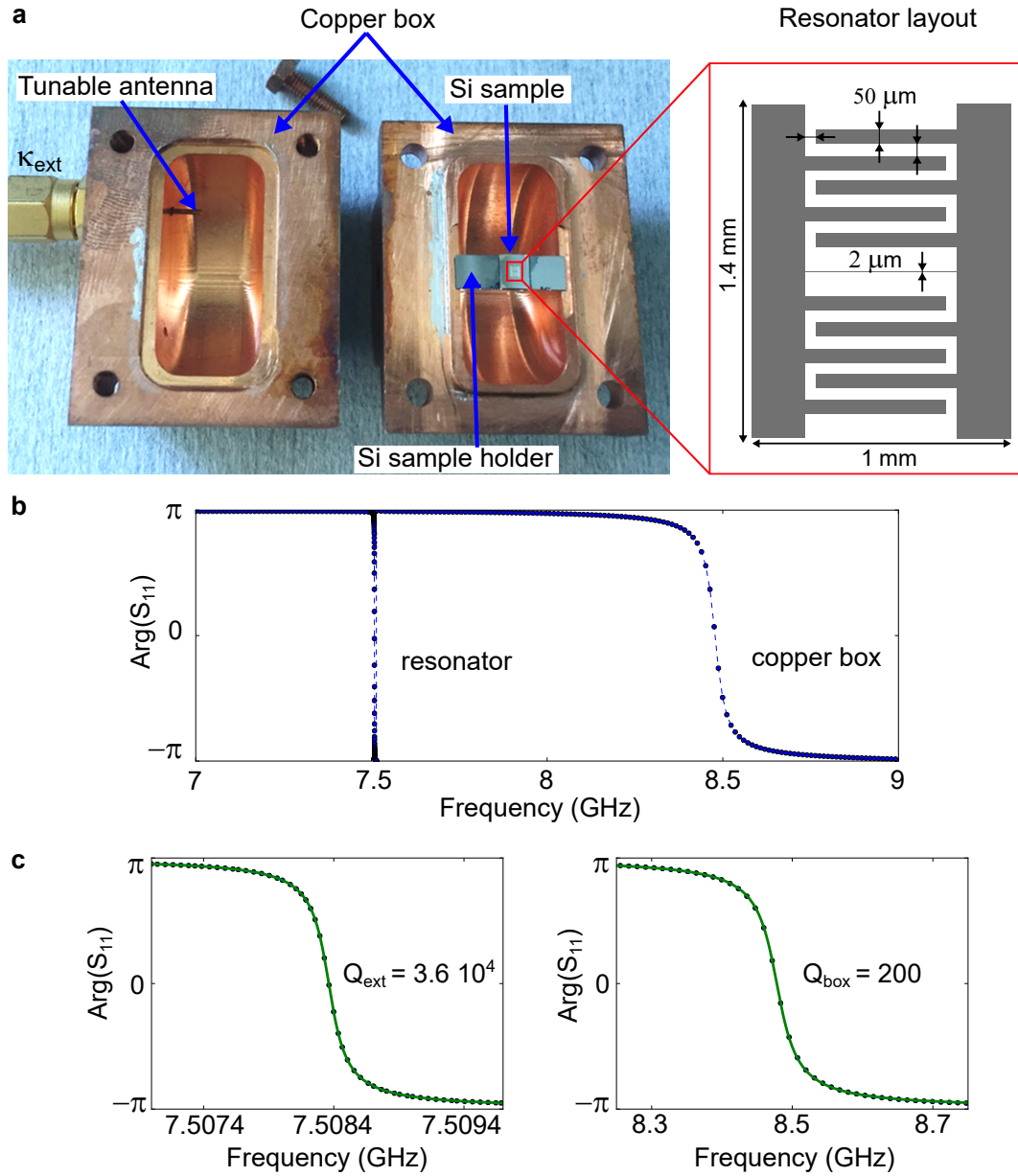Figure 5.1:   **Electromagnetic simulation.**   **a** Copper box with the LC oscillator coupled to the measurement line via a tunable antenna mounted on a SMA through. On the right, the resonator layout. **b** Phase of the simulated S_{11} parameter. **c** The first mode of the resonator (left) and of the copper sample holder (right). The coupling quality factors of the two modes are extracted from the fit (green line) with Eq.2.31.

phase signals we extract the two resonance frequencies and coupling rates. The resonator external coupling quality factor of the order of 10^4 is sufficiently low compared to the expected internal quality factor of 10^5 in order to be in the targeted overcoupled regime. Further reduction is however realized in the experiment by increasing the antenna length.

The resonator impedance is extracted by determining the AC current $I_{sim} \cos(\omega_0 t)$ flowing in the inductor for the simulated input power $P_{in} = 0.5\,\text{W}$ at the port. We find that $I_{sim} = 57\,\text{A}$. Together with the fitted $Q_{ext} = 3.6 \times 10^4$, this gives the intra-cavity mean photon number $\bar{n}$ by using Eq.2.27. The resonator current vacuum fluctuations δI and impedance Z_0 are then obtained via Eqs. 2.12 and 2.12:

$$\delta I = I_{sim}/2\sqrt{\bar{n}} = 50\,nA \tag{5.1}$$

$$Z_0 = \frac{\hbar \omega_0^2}{2\delta I^2} = 46\,\Omega, \tag{5.2}$$

corresponding to an inductance $L \sim 1\,\text{nH}$ and a capacitance $C \sim 0.5\,\text{pF}$. In the simulation we have neglected the contribution of the superconducting film kinetic inductance. However, a surface kinetic inductance of about $0.1\,\text{pH/square}$ has been measured for our sputtered niobium of $50\,\text{nm}$ thickness. Given the inductor wire dimension, this would correspond to kinetic contribution to the total inductance of about $40\,\text{pH}$, resulting in an expected resonance frequency lower by a few percent.

5.1.3 Experimental implementation

Resonator fabrication

The resonator is patterned on the sputtered niobium film with an optical lithography process followed by reactive ion etching. A preliminary HF surface cleaning step is performed to minimize the contribution of the silicon-metal interface to the resonator microwave losses [98].
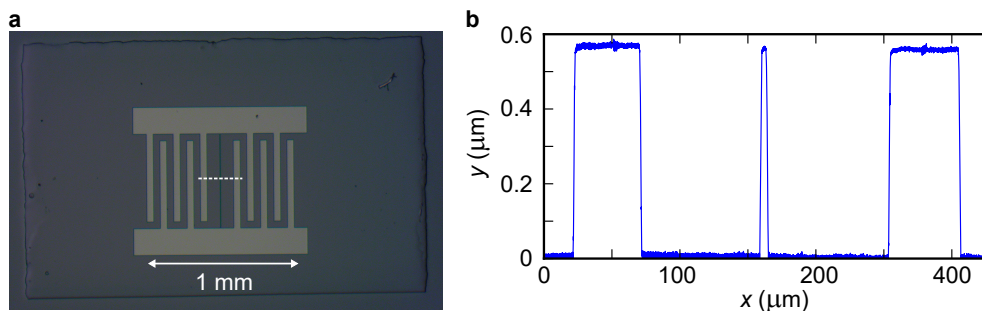
Figure 5.2: **Niobium resonator. a** Micrograph of the niobium resonator. **b** Profilometer measurement around the central inductor wire.

Due to the chip small size of $3.5\,\text{mm} \times 4\,\text{mm}$, a thicker optical resist is formed at the chip edges after spin-coating. The insufficient UV exposure of these thick resist edges yield to residual niobium after the first etching step. A second reactive ion etching step is thus performed after resist development to remove the niobium from the silicon chip edges, otherwise causing additional losses. During this final etching step a hard silicon mask protects the center of the silicon chip and the resonator. The fabrication steps are:

- **Substrate cleaning**: 10' in a Piranha acid mixture at 120 °C followed by deion- ized water rinsing and blowing dry.

- **Surface deoxidation:** 10" in HF followed by deionized water rinsing and blowing dry.

- **Niobium sputtering:** 25" deposition for a final thickness of 50 nm.

- **Optical lithopgraphy:** Hard contact 20" UV exposure of positive photoresist S1813.

- **Resist development:** 1'30" MF319 followed by deionized water rinsing and blowing dry.

- **Etching:** Reactive ion etching with a plasma of SF_6 with 30% Ar for 50" at 155 V acceleration voltage and 13 μbar.

- **Resist removal:** 10' in 65 °C acetone followed by IPA rinsing and blowing dry.

- **Silicon chip edge etching:** SF_6 Reactive ion etching for 1'. During this step the resonator is protected by a silicon hard mask.

During the first reactive ion etching step, after the unprotected niobium is removed, the silicon substrate is etched all around the resonator. Profilometer measurement reveals 500 nm silicon over-etching, as shown in the resonator inductor wire cross section reported in Fig.5.2.

Sample mounting
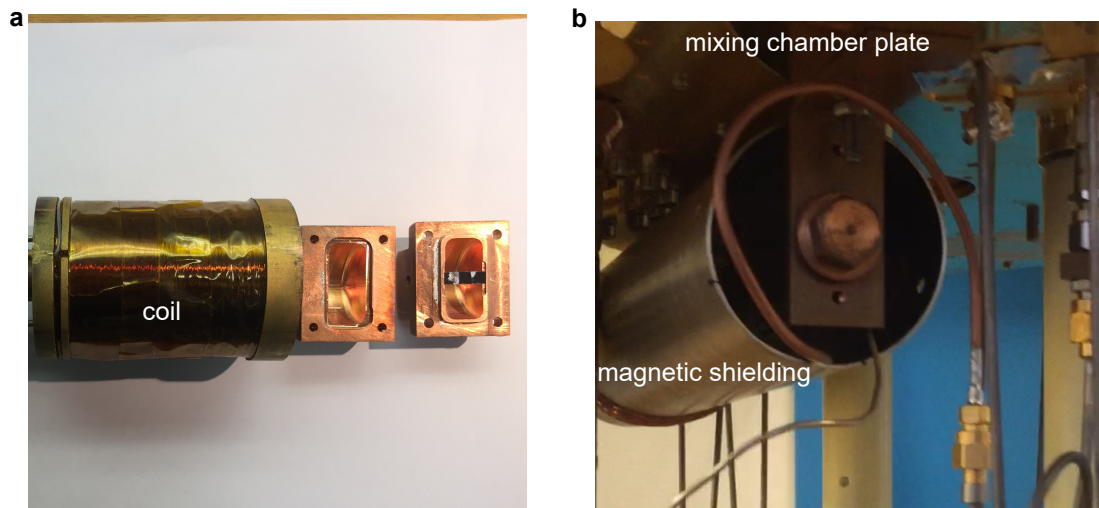
Figure 5.3: **Sample mounting. a** Open copper box next to the coil inside which it is mounted. **b** Sample and coil inside the cryoperm magnetic shielding thermally anchored to the mixing chamber plate.

The fabricated sample is inserted in the copper box by gluing it to a silicon sample holder with small amounts of vacuum grease. The silicon sample holder is then glued in the copper box sample groove, also using vacuum grease (see Fig.5.1a). Finally, the

closed copper box is mounted in a coil providing a static magnetic field B_0 parallel to the resonator inductive wire (see Fig.5.3a) up to 140 mT.

The last step to guarantee a high-quality factor is to protect the superconducting thin film from losses occurring through out-of-equilibrium quasi-particles and vortices. Low-pass filters containing absortive material are put on each line to minimize the quasi-particles (see Fig.5.2.1. The coil is inserted in a 1-mm-thick cryoperm magnetic shield to minimize stray magnetic field which may introduce vortices in the film during cool down of the film through its critical temperature (see Fig.5.3b).
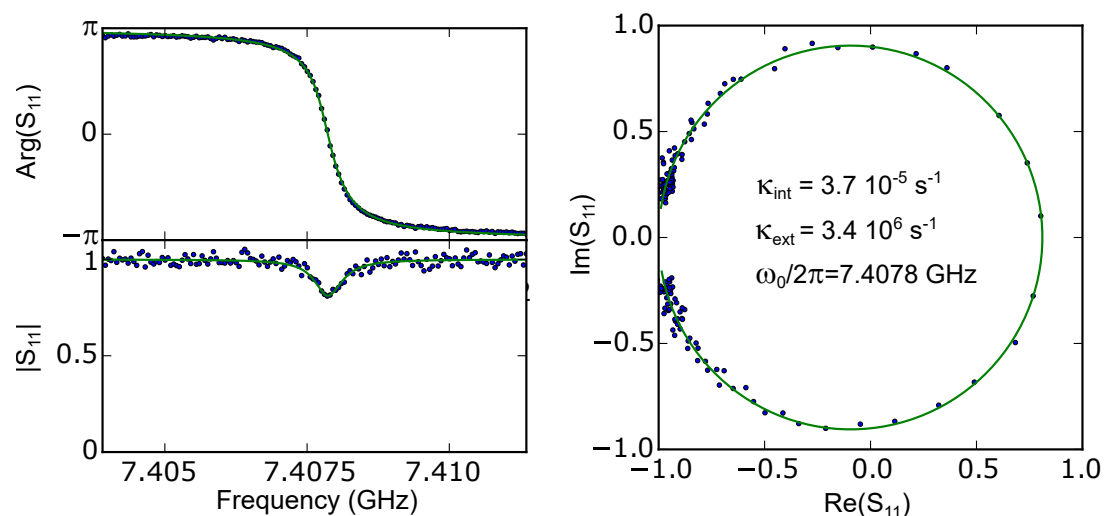
5.1.4 Microwave characterization

Figure 5.4: **Characterization of the superconducting resonator at 15 mK.** The input power used to probe the resonator corresponds to $\bar{n} \approx 0.1$. In the left panel, phase (top) and amplitude (bottom) of S_{11} are shown together with the fit (green solid line). In the right panel, the same data are reported in the complex plane.

We characterized the LC resonator by measuring the reflection coefficient S_{11} at 15 mK with the VNA. The detailed setup is depicted in Figs.5.8-5.9.

From the fit of S_{11} with Eq.2.31 we extract the internal and external loss rates $\kappa_{\text{int}}, \kappa_{\text{ext}}$ together with the resonance frequency ω_0 (see Fig.5.4). The internal loss rate is about 10 times lower than the external loss rate at a mean number of intra-cavity photon $\bar{n} \approx 0.1$, placing the resonator in the targeted overcoupling regime where its mode temperature can be set by the input microwave thermal radiation. The external coupling rate is about 3 times larger than what obtained from simulation, meaning that the antenna is inserted a little deeper in the copper box, which is consistent with a measured $Q_{\text{box}} \approx 40$. As discussed in Sc.5.1.2, the lower ω_0 of about ~ 100 MHz with respect to the simulated value is probably due to the kinetic inductance contribution.

Slight variations of the resonator parameters are observed for each experimental realization, corresponding to different cooldowns of the cryostat. The resonator frequency decreased since its fabrication by a few MHz, possibly due to aging of the niobium oxide layer. Variations of κ_{ext} are instead attributed to small differences in the thermal contraction of the antenna from room temperature to below 1 K.
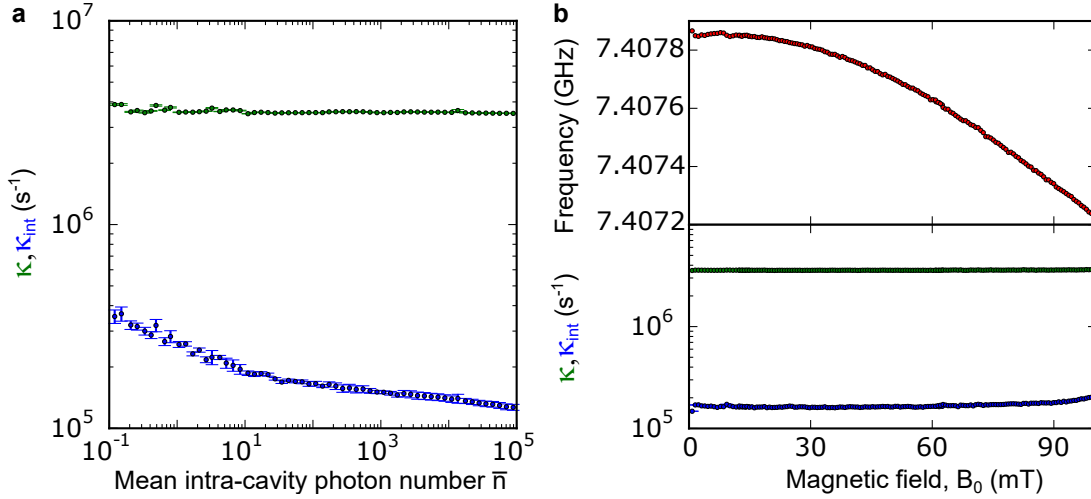
Figure 5.5: **Power and Magnetic field dependence of the resonator properties.** **a** Input power dependence of the resonator loss rates extracted from the fit of S_{11}. $\bar{n}$ is given by Eq.2.27. **b** Magnetic field dependence of resonance frequency (top) and loss rates (bottom).

Power dependence of the internal loss rate

Measuring S_{11} as a function of the input power P_{in} gives information on the origin of internal losses. Two-Level Systems are known to cause power-dependent losses in superconducting micro-resonators [93], as observed also in our measurements.. The measured increased losses at low $\bar{n}$ by more than a factor 2 (see Fig.5.5a), indicates that dielectric losses contribute to about half of the total internal losses.

Magnetic field dependence

The application of the static magnetic field B_0 parallel to the superconducting film surface, has almost unmeasurable effect to the internal losses up to $100\,\mathrm{mT}$ while the resonance frequency is reduced quadratically by $\sim 0.6\,\mathrm{MHz}$ due to the increase of the thin-film kinetic inductance (see Fig.5.5b). Above $10\,\mathrm{mT}$, systematic fitting of the resonator reflection is required to determine its frequency and apply a resonant drive to the spins.

5.1.5 Schottky barrier

The niobium thin-film deposited directly on top of the silicon substrate gives rise to a Schottky barrier in which donor may be ionized. The difference in the work function of niobium and silicon causes band-bending responsible for the ionization of the donor over an area called depletion region.

In Fig.5.6 we report the results of the depletion region calculation for our device performed by Yann-Michel Niquet. A Schottky barrier height of $0.5\,\mathrm{eV}$ is assumed based on [99]. Given the donor implantation profile (see Fig.4.17), the electrostatic potential shown in Fig.5.6a is obtained. The resulting depletion region extends for $170\,\mathrm{nm}$ below the surface. In the following, we take into account this donor ionization in the cal-
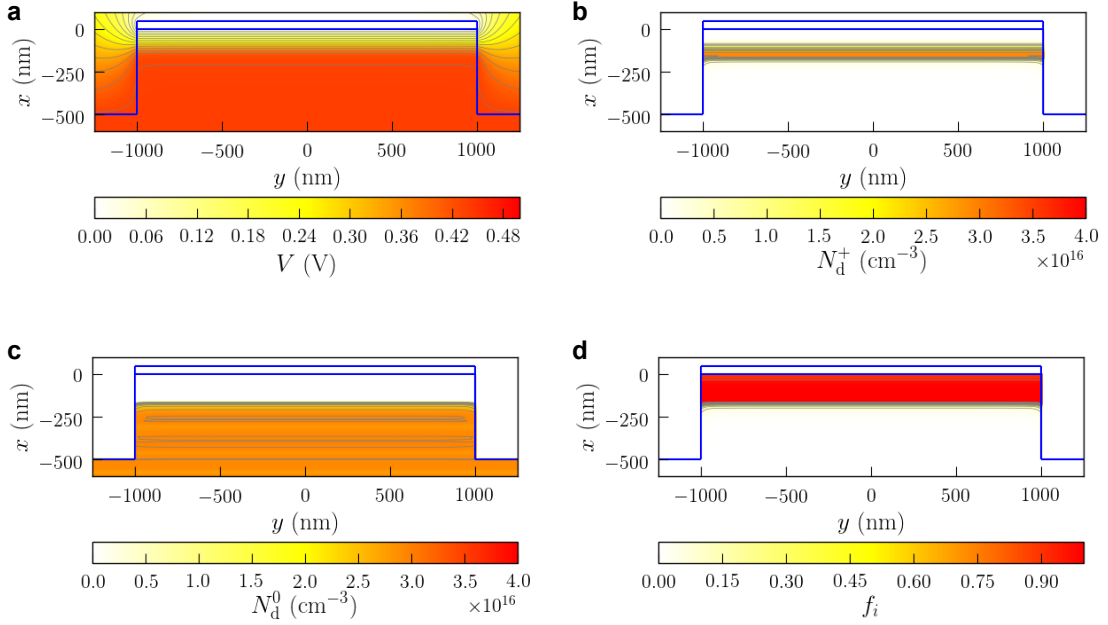
Figure 5.6: **Schottky barrier at the Si/Nb interface below the inductor wire.** **a** Electrostatic potential. **b** Density of ionized bismuth donors. **c** Density of neutral bismuth donors. **d** Fraction of ionized over neutral donors $f_i = N_d^+/N_d^0$.

culation of the coupling distribution $\rho(g)$. The difference with respect to the scenario without Schottky barrier is however small.

5.1.6 Estimate of spin-photon coupling distribution

The coupling of the bismuth donors to the resonator mode is obtained by calculating the amplitude of the magnetic field vacuum fluctuations δB_1 generated by the current fluctuations δI in the inductor wire. The magnetic field is computed using the COMSOL magnetostatic solver. The static approximation is sufficient since the length scales that come into play are very much smaller than the wavelength.

In order to calculate the field fluctuations, we first need the estimate of the current fluctuations magnitude and its distribution along the wire transverse direction. As detailed in Sec.5.1.2, we extract from CST simulation the amplitude of the current vacuum fluctuations $\delta I = 50\,nA$. The current distribution over the superconducting wire cross-section used in the magnetostatic simulation is given by the following formula [6, 100]:

$$f(x) = \begin{cases} \delta J(0)[1-(2y/w_r)^2]^{-1/2} & \text{for } |y| \leqslant |w_r/2 - \lambda^2/(2b)| \\ \delta J(w_r/2)e^{-(w_r/2-|y|)b/\lambda^2} & \text{for } |w_r/2 - \lambda^2/(2b)| < |y| < w_r/2 \\ (1.165/\lambda)\sqrt{w_r b}\delta J(0) & \text{for } y = w_r/2, \end{cases}$$

In these expressions y is the wire transverse coordinate indicated in Fig.5.7a, $w_r = 2\,\mu m$ is the wire width, $b = 50\,nm$ is its thickness and $\lambda = 110\,nm$ is the penetration depth of the niobium film [101]. The normalization constant $\delta J(0)$ is determined by the condition $\int_{-w_r/2}^{w_r/2} \delta J(y)dy = \delta I$. We finally use $\delta J(y)$ to compute the magnitude of the field fluctuations $\delta B_1(x,y)$ using COMSOL magnetostatic solver (see Fig.5.7a).
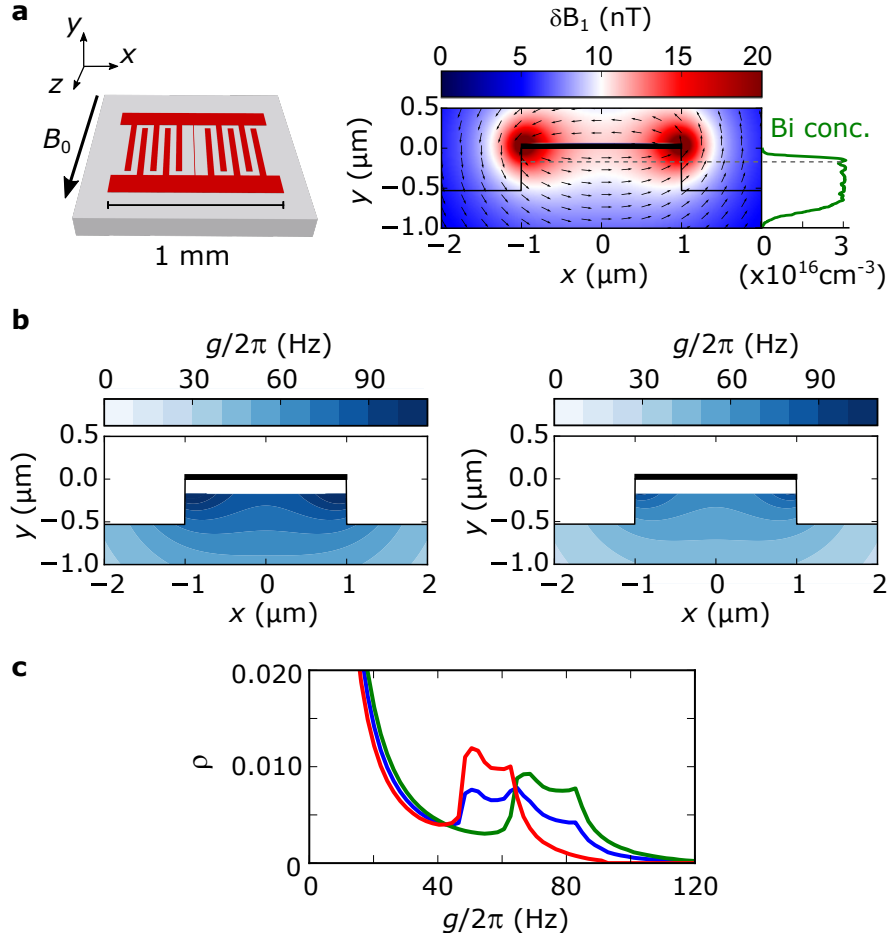
Figure 5.7: **Spin-photon coupling** g. **a** Niobium resonator on the silicon chip. Right, map of the magnetic field vacuum fluctuations δB_1 at the device cross section around the inductor wire (black). The direction of the field at each location is represented by black arrows. The bismuth implantation profile is as well shown, with the border of the depletion region indicated by the dashed line. **b** Left, map of the spin photon coupling rate g computed for $|\langle S_x \rangle| = 0.28$, corresponding to the $|-,-1\rangle \leftrightarrow |+,0\rangle$ transition at $62.5\,\mathrm{mT}$ and to the $|-,0\rangle \leftrightarrow |+,1\rangle$ transition at $10\,\mathrm{mT}$. Right, map of the spin photon coupling rate g computed for $|\langle S_x \rangle| = 0.21$, corresponding to the $|-,0\rangle \leftrightarrow |+,-1\rangle$ transition at $62.5\,\mathrm{mT}$ and to the $|-,1\rangle \leftrightarrow |+,0\rangle$ transition at $10\,\mathrm{mT}$. **c** Coupling distribution for the resonant transitions at $62.5\,\mathrm{mT}$ and $10\,\mathrm{mT}$ (blue), sum of the coupling distribution calculated for $|\langle S_x \rangle| = 0.28$ (green) and $|\langle S_x \rangle| = 0.21$ (red).

The AC magnetic field δB_1 is located in the $x - y$ plane perpendicular to the resonator wire and to the applied static field B_0 directed along z. The spin-photon coupling g for the S_x transition between the states $|-, m\rangle$ and $|+, m'\rangle$ is thus $g = \gamma_e \delta B_1 |\langle -, m|S_x|+, m'\rangle|$. Fig.5.7b shows the coupling $g(x, y)$ of the donors closer to the inductor wire obtained from the δB_1 map for the two quasi-degenerate resonant transitions at $62.5\,\text{mT}$ $|-, -1\rangle \leftrightarrow |+, 0\rangle$ and $|-, 0\rangle \leftrightarrow |+, -1\rangle$, having S_x matrix elements equal to 0.28 and 0.21, respectively. The two contributions are used for computing the coupling distribution $\rho(g)$ expected at $62.5\,\text{mT}$. The same distribution is also valid for the two quasi-degenerate transitions that are instead resonant with the cavity at $10\,\text{mT}$, $|-, 0\rangle \leftrightarrow |+, 1\rangle$ and $|-, 1\rangle \leftrightarrow |+, 0\rangle$, since they have matrix elements identical to the the other two transitions.

5.2 Experimental setup

5.2.1 Low-temperature setup

The experiment reported in this chapter is performed at $15\,\text{mK}$ in a cryogen free dilution refrigerator fabricated by the company Cryoconcept. This refrigerator has five stages at different temperatures ($70\,\text{K}$, $4\,\text{K}$, $900\,\text{mK}$, $100\,\text{mK}$ and $12\,\text{mK}$) separated by radiation shields. Both the ESR resonator and the TWPA are anchored at a temperature of $15\,\text{mK}$. As shown in Fig.5.8, the resonator is connected via the antenna to the circulator, separating input and output signals.

Coaxial transmission lines link the room-temperature apparatus to the resonator and the TWPA. To prevent heat transfer from higher to lower temperature stages, the transmission lines are made of CuNi (or Silver-plated-CuNi) coaxial cables from room-temperature to $4\,\text{K}$ and of NbTi superconducting cables from $4\,\text{K}$ to $15\,\text{mK}$. In order for the microwave field to be at thermal equilibrium at $15\,\text{mK}$, it is also needed to stop thermal and technical noise coming from the room temperature apparatus. This common experimental challenge for all cQED experiments, is tackled differently for input and output lines.

For input lines, the solution is to thermalize the incoming modes to the cryostat temperature by means of impedance matched attenuators. As described in Sec.2.3.5, the number of input noise photons is reduced by the attenuation factor while the thermal radiation at the attenuator temperature is added. As shown in Fig.5.8, we use a $20\,\text{dB}$ attenuator at $4\,\text{K}$ followed by $30\,\text{dB}$ more attenuation at $15\,\text{mK}$. Using Eq.2.34, we find that the number of propagating $\sim 7\,\text{GHz}$ room-temperature noise photons $n_{\text{th}}(300\,\text{K}) \approx 900$ is reduced to $n_{\text{th}} \approx 0.01$ at the resonator input, corresponding to a mode temperature of about $75\,\text{mK}$.

For the output line however the signal cannot be attenuated without degrading the signal-to-noise ratio of the measurement. To nevertheless protect the sample from thermal photons and noise photons emitted by the amplifiers, microwave circulators are placed along the line at $15\,\text{mK}$ together with filters. The isolation provided by each circulator is of about $18\,\text{dB}$, thus approximately doubled for the two circulators in series. All input and output lines are provided with infrared filters to limit the out-of-equilibrium quasi-particle generation in the superconducting devices.

The output signal is first amplified by the TWPA and then by the HEMT at $4\,\text{K}$. The 3-12 GHz isolator realizes a $50\,\Omega$ load for the TWPA output in the whole amplification range, while the following filters prevents noise coming from the HEMT to reach the
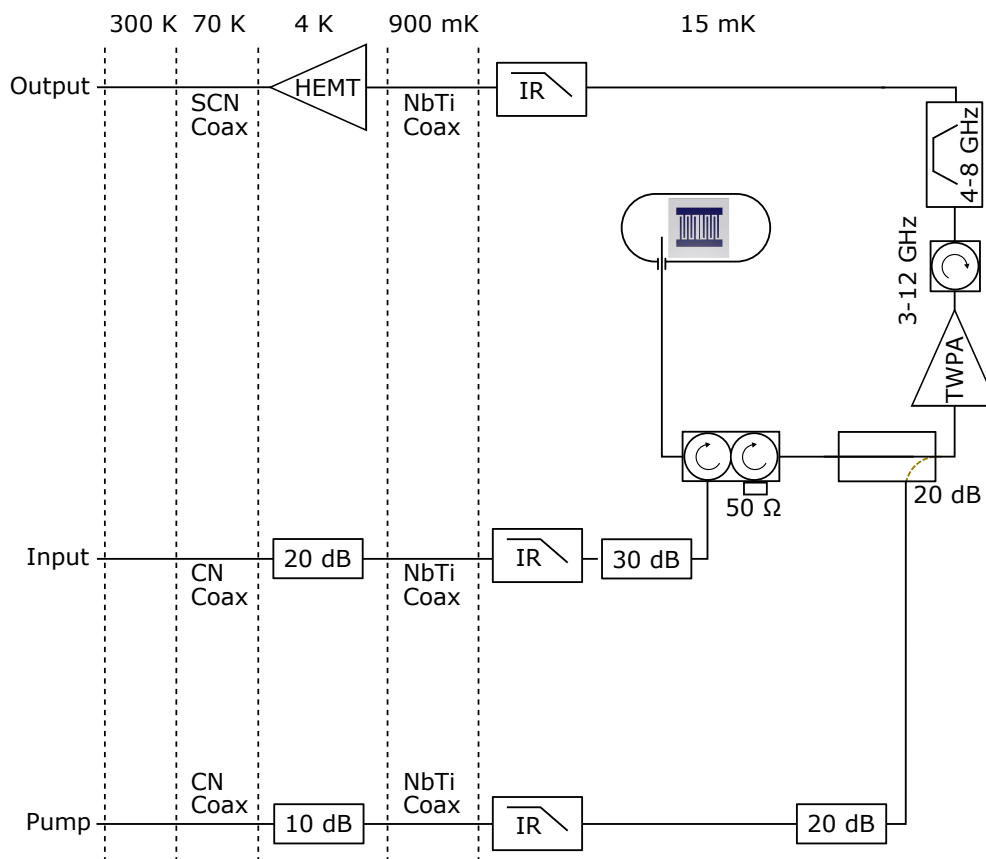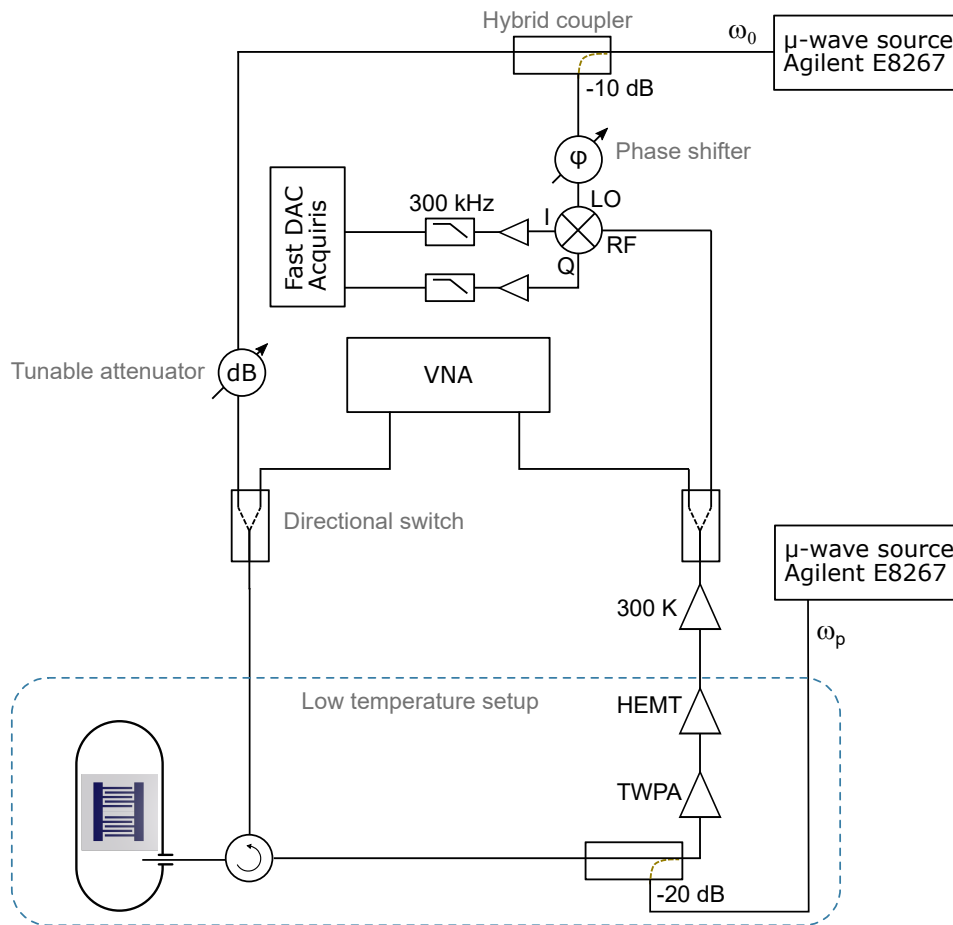
Figure 5.8:   **Low temperature setup.**   Microwave setup connecting the room-temperature apparatus to the 15 mK experimental stage, on which is mounted the ESR resonator.

TWPA. The double circulator in between the TWPA and the resonator, in addiction to protect the resonator from the incoming noise and pump tone leakage, prevents interferences between the two devices. The TWPA pump tone is sent via a dedicated line and a hybrid coupler to the TWPA input. A total 50 dB attenuation of the TWPA pump line, prevents the room temperature noise to couple to the output.

5.2.2   Room-temperature setup

The room-temperature setup is depicted in Fig.5.9. The resonator and the TWPA can be characterized either by a commercial VNA, or direct homodyne demodulation followed by digitalization with a rapid acquisition card. Microwave switches allow to use eiher the VNA or homodyne setup on-demand.

For homodyne detection a microwave source provides both a coherent signal sent towards the resonator as well as continuous tone which serves as the local oscillator of an *IQ* mixer to demodulate the output signal. The resulting *I* and *Q* quadratures are then amplified and filtered in several stages before being recorded by a fast digitizer (Acquiris DC282) and transfered to a computer for processing. The phase of the homodyne detection is set manually via a tunable phase-shifter. A 10-MHz-synchronization

Figure 5.9: **Room temperature setup.**

loop running through every instrument guarantees phase stability.

5.2.3 TWPA characterization

The TWPA is pumped with a microwave tone whose frequency and power can be tuned to optimize its figures of merit. The pump frequency ranges from 7.85 GHz to 8.15 GHz, while the power is tuned by few dB around -70 dBm. In each experimental realization the optimal parameters are slightly changed. Gain up to G_{TWPA} =25 dB can be reached. As a general tendency, we observe that to larger gains corresponds lower saturation power, higher noise and more pronounced ripples in the gain frequency dependence.

In Fig. 5.10a it is shown the typical gain spectrum after optimization of the pump parameters. The onset of saturation is observed at input power of about -100 dBm, where the gain is changed by ~ 1 dB with respect to the low power value (see Fig 5.10b). We check that the TWPA added noise is the dominating source of noise of the amplification chain by comparing the noise power spectrum on the output line with and without the TWPA pump. To do so, we connect a spectrum analyzer to the output line after the room-temperature microwave amplifier. This measurement is performed with G_{TWPA} =25 dB. The noise power level at a frequency detuned of a few MHz from the resonator is observed to increase by ~ 10 dB when the pump is turned on (see
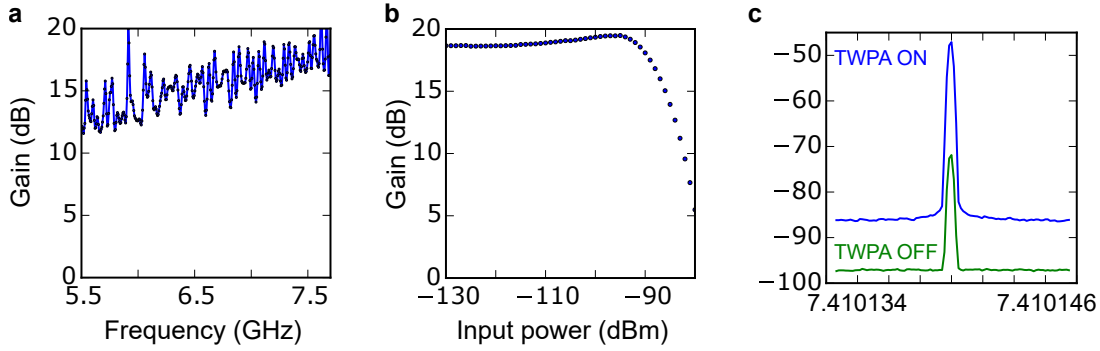
Figure 5.10: **TWPA characterization. a** Gain spectrum. **b** Gain saturation. **c** Noise power spectral density measured at the end of the amplification chain for the on and off TWPA states. A coherent tone at 7.410146 GHz is sent to the TWPA input. The power increase of the coherent signal reveals a TWPA gain $G_{\text{TWPA}} = 25$ dB for this experiment.

Fig 5.10c). This provides a way to estimate the improvement in signal-to-noise ratio. From Eq.2.42 we get the following expression for the measured noise power ratio $S_{\text{ON}}/S_{\text{OFF}}$:

$$\frac{S_{\text{ON}}}{S_{\text{OFF}}} = \frac{S_{\text{bg}} + (G_{\text{TWPA}} - 1)S_{\text{TWPA}}}{S_{\text{bg}}}, \tag{5.3}$$

where S_{TWPA} is the noise added by the TWPA and S_{bg} is the contribution to the noise coming from the rest of the amplification chain: the HEMT and the room-temperature amplifiers. Eq.5.3 yields for the measured $S_{\text{ON}}/S_{\text{OFF}} = 10$ dB and $G_{\text{TWPA}} = 25$ dB the ratio of the two noise contributions $S_{\text{bg}}/S_{\text{TWPA}} = 35$, which corresponds to a SNR improvement by $\sqrt{35} = 5.9$.

5.3   Hahn echo detection

The spin signal of our spectrometer is in all that follows given by the area of the spin echoes generated via Hahn echo sequences $\pi/2 - \tau - \pi - \tau$, often followed by the CPMG train of π pulses to detect additional refocused echoes. We briefly outline here the implementation of this detection technique.

5.3.1   Pulse generation and echo acquisition

We generate the microwave pulses with the setup of Fig.5.11, part of the room-temperature setup of Fig.5.9. The two main requirements for the drive pulses are an high on/off ratio to avoid heating the spins while not driving, and MHz bandwidth to drive all the spins within the resonator linewidth. This is realized by shaping the pulses with microwave switches with an on/off ratio of 80 dB controlled by an arbitrary waveform generator (AWG5011C from Tektronix).

Two pulses of different amplitude are obtained by using two switches in parallel, each in series with a tunable attenuator. The relative phase is adjusted manually with a phase shifter. After adding the two parallel lines, a power amplifier allows to increase the dynamic range. A third switch isolates the resonator from the amplifier noise when
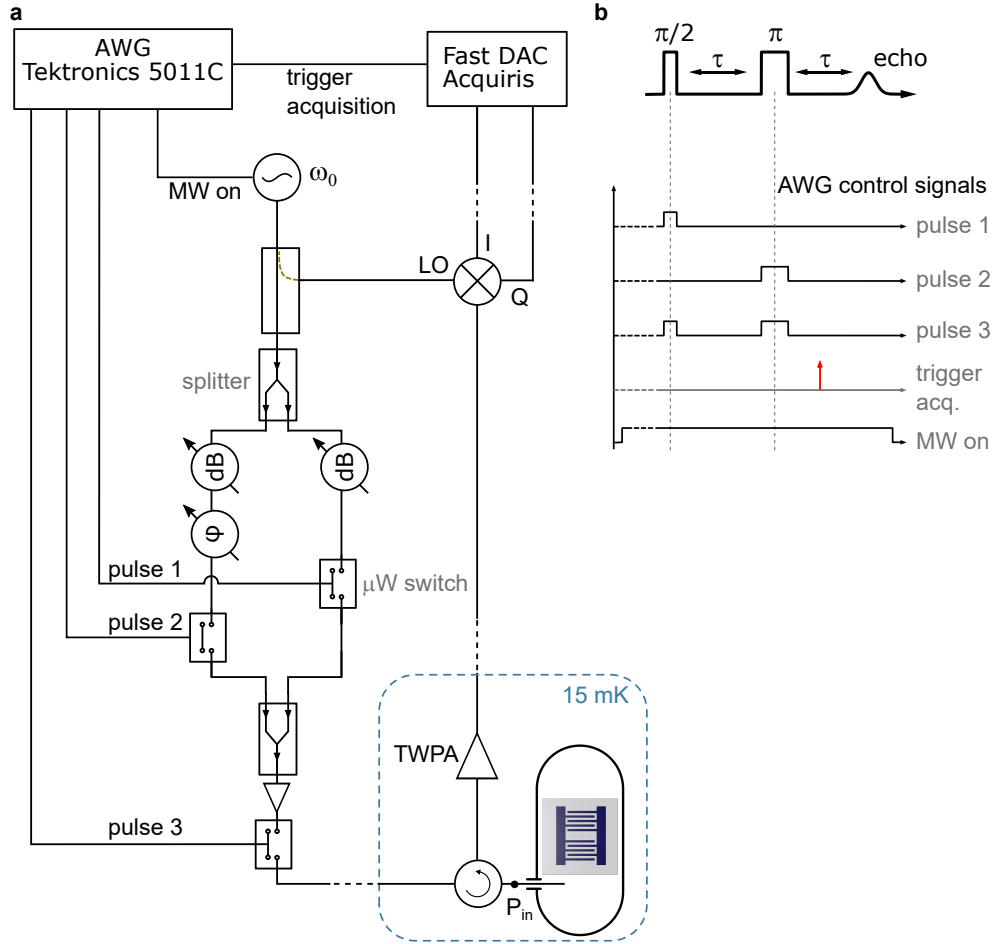
Figure 5.11: **Pulse setup.** Two independent microwave pulses can be generated via two microawave switches in parallel, each being in series with a tunable attenuator to control the pulse input power P_{in} referred to the port of the resonator. The pulses' phases are set by a manual phase shifter. All signals are controlled with an AWG.

pulses are not applied. Moreover, the microwave source is switched off during the waiting time between two pulse sequences. Given the total attenuation of the line after the last switch, we can deliver at the resonator input pulses of power P_{in} up to -40 dBm.

The reflected pulses and the emitted echo signal are demodulated at ω_0 and their I and Q quadratures are detected using the setup shown in Fig.5.9. The acquisition by the digitizer is triggered by the AWG.

5.3.2 Hahn echo sequence and CPMG

Before discussing the ESR spectroscopy, we first detail the acquisition of the spin signal with the CPMG sequence. The 301 echoes shown in Fig.5.12a are detected at $B_0 = 62.5$ mT, where transitons $|-, -1\rangle \leftrightarrow |+, 0\rangle$ and $|-, 0\rangle \leftrightarrow |+, -1\rangle$ are resonant with the superconducting cavity. A $\pi/2$ pulse of duration $t_{\pi/2} = 125$ ns is followed after a time $\tau = 15\,\mu$s by a π pulse of duration $t_\pi = 250$ ns. Unless specified, the same t_π and $t_{\pi/2}$ are used all througout this thesis. After a second delay τ the first echo is emitted (first echo in the inset of Fig.5.12a and blue dots in Fig.5.12b). The pulse power P_{in} is calibrated by performing Rabi oscillations, as will be explained in the following.
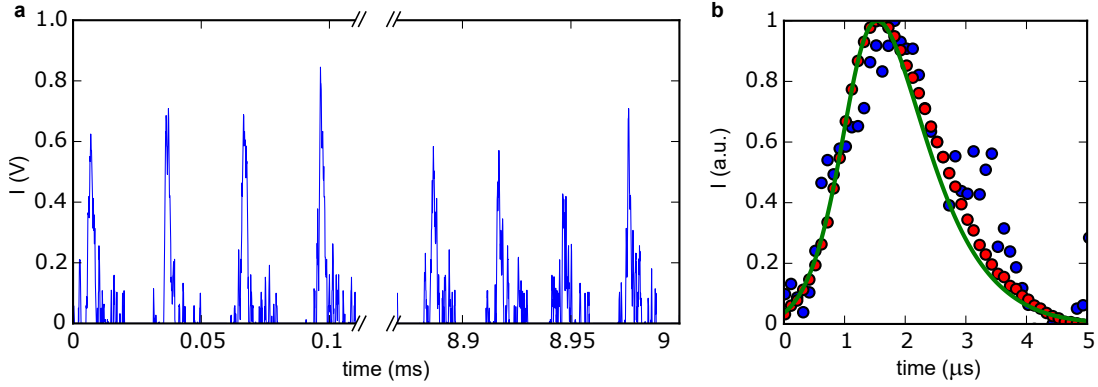
Figure 5.12: **Hahn echo detection. a,** First and last four echoes in the CPMG sequence at 62.5 mT. All π pulses have been removed from the plot. **b,** First echo of the CPMG sequence (blue), CPMG average (red) and simulation of the Hahn echo (green) obtained by using the $\rho(g)$ shown in Fig.5.7c.

This echo is refocused N times by as many π pulses of same amplitude and duration as the first one, equally spaced by 2τ. As shown in Fig.5.12a, 300 echoes with slightly reduced amplitudes are being recorded at 62.5 mT, spaced by $2\tau = 30\,\mu$s. All echoes are averaged with a weight given by the measured amplitude decay, in order to optimize the signal to noise improvement (see Fig.5.12b). The whole sequence is repeated with period t_{rep} of the order of the spin relaxation time Γ_1^{-1}. In the following, we quantify the echo signal using the integrated quadrature signal denoted A_{e}.

Simulation of the first Hahn echo is shown in Fig.5.12b, and is in good agreement with the data. No adjustable parameters are used and the CPMG sequence is not included in the simulation. The Hahn-echo simulation is performed for g values in the 5-200 Hz range and the results are averaged using the g distribution shown in Fig.5.7c.

5.3.3   Rabi oscillations

We calibrate the pulse power by performing Hahn-echo detected Rabi oscillations. To do so, we measure the echo amplitude as a function of the refocusing pulse tipping angle θ_{p}, which is varied by changing the pulse power P_{in} (see Fig.5.13). This results in the appearance of oscillations in the integrated echo signal A_{e}, as shown in Fig.5.13. As detailed in Sc.3.2.1, or each subset of spins coupled to the resonator with strength g, the echo signal is $A_{\mathrm{e}} \propto \frac{p}{2}(1 - \cos\theta_{\mathrm{p}})$, where p is the initial spin polarization. A spin driven by a resonant coherent drive rotates at frequency $\omega_1(t) = 2g\langle\hat{a}(t)\rangle$ (see Sec.3.1.2). As a result, upon a square pulse of duration t_{p} the spin undergoes a Rabi oscillation of angle:

$$\theta_{\mathrm{p}} = \int_t \omega_1(t) = 2g\sqrt{\bar{n}}t_{\mathrm{p}}, \tag{5.4}$$

where $\bar{n}$ is the steady-state intra-resonator photon number linked to P_{in} by Eq.2.27.

Since we probe an ensemble of spins with a broad coupling distribution, the measured Rabi oscillations are a sum of oscillations largely spread in frequency. Each spin subset of coupling g experiences a different tipping angle $\theta_{\mathrm{p}}(g)$ that for large rotations yield A_{e} in Eq.3.35 to the averaged value of $p/2$. This damping of the Rabi oscillations for large tipping angle is visible in Fig.5.13 and is well reproduced by the simulation.
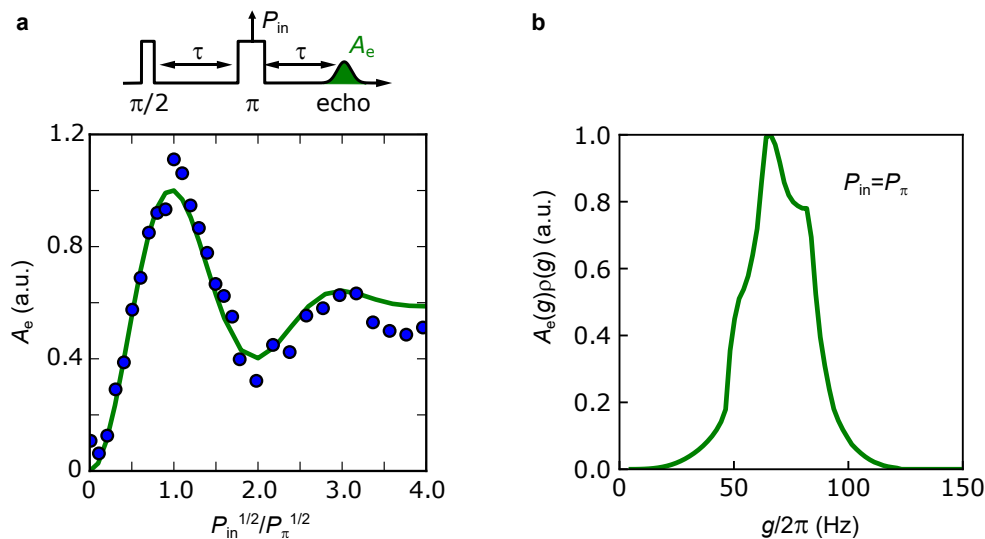
Figure 5.13: **Rabi oscillations. a,** Top, pulse sequence used to measure Rabi oscillations. Bottom, measured (blue dots) and simulated (green line) integrated echo amplitude A_e as a function of the second pulse input power P_{in}. The value of P_π is calibrated with the first maximum of the signal. **b** Relative contribution $A_e(g)\rho(g)$ to the echo amplitude A_e at $P_{in} = P_\pi$ as a function of the spin-resonator coupling g. $A_e(g)$ is the echo amplitude simulated for an ensemble of N spins with the same coupling g.

We have until now neglected the effect of the cavity bandwidth on the spin dynamics. However, in our experiment the ESR linewidths are much broader than the cavity and the finite pulse excitation bandwidth must be taken into account. Since we apply short pulses satisfying $t_p << 2\pi/\kappa$, the excitation bandwidth of a π pulse is set by κ due to the cavity filtering. This means that spins within the ESR linewidth have different Rabi frequencies and undergo rotations of different angles under the same pulses. The Rabi frequencies Ω_R depends indeed on their detuning Δ_s, $\Omega_R = \sqrt{\Delta_s^2 + \omega_1}$, and their rotation axis is tilted in the $x - z$ plane by an angle $\phi = \arctan(\Delta_s/\omega_1)$ (see Ch.3).

A quick and rough consistency check is easily performed using the Rabi oscillations in Fig.5.13, by evaluating the input power corresponding to a π pulse using the estimated input line attenuation. We find $P_\pi = 6$ nW, corresponding to $\bar{n} \approx 10^9$. Using Eqs.2.27 and Eq.5.4, we find then that the average value of g for the spins most contributing to the echo signal is $\bar{g}/2\pi = 30$ Hz. This value is only about a factor 2 lower than the value of coupling maximally contributing to the echo amplitude $g/2\pi = 65$ Hz obtained from the simulation (see Fig.5.13). We attribute this discrepancy to the poor calibration of the power P_{in}.

5.4 Strain broadened transitions

The coil inside which the sample is mounted provides a static magnetic field B_0 up to 140 mT. In this field range the resonator crosses 11 transitions, among which 5 couples of quasi degenerate transitions. The magnetic field, matrix element and slope of these transitions at resonance are reported in Table 5.1.

Transition	Field (mT)	$\langle S_x \rangle$	df/dB (MHz/mT)
$\lvert -,4\rangle \leftrightarrow \lvert +,5\rangle$	1.25	0.47	25.22
$\lvert -,4\rangle \leftrightarrow \lvert +,3\rangle$	1.6	0.07	19.7
$\lvert -,3\rangle \leftrightarrow \lvert +,4\rangle$	1.6	0.42	19.7
$\lvert -,3\rangle \leftrightarrow \lvert +,2\rangle$	2.25	0.12	14.2
$\lvert -,2\rangle \leftrightarrow \lvert +,3\rangle$	2.25	0.37	14.2
$\lvert -,2\rangle \leftrightarrow \lvert +,1\rangle$	3.7	0.17	8.75
$\lvert -,1\rangle \leftrightarrow \lvert +,2\rangle$	3.7	0.32	8.75
$\lvert -,1\rangle \leftrightarrow \lvert +,0\rangle$	9.6	0.21	3.8
$\lvert -,0\rangle \leftrightarrow \lvert +,1\rangle$	9.6	0.28	3.8
$\lvert -,0\rangle \leftrightarrow \lvert +,-1\rangle$	62.7	0.21	3.8
$\lvert -,-1\rangle \leftrightarrow \lvert +,0\rangle$	62.9	0.28	3.8

Table 5.1: **Expected ESR transitions** at $\omega_0/2\pi = 7.4087$ GHz, with their respective matrix elements and field dependence df/dB. Quasi degenerate transitions are grouped by dashed lines. The results are obtained from analytical solution of Eq.4.4

.

5.4.1 Spectrum

We first measure the echo amplitude A_e as a function of the static field B_0 applied along z (see Fig 5.14). The six peaks of echo signal coincide with the calculated magnetic fields at which the spin transitions are resonant with the superconducting cavity. The two spectra reported in Fig 5.14 are measured in two different runs of the experiment, where resonator parameters slightly varied with negligible consequences. Due to the resonator frequency dependence on magnetic field, at each B_0 the resonator reflection is measured, fitted and the microwave source adjusted to this frequency using an automated routine; after that the echo sequence is run. CPMG averaging is used to improve the SNR and a repetition rate of the order of the spin relaxation rate Γ_1 is used.

The different peak height of the measured ESR lines is mainly due to three reasons. The first is that the reported spectra are measured with constant pulse amplitude, while the matrix elements of most transitions are different. This makes the tipping angle of the pulses in the Hahn echo sequence to vary from peak to peak. This effect is clearly visible comparing the two measurement in the two panels of Fig 5.14. While the spectrum of Fig 5.14a is measured using P_π calibrated on the first transition at 1.25 mT, for the spectrum of Fig 5.14b P_π is calibrated at 9.6 mT. The second contribution to the peak height differences has to be found in the dependence of the spin coherence time on field, as we discuss in the rest of this chapter. In particular the coherence times of the 10 mT and 60 mT transitions is more than one order of magnitude larger with respect to the lower field transitions. Both effects are amplified by the use of CPMG averaging, as highlighted in Fig 5.14b. Finally, the repetition time t_{rep} affects the relative amplitude of the spin signal at the six transitions due to the different associated relaxation times. t_{rep} is in both cases chosen to be of the order of the longest measured spin relaxation time.

By fitting the ESR spectrum in Fig. 5.14 with a sum of Lorentzians, we extract the linewidths of the six resolvable ESR lines; the fit results are reported in Table 5.2. As we discussed in Ch.4, the expected linewidth of Si:Bi is 0.4 mT due to the inhomogeneous linewidth caused by the ^{29}Si nuclear spin bath. However, we observe for increasing field linewidths going from 0.4 mT up to 1.4 mT. The value for the last two transitions is
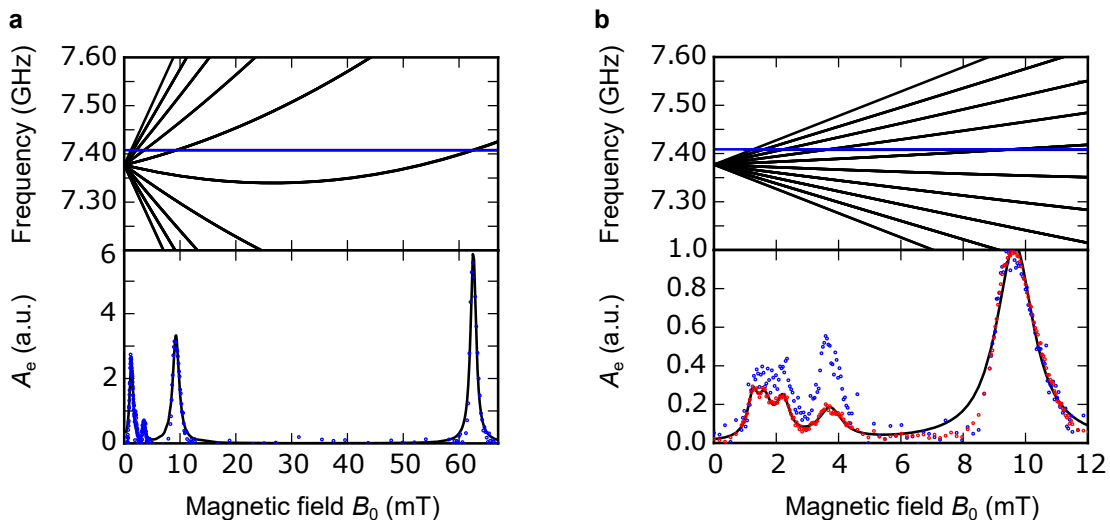
Figure 5.14: **Spectrum. a,** Top, black lines are calculated electron spin resonance transitions of the bismuth donors. The resonator frequency $\omega_0/2\pi = 7.4078\,$GHz (blue line) is resonant with 6 transitions in the 0-70 mT range. Bottom, measured integrated spin-echo amplitude A_e (blue) as a function of B_0, showing the expected transitions. The Hahn-echo pulse power P_{in} is calibrated on the first transition, CPMG averaging is used and the experiment repetition time is $t_{\mathrm{rep}} = 5.8\,$s. The black line is a fit with a sum of six Lorentzians. **b** Top, calculated transitions in the 0-12 mT range (black). The resonator frequency $\omega_0/2\pi = 7.4087\,$GHz (blue) is about one MHz lower than in the measurement of panel **a**. Bottom, measured integrated spin-echo amplitude A_e with (red) and without (blue) CPMG averaging. The Hahn-echo pulse power P_{in} is calibrated on the fifth transition at 9.7 mT, $t_{\mathrm{rep}} = 10\,$s. The black line is a fit with a sum of five Lorentzians.

Field (mT)	Linewidth (mT)	Linewidth (MHz)
1.2	0.4	10
1.6	0.5	9.8
2.2	0.5	7.1
3.7	0.9	7.9
9.6	1.4	5.3
62.5	1.3	4.9

Table 5.2: **Fitted ESR lines parameters.**Results of the Lorentzian fit shown in Fig 5.14a for the first 5 lines, and from fit shown in Fig 5.14b for the 62.5 mT transition. The frequency linewidth is extracted using the df/dB values reported in Table 5.1.

thus more than 3 times larger than the expected ^{29}Si-induced broadening, meaning that another effect is dominating. As we anticipated in Ch.4, we attribute this additional broadening to strain induced by the niobium thin film.

5.4.2   Strain simulation

The measured linewidth of 5 MHz at 62.5 mT gives us an estimate of the strain-induced frequency shift. At lower magnetic fields this effect is instead masked by the ^{29}Si-induced broadening that reaches 10 MHz on the first transition due to the large df/dB.

We attribute the origin of the strain to the different thermal contraction of the niobium film with respect to the silicon substrate when cooling down the sample from room temperature. In order to confirm the physical validity of the strain-induced frequency shift hypothesis, we performed strain simulation using COMSOL software. The results are shown in Fig.5.15.
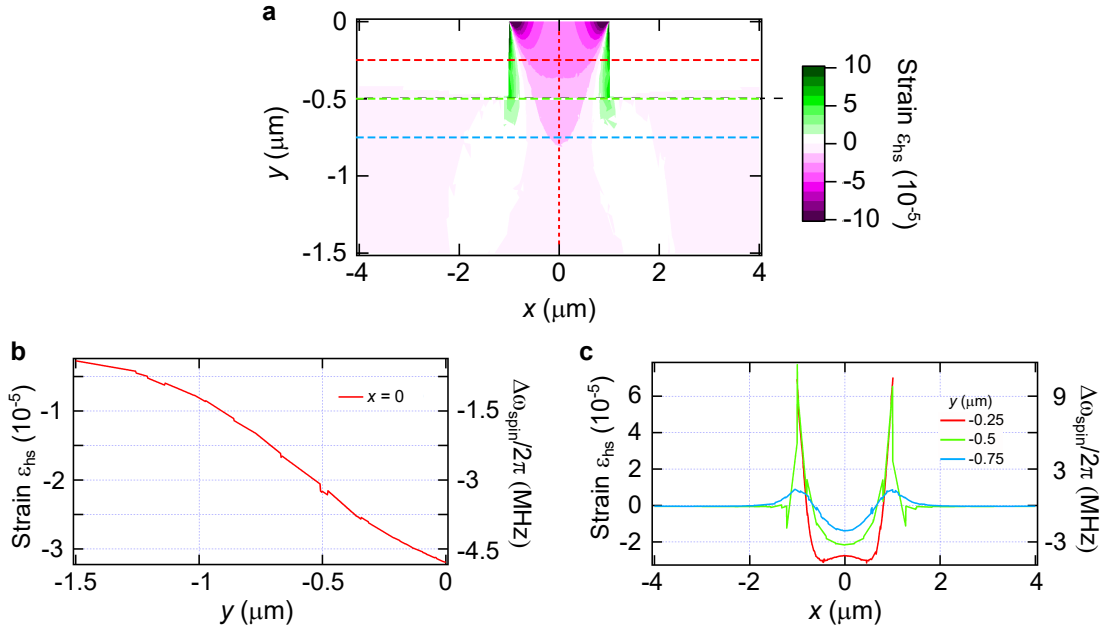

Figure 5.15: **Strain simulation. a,** Hydrostatic strain ϵ_{hs} map at the inductor-wire cross-section. Dashed lines represent the cuts shown in panels **b-c**. **b,** Cut along y at $x = 0$ of the ϵ_{hs} map. **c,** Three cuts along x of the ϵ_{hs} map. The corresponding bismuth donor spin frequency shift is reported on the right axis of panels **b-c**.

Simulations show that in the region below the wire, were the donors more contributing to the signal lie, the hydrostatic strain ϵ_{hs} varies of a few 10^{-5}. For example, at the center of the wire it goes from -3×10^{-5} at the surface to -1×10^{-5} at $y \sim -1\mu m$ (see Fig.5.15). This corresponds to a frequency shift $df/d\epsilon_{\mathrm{hs}} = 5(dA/d\epsilon_{\mathrm{hs}})\epsilon_{\mathrm{hs}}$ varying of about 4.5 MHz. Variations of similar magnitude are expected on x direction in the middle of the implanted region. This simulated strain-induced shift of a few MHz is in good agreement with the additional broadening measured in the spectral lines.

5.4.3   Rabi frequency dependence on B_0

We performed a second measurement to confirm the strain-induced broadening of ESR linewidths. Due to the spatial dependence of the coupling $g(x, y)$ and of the strain-

induced frequency shift, the Rabi frequency and the Larmor frequency are expected to show correlations that are absent in usual ESR experiments. By measuring Rabi oscillations as a function of the applied B_0, we indeed observe slower oscillations at higher field, confirming that g and ω_{spin} are correlated in agreement with the calculated strain effect. However, a quantitative analysis has not been carried out.
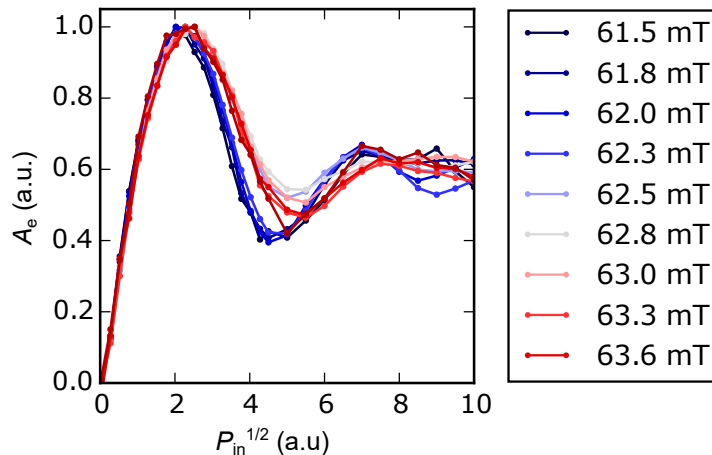

Figure 5.16: **Rabi oscillations versus B_0 at the sixth ESR line.**

5.5 Coherence time

At each ESR peak of the spectrum we have measured the echo decay by varying the delay τ between the two pulses in the Hahn-echo sequence (see Ch.4). We define the coherence time T_2 by fitting the echo decay with a Gaussian. The results reported in Fig.5.17 show a significant reduction of T_2 by more than one order of magnitude as the field is reduced from $62.5\,\mathrm{mT}$ to $1.3\,\mathrm{mT}$. Moreover, clear echo amplitude oscillations are observed at intermediate magnetic fields.

The $T_2 = 600\,\mu\mathrm{s}$ at $62.5\,\mathrm{mT}$ is in the range of expected values for bismuth donors in natural silicon (see Sec.4.3.1). The Gaussian decay at $62.5\,\mathrm{mT}$ can thus be attributed to spectral diffusion induced by the ^{29}Si nuclear spin bath dynamics. The observed shortening of T_2 for lower field is instead incompatible with spectral diffusion. The spectral diffusion rate would indeed be proportional to the spin transition df/dB, while the observed dependence of the decoherence rate on df/dB is not (see Fig.5.18). We ascribe the coherence decay of the first four transitions to the ESEEM phenomenon, as we discuss in the following.

5.5.1 ESEEM

The ^{29}Si nuclear spins closer to the resonant donors give rise to the ESEEM phenomenon (see Sec.4.3.1). ESEEM oscillations on top of the spectral-diffusion decoherence at $9.7\,\mathrm{mT}$ are clearly visible in Fig.5.17e. Fig.5.19a shows these oscillations normalized to the mean value extracted with the Gaussian fit and represented around zero. A Fourier transform of this ESEEM signal is shown in Fig.5.19b, highlighting two main frequency
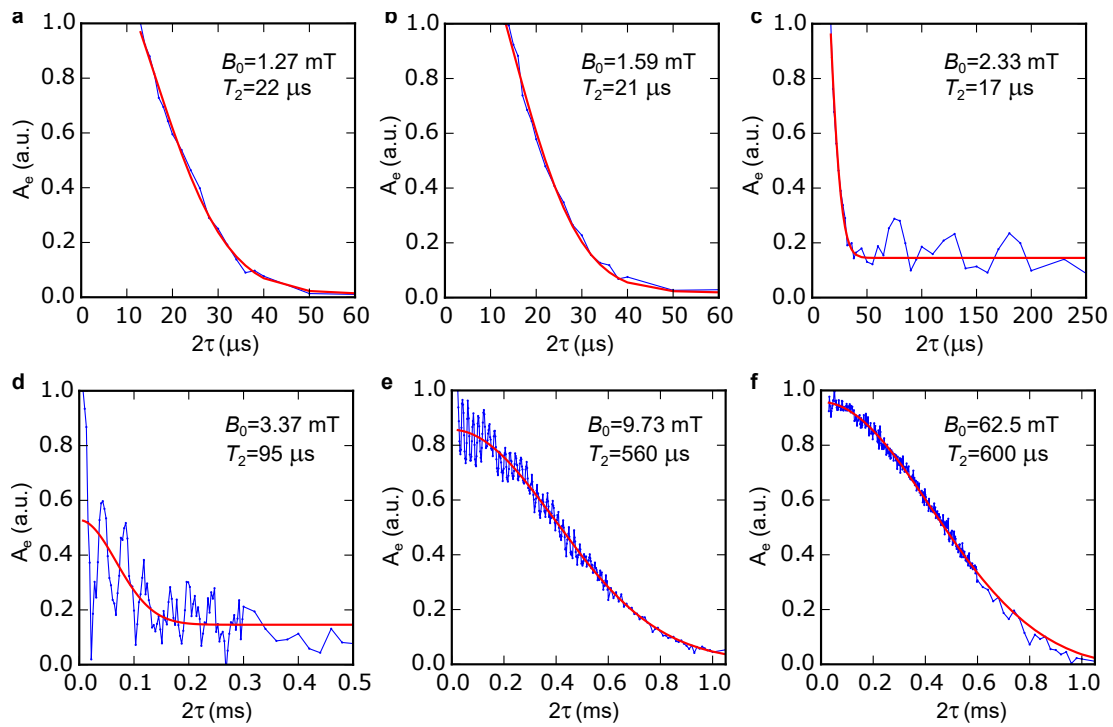
Figure 5.17: **Coherence time at the six resonant transitions.** Measured (blue) integrated echo A_e as a function of pulse delay τ in the Hahn echo sequence. Red lines gaussian fit of time constant T_2.
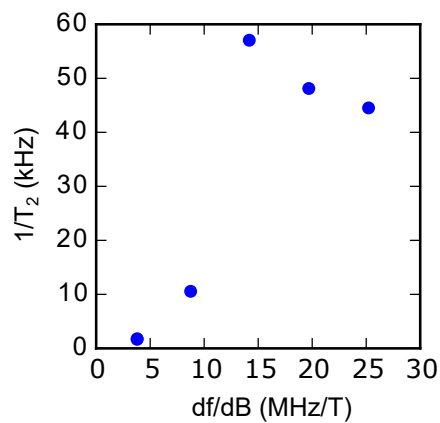

Figure 5.18: **Decoherence rate dependence on df/dB.** The decoherence rate is extracted from the Gaussian fit of the measured echo decay (see Fig.5.17).

components at $100\,\mathrm{kHz}$ and at $15\,\mathrm{kHz}$. The nuclear spin Larmor frequency at $9.7\,\mathrm{mT}$ is $\omega_I/2\pi = \gamma_{\mathrm{Si}}B_0 = 82kHz$, where $\gamma_{\mathrm{Si}}/2\pi = 8.45\,\mathrm{MHz/T}$ is the $^{29}\mathrm{Si}$ gyromagnetic ratio. The discrepancy between ω_I and the ESEEM frequencies suggests that the weak-coupling approximation is not valid.
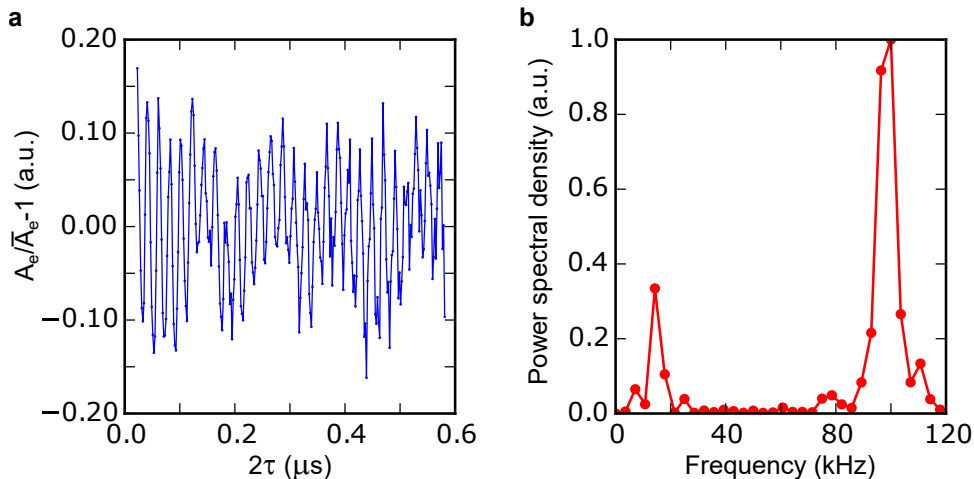

Figure 5.19: **ESEEM oscillations at 9.7 mT. a,** ESEEM oscillations normalized to the mean value and referred to zero. **b** Power spectrum of the ESEEM oscillations.

At the lower field of $3.4\,\mathrm{mT}$, the ESEEM oscillations have larger amplitude and are slower, compatibly with smaller ω_I. Moreover, the overall coherence decay is about 5 times faster than at $9.7\,\mathrm{mT}$. Even more pronouced shortening of the coherence time is observed at $2.3\,\mathrm{mT}$. At this field the signal drops by $\sim 80\%$ in $20\,\mu\mathrm{s}$ while small oscillations around this value survives for a few hundreds of microseconds. A full decay to zero in $\sim 20\,\mu\mathrm{s}$ is then recorded at the two lowest fields (we note here that the fist two transitions are highly overlapping, as seen in the spectrum in Fig.5.14a). We attribute this effective faster decoherence to the interference of several ESEEM oscillations of large amplitude. The different contributions that interfere destructively originates from all the possible configurations of the $^{29}\mathrm{Si}$ in the silicon lattice sites close to the donor. More analysis is needed for a quantitative account of this phenomenon.

5.6 Purcell limited energy relaxation

We now analyze the longitudinal relaxation of the various ESR transitions comparing it to the predicted radiative relaxation enhanced by the Purcell effect (see Sec.3.1). We measure the relaxation using the inversion recovery sequence (see inset of Fig.5.20b). A first π pulse inverts the spins bringing the population in the excited state. After a varying delay time Δt, during which the spins relax to the ground state, we detect the polarization with the Hahn-echo sequence. For a spin ensemble coupled to an effective Markovian thermal bath, the echo area A_e is expected to decay exponentially $A_e \propto (1 - 2e^{-\Gamma_1 \Delta t})$.

In Fig.5.20 we report the spin relaxation measurement performed at $62.5\,\mathrm{mT}$. Echo curves for $\Delta t \ll \Gamma_1^{-1}$ and $\Delta t \gg \Gamma_1^{-1}$ are shown in Fig.5.20a. At short Δt the phase of the echo is inverted with respect to the long Δt, as expected from the application of the first π pulse. The shape of the inverted echo is a consequence of the dependence of
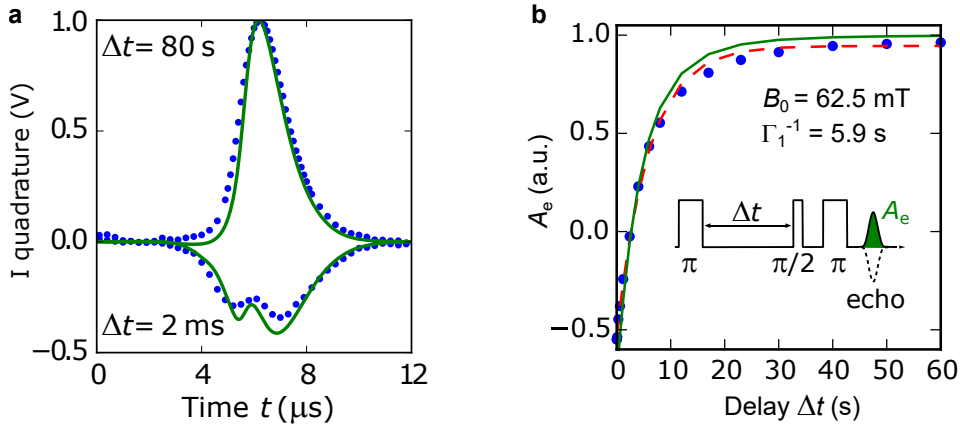
Figure 5.20: **Energy relaxation at 62.5 mT. a,** Measured (blue dots) and simulated (green line) echo signals at short and long Δt. **b** Measured (blue dots) and simulated (green line) integrated echo A_e as a function of Δt. The dashed red line is an exponential fit of time constant Γ_1^{-1}. The used inversion recovery pulse sequence is shown in the inset.

the tipping angle θ_p on the spin-cavity detuning Δ_s, as we discussed in Sec.5.3.3, and it is well reproduced by the simulation (see Fig.5.20a).

The decay of $A_e(\Delta t)$ is well fitted by an exponential decay of time constant $\Gamma_1^{-1} = 5.9\,\mathrm{s}$ (see Fig.5.20b). The data are in agreement with the simulation of the experiment that considers only radiative relaxation at rate Γ_{phot} induced by the Purcell effect. This is a strong indication that the spins are indeed in the Purcell regime $\Gamma_1^{-1} \approx \Gamma_{\mathrm{phot}} \ll \Gamma_{\mathrm{phon}}$. Using the extracted value of Γ_{phot} and the value of κ for this experimental realization (reported in Fig.5.4) in Eq.3.10, we get $\bar{g} \approx 65\,\mathrm{Hz}$, consistently with the Rabi oscillations measurement and simulation.

The result of the inversion-recovery measurement on all the 6 resonant transitions is reported in Fig5.21. We first focus on the transition at 9.7 mT, since it has almost identical properties with respect to the 62.5 mT transition. In particular it has the same matrix elements (see Table 5.1) and thus the same coupling distribution $\rho(g)$. Besides a correction due to slightly different resonator linewidth when measuring the first five transitions ($\kappa_{\mathrm{ext}} = 4.2 \times 10^6\,\mathrm{s}^{-1}$ and $\kappa_{\mathrm{int}} = 3 \times 10^5\,\mathrm{s}^{-1}$), we would expect the same decay observed at 62.5 mT. However, the relaxation shown in Fig5.21e is poorly fitted by an exponential. Moreover, contrary to the 62.5 mT case, simulations are poorly reproducing the data. We thus conclude that a competing relaxation mechanism is present at lower magnetic field impacting the echo decay. In Chapter 7 we discuss how this effect can be attributed to polarization transfer to the non-resonant bismuth donor transitions.

A qualitatively similar relaxation with the respect to the 9.7 mT measurement is observed at the first five transitions. In a time of the order of 1 s the polarization relaxes to $\sim 2/3$ of its equilibrium value while the rest of the decay happens at a much slower rate.
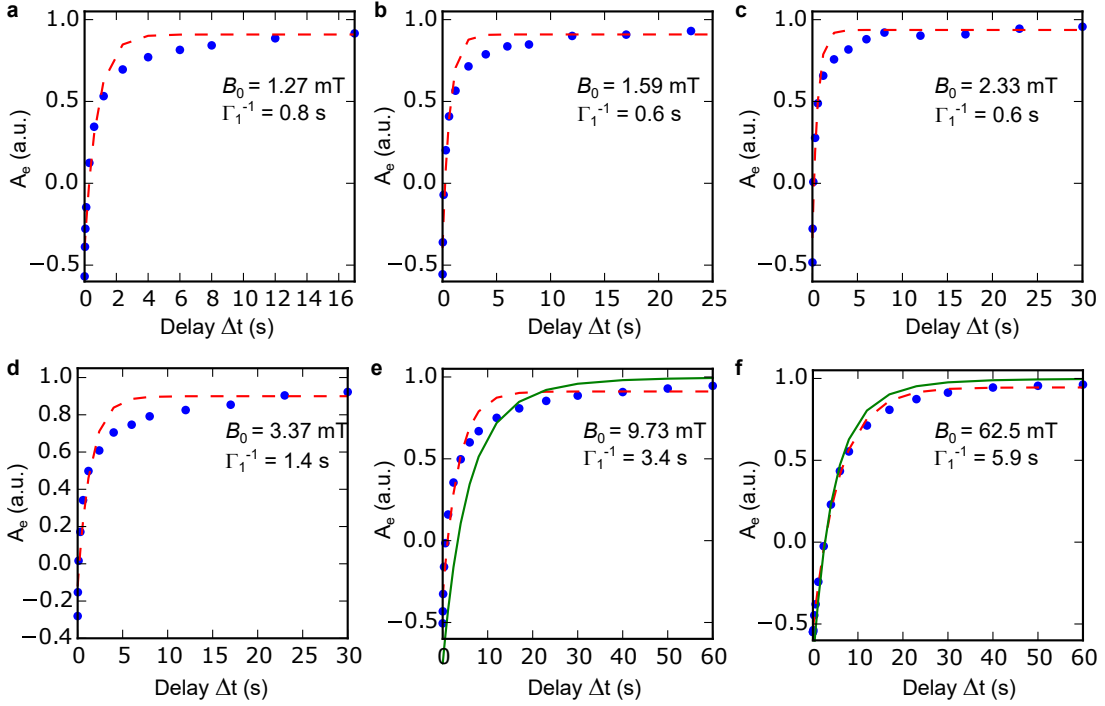
Figure 5.21: **Energy relaxation at the six resonant transitions.** Measured (blue) integrated echo A_e as a function of the waiting time Δt. Dashed red line is an exponential fit of time constant Γ_1^{-1}. The solid green line in panels **e** and **f** are simulations. The resonator parameters for measurements in panels **a-e** are: $\omega_0/2\pi = 7.4087\,\mathrm{GHz}$, $\kappa_\mathrm{ext} = 4.2 \times 10^6\,\mathrm{s}^{-1}$ and $\kappa_\mathrm{int} = 3 \times 10^5\,\mathrm{s}^{-1}$. The resonator parameters for measurements in panels **f** are $\omega_0/2\pi = 7.4078\,\mathrm{GHz}$, $\kappa_\mathrm{ext} = 3.4 \times 10^6\,\mathrm{s}^{-1}$ and $\kappa_\mathrm{int} = 3.7 \times 10^5\,\mathrm{s}^{-1}$.

5.6.1 Relaxation rate dependence on spin-cavity detuning

The integral of the echo signal is only part of the information carried by its temporal shape. The Fourier transform of each echo trace gives the contribution to the signal $A_e(\Delta)$ as a function of their detuning to the cavity Δ. The limit on the spin detuning is in our case given by the cavity filtering of the signal emitted by the spins and is then of the order of κ. By Fourier transforming the echo decay $A_e(\Delta t)$ recorded at 62.5 mT (see Fig.5.20), we thus get the spin relaxation for different detuning values within the cavity bandwidth. In Fig.5.22a we report the relaxation of two normalized Fourier components ($\Delta = 0$ and $\Delta = 0.5\kappa$), showing a relaxation rate Γ_1 slower of a factor ~ 1.5 for the detuned spins. The Γ_1 dependence on the detuning Δ is another proof that the spin relaxation is Purcell-enhanced.

In Fig.5.20b we compare $\Gamma_1(\Delta)$ obtained from the exponential fit of the Fourier components $\tilde{A}_\mathrm{e}\Delta t$ with the dependence on the detuning given by the Purcell formula Eq.3.10, revealing a discrepancy. To understand this difference $\Gamma_1(\Delta)$ is extracted from the Fourier transform of the simulated echoes, showing a good agreement with the data. The deviation from Eq.3.10 is due to the broad coupling distribution $\rho(g)$. The large-Δ components of the spin echo come from spins more strongly coupled than those contributing to the $\Delta = 0$ component. We attribute this to the tipping angle θ dependence on Δ.
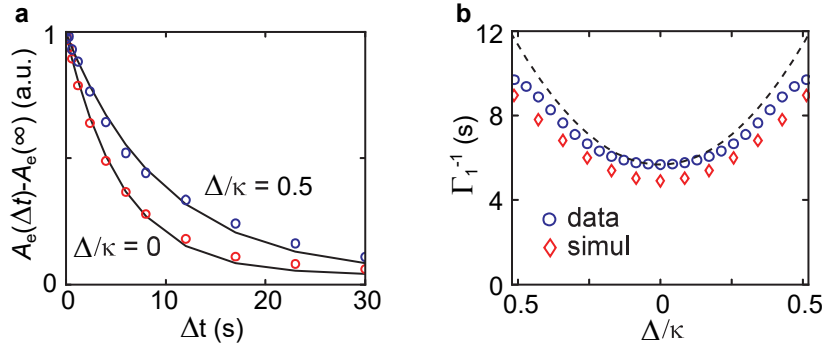
Figure 5.22: **Relaxation rate dependence on spin-cavity detuning Δ. a,** Normalized Fourier component of the echo at $\Delta = 0$ (red) and $\Delta = 0.5\kappa$ as a function of the delay time Δt of the inversion recovery sequence. The solid line is an exponential fit of time constant Γ_1^{-1}. **b** Relaxation time Γ_1^{-1} as a function of the detuning Δ for measured (blue) and simulated (red) inversion recovery. Dashed line is the expected $\Gamma_1^{-1}(\Delta)$ dependence based on the Purcell formula Eq.3.10 and on the measured Γ_1^{-1} at $\Delta = 0$.

5.6.2 Spin ensemble cooperativity

In our model of the spin dynamics in the Purcell regime we assume that the N spins coupled to the cavity radiate independently at the Purcell rate Γ_{phot}. We provide experimental evidence of the validity of this assumption by measuring the resonator losses induced by resonant spins.
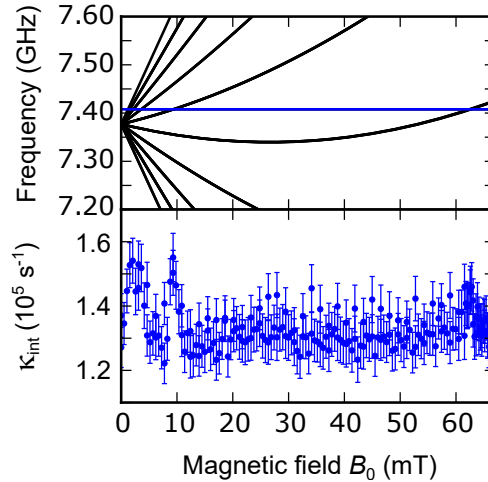
Figure 5.23: **Spin-induced resonator internal losses.** Top, bismuth donor spin transitions frequency (black) as a function of the applied field. Resonator frequency is shown in blue. Bottom, resonator internal losses κ_{int} measured at $P_{\mathrm{in}} = -120\,\mathrm{dBm}$ as a function of B_0.

The radiative properties of an ensemble of N identical spins are deeply modified by collective effects, that range from supperradiance to dark state trapping [102]. However, spin decoherence and inhomogeneous broadening can lead to suppression of any collective phenomenon, recovering the single spin dynamics [18, 103, 104]. To discriminate between the 'independent' or 'collective' radiative regime, one has to consider a

dimensionless parameter called the ensemble cooperativity and defined as:

$$C = \frac{2Ng^2}{\kappa\Gamma_{\mathrm{inh}}} \tag{5.5}$$

Independent radiation from each spin at Γ_{phon} is expected for $C \ll 1$, the so-called weak collective coupling regime.

Cooperativity can be estimated by measuring the resonator reflection. When the spins are at resonance with the cavity they cause an increase of the resonator internal losses $\Delta\kappa_{\mathrm{int}}$ that is indeed proportional to the cooperativity [105]. It can be shown that the cooperativity is given by:

$$C = \frac{\Delta\kappa_{\mathrm{int}}}{\kappa} \tag{5.6}$$

In order to determine the cooperativity we measure the resonator reflection as a function of B_0 using low input power to limit spin saturation. The result reported in Fig.5.23 shows $\Delta\kappa_{\mathrm{int}} \sim 2 \times 10^4\,\mathrm{s}^{-1}$ when the spins are resonant with the cavity. Given $\kappa = 3.5 \times 10^6\,\mathrm{s}^{-1}$ we found $C \sim 0.005$, demonstrating that spins are in the independent radiative regime as expected from the energy relaxation measurements.

Chapter 6

Radiative cooling of a spin ensemble with a cavity

6.1 Introduction

Spins in solid are generally thermalizing at rate Γ_{phon} to the lattice of temperature T_{phon} in which they are embedded. The recent demonstration of the Purcell regime for an ensemble of electron spins [5], however, showed that the coupling to the electromagnetic mode of a microwave cavity at rate Γ_{phot} can become their dominant relaxation channel. Having the electron spins predominantly coupled to cavity opens the possibility to cool them below T_{phon} by reducing the electromagnetic mode temperature T_{phot}. In the following, we demonstrate such a radiative spin cooling introducing a new universal method to increase the electron spin polarization above thermal equilibrium, what we refer to as hyperpolarization.
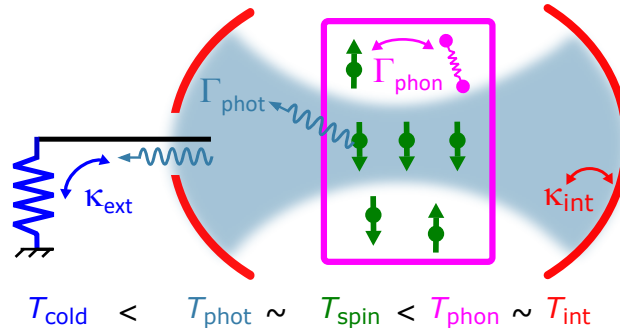
Figure 6.1: **Radiative spin cooling principle.** Spins (green) in a crystal (magenta) are coupled both to a bath of phonons at temperature T_{phon} with a rate Γ_{phon} and to a bath of microwave photons at a temperature T_{phot} with a rate Γ_{phot}, which determines their equilibrium temperature T_{spin}. The temperature of the photons T_{phot} is determined by their coupling with rate κ_{int} to the cavity internal losses at temperature T_{int} and with rate κ_{ext} to the load located at the cavity input. When this load is placed at low temperature T_{cold}, the intra-cavity field is radiatively cooled provided that $\kappa_{\mathrm{ext}} \gg \kappa_{\mathrm{int}}$ and the spins are cooled in turn if $\Gamma_{\mathrm{phot}} \gg \Gamma_{\mathrm{phon}}$.

The principle of the method is illustrated in Fig.6.1. The electromagnetic mode of a cavity is cooled by connecting the cavity input to a resistor at temperature T_{cold}, colder than the cavity internal loss bath of temperature $T_{\mathrm{int}} \approx T_{\mathrm{phon}}$. Provided that

the cavity coupling rate κ_{ext} to the cold resistor is much larger than its internal loss rate κ_{int}, $T_{\text{phot}} \approx T_{\text{cold}}$ (see Sc.2.3.5). The spins inside the cavity mode volume are in the Purcell regime $\Gamma_{\text{phot}} \gg \Gamma_{\text{phon}}$ and thus thermalize to the cold cavity mode $T_{\text{spin}} \approx T_{\text{cold}}$ (Sc.3.1.2), realizing the purpose of a spin ensemble colder than the host lattice.

6.2 Purcell regime in a hot cavity

In the previous chapter we have seen how the two quasi-degenerate electron spin transitions at $62.5\,\text{mT}$ are in the Purcell regime at $15\,\text{mK}$, relaxing to thermal equilibrium with an exponential decay of time constant $\Gamma_1^{-1} = \Gamma_{\text{phot}}^{-1} = 5.9\,\text{s}$ given by Eq.3.10. However, in the radiative cooling experiment the sample is anchored at about $1\,\text{K}$ and we therefore need to test whether the spins are still in the Purcell regime up to this temperature.

In order to verify this condition necessary for the radative cooling, in a first experiment we measure the spin relaxation to thermal equilibrium as a function of temperature. Because the JTWPA can only work at $T < 300\,\text{mK}$, we removed it from the setup.

6.2.1 Temperature dependence of the energy relaxation rate

In Sc.3.1.2 we have shown that in the presence of n_{th} thermal photons in the cavity, the spin relaxation rate in the Purcell regime is expected to be $\Gamma_1 = \Gamma_{\text{phot}}[2n_{\text{th}}(T_{\text{phot}}) + 1]$, due to absorption and stimulated emission. In the setup used for this experiment $T_{\text{phot}} = T_{\text{phon}} = T_{\text{spin}} = T$, where T is the temperature of the mixing chamber plate to which the sample is anchored and the microwave field is thermalized.
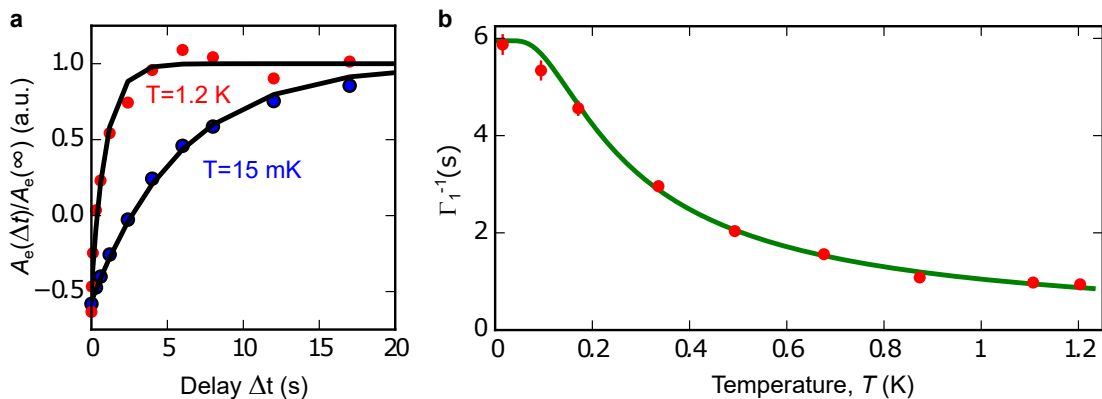
Figure 6.2: **Relaxation time dependence on temperature at 62.5 mT. a,** Measured integrated echo A_e as a function of the waiting time Δt at $T = 15\,\text{mK}$ (blue) and $T = 1.2\,\text{K}$ (red). Black lines are exponential fit of time constant Γ_1^{-1}. The data are normalized to the baseline of the corresponding fits. **b** Measured relaxation time Γ_1^{-1} (red dots) as a function of the mixing chamber temperature T. The green curve is a fit to the data between $300\,\text{mK}$ and $1.2\,\text{K}$ using the function $\Gamma_{\text{phot}}^{-1}/(2n_{\text{th}}(T) + 1)$, with $\Gamma_{\text{phot}}^{-1}$ as an adjustable parameter.

We measure the energy relaxation with the inversion recovery sequence as a function of T and an exponential fit yields $\Gamma_1(T)$, as reported in Fig.6.2. The measurement shows the agreement of the relaxation time with the expected $1/[2n_{\text{th}}(T) + 1]$ dependence,

demonstrating that the bismuth donor spins are in the Purcell regime at least up to $1\,\mathrm{K}$.

6.2.2 Temperature dependence of polarization

As the temperature is increased from $15\,\mathrm{mK}$, the thermal equilibrium polarization $p_{\mathrm{Bi}}(T)$ of the bismuth donor spins is expected to decrease. For an electron spin $1/2$ it would follow the exact same temperature dependence as the Purcell relaxation time, $p_{1/2}(T) = 1/[2n_{\mathrm{th}}(T) + 1]$. However, as we discuss in Sc.4.2.3, a slight deviation from this law is expected at temperatures lower than $300\,\mathrm{mK}$ for p_{Bi} due to the thermal occupancy of the hyperfine levels.

The observation of the calculated $p_{\mathrm{Bi}}(T)$ is slightly complicated by the existence of non-equilibrium processes, as evidenced below. We first measure the polarization's temperature dependence of the quasi-degenerate transitions $|4, 0\rangle \leftrightarrow |5, -1\rangle$ and $|4, -1\rangle \leftrightarrow |5, 0\rangle$ at $B_0 = 62.5\,\mathrm{mT}$. We wait several hours at each temperature value before measuring the echo amplitude A_{e} with a repetition time $t_{\mathrm{rep}} = 120\,\mathrm{s} \gg \Gamma_1^{-1}$. The result reported in Fig.6.3a (red dots) shows a significant deviation below $200\,\mathrm{mK}$ from the calculated $p_{\mathrm{Bi}}(T)$ (red line).

In Fig.6.3b we report the same experiment but performed at $9.3\,\mathrm{mT}$, measuring the polarization of transitions $|4, 1\rangle \leftrightarrow |5, -1\rangle$ and $|4, -1\rangle \leftrightarrow |5, 0\rangle$. In this case the measured polarization follows the calculated $p_{\mathrm{Bi}}(T)$ for these two transitions at temperatures as low as $\sim 100\,\mathrm{mK}$.

We then repeat the polarization measurement for the transitions $|4, 0\rangle \leftrightarrow |5, -1\rangle$ and $|4, -1\rangle \leftrightarrow |5, 0\rangle$ using a different protocol. At each temperature we first set $B_0 = 9.3\,\mathrm{mT}$ for $20\,\mathrm{min}$, then set back $B_0 = 62.5\,\mathrm{mT}$, wait $4\,\mathrm{min}$ and finally measure A_{e}. The so obtained result is reported in Fig.6.3a (black dots) and shows agreement with the $p_{\mathrm{Bi}}(T)$ calculated for the considered transitions as if it was measured at $9.3\,\mathrm{mT}$.

The above results lead us to the following conclusions. At $9.3\,\mathrm{mT}$, the spin system is well thermalized to the cryostat from the highest temperature down to at least $\sim 100\,\mathrm{mK}$, as evidenced by the measurement of the two couples of transitions at this field (black dots in the two panels of Fig.6.3). At $62.5\,\mathrm{mT}$ an unknown process dominates over the thermalization dynamics at temperature lower than $200\,\mathrm{mK}$ and drives the spins toward a non-thermal state (red dots in Fig.6.3a). A possible origin of this phenomenon could be residual infrared radiation reaching the sample. We have indeed seen in Sc.4.5 how this can cause redistribution of population in the bismuth hyperfine levels.

In a fourth measurement we investigate the dynamics of the depolarization process taking place at $62.5\,\mathrm{mT}$. At $T = 83\,\mathrm{mK}$ we first set $B_0 = 9.3\,\mathrm{mT}$ during $20\,\mathrm{min}$, then we set $B_0 = 62.5\,\mathrm{mT}$ and immediately after we record continuously A_{e} as a function of time. The result reported in the inset of Fig.6.3a shows the spins reaching the equilibrium non-thermal state in the time-scale of hours, orders of magnitude longer than the $4\,\mathrm{min}$ waiting time used to detect the thermal equilibrium polarization after the field sweep from $9.3\,\mathrm{mT}$ to $62.5\,\mathrm{mT}$. This long timescale is consistent with our hypothesis that the non-equilibrium processes observed affect the hyperfine level manifold occupation probabilities, and not so much the EPR transition itself.
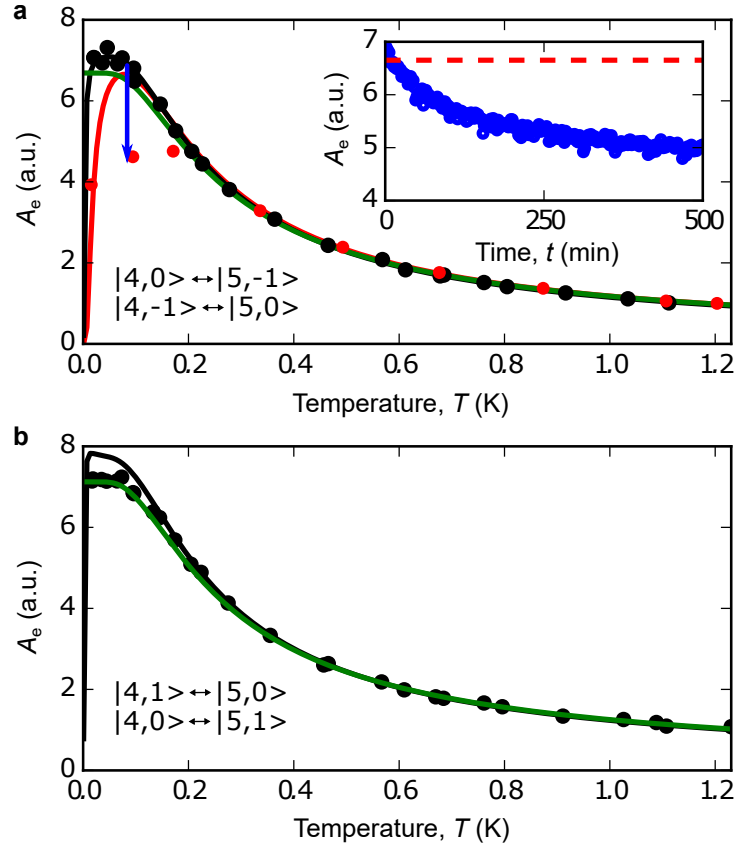
Figure 6.3: **Polarization dependence on temperature. a,** Transitions $|4,0\rangle \leftrightarrow$ $|5,-1\rangle$ and $|4,-1\rangle \leftrightarrow |5,0\rangle$. Equilibrium polarization measured at $62.5\,\mathrm{mT}$ (red dots). Several hours are waited at each temperature before recording A_e. The red line is the calculated $p_{\mathrm{Bi}}(T)$ for the considered transitions at $62.5\,\mathrm{mT}$. A second polarization measurement of the same transition is reported (black dots). In this second experiment, for each temperature value, B_0 is first set to $9.3\,\mathrm{mT}$ during $20\,\mathrm{min}$, then it is set to $62.5\,\mathrm{mT}$ and finally after $4\,\mathrm{min}$ A_e is recorded. The black line is the calculated $p_{\mathrm{Bi}}(T)$ for the same transitions at $9.3\,\mathrm{mT}$. The polarization $p_{1/2}(T) = 1/(2n_{\mathrm{th}}(T) + 1)$ of a spin $1/2$ is also shown for comparison (green). A_e as a function of time is measured at $T = 83\,mK$ and $B_0 = 62.5$ after B_0 has been set to $9.3\,\mathrm{mT}$ for $20\,\mathrm{min}$. The same data are represented in the main plot with a blue arrow. **b,** Transitions $|4,1\rangle \leftrightarrow |5,0\rangle$ and $|4,0\rangle \leftrightarrow |5,1\rangle$. Equilibrium polarization measured at $9.3\,\mathrm{mT}$ (black dots). The black line is the calculated $p_{\mathrm{Bi}}(T)$ for the considered transitions at $9.3\,\mathrm{mT}$. The $p_{1/2}(T)$ is also shown for comparison (green).
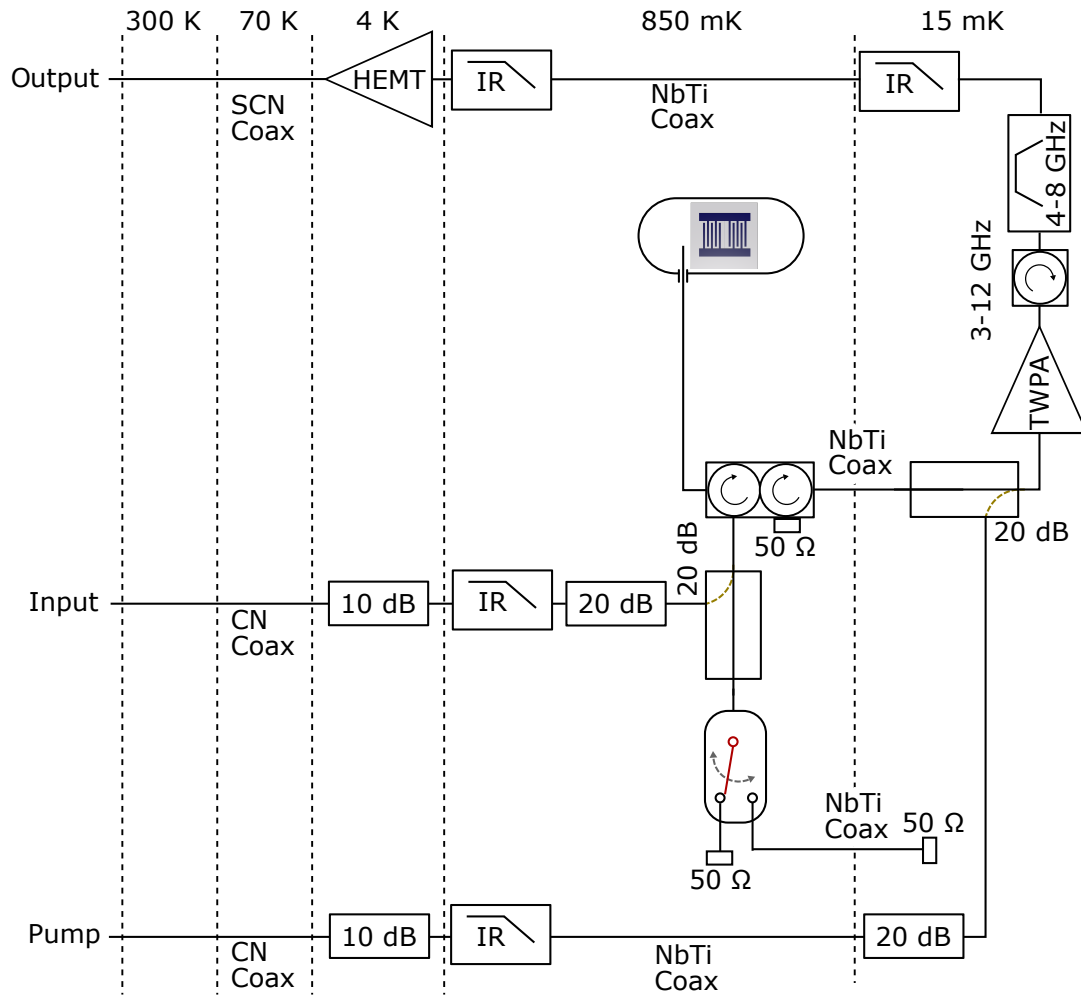
Figure 6.4: **Radiative cooling setup.** The sample is mounted at the still plate of the cryostat. The cavity port is connected to a circulator separating the resonator input and output modes. An electromechanical switch connects the input either to a *hot* or a *cold* 50 Ω impedance-matched load. Control microwave pulses are sent to the input via a 20 dB coupler. The output signal is amplified by first by the JTWPA at 15 mK and then by the HEMT at 4 K.

6.3   Radiative cooling setup

For demonstrating the electron spin radiative cooling we modify the setup described in the last chapter as follows (see Fig.6.4). The sample is now mounted at the still plate of the cryostat, at a temperature $T_{\text{phon}} = 850\,\text{mK}$. The cavity port is connected via an antenna to a circulator, separating input and output modes. The resonator input is connected via an electromechanical switch either to a $50\,\Omega$ resistor thermalized at the same temperature T_{phon} of the sample (*hot* configuration) or to a $50\,\Omega$ resistor thermalized at the mixing chamber plate of the cryostat, at a temperature $T_{\text{cold}} = 15\,\text{mK}$ (*cold* configuration). The $50\,\Omega$ load at T_{cold} is connected to the switch sitting at T_{phon} via a NbTi superconducting cable that is thermally insulating and whose MW losses are of the order of $0.1\,\text{dB}$. The control microwave pulses are now sent via a $20\,\text{dB}$ coupler in order to minimize the thermal noise reaching the cavity from the pulse input line. This ensures that the temperature of the microwave radiation field incident onto the resonator, and therefore the mode temperature T_{phot}, is dominantly determined by the switch setting.

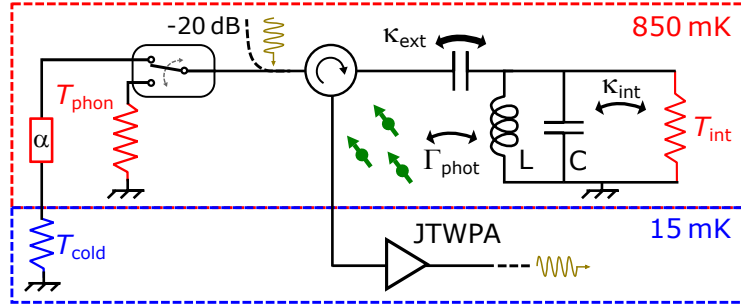### 6.3.1   Equivalent electrical circuit

Figure 6.5:   **Simplified equivalent electrical circuit.** The LC resonator and the spins are thermally anchored at $T_{\text{phon}} = 850\,\text{mK}$ and are coupled with rate Γ_{phot}. The resonator is then coupled with rate κ_{int} to the internal loss bath of temperature T_{int} and with rate κ_{ext} either to a *hot* or a *cold* $50\,\Omega$ thermal source. The signal emitted or reflected by the resonator is routed by the circulator to the output line.

The equivalent electrical circuit that we use to estimate the equilibrium temperatures T_{phot} of the cavity mode and T_{spin} of the spins is shown in Fig.6.5. The resonator is coupled with rate κ_{int} to the internal losses bath of temperature T_{int} and with rate κ_{ext} to the incoming microwave radiation on the input. The switch connects the input to a resistor thermalized either at T_{phon} or at T_{cold}. Losses in between the circulator and the cold $50\,\Omega$ are modeled by an attenuator at T_{phon}, absorbing a fraction α of the photons. Such a model is an over-simplification since a fraction of the losses necessarily takes place at an intermediate temperature in between T_{phon} and T_{cold}. However, its physical justification originates from the fact that only the superconducting cable is in between the two temperatures. With our model we are thus assuming that all the temperature drop happens across the cable and that its microwave losses are negligible.

Cooling factor

To infer $T_{\text{spin}}^{\text{hot,cold}}$ in the two switch configurations, we measure the echo amplitude A_{e}, proportional in the spin $1/2$ approximation to the temperature-dependent polarization $p(T_{\text{spin}}^{\text{hot,cold}}) = 1/[2n_{\text{th}}(T_{\text{spin}}^{\text{hot,cold}}) + 1]$. We thus define the spin radiative cooling factor η as the ratio of the polarization in the *cold* and *hot* setting, $\eta \equiv p^{\text{cold}}/p^{\text{hot}}$. From Eq.3.25, η coincides then with the ratio of spin relaxation times in the two switch configurations $\Gamma_1^{\text{hot}}/\Gamma_1^{\text{cold}}$:

$$\eta \equiv p^{\text{cold}}/p^{\text{hot}} = \frac{\Gamma_{\text{phot}}[2n_{\text{th}}(T_{\text{phot}}^{\text{hot}}) + 1] + \Gamma_{\text{phon}}[2n_{\text{th}}(T_{\text{phon}}) + 1]}{\Gamma_{\text{phot}}[2n_{\text{th}}(T_{\text{phot}}^{\text{cold}}) + 1] + \Gamma_{\text{phon}}[2n_{\text{th}}(T_{\text{phon}}) + 1]}. \tag{6.1}$$

Since we have demonstrated that spins are in the Purcell regime, Eq.6.1 for our experiment simplifies to:

$$\eta = \frac{2n_{\text{th}}(T_{\text{phot}}^{\text{hot}}) + 1}{2n_{\text{th}}(T_{\text{phot}}^{\text{cold}}) + 1}. \tag{6.2}$$

6.4 Cavity mode temperature

In a first series of experiments, we perform noise measurements to directly determine the temperature T_{phot} in the two switch configurations.

6.4.1 Internal loss temperature

As a first test, we measure the resonator reflection coefficient with switch in cold and hot configurations. No difference is expected, since the resonator physical properties are entirely unchanged by the switch setting. The results are shown in Fig.6.6. At high power, we find that the reflection coefficients are indeed identical, which confirms that the switch setting has no measurable influence on the impedance seen by the resonator. However, at low powers, we observe a sizeable difference: the internal loss rate κ_{int} is more than 30% higher in the *cold* configuration.

We interpret this surprising result as an evidence for radiative cooling of the two-level systems (TLS) that are known to play an important role in superconducting resonator losses. In the *hot* configuration, such TLS are highly saturated and absorb little energy from the resonator. On the contrary, in the *cold* configuration TLS are radiatively cooled, increasing their degree of polarization and thus making them more absorptive. In agreement with this hypothesis, the measurement of κ_{int} as a function of the input power P_{in} shows that this effect decreases for larger intra-cavity photon number $\bar{n}(P_{\text{in}})$, disappearing for $\bar{n} \approx 10$ where TLS are highly saturated in both switch states. We will then consider T_{int} to be in-between T_{phon} and T_{phot}, and will treat it as an adjustable parameter to obtain the best fit to our final data.

6.4.2 JTWPA gain and added noise

We estimate the JTWPA added noise by setting the switch in the *hot* configuration and measuring the noise power S^{hot} at the output as a function of the still temperature T_{phot}. Far from resonance, the noise at the input of the JTWPA is the thermal radiation
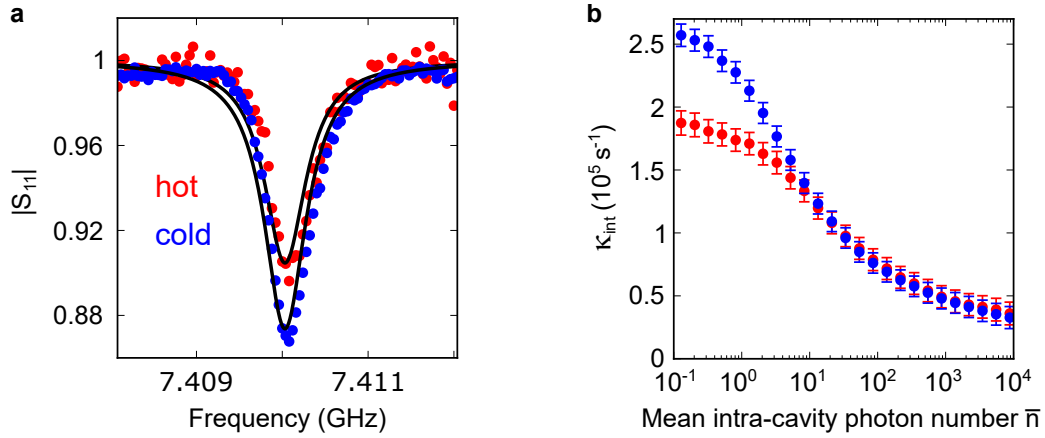
Figure 6.6: **Resonator internal losses in the two switch configurations. a,** Magnitude of S_{11} at $\bar{n} \approx 0.1$ for the *hot* (red) and *cold* (blue) configurations. Black lines are fit with Eq.2.31. **b** κ_{int} obtained from the fit of S_{11} as a function of the $\bar{n}(P_{\text{in}})$ for the two switch configurations.

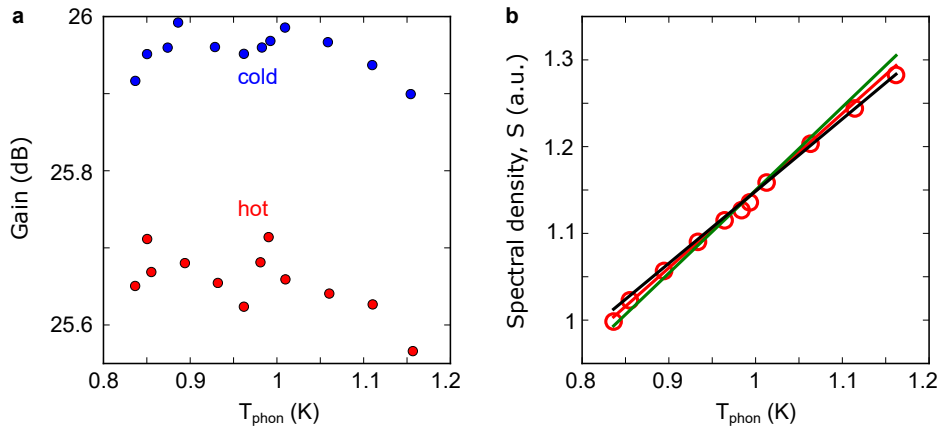Figure 6.7: **TWPA gain and added noise. a,** TWPA gain for the *cold* (blue) and *hot* (red) switch state as a function of the still plate temperature T_{phon}. **b** Noise power spectral density S measured 2.7 MHz detuned from the resonator (red triangles). Solid lines are fit to the data with S^{hot} for $S_{\text{JTWPA}} = 1$ (black), $S_{\text{JTWPA}} = 0.75$ (red) and $S_{\text{JTWPA}} = 0.5$ (green).

$n_{\text{th}}(T_{\text{phon}})$ of the *hot* 50Ω resistor that is reflected at the resonator input and routed by the circulator toward the JTWPA. The output noise power spectral density at the end of the amplification chain of gain G is then:

$$S^{\text{hot}}(T_{\text{phon}})/G = n_{\text{th}}(T_{\text{phon}}) + 1/2 + S_{\text{JTWPA}}. \quad (6.3)$$

We measure $S^{\text{hot}}(T_{\text{phon}})$ at $(\omega_0 - \omega)/2\pi = 2.7\,\text{MHz}$ for T_{phon} ranging from $840\,\text{mK}$ to $1.15\,\text{K}$ (see Fig.6.7b). Fitting the result with Eq.6.3 we extract $S_{\text{JTWPA}} = 0.75 \pm 0.25$, indicating that the JTWPA operates close to the quantum limit $S_{\text{JTWPA}} = 1/2$. In the same temperature range we measure the JTWPA gain in the two switch configurations (see Fig.6.7b). The T_{phon} dependence of the gain is negligible, however a $0.3\,\text{dB}$ larger gain is observed in the cold configuration.

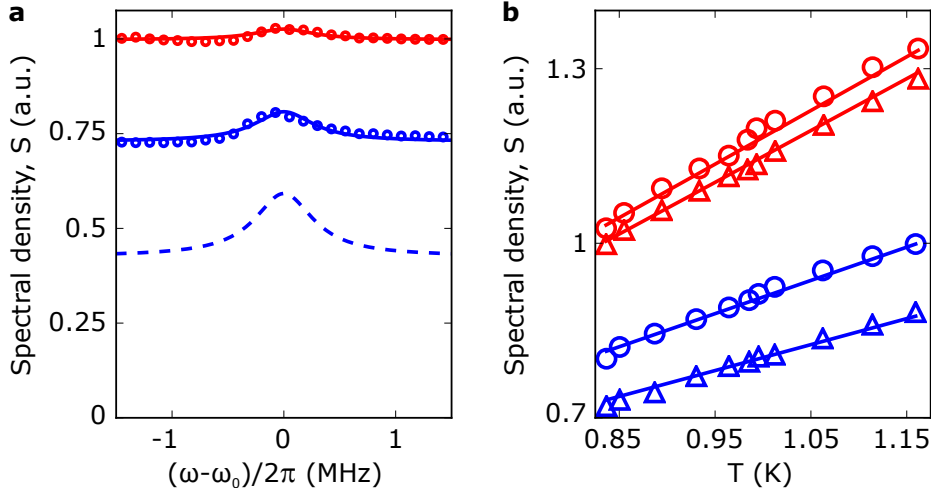Figure 6.8: **Noise power spectral density measurement. a** Frequency dependence of the noise power spectral density S measured at $T_{\text{phon}}=840\,\text{mK}$ for the *hot* (red circles) and *cold* (blue circles) switch configurations. Solid lines are fit with $S^{\text{hot}}(\omega)$ (solid red) and $S^{\text{cold}}(\omega)$ (solid blue). The blue dashed line indicates the expected $S^{\text{cold}}(\omega)$ for $\alpha=0$. **b**, Still temperature T_{phon} dependence of S measured at $\omega = \omega_0$ (open circles) and at $\omega - \omega_0 = -2.7\,\text{MHz}$ (open triangles) for both *hot* (red) and *cold* (blue) configurations. Solid lines are plot of S^{hot} (red) and S^{cold} (blue) with parameters obtained from the frequency dependence fits performed at all T_{phon}, and with $S_{\text{JTWPA}} = 0.75$.

6.4.3 Cavity mode temperature estimate

As detailed in Sc.2.3.5, by measusuring the output noise across the cavity resonance we can extract T_{phot} in the two switch states. From Eqs.2.35-2.37 and Eq.2.42 we get:

$$S^{\text{hot}}(\omega, T_{\text{phon}})/G = |S_{11}(\omega)|^2 \, n_{\text{th}}(T_{\text{phon}}) + (1 - |S_{11}(\omega)|^2)n_{\text{th}}(T_{\text{int}}^{hot}) + 1/2 + S_{\text{JTWPA}}$$
$$S^{\text{cold}}(\omega, T_{\text{phon}})/G = \alpha \, |S_{11}(\omega)|^2 \, n_{\text{th}}(T_{\text{phon}}) + (1 - |S_{11}(\omega)|^2)n_{\text{th}}(T_{\text{int}}^{cold}) + 1/2 + S_{\text{JTWPA}}.$$
$$(6.4)$$
$$(6.5)$$

where $|S_{11}(\omega)|$ is the measured resonator reflection function. Fig.6.8a shows the measured $S^{\text{hot,cold}}$ at $T_{\text{phon}} = 840\,\text{mK}$, all normalized to the value of S^{hot} at large detuning.

The measured $S^{\mathrm{hot}}(\omega)$ shows a small peak at resonance, indicating that T^{hot}_{int} is slightly higher than the *hot* $50\,\Omega$ resistor, possibly due to poor sample thermalization. The fit of $S^{\mathrm{hot}}(\omega)$ gives $T^{hot}_{\mathrm{int}} = 910\,\mathrm{mK}$. Conversely, by then fitting the measured $S^{\mathrm{cold}}(\omega)$ we extract $T^{cold}_{\mathrm{int}} = 770\,\mathrm{mK}$, in agreement with the resonator reflection measurement suggesting the radiative cooling of the internal losses when connecting to the *cold* load. The second parameter obtained from the fit of $S^{\mathrm{cold}}(\omega)$ is the parasitic losses $\alpha = 0.47 \pm 0.1$. The extracted parameters allow then to calculate the cavity thermal photon population $n_{\mathrm{th}}(T^{\mathrm{hot,cold}}_{\mathrm{phot}})$. From Eq.2.38 we get for the two switch configurations:

$$n_{\mathrm{th}}(T^{\mathrm{hot}}_{\mathrm{phot}}) = \frac{\kappa_{\mathrm{ext}}}{\kappa} n_{\mathrm{th}}(T_{\mathrm{phon}}) + \frac{\kappa_{\mathrm{int}}}{\kappa} n_{\mathrm{th}}(T^{\mathrm{hot}}_{\mathrm{int}}) \tag{6.6}$$

$$n_{\mathrm{th}}(T^{\mathrm{cold}}_{\mathrm{phot}}) = \alpha \frac{\kappa_{\mathrm{ext}}}{\kappa} n_{\mathrm{th}}(T_{\mathrm{phon}}) + \frac{\kappa_{\mathrm{int}}}{\kappa} n_{\mathrm{th}}(T^{\mathrm{cold}}_{\mathrm{int}}). \tag{6.7}$$

Using the parameters obtained from the noise measurements in Eqs.6.6-6.7 we find $T^{\mathrm{hot}}_{\mathrm{phot}} = 850\,\mathrm{mK}$ and $T^{\mathrm{cold}}_{\mathrm{phot}} = 500 \pm 60\,\mathrm{mK}$, which, according to Eq.6.2 corresponds to a spin cooling factor $\eta = 1.65 \pm 0.2$. The measurement of S thus proves that the cavity microwave mode is indeed cooled radiatively, but that this cooling is only partial due to the presence of the microwave losses α in between the load at T_{cold} and the sample at T_{phon}.

We finally repeat the measurement of $S^{\mathrm{hot,cold}}(\omega)$ for T_{phon} in the range $840\,\mathrm{mK}$-$1.15\,\mathrm{K}$. In Fig.6.8b we compare it with the temperature dependence that we calculate using the fit results obtained at $T_{\mathrm{phon}} = 840\,\mathrm{mK}$. The agreement between the data and the calculation validates our model.

Similar demonstration of radiative cooling of a resonator has been recently shown in two works by Xu et al. [106] and Wang et al. [107]. In their experiment the superconducting resonator is mounted at $1\,\mathrm{K}$ and radiatively linked to a cold source noise at about $70\,\mathrm{mK}$ with $\kappa_{\mathrm{int}}/\kappa \sim 0.3$. By measuring the resonator output noise they extract $T_{\mathrm{phot}} \sim 450\,\mathrm{mK}$.

6.5   Spin radiative cooling

6.5.1   Demonstration at 62.5 mT

The first evidence of the bismuth donor spin radiative cooling is the echo signal enhancement. Hahn-echoes are measured for the two switch settings, under the exact same conditions (puse amplitude and repetition time). Fig.6.9 shows that echo amplitude is more than doubled when the switch is connected to the *cold* load, demonstrating radiative spin hyperpolarization with $\eta = 2.3$.

The radiative nature of the effect is confirmed by the energy relaxation time measured with the inversion recovery sequence for the two switch states. As reported in Fig.6.9, we indeed observe the decrease of the Purcell relaxation rate in the *cold* configuration, and find $\Gamma^{\mathrm{hot}}_1/\Gamma^{\mathrm{cold}}_1 = \eta$, as expected. Note that in this experiment $\kappa_{\mathrm{ext}} = 4.8 \times 10^6\,\mathrm{s}^{-1}$, 1.4 times larger than its value in the measurement of the relaxation rate temperature dependence. The measured Purcell rate are consistently 1.4 times larger here with respect to the value reported in Fig.6.2.

From the cooling factor $\eta = 2.3 \pm 0.1$, we obtain that the spin temperature is cooled from $T^{\mathrm{hot}}_{\mathrm{spin}} = 850\,\mathrm{mK}$ to $T^{\mathrm{cold}}_{\mathrm{spin}} = 350 \pm 10\,\mathrm{mK}$. This value is slightly lower than the measured cavity mode temperature $T^{\mathrm{cold}}_{\mathrm{phot}} = 500 \pm 60\,\mathrm{mK}$. Given the possibly oversimplified model
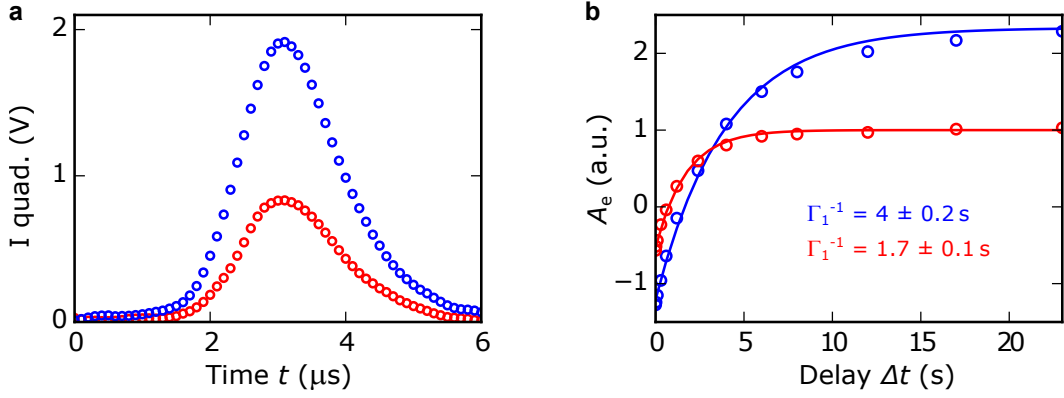
Figure 6.9: **Radiative cooling demonstration at 62.5 mT. a,** Measured spin-echo signal showing a $\eta = 2.3$ increase in amplitude in the *cold* configuration (blue). **b** Measurements (open circles) and exponential fits (solid lines) with time constant Γ_1^{-1} of the integrated echo area A_e as a function of the waiting time Δt of the inversion recovery pulse sequence.

used to extract $T_{\text{phot}}^{\text{cold}}$, the agreement between the two measurements confirms that the value of η is limited by the efficiency with which we cool the cavity mode, thus ultimately by the microwave losses α, and not by the competition with non-radiative relaxation. We get from $T_{\text{spin}}^{\text{cold}} = 350 \pm 10$ mK the more accurate estimate $\alpha = 0.23 \pm 0.03$, corresponding to 1.15 ± 0.15 dB. This is a plausible value for the combined effect of circulator insertion losses, directional coupler contribution and possible spurious reflections due to impedance mismatch in the line.
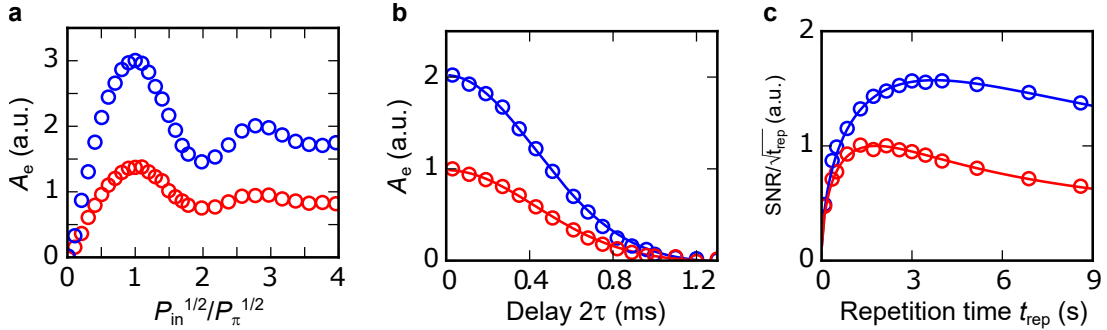

Figure 6.10: **Rabi oscillations, coherence time and SNR improvement with cooling. a,** Rabi oscillations measured for the two switch settings. **b,** Measured (circles) and Gaussian fit (solid line) of the echo are A_e decay as a function of the waiting time τ in the Hahn-echo sequence, yielding $T_2 = 600\,\mu$s in both switch configurations. **c,** Measured (open circles) signal-to-noise ratio SNR, obtained by dividing the mean value of 500 echo samples by their standard deviation, as a function of the repetition time t_{rep} (see pulse sequence on top), for both switch configurations. Solid lines are fit with $p(1 - e^{-\Gamma_1 t_{\text{rep}}})/(\bar{\sigma}\sqrt{t_{\text{rep}}})$, where $\bar{\sigma}$ is the mean of all the σ_e and p is the equilibrium polarization, yielding $\eta = \Gamma_1^{\text{hot}}/\Gamma_1^{\text{cold}} = p^{\text{cold}}/p^{\text{hot}} = 2.1$.

The Rabi oscillations reported in Fig.6.10a shows that the rotation angle induced by the drive pulses is not affected by the switch state and the same cooling efficiency is recorded at all input powers. We verify that the increase in echo amplitude is not due to a change in coherence time by measuring T_2 in the two switch states. Fig.6.10b

shows that the same $T_2 = 600\,\mu$s is recorded in the two cases.

The sensitivity enhancement obtained by radiative spin hyperpolarization does not scale like η as in other hyperpolarization schemes such as DNP but only as $\sqrt{\eta}$, because the optimal waiting time t_{rep} between subsequent experimental sequences is of order Γ_1^{-1} and thus scale as η. We demonstrate this by measuring the mean value and standard deviation of A_e for 500 echo traces as a function of the repetition time t_{rep} (see Fig. 6.10c). The highest sensitivity is obtained for $t_{\mathrm{rep}} \simeq 1.25[\Gamma_1^{\mathrm{cold,hot}}]^{-1}$, both in the cold and the hot load cases. It is 1.6 times larger in the *cold* than in the *hot* configuration, slightly larger than $\sqrt{\eta} = 1.52$ because switching to the cold load also substantially reduces the effective noise temperature of our detection chain: the echo standard deviation is smaller by 7%, consistently with the noise power measurement of Fig 6.8.

6.5.2   Radiative cooling at lower field

We now consider radiative cooling of the other bismuth donor spin transitions. As seen in the spectrum reported in Fig.6.11, we measure larger echo amplitude in the *cold* load case at all the six resonant transitions. The signal enhancement in between 1.5 and 1.75 is to be attributed to $t_{\mathrm{rep}} = 5\,$s, short compared to the average spin relaxation time. Despite the fact that at lower field another relaxation mechanism is acting in addition to Purcell (see Sc.5.21), radiative relaxation is still effective.
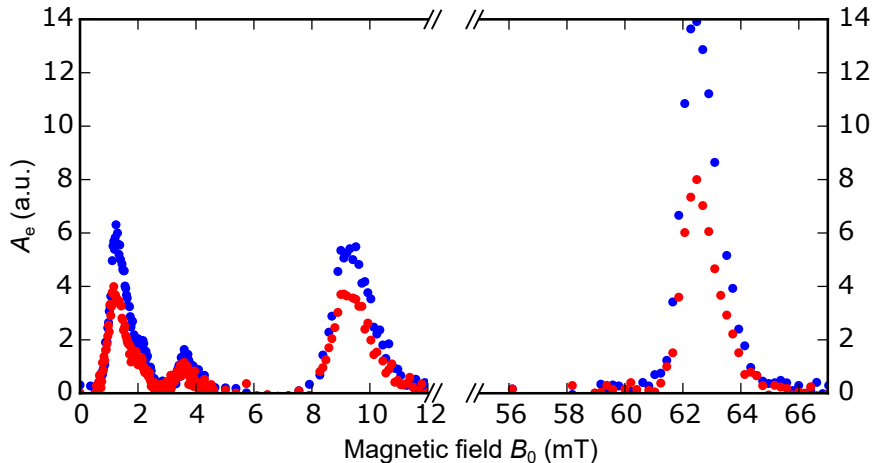

Figure 6.11: **Radiative cooling the first six ESR lines.** Measured echo area A_e as a function of the applied magnetic field for the *cold* (blue) and *hot* (red) switch configurations, with $t_{\mathrm{rep}} = 5\,s.$.

We then measure the spin relaxation for the two switch configurations at $9.3\,$mT (see Fig.6.12). The baseline, corresponding the echo amplitude at equilibrium, increases by a factor $\eta = 2$ in the *cold* load case. Even if the exponential fit is poor (see Chapter 5, Sc.5.6), the extracted relaxation rates satisfy $\Gamma_1^{\mathrm{hot}}/\Gamma_1^{\mathrm{cold}} = \eta$. It thus seems that radiative relaxation works even when the competing relaxation mechanism discussed in Chapter 5 plays a role. We defer to Chapter 7 a qualitative explanation of this observation.
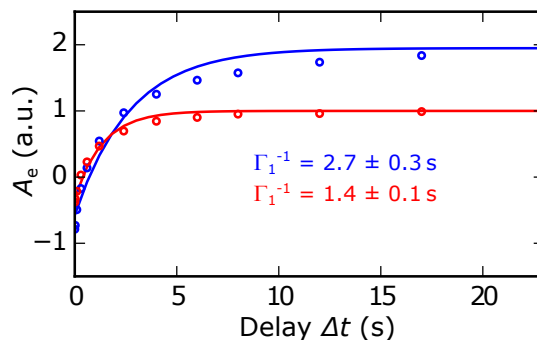
Figure 6.12: **Radiative relaxation and cooling at 9.3 mT.** Measurements (open circles) and exponential fits (solid lines) with time constant Γ_1^{-1} of the integrated echo area A_e as a function of the waiting time Δt of the inversion recovery pulse sequence.

6.6 Controlling the cooling with a tunable spin relaxation channel

We now study how the radiative hyperpolarization works when spins are coupled to a second bath of temperature T_{IR} by a relaxation mechanism of rate Γ_{IR}. We introduce this second relaxation channel by applying infrared illumination (IR) to the sample with a 950 nm light emitting diode (LED), known to reduce the spin relaxation time of donors [30] (see Sc.4.5).

6.6.1 Superconducting resonator response under IR illumination

The LED illumination has two effects on the sample: it generates quasi-particles in the superconductor and, since it is slightly above the silicon energy gap, conduction electrons in the substrate. These two phenomena increase the resonator losses and affect its resonance frequency. Quasi particles increase the microwave Ohmic losses of the superconductor and its kinetic inductance, thus decreasing the resonance frequency [108]. On the other hand, the photo-generated conduction electrons increase the energy dissipation in the substrate, and decrease the capacitance leading to an increase of the resonance frequency [109]

We characterize the resonator parameters dependence on the IR light intensity by measuring the resonator reflection S_{11} as a function of the LED drive current I. Fig.6.13a shows that the resonator internal loss rate κ_{int} increases by one order of magnitude when I reaches $100\mu A$, bringing the resonator close to the critical coupling regime. This effect is expected to contribute to the reduction of η by both affecting Γ_{phot} and $\bar{n}(T_{phot}^{cold})$ (see Fig.6.14b). The resonance frequency increases by $\sim 1\,MHz$ in the same range of I (Fig.6.13b). This resonance frequency increment indicates that the dominant origin of the resonator microwave losses is probably the photo-excited silicon conduction electrons.

6.6.2 Suppression of radiative cooling

We then measure the spin relaxation in the *hot* configuration $\Gamma_1^{hot}(I)$ and from this we extract $\Gamma_{IR}(I)$ (see Fig.6.14a). Neglecting Γ_{phon}, the introduction of $\Gamma_{IR}(I)$ modifies Eq.6.1 for the cooling factor η as follows:
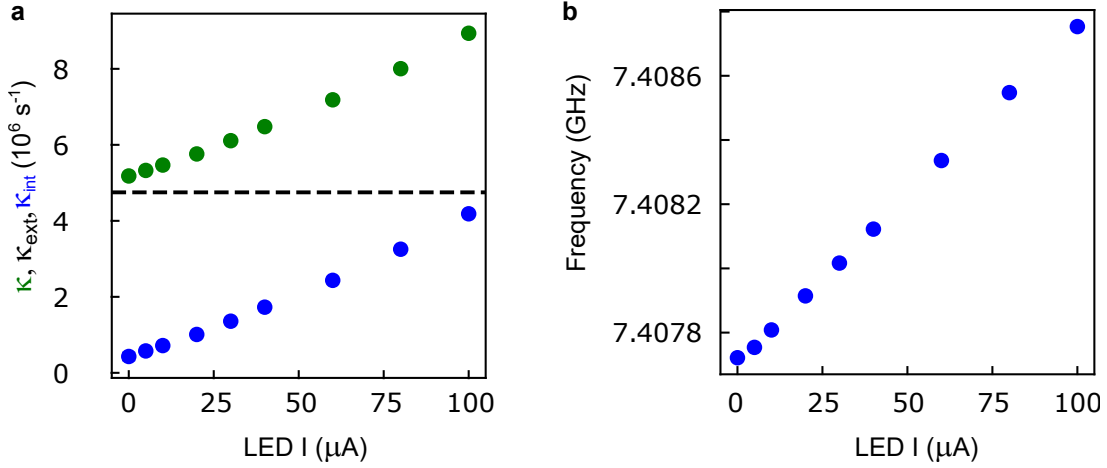
Figure 6.13: **Effect of LED illumination on the resonator. a** Extracted κ, κ_{int} and κ_{ext} from the fit of the measured resonator reflection S_{11} as a function of I. **b** Extracted resonator frequency ω_0 from the S_{11} measurement.

$$\eta(I) = \frac{\Gamma_{\text{IR}}(I) + \Gamma_{\text{phot}}(2\bar{n}(T_{\text{phot}}^{\text{hot}}) + 1)}{\Gamma_{\text{IR}}(I) + \Gamma_{\text{phot}}(2\bar{n}(T_{\text{phot}}^{\text{cold}}) + 1)}, \tag{6.8}$$

where Γ_{phot} and $T_{\text{phot}}^{\text{cold}}$ are indirectly dependent on the current I via the resonator $\kappa_{\text{int}}(I)$. The measurement of $\kappa_{\text{int}}(I)$ and $\Gamma_{\text{IR}}(I)$ then allows to estimate with Eq.6.8 the expected $\eta(I)$ and the relative contributions of the resonator internal losses and of the light-induced relaxation (see Fig.6.14b).

Finally, we measure the cooling efficiency $\eta(I)$ by recording the echo amplitude as a function of I in the two switch states. The $\eta(I)$ dependence predicted by our model agrees semi-quantitatively with the data. The ratio of relaxation rates $\Gamma_1^{hot}/\Gamma_1^{cold}$ also closely follows the measured $\eta(I)$, as expected.

6.6.3   Polarization dependence on IR illumination

In addition to changes in the spin relaxation rate, we also observe that the echo amplitude is reduced upon optical illumination (see Fig.6.15, magenta curve). This reduction is in part due to the changes of the resonator properties. The increased resonator losses lead to a reduced pulse amplitude inside the resonator and to a larger fraction of the spin-echo signal dissipated rather than emitted into the output line. Both effects thus yield a smaller echo amplitude for larger κ_{int}. Simulation provides an easy estimate of expected echo reduction. The red curve in Fig.6.15 shows the measured A_{I} normalized by the simulated decay, demonstrating that the increased resonator losses do not explain the observed echo amplitude reduction.

As a tentative to account for the observations, we model the relaxation mechanism induced by the IR light as driving the spin toward the equilibrium spin polarization of the photo-generated carriers. The physical interpretation is the following. The absorption of the above-gap light by the silicon generates conduction electrons whose spin has a low polarization $p_{\text{el}} \approx 0.05$ at $62.5\,\text{mT}$ and $850\,\text{mK}$. We then assume that that the donors are ionized at rate Γ_{IR} under illumination. Following the ionization, donors recapture a conduction electron on a much faster timescale, leading to an effective
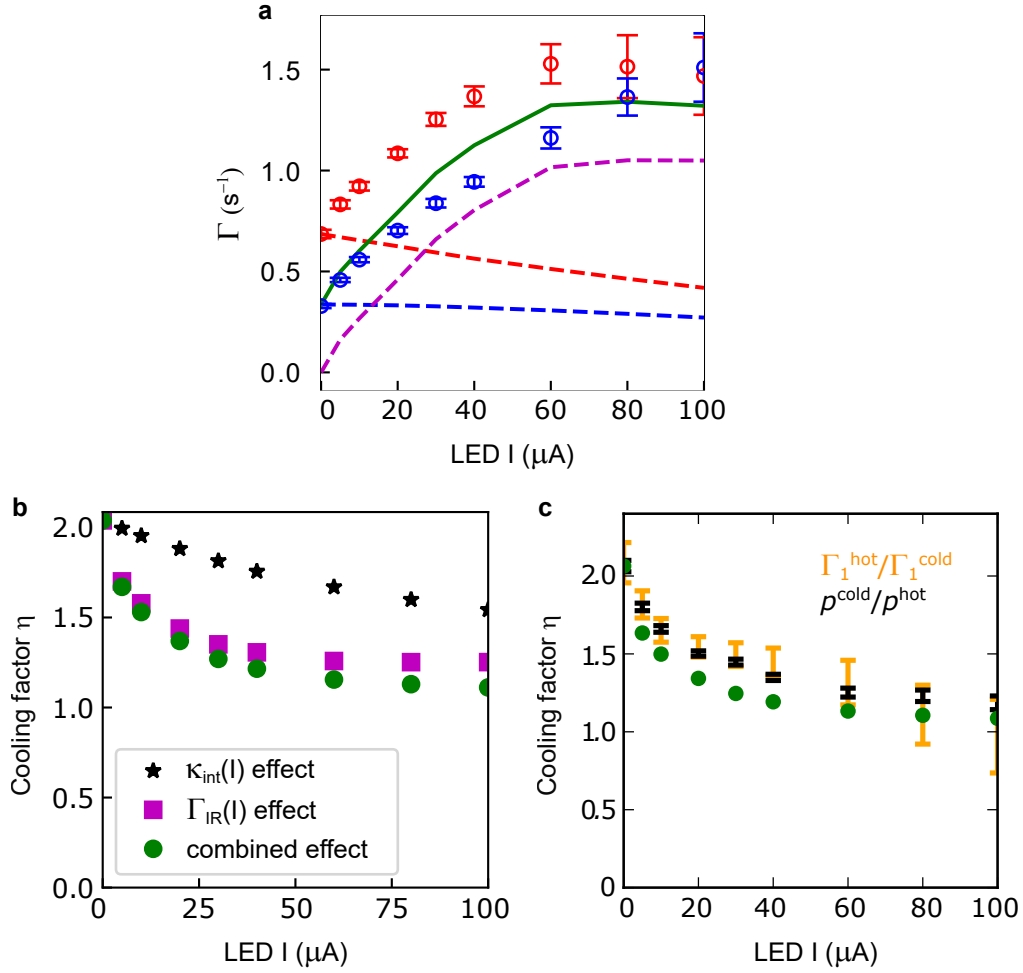
Figure 6.14: **Suppression of cooling by carrier injection. a,** Measured relaxation rate $\Gamma_1^{\text{hot,cold}}$ as a function of I in the *hot* (red circles) and *cold* (blue circles) settings. Calculated Purcell rates $\Gamma_{\text{phot}}(I)(2n_{\text{th}}(T_{\text{phot}}^{\text{hot,cold}}) + 1)$ using the measured $\kappa_{\text{int}}(I)$ in the the *hot* (red dashed line) and *cold* (blue dashed line) cases are also shown, together with the extracted $\Gamma_{\text{IR}}(I) = \Gamma_1^{\text{hot}}(I) - \Gamma_{\text{phot}}(I)[2n_{\text{th}}(T_{\text{phot}}^{\text{hot}}) + 1]$ (magenta dashed line). The calculated $\Gamma_1^{\text{cold}}(I) = \Gamma_{\text{IR}}(I) + \Gamma_{\text{phot}}(I)(2n_{\text{th}}(T_{\text{phot}}^{\text{cold}}) + 1)$ (green solid line) shows partial agreement with the data (blue circles). **b** Calculated cooling factor $\eta(I)$ using Eq.6.8 in three cases: including only the effect of $\kappa_{\text{int}}(I)$ (black stars), only the effect of $\Gamma_{\text{IR}}(I)$ (magenta squares), and the two combined contributions (green circles). **c** Measured $p^{\text{cold}}/p^{\text{hot}}$ (black) and $\Gamma_1^{\text{cold}}/\Gamma_1^{\text{hot}}$ (orange) as a function of I. The calculated $\eta(I)$ (green circles, same as panel **b**) is in semi-quantitative agreement with the measurement.

transfer of the conduction electron polarization to the bismuth ESR transitions. Such process could be caused by donor-bound exciton formation and relaxation (see Sc.4.5). The donor polarization is then resulting from the competition between the Purcell rate and Γ_{IR} driving it toward $p(T_{\mathrm{phot}}^{\mathrm{hot}})$ and p_{el}, respectively. The current dependence of the polarization is thus given by:

$$p(I) = \frac{\Gamma_{\mathrm{phot}}[2n_{\mathrm{th}}(T_{\mathrm{phot}}^{\mathrm{hot}}) + 1]}{\Gamma_1^{\mathrm{hot}}(I)} p(T_{\mathrm{phot}}^{\mathrm{hot}}) + \frac{\Gamma_{\mathrm{IR}}(I)}{\Gamma_1^{\mathrm{hot}}(I)} p_{\mathrm{el}}. \tag{6.9}$$
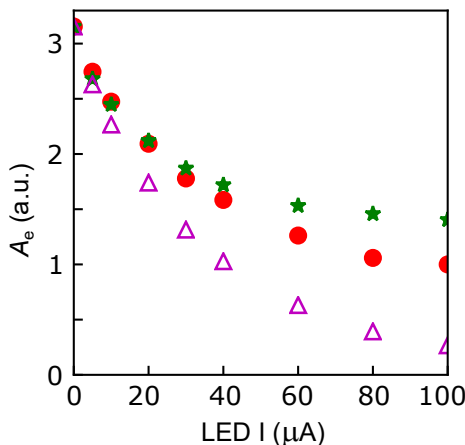

Figure 6.15: **Polarization dependence on LED illumination.** Measured (triangles) A_{e} reduction as a function of the applied LED current I in the *hot* configuration. The measured decay normalized by the simulated effect of $\kappa_{\mathrm{int}}(I)$ on the echo amplitude (circles) is also shown. $p(I)$ calculated with Eq.6.9 (stars) reproduces semi-quantitatively the normalized data (circles).

The measured echo decay as a function of I, normalized by the simulated effect of $\kappa(I)$ on A_{e} (red curve in Fig.6.15), shows a semi-quantitative agreement with the decay calculated with Eq.6.9 (green curve), supporting our model. The less good agreement at higher I could be caused by heating caused by the IR light.

We finally consider the hypothesis of the echo amplitude reduction caused entirely by heating of the sample, rather than the ionization process described above. In order to account for an echo reduction of more than a factor 3 (red curve in Fig.6.15), the sample temperature should rise from 850 mK up to 2.7 K. Two observations are against this possibility. The first being that the cryostat temperature changes less than 15 mK. The second reason lies in the positive resonator frequency shift, incompatible with the generation of quasi-particles expected for such a temperature increase.

6.7   Cooling dynamics

In a last experiment we investigate the dynamics of the spin radiative hyperpolarization. For that, we replace the electromechanical switch with the superconducting switch described in 2.5, able to switch in a few nanoseconds without heating [15]. The switch is this time placed at the mixing chamber plate.

As seen in Fig.6.16, the echo area A_{e} is measured at 9.5 mT as a function of the delay Δt after the switch configuration is changed, either from *cold* to *hot* or vice-versa. The
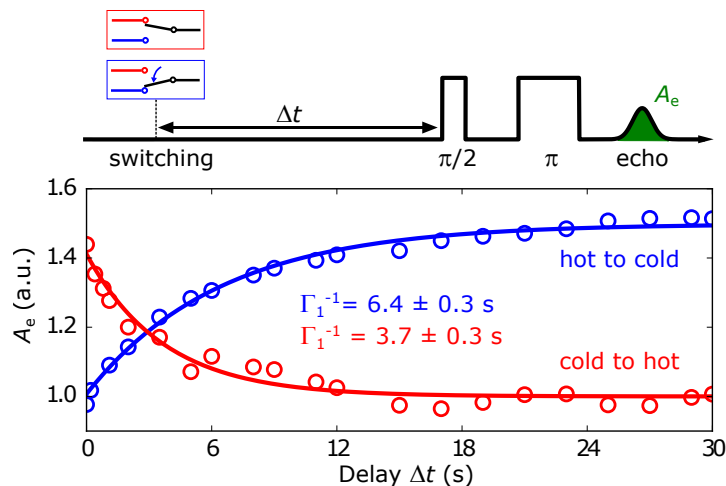
Figure 6.16:   **Cooling dynamics.** Measured integrated echo area A_e (open circles) at $9.5\,$mT as a function of the waiting time Δt between a rapid change of switch configuration and the echo sequence shown on top. Solid lines are exponential fits, yielding $\Gamma_1^{-1} = 6.4 \pm 0.3\,$s from *hot* to *cold* (blue) and $\Gamma_1^{-1} = 3.7 \pm 0.3\,$s from *cold* to *hot* (red)

relaxation times in the two cases are expected to be the two values $\Gamma_{\mathrm{phot}}[2n_{\mathrm{th}}(T_{\mathrm{phot}}^{\mathrm{hot,cold}})+1]$ determined by the new thermal population n_{th} after the switching. n_{th} is instead expected to reach the equilibrium value in a few μs, the relaxation time-scale of the resonator. An exponential fit of the two curves gives $(\Gamma_1^{\mathrm{hot}})^{-1} = 3.7\,$s and $(\Gamma_1^{\mathrm{cold}})^{-1} = 6.4\,$s. The approximate equality of the two measured ratios, $\Gamma_1^{\mathrm{hot}}/\Gamma_1^{\mathrm{cold}} = 1.7$ and $p^{\mathrm{cold}}/p^{\mathrm{hot}} = 1.5$, is again in agreement with our model. The reduced η with respect to the previously presented result is explained by a measured $3\,$dB insertion loss of the superconducting switch.

6.8   Conclusion

In this chapter we have reported the thermalization of an electron spin ensemble to the electromagnetic environment consisting in the resonant mode of a superconducting cavity. We have then shown that having the spins at thermal equilibrium with the microwave field makes possible to cool them below the host lattice temperature, enhancing their polarization.

We now consider the real world applications of such new hyperpolarization technique. In our scheme, the sample is thermally anchored at a temperature higher than the lowest temperature stage in the cryostat, which is instead used to cool the thermal radiation source. Keeping the sample hot while cooling only the spins can be useful in situations in which large cooling powers are needed, for example in spin-based microwave–optical transduction experiments, which require large optical powers [110]. The fact that the minimum achievable spin temperature is set by the cryostat base temperature is however the main drawback of the method presented here. Nevertheless, one could imagine to radiative hyperpolarize the electron spins at an arbitrarily low temperature by cooling the resonator field with parametric processes in a circuit quantum electrodynamics platform. We briefly introduce our proposal to realize this

idea in Chapter 8.

Regarding the applications to magnetic resonance spectroscopy, we first notice that to our knowledge the only existing hyperpolarization methods for electron spins are based on optical illumination[72, 111, 112]. As an example in the solid state, we have seen in Sc. 4.5 that the optical transitions of donors in silicon can be exploited to hyperpolarize both the electron and nuclear spin of the donor[68, 72]. Similarly, NV centers can be optically hyperpolarized even at room temperature [112]. Optical hyperpolarization works only for certain electron spin systems possessing the appropriate level structure. On the contrary, radiative cooling only requires a spin transition and is thus potentially universal.

The demonstrated sensitivity increase of at least $\sqrt{\eta}$, corresponding to a reduction of the measurement time by a factor η, could be of practical interest for a large variety of ESR measurements (including field-sweeps, g-tensor measurements, HYSCORE, DEER, ENDOR etc.). This approach would exclude only ESR studies of the spin-lattice relaxation processes in itself.

Concerning the spin-species suitable for radiative cooling, the main criterion is the possibility to reach the Purcell regime at cryogenic temperature, where electron spin-lattice relaxation time Γ_1^{-1} lies typically in the range $10^{-3} - 10^3$ s [113–115]. Since a Purcell time of $\sim 10^{-3}$ s has been demonstrated with a different resonator geometry [89], we can then envision this technique to be applicable to most species.

Another requirement of our scheme is the low resonator internal losses, which can only be achieved with superconducting materials and therefore sets an upper bound to the sample temperature. High quality factor resonators made out of NbTiN, which has higher critical temperature (Tc) than niobium and and withstands larger magnetic fields, have been demonstrated [116]. Radiative cooling at liquid Helium temperature should then be possible using this material, with the additional advantage of the application of larger magnetic field B_0. Approaching liquid nitrogen sample temperature would require high-Tc superconductors. Spin-photon coupling of the order of 1 Hz have been reached in YBCO resonators, with quality factor of $\sim 10^4$ at 50 K [117]. However, resonators with such materials seem to suffer from higher internal losses if μm-constrictions are patterned on thin films [118], making it challenging to reach larger spin-photon coupling g.

Besides its application to ESR, hyperpolarization of electron spins may be of interest for nuclear magnetic resonance. The non-thermal electron polarization can indeed be transferred to nuclear spins by Dynamical Nuclear Polarization (DNP) [119]. The possible application of radiative cooling to the radicals used in DNP as polarizing agents could lead to a large nuclear spin signal enhancement in less demanding conditions that those usually required, namely lower magnetic field, lower microwave frequencies or higher temperature [120].

Chapter 7

Polarization transfer in bismuth donors

In this chapter we report our experimental investigation of the phenomenon of polarization transfer via spin flip-flops introduced in Sc.4.3.3, to which we attribute the non-exponential longitudinal relaxation measured at $9.3\,\mathrm{mT}$ (see Sc.5.6).

Fig.7.1 illustrates schematically how the flip-flops at rate Γ_{ff}, in competition with the Purcell relaxation at rate Γ_1, would affect the inversion recovery measurement of the spin relaxation. Consider the case $B_0 = 9.3\,\mathrm{mT}$, where the echo amplitude is proportional to the population unbalance $\Delta N = N_{|16\rangle} + N_{|15\rangle} - N_{|5\rangle} - N_{|4\rangle}$. After the π pulse, flip-flop processes tend to refill the ground states $N_{|5\rangle}$ and $N_{|4\rangle}$, while emptying the excited states $N_{|16\rangle}$ and $N_{|15\rangle}$. If Γ_{ff} is sufficiently fast compared to Γ_1, deviation from the Purcell exponential relaxation are then expected.
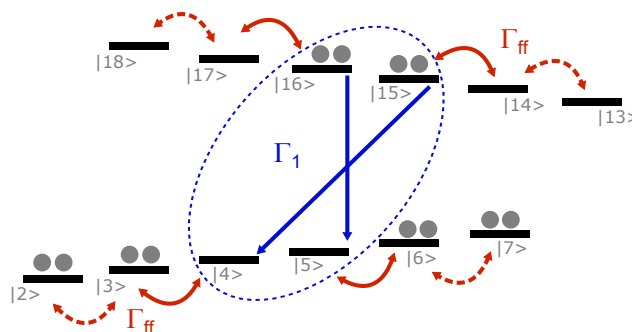

Figure 7.1: **Polarization transfer after population inversion.** Spin population (gray circles) represented in the bismuth donor spin energy levels (black) immediately after an ideal π pulse inverting the population of the $|16\rangle \leftrightarrow |5\rangle$ and $|15\rangle \leftrightarrow |4\rangle$ quasi-degenerate transitions (blue). Flip-flop processes (red arrows) of rate Γ_{ff} may compete with the Purcell relaxation rate Γ_1, leading to a non-exponential spin relaxation of the population unbalance $\Delta N = N_{|16\rangle} + N_{|15\rangle} - N_{|5\rangle} - N_{|4\rangle}$.

In the following, we provide evidence of such polarization transfer at low field by performing double resonance experiments. Even if a quantitative understanding of the observed spin longitudinal relaxation is still missing, our results shows that the polarization transfer can qualitatively explain the observed non-exponential decay.

7.1   Double resonance spectroscopy

The principle of the double resonance experiment is illustrated in Fig.7.2. The Hahn-echo amplitude is measured repeatedly at one field while the frequency ω_{pump} of a continuous-wave pump tone sent to the resonator input is varied. Whenever a bismuth transition is resonant with ω_{pump}, it is saturated by the long pump drive. In the absence of polarization transfer between hyperfine levels, the polarization of the probed transition is unaffected by the pump tone and the echo signal should show no dependence on ω_{pump}. If on the other hand polarization transfer is significant, we expect a reduction of echo signal when ω_{pump} is resonant with another transition. This experiment is thus sensitive to the polarization transfer in a complementary way with respect to the inversion recovery measurement, where the polarization is transferred from the non-resonant to the probed transition.

To perform the experiment, we modify the setup used in Ch.5 by removing the JTWPA and by connecting a second microwave source, via a 3 dB splitter at room temperature, to the input line. We use this second source to generate the microwave pump tone. The pump signal is switched off only during the Hahn-echo sequence, starting from 1 ms before the $\pi/2$ pulse, to avoid saturation of the amplifiers. It is thus off for less than 1/10000 of the experimental time.
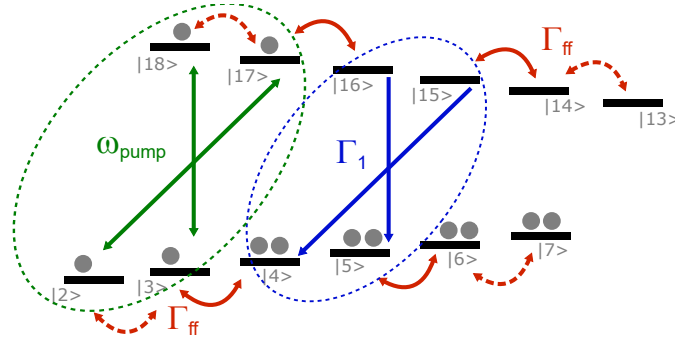

Figure 7.2:   **Polarization transfer in a double resonance experiment.** Spin population (gray circles) represented in the bismuth donor spin energy levels (black) in the presence of a pump tone saturating the $|18\rangle \leftrightarrow |3\rangle$ and $|17\rangle \leftrightarrow |2\rangle$ quasi-degenerate transitions. Flip-flop processes may redistribute the population as illustrated by the red arrows, leading to a reduced polarization of the probed transition resonant with the cavity (blue).

7.1.1   Double resonance at 9.5 mT

We first measure A_{e} at 9.5 mT for ω_{pump} going from 7.12 GHz to 7.65 GHz. In this range of frequencies, the pump tone crosses all bismuth ESR transitions (see Fig.7.3a). The echo amplitude $A_{\mathrm{e}}(\omega_{\mathrm{pump}})$, proportional to the population unbalance in the probed transitions $\Delta N = N_{|16\rangle} + N_{|15\rangle} - N_{|5\rangle} - N_{|4\rangle}$, shows a dip at pump frequencies resonant with spin transitions (see Fig.7.3b). Their amplitude decreases as the pump-resonator detuning increases and the pump tone gets more and more filtered. The observed dips validate the hypothesis that polarization transfer takes place at 9.5 mT, leading to a reduction of ΔN when any other transition is saturated by the pump. Complete echo
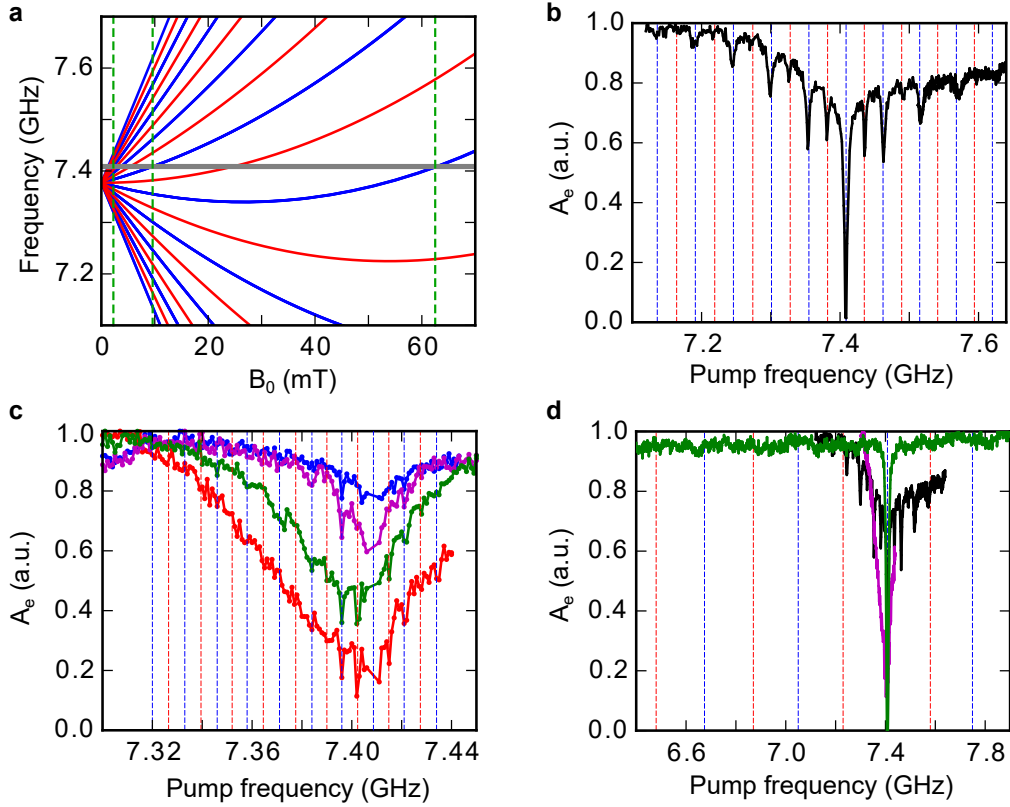
Figure 7.3: **Double resonance spectroscopy. a,** Calculated S_x (blue) and S_z (red) bismuth donor spin transitions as a function of B_0. The resonator frequeny is reported (gray), as well as the three pump frequency sweeps (green) at $2.3\,\text{mT}$, $9.5\,\text{mT}$ and $62.5\,\text{mT}$. **b,** $A_\text{e}(\omega_\text{pump})$ measured at $9.5\,\text{mT}$ with $t_\text{rep} = 60\,\text{s}$ and $P_\text{pump} = -37\,\text{dBm}$. S_x (blue) and S_z (red) transition frequencies are represented by dashed lines. **c,** $A_\text{e}(\omega_\text{pump})$ measured at $2.25\,\text{mT}$, for $P_\text{pump} = -47\,\text{dBm}$ (red), $P_\text{pump} = -67\,\text{dBm}$ (green), $P_\text{pump} = -87\,\text{dBm}$ (purple). Repetition times are $40\,\text{s}$ (red) and $10\,\text{s}$ (green and purple). S_x (blue) and S_z (red) transition frequencies are represented by dashed lines. **d,** $A_\text{e}(\omega_\text{pump})$ measured at $62.5\,\text{mT}$ (green) with $t_\text{rep} = 60\,\text{s}$ and $P_\text{pump} = -37\,\text{dBm}$. S_x (blue) and S_z (red) transition frequencies at the same field are represented by dashed lines. $A_\text{e}(\omega_\text{pump})$ measured at $9.5\,\text{mT}$ (black) and $2.3\,\text{mT}$ (red) are also shown for comparison.

suppression is trivially reached for $\omega_{\text{pump}} = \omega_0$, when the probed transition is directly saturated.

Interestingly, a relatively smaller echo reduction is also observed in correspondence of S_z transitions. Even if S_z transitions should not be allowed in our geometry, a small misalignment of B_0 with respect to the z direction could explain the result .We note that S_z transitions happen at the same frequency as two-photon processes, which we can thus not exclude. We finally notice that the pump tone decreases the echo amplitude also when no resonance condition is satisfied, yielding a background signal centered at the resonator frequency. More insight on these effect is provided in the following.

7.1.2   Double resonance at 2.3 mT and 62.5 mT

The same measurement is repeated at 2.3 mT, where all spin transitions lie in the 7.32 GHz-7.44 GHz range (see Fig.7.3a). The non-resonant background signal is much stronger than at 9.3 mT and only few double-resonance dips are visible in $A_{\text{e}}(\omega_{\text{pump}})$. Performing the measurement at different pump powers P_{pump} confirms the few visible double-resonance dips at $\omega_{\text{pump}}/2\pi = 7.384$, 7.396, 7.40235, 7.4148 and 7.421 GHz. Moreover, it shows that the overall effect of the pump tone on A_{e} is enhanced as the pump power increases.

We finally measure $A_{\text{e}}(\omega_{\text{pump}})$ at 62.5 mT in the 6.5 GHz to 7.9 GHz range of ω_{pump} (see Fig.7.3d). No double-resonance signal is observed at this field and also the non-resonant background is suppressed: only the $\omega_{\text{pump}} = \omega_0$ dip is visible. The magnetic-field dependence of the large background signal indicates that its origin is not a direct effect of the pump tone on the probed transition or on the resonator (such as heating). We thus think that it is caused by the overlap of the double-resonance echo dips.

The absence of any evidence of polarization transfer at 62.5 mT is in agreement with the model detailed in Sc.4.3.3 and with the inversion recovery measurement at the same field: spin flip-flops would indeed be largely inhibited due to the larger detuning of neighbouring spins. However, we notice that the absence of double-resonance signal can be, at least in part, due to the larger pump-resonator detuning necessary to drive the other spin transitions.

7.2   Dynamics of polarization transfer

We investigate the timescale at which the polarization is transferred by performing a pulsed double resonance experiment. As shown in Fig.7.4, a pump pulse of duration t_{pump} is sent to the resonator and after a delay time Δt the polarization of the transition resonant with the cavity is measured with the Hahn-echo. We enhance the saturation of the broad spin lines induced by the short pump pulse by sweeping ω_{pump} in a range of a few MHz during t_{pump}. The waiting time between two repetitions of the pulse sequence t_{wait} is chosen to be $t_{\text{wait}} = t_{\text{rep}} - \Delta t$, to keep the time interval t_{rep} between two Hahn-echo sequences fixed. Doing so, the probed spin transition has the same time to relax to equilibrium after the $\pi/2$ pulse independently of Δt. $A_{\text{e}}(\Delta t)$ is thus constant, unless ΔN dynamics is induced by the pump. In the following $t_{\text{rep}} = 60$ s, $t_{\text{pump}} = 10$ ms and the pump frequency is swept from $\omega_{\text{pump}} - 5$ MHz to $\omega_{\text{pump}} + 5$ MHz.
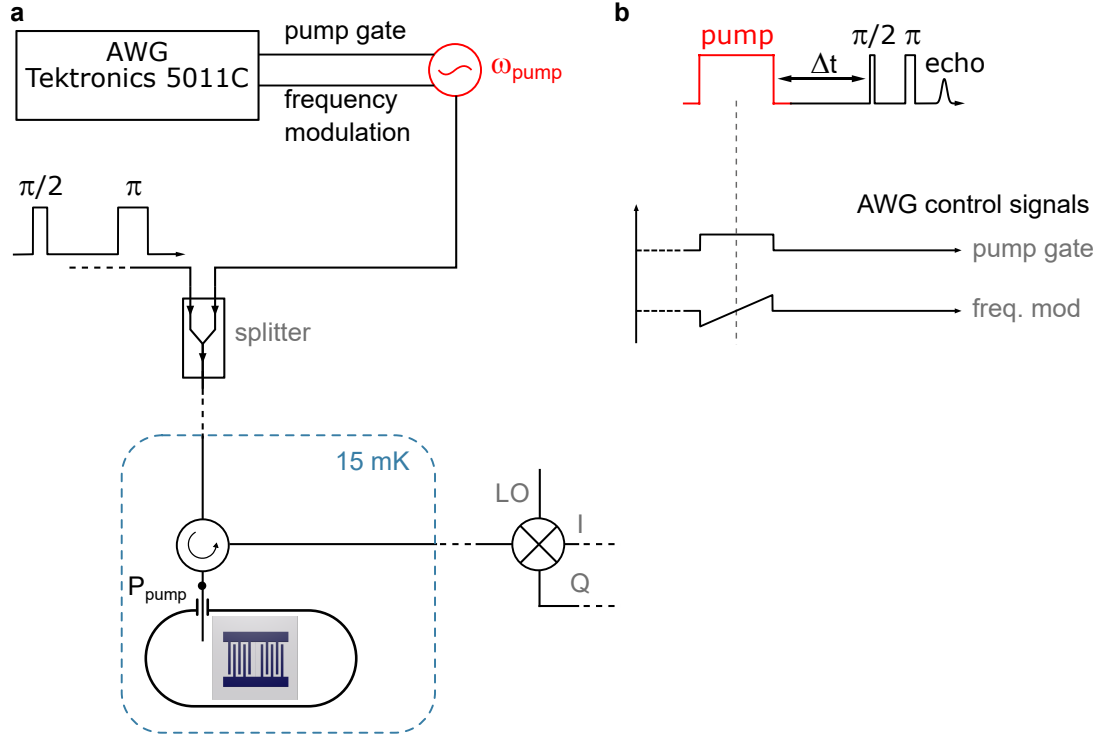
Figure 7.4: **Pulse setup and sequence. a,** Pump line added to the room-temperature setup of Fig.5.11. **b,** Pulse sequence. ω_{pump} is shifted during the pump pulse proportionally to the frequency modulation signal.

7.2.1 Polarization dynamics at 9.5 mT

We measure $A_{\text{e}}(\Delta t)$ for four values of ω_{pump} (see Fig.7.5a). The results for $\omega_{\text{pump}}/2\pi =$ 7.246 GHz, 7.301 GHz and 7.518 GHz reported in Fig.7.5b show the same qualitative behaviour. In the first few seconds the echo amplitude decreases with Δt before increasing again at a slower rate. In the measurements at $\omega_{\text{pump}}/2\pi = 7.301$ GHz (green) and $\omega_{\text{pump}}/2\pi = 7.518$ GHz (magenta) the pump drives two transitions symmetric with respect to ω_0. The two $A_{\text{e}}(\Delta t)$ curves show almost the same polarization dynamics, with an echo minimum at about 4 s. On the other hand, the measurement at $\omega_{\text{pump}}/2\pi = 7.246$ GHz (blue dots), where a transition more detuned from ω_0 is excited, shows a smaller echo reduction and a slower dynamics.

A radically different result is instead observed for $\omega_{\text{pump}} = 7.355$ GHz (see Fig.7.5c). Here the echo amplitude is minimum for the smaller Δt and increases monotonically at slower rate for large delay.

The above results agree qualitatively with our polarization transfer model. Because of the time needed for the polarization transfer to happen, no effect is expected immediately after the saturation, consistently with the observations. Then, polarization transfer progressively takes place over some delay from the probed transition via flip-flop processes and ΔN reaches its minimum value. The presence of the Purcell relaxation at rate Γ_1 prevails for larger Δt when ΔN increases again toward its thermal equilibrium value. The longer delay at which the minimum of A_{e} appears for $\omega_{\text{pump}} = 7.246$ GHz (blue dots) is explained by the fact that more flip-flop processes are needed for ΔN to be affected. The measurement reported in Fig.7.5c provides a consistency check of our analysis. The pump pulse with $\omega_{\text{pump}} = 7.355$ GHz directly reduces ΔN by de-

populating $|5\rangle$ and exciting spins in $|15\rangle$. No delay between the pump pulse and the appearance of a minimum in A_e is thus expected, as confirmed by the measurement outcome.
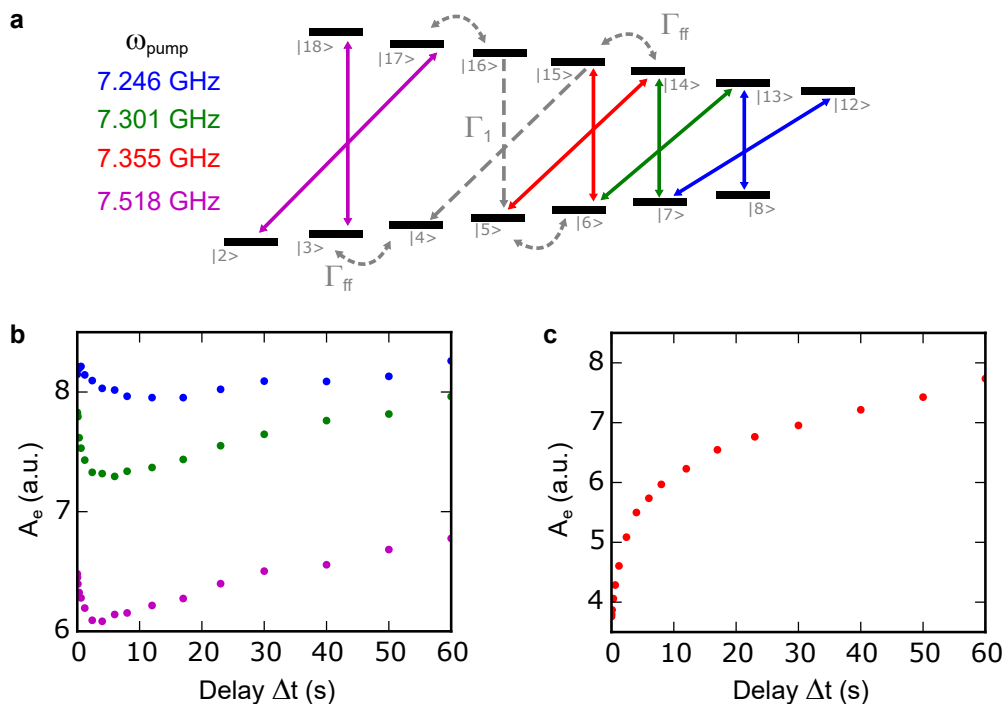

Figure 7.5: **Polarization transfer dynamics at 9.5 mT. a,** Spin transitions resonant with the four different pump frequencies are represented by coloured solid arrows. Purcell relaxation and flip-flop processes determining the dynamics of $\Delta N = N_{|16\rangle} + N_{|15\rangle} - N_{|5\rangle} - N_{|4\rangle}$ are illustrated by gray dashed arrows. **b,** $A_e(\Delta t)$ measured for 3 values of ω_{pump}: 7.246 GHz (blue), 7.301 GHz (green) and 7.518 GHz (magenta). **c,** $A_e(\Delta t)$ measured with $\omega_{pump} = 7.355$ GHz.

7.2.2 Polarization dynamics at 2.3 mT

At 2.3 mT the $|18\rangle \leftrightarrow |3\rangle$ and $|17\rangle \leftrightarrow |2\rangle$ quasi-degenerate transitions are resonant with the cavity, and thus A_e is proportional to $\Delta N = N_{|18\rangle} + N_{|17\rangle} - N_{|3\rangle} - N_{|2\rangle}$ (see Fig.7.6a). We measure $A_e(\Delta t)$ at this field with $\omega_{pump} = 7.384$ GHz. The pump pulse then excites the transitions $|16\rangle \leftrightarrow |5\rangle$ and $|15\rangle \leftrightarrow |4\rangle$, that are resonant with the cavity at 9.5 mT (see Fig.7.6b). The $A_e(\Delta t)$ measurement at 2.3 mT (yellow dots in Fig.7.6b) is thus complementary to the $A_e(\Delta t)$ recorded at 9.5 mT with $\omega_{pump} = 7.518$ GHz (magenta curves in Fig.7.6b and Fig.7.5b), meaning that the probed and the pumped transitions are exchanged in the two experiments.

Comparing the two results reported in Fig.7.6b, we notice that at 2.3 mT the ΔN dynamics after the pump pulse is significantly faster and the echo reduction more evident with respect to the measurement at 9.5 mT.

7.2.3 Comparison with the estimated flip-flop rate

In Sc.4.3.3 we have presented a model of the flip-flop processes between adjacent donors that could explain the observed polarization transfer. The flip-flop rate Γ_{ff} is found to
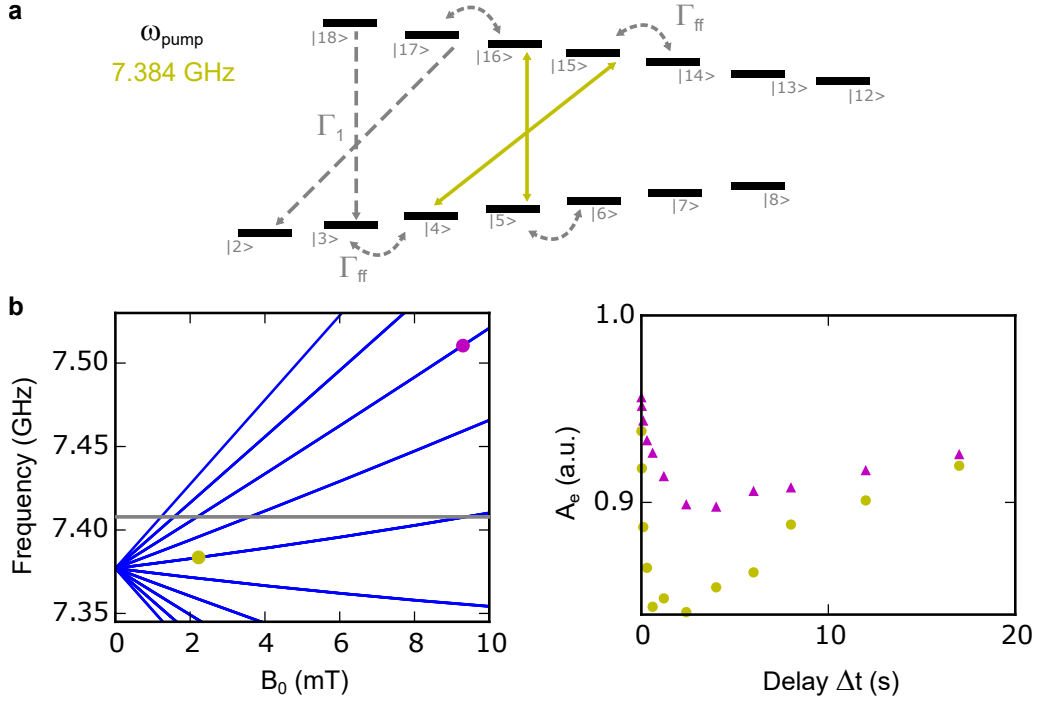
Figure 7.6: **Polarization transfer dynamics at 2.3 mT. a,** Transitions resonant with the pump drive of frequency $\omega_{\text{pump}} = 7.384\,\text{GHz}$ (yellow). Gray arrows illustrate the competing Purcell relaxation rate Γ_1 and the spin flip-flop processes at rate Γ_{ff}. **b,** Comparison of polarization dynamics at 2.3 mT and at 9.5 mT. Left, S_x transition frequencies (blue) and resonator frequency (gray). Pump frequencies in the considered experiment at 9.5 mT (magenta dot) and in the 2.3 mT experiment (yellow dot). Right, $A_{\text{e}}(\Delta t)$ measured at 2.3 mT (yellow) and at 9.5 mT (magenta, same curve as in panel b of Fig.7.5b). The two curves are normalized by $A_{\text{e}}(\Delta t = 60\,\text{s})$.

be dependent on the effective spin line broadening γ_{eff} caused by the ESEEM phenomenon that at low field partially compensates the detuning between the bismuth hyperfine transitions. We then calculate with Eq.4.37 the average flip-flop rate expected at 9.5 mT, finding $\Gamma_{\text{ff}}^{-1} \approx 10\,\text{s}$.

The pulsed double-resonance experiment at 9.5 mT reveals a polarization transfer that takes place on the order of a few seconds, which is not too far off compared to the estimated Γ_{ff}. The calculated Γ_{ff} is thus probably about one order of magnitude too slow to explain our observations. We thus find that our results with the oversimplified model of Sc.4.3.3 are encouraging to confirm the validity of the proposed physical process.

Measurements at 2.3 mT provide further support to the model. The observed acceleration of polarization transfer can be indeed explained by two effects included in our model. The first is that lowering the field reduces the average detuning between the hyperfine transitions, leading to an increased probability of finding neighbouring resonant donors. At 9.3 mT, this detuning ranges from $\sim 100\,\text{kHz}$ to $\sim 2\,\text{MHz}$, while at 2.3 mT it goes from $\sim 10\,\text{kHz}$ to $\sim 100\,\text{kHz}$. The second (and possibly dominant) effect is that the amplitude of ESEEM oscillations is larger at 2.3 mT (see Sc.5.5), yielding an increase of γ_{eff}.

To go beyond this preliminary study, we are working in collaboration with W. Coish

from McGill University to develop a complete model able to quantitatively reproduce our measurements. In particular, a rigorous treatment requires considering all different hyperfine transition frequencies and matrix elements, and proper averaging of flip-flop processes between neighbouring donors at different angles and distances.

7.3   Conclusion

The double resonance experiments discussed in this chapter demonstrate that polarization transfer in the bismuth donor spin manifold happens at $B_0 < 10\,\mathrm{mT}$ with characteristic times comparable to and even faster than the Purcell rate. The observed phenomenon seems thus to be compatible with the non-exponential spin relaxation measured with the inversion recovery sequence at B_0 as high as $10\,\mathrm{mT}$. However, a quantitative analysis is needed for a conclusive answer.

The reported results encourage us to confirm the spin flip-flop mechanism described in Sc.4.3.3 as the cause of the observed population dynamics, even if a quantitative agreement is missing. The calculated average flip-flop rate of $10^{-1}\,\mathrm{s}^{-1}$ is comparable even though slightly smaller than the characteristic rate of the polarization transfer measured. However, a more detailed calculation could possibly demonstrate the validity of the proposed physical process.

We finally come to the efficiency of radiative cooling in the presence of polarization transfer. The measurements performed at $9.3\,\mathrm{mT}$ show radiative cooling with $\eta = 2$, only slightly lower than $\eta = 2.3$ recorded at $62.5\,\mathrm{mT}$. This demonstrates that radiative cooling can be efficient also for an interacting spin ensemble. While spin-lattice and radiative relaxation put the spins in thermal contact with two different baths, polarization transfer represents a thermalization process internal to the spin system that does not prevent its cooling. Despite the fact that Purcell relaxation acts only on the resonant transitions, polarization transfer would, in a sufficiently long time, lead to hyperpolarization of all the ESR donor transitions. However, we have no experimental evidence of this interpretation.

Chapter 8

Conclusion and future directions

8.1 Radiative cooling of a spin ensemble

The experiments reported in this thesis show that an ensemble of electron spins can thermalize to their electromagnetic environment. We have then exploited this regime to radiative cool the ensemble below the temperature of the crystal in which it is hosted, demonstrating a novel universal method of electron spin hyperpolarization.

To demonstrate this effect, we have used an ensemble of bismuth donors in silicon coupled to a superconducting resonator. We have shown that, in appropriate conditions, the relaxation of these donors can be dominated by radiative processes at temperatures between $10\,\mathrm{mK}$ and $1\,\mathrm{K}$.

The demonstration of radiative cooling is reported in Chapter 6. Connecting the resonator input to a resistor colder than the sample we record a more than twofold increase of spin polarization, showing that spins are indeed cooled below the lattice temperature.

In the last chapter Ch. 7 we report evidences of a polarization transfer process in Si:Bi present at low applied magnetic field. By performing double resonance experiment we show that spin population is transferred from one bismuth transition to another on timescales of the order of seconds. This suggests that all Si:Bi hyperfine levels may be cooled by the radiative cooling of the resonant transition, although we have no direct proof.

8.2 Future direction: active radiative cooling

Radiative spin cooling is potentially able to cool an arbitrary spin species below the sample temperature. The main drawback of this technique is that the minimum reachable spin temperature is ultimately limited by the lowest temperature stage in the cryostat because of the necessity to physically cool down the cold $50\,\Omega$ resistor. This raises the question: is it possible to do better, and to cool down arbitrary electron spins to an arbitrarily low temperature (i.e., even lower than the lowest physically available in the cryostat) using radiative cooling? This would constitute an interesting development for ESR spectroscopy. However, such a goal requires cooling the microwave field by a method different from the one demonstrated here. In the rest of this paragraph, we outline an idea of how to achieve this.

This idea consists in actively cooling the cavity mode with a parametric process enabled by a non-linear microwave circuit, as demonstrated in recent experiments [121]. The

127

intra-cavity thermal photons would be upconverted to a higher frequency, and then dissipated in a resistor at the sample temperature. If sufficient energy is provided, this active cooling scheme could in principle reduce the photon and thus the spin temperature to an arbitrary value below the cryostat base temperature.
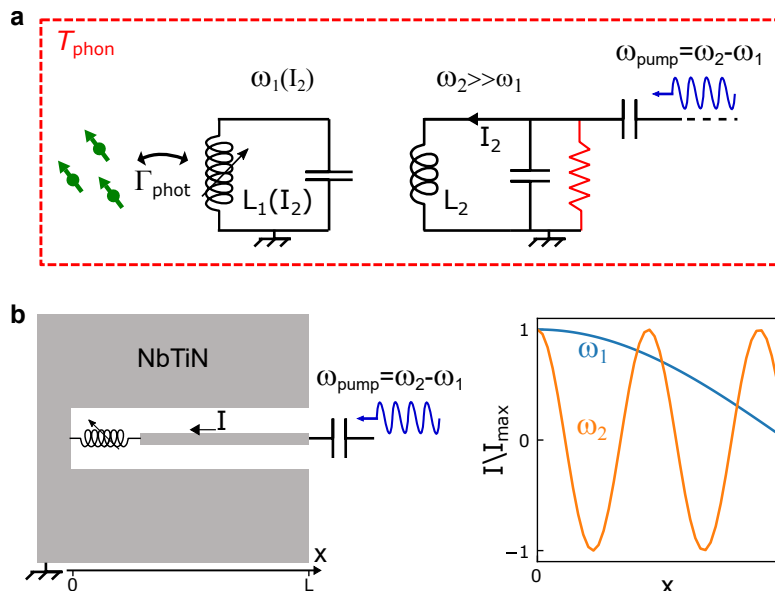

Figure 8.1: **Active cooling principle. a,** Active cooling principle. **b,** Left, schematic representation of a $\lambda/4$ CPW resonator mad of NbTiN (gray), where the kinetic inductance contribution is represented by the non linear inductor in the inner conductor. Right, current profile of the first mode (blue) and of the $m-$th harmonic of the CPW resonator.

The principle of such active radiative cooling is illustrated in Fig.8.1a. In a sample at temperature T_{phon}, the spins are resonantly coupled to a microwave resonator of frequency ω_1 populated at thermal equilibrium by $n_{\mathrm{th}}(\omega_1, T_{\mathrm{phon}})$ microwave photons. A second resonator of frequency $\omega_2 \gg \omega_1$ has instead a thermal equilibrium population $n_{\mathrm{th}}(\omega_2, T_{\mathrm{phon}}) \ll n_{\mathrm{th}}(\omega_1, T_{\mathrm{phon}})$. If the non-linear inductance of one resonator depends on the current flowing in the other one, parametric processes can be activated by a proper pump current satisfying the energy conservation conditions. It can indeed be shown that a pump tone of frequency $\omega_{\mathrm{pump}} = \omega_2 - \omega_1$ enables conversion of photons from low to high frequency. We notice that the described mechanism is similar to the sideband cooling in optomechanical systems, where the frequency of the optical cavity depends on the displacement of the mechanical resonator. If the high frequency resonator is well thermalized to a resistor at T_{phon}, we then reduce the low frequency mode thermal population down to $n_{\mathrm{th}}(\omega_1) \approx n_{\mathrm{th}}(\omega_2, T_{\mathrm{phon}})$. This means that its temperature is effectively lowered below T_{phon}. Spins in the Purcell regime coupled to the low frequency cavity are then radiatively cooled below the sample temperature, as desired.

The design of the non-linear superconducting circuit offers a few possible alternative approaches. One possibility is represented by the use of the intrinsic non-linearity of disordered superconductors like NbTiN, whose main advantage would be its compatibility with the magnetic field needed in ESR experiments. The two LC resonators could be implemented with two modes of a distributed-parameter resonator, such as the coplanar waveguide (CPW) resonator illustrated in Fig.8.1b. The first and the m-th harmonics would realize the low and high frequency mode, respectively (see Fig.8.1b). The non-

linearity originated by the current dependence of the NbTiN kinetic inductance would then make possible to implement the parametric processes described above.

Appendix A

Thermalization of a quantum system interacting with N baths

Throughout this thesis we deal with quantum systems interacting with their environment. If the environment is a bath satisfying the conditions of a Markov approximation, then the system quantum state at time t, described by the density matrix $\rho(t)$, evolves according to a master equation that can be expressed in the Lindblad form:

$$\frac{d\rho}{dt} = -\frac{i}{\hbar}[\hat{H}, \rho] + \sum_\mu (L_\mu \rho L_\mu^\dagger - \frac{1}{2}L_\mu^\dagger L_\mu \rho - \frac{1}{2}\rho L_\mu^\dagger L_\mu) \tag{A.1}$$

where L_μ is a non-hermitian operator describing an interaction of the system with the environment.

Central to this thesis is the question: what is the effective temperature T_{sys} of a quantum system coupled with strength Γ_j to N reservoirs of different temperatures T_j. We assume that these reservoirs consist of a continuum of bosonic modes (which can represent the lattice vibrations, or the microwave field). The system thermalizes by emission into and absorption from the environment of energy quanta $\hbar\omega_{\text{sys}}$. Γ_j is defined as the rate at which the system spontaneously emits such a quantum of excitation into bath j if the latter is in its ground state. The emission process corresponds to the annihilation of a system excitation described by the operator $\hat{o}_-$. On the other hand, the absorption corresponds to the action of the creation operator $\hat{o}_+ = \hat{o}_-^\dagger$. In the master equation for such a system, for each bath j the Lindblad operator $L_{j-} = \sqrt{\Gamma_{j-}}\hat{o}_-$ accounts for emission into the bath j at rate Γ_{j-}, while the operator $L_{j+} = \sqrt{\Gamma_{j+}}\hat{o}_+$ accounts for absorption from the same bath at rate Γ_{j+}.

The Γ_{j-} and Γ_{j+} rates can be obtained from generic thermodynamical arguments, as reported in [17]. The emission (absorption) process corresponds indeed to a jump upwards (downwards) between two levels in the bath j separated by the energy $\hbar\omega_{\text{sys}}$. The ratio of emission and absorption rates Γ_{j-}/Γ_{j+} is then equal to the probability of finding the bath in the lower energy state divided by the probability of finding it in the excited state, that assuming the bath is in thermal equilibrium is given by the Boltzmann distribution:

$$\frac{\Gamma_{j-}}{\Gamma_{j+}} = e^{\hbar\omega_{\text{sys}}/kT} = \frac{n_{\text{th}}(T_j) + 1}{n_{\text{th}}(T_j)}, \tag{A.2}$$

where

$$n_{\text{th}}(T) = \frac{1}{e^{\hbar\omega_{\text{sys}}/kT} - 1} \tag{A.3}$$

is the occupation number of a bosonic mode of frequency ω_{sys}. The two rates can then be expressed as a function of the spontaneous emission rate Γ_j as:

$$\Gamma_{j-} = \Gamma_j[n_{\text{th}}(T_j) + 1] \tag{A.4}$$
$$\Gamma_{j+} = \Gamma_j n_{\text{th}} \tag{A.5}$$

Eq.A.1 for the system coupled to N bosonic baths takes then the form:

$$\frac{\mathrm{d}\rho}{\mathrm{d}t} = -\frac{i}{\hbar}[\hat{H}, \rho] - \sum_{j=1}^{N} \frac{\Gamma_j[n_{\text{th}}(T_j) + 1]}{2}(\hat{o}_+\hat{o}_-\rho + \rho\hat{o}_+\hat{o}_- - 2\hat{o}_-\rho\hat{o}_+)$$
$$- \sum_{j=1}^{N} \frac{\Gamma_j n_{\text{th}}(T_j)}{2}(\hat{o}_-\hat{o}_+\rho + \rho\hat{o}_-\hat{o}_+ - 2\hat{o}_+\rho\hat{o}_-). \tag{A.6}$$

It is however possible to rewrite Eq.A.6 in terms of a single effective bath of temperature T_{sys}:

$$\frac{\mathrm{d}\rho}{\mathrm{d}t} = -\frac{i}{\hbar}[\hat{H}, \rho] - \frac{\Gamma[n_{\text{th}}(T_{\text{sys}}) + 1]}{2}(\hat{o}_+\hat{o}_-\rho + \rho\hat{o}_+\hat{o}_- - 2\hat{o}_-\rho\hat{o}_+)$$
$$- \frac{\Gamma n_{\text{th}}(T_{\text{sys}})}{2}(\hat{o}_-\hat{o}_+\rho + \rho\hat{o}_-\hat{o}_+ - 2\hat{o}_+\rho\hat{o}_-), \tag{A.7}$$

where $\Gamma = \sum_{j=1}^{N} \Gamma_j$ is the total system-bath coupling. The system temperature T_{sys} is so obtained from the new effective bath occupation number:

$$n_{\text{th}}(T_{\text{sys}}) = \sum_{j=1}^{N} \frac{\Gamma_j}{\Gamma} n_{\text{th}}(T_j). \tag{A.8}$$

If the coupling of the system to one bath $j0$ is dominant ($\Gamma_0 \gg \Gamma_{j \neq j0}$) the system will therefore equilibrate to $T_{\text{sys}} \approx T_{j0}$ regardless of the other baths.

Bibliography

[1] I. I. Rabi, J. R. Zacharias, S. Millman, and P. Kusch, "A New Method of Measuring Nuclear Magnetic Moment," Physical Review **53**, 318–318 (1938).

[2] F. Bloch, "Nuclear Induction," Physical Review **70**, 460–474 (1946).

[3] E. M. Purcell, H. C. Torrey, and R. V. Pound, "Resonance Absorption by Nuclear Magnetic Moments in a Solid," Physical Review **69**, 37–38 (1946).

[4] T. Sleator, E. L. Hahn, C. Hilbert, and J. Clarke, "Nuclear-spin noise," Physical Review Letters **55**, 1742–1745 (1985).

[5] A. Bienfait, J. Pla, Y. Kubo, X. Zhou, M. Stern, C.-C. Lo, C. Weis, T. Schenkel, D. Vion, D. Esteve, J. Morton, and P. Bertet, "Controlling Spin Relaxation with a Cavity," Nature **531**, 74 – 77 (2016).

[6] A. Bienfait, J. J. Pla, Y. Kubo, M. Stern, X. Zhou, C. C. Lo, C. D. Weis, T. Schenkel, M. L. W. Thewalt, D. Vion, D. Esteve, B. Julsgaard, K. Mølmer, J. J. L. Morton, and P. Bertet, "Reaching the quantum limit of sensitivity in electron spin resonance," Nature Nanotechnology **11**, 253–257 (2016).

[7] B. Albanese, S. Probst, V. Ranjan, C. W. Zollitsch, M. Pechal, A. Wallraff, J. J. L. Morton, D. Vion, D. Esteve, E. Flurin, and P. Bertet, "Radiative cooling of a spin ensemble," Nature Physics , 1–5 (2020).

[8] E. M. Purcell, "Spontaneous emission probabilities at radio frequencies," Phys. Rev. **69**, 681 (1946).

[9] D. M. Pozar, *Microwave Engineering* (Wiley, 4 edition, 2011).

[10] A. A. Clerk, M. H. Devoret, S. M. Girvin, F. Marquardt, and R. J. Schoelkopf, "Introduction to quantum noise, measurement, and amplification," Reviews of Modern Physics **82**, 1155–1208 (2010).

[11] H. A. Haus and J. A. Mullen, "Quantum Noise in Linear Amplifiers," Physical Review **128**, 2407–2413 (1962).

[12] C. M. Caves, "Quantum limits on noise in linear amplifiers," Phys. Rev. D **26**, 1817–1839 (1982).

[13] C. Macklin, K. O'Brien, D. Hover, M. E. Schwartz, V. Bolkhovsky, X. Zhang, W. D. Oliver, and I. Siddiqi, "A near–quantum-limited Josephson traveling-wave parametric amplifier," Science **350**, 307–310 (2015).

[14] B. Yurke, L. R. Corruccini, P. G. Kaminsky, L. W. Rupp, A. D. Smith, A. H. Silver, R. W. Simon, and E. A. Whittaker, "Observation of parametric amplification and deamplification in a Josephson parametric amplifier," Physical Review A **39**, 2519–2533 (1989).

[15] M. Pechal, J.-C. Besse, M. Mondal, M. Oppliger, S. Gasparinetti, and A. Wallraff, "Superconducting Switch for Fast On-Chip Routing of Quantum Microwave Fields," Physical Review Applied **6**, 024009 (2016).

[16] D. F. Walls and G. J. Milburn, *Quantum Optics* (Springer, 2008).

[17] S. Haroche and J.-M. Raimond, *Exploring the quantum* (Oxford University Press, 2006).

[18] M. C. Butler and D. P. Weitekamp, "Polarization of nuclear spins by a cold nanoscale resonator," Physical Review A **84**, 063407 (2011).

[19] B. Julsgaard and K. Mølmer, "Measurement-induced two-qubit entanglement in a bad cavity: Fundamental and practical considerations," Physical Review A **85**, 032327 (2012).

[20] J. Wang, H. M. Wiseman, and G. J. Milburn, "Dynamical creation of entanglement by homodyne-mediated feedback," Physical Review A **71**, 042309 (2005).

[21] V. Ranjan, S. Probst, B. Albanese, A. Doll, O. Jacquot, E. Flurin, R. Heeres, D. Vion, D. Esteve, J. J. L. Morton, and P. Bertet, "Pulsed electron spin resonance spectroscopy in the Purcell regime," Journal of Magnetic Resonance **310**, 106662 (2020).

[22] E. L. Hahn, "Spin Echoes," Physical Review **80**, 580–594 (1950).

[23] A. Honig, "Polarization of Arsenic Nuclei in a Silicon Semiconductor," Physical Review **96**, 234–235 (1954).

[24] G. Feher, R. C. Fletcher, and E. A. Gere, "Exchange Effects in Spin Resonance of Impurity Atoms in Silicon," Physical Review **100**, 1784–1786 (1955).

[25] B. E. Kane, "A silicon-based nuclear spin quantum computer," Nature **393**, 133–137 (1998).

[26] G. Wolfowicz, A. M. Tyryshkin, R. E. George, H. Riemann, N. V. Abrosimov, P. Becker, H.-J. Pohl, M. L. W. Thewalt, S. A. Lyon, and J. J. L. Morton, "Atomic clock transitions in silicon-based spin qubits," Nat Nano **8**, 881–881 (2013).

[27] E. B. Hale and R. L. Mieher, "Shallow Donor Electrons in Silicon. I. Hyperfine Interactions from ENDOR Measurements," Physical Review **184**, 739–750 (1969).

[28] R. K. Zhukavin, K. A. Kovalevsky, V. V. Tsyplenkov, V. N. Shastin, S. G. Pavlov, H.-W. Hübers, H. Riemann, N. V. Abrosimov, and A. K. Ramdas, "Spin-orbit coupling effect on bismuth donor lasing in stressed silicon," Applied Physics Letters **99**, 171108 (2011).

[29] A. K. Ramdas and S. Rodriguez, "Spectroscopy of the solid-state analogues of the hydrogen atom: donors and acceptors in semiconductors," Reports on Progress in Physics **44**, 1297–1387 (1981).

[30] G. Feher and E. A. Gere, "Electron Spin Resonance Experiments on Donors in Silicon. II. Electron Spin Relaxation Effects," Physical Review **114**, 1245–1256 (1959).

[31] R. de Sousa, J. D. Delgado, and S. Das Sarma, "Silicon quantum computation based on magnetic dipolar coupling," Physical Review A **70**, 052304 (2004).

[32] J. M. Luttinger and W. Kohn, "Motion of Electrons and Holes in Perturbed Periodic Fields," Physical Review **97**, 869–883 (1955).

[33] P. YU and M. Cardona, *Fundamentals of Semiconductors: Physics and Materials Properties* (Springer Science & Business Media, 2010).

[34] D. K. Wilson and G. Feher, "Electron Spin Resonance Experiments on Donors in Silicon. III. Investigation of Excited States by the Application of Uniaxial Stress and Their Importance in Relaxation Processes," Physical Review **124**, 1068–1083 (1961).

[35] M. J. Calderón, B. Koiller, and S. Das Sarma, "External field control of donor electron exchange at the Si/SiO$_2$ interface," Physical Review B **75**, 125311 (2007).

[36] C. C. Lo, S. Simmons, R. Lo Nardo, C. D. Weis, A. M. Tyryshkin, J. Meijer, D. Rogalla, S. A. Lyon, J. Bokor, T. Schenkel, and J. J. L. Morton, "Stark shift and field ionization of arsenic donors in 28Si-silicon-on-insulator structures," Applied Physics Letters **104**, 193502 (2014).

[37] A. Bienfait, *Magnetic resonance with quantum microwaves*, thesis, Paris Saclay (2016).

[38] R. E. George, W. Witzel, H. Riemann, N. V. Abrosimov, N. Nötzel, M. L. W. Thewalt, and J. J. L. Morton, "Electron Spin Coherence and Electron Nuclear Double Resonance of Bi Donors in Natural Si," Physical Review Letters **105**, 067601 (2010).

[39] M. H. Mohammady, G. W. Morley, and T. S. Monteiro, "Bismuth Qubits in Silicon: The Role of EPR Cancellation Resonances," Physical Review Letters **105**, 067602 (2010).

[40] S. J. Balian, "Quantum-Bath Decoherence of Hybrid Electron-Nuclear Spin Qubits," arXiv:1510.08944 [cond-mat, physics:quant-ph] (2015).

[41] G. W. Morley, P. Lueders, M. Hamed Mohammady, S. J. Balian, G. Aeppli, C. W. M. Kay, W. M. Witzel, G. Jeschke, and T. S. Monteiro, "Quantum control of hybrid nuclear–electronic qubits," Nature Materials **12**, 103–107 (2013).

[42] M. H. Mohammady, G. W. Morley, A. Nazir, and T. S. Monteiro, "Analysis of quantum coherence in bismuth-doped silicon: A system of strongly coupled spin qubits," Physical Review B **85**, 094404 (2012).

[43] A. Schweiger and G. Jeschke, *Principles of pulse electron paramagnetic resonance* (Oxford University Press, 2001).

[44] E. Abe, A. M. Tyryshkin, S. Tojo, J. J. L. Morton, W. M. Witzel, A. Fujimoto, J. W. Ager, E. E. Haller, J. Isoya, S. A. Lyon, M. L. W. Thewalt, and K. M. Itoh, "Electron spin coherence of phosphorus donors in silicon: Effect of environmental nuclei," Physical Review B **82**, 121201 (2010).

[45] G. W. Morley, M. Warner, A. M. Stoneham, P. T. Greenland, J. v. Tol, C. W. M. Kay, and G. Aeppli, "The initialization and manipulation of quantum information stored in silicon by bismuth dopants," Nature Materials **9**, 725–729 (2010).

[46] M. Belli, M. Fanciulli, and N. V. Abrosimov, "Pulse electron spin resonance investigation of bismuth-doped silicon: Relaxation and electron spin echo envelope modulation," Physical Review B **83**, 235204 (2011).

[47] Y. M. Niquet, D. Rideau, C. Tavernier, H. Jaouen, and X. Blase, "Onsite matrix elements of the tight-binding Hamiltonian of a strained crystal: Application to silicon, germanium, and their alloys," Physical Review B **79**, 245201 (2009).

[48] R. d. Sousa and S. D. Sarma, "Theory of nuclear-induced spectral diffusion: Spin decoherence of phosphorus donors in Si and GaAs quantum dots," Physical Review B **68** (2003), 10.1103/physrevb.68.115322.

[49] S. Probst, G. L. Zhang, M. Rancic, V. Ranjan, M. L. Dantec, Z. Zhong, B. Albanese, A. Doll, R. B. Liu, J. J. L. Morton, T. Chanelilere, P. Goldner, D. Vion, D. Esteve, and P. Bertet, "Hyperfine spectroscopy in a quantum-limited spectrometer," arXiv:2001.04854 [quant-ph] (2020).

[50] W. M. Witzel, X. Hu, and S. Das Sarma, "Decoherence induced by anisotropic hyperfine interaction in Si spin qubits," Physical Review B **76**, 035212 (2007).

[51] A. Honig and E. Stupp, "Electron Spin-Lattice Relaxation in Phosphorus-Doped Silicon," Physical Review **117**, 69–83 (1960).

[52] L. M. Roth, "g Factor and Donor Spin-Lattice Relaxation for Electrons in Germanium and Silicon," Physical Review **118**, 1534–1540 (1960).

[53] H. Hasegawa, "Spin-Lattice Relaxation of Shallow Donor States in Ge and Si through a Direct Phonon Process," Physical Review **118**, 1523–1534 (1960).

[54] A. Morello, J. J. Pla, F. A. Zwanenburg, K. W. Chan, K. Y. Tan, H. Huebl, M. Möttönen, C. D. Nugroho, C. Yang, J. A. van Donkelaar, A. D. C. Alves, D. N. Jamieson, C. C. Escott, L. C. L. Hollenberg, R. G. Clark, and A. S. Dzurak, "Single-shot readout of an electron spin in silicon," Nature **467**, 687–691 (2010).

[55] A. Abragam and B. Bleaney, *Electron Paramagnetic Resonance of Transition Ions* (OUP Oxford, 2012).

[56] T. G. Castner, "Orbach Spin-Lattice Relaxation of Shallow Donors in Silicon," Physical Review **155**, 816–825 (1967).

[57] T. G. Castner, "Raman Spin-Lattice Relaxation of Shallow Donors in Silicon," Physical Review **130**, 58–75 (1963).

[58] G. Wolfowicz, S. Simmons, A. M. Tyryshkin, R. E. George, H. Riemann, N. V. Abrosimov, P. Becker, H.-J. Pohl, S. A. Lyon, M. L. W. Thewalt, and J. J. L. Morton, "Decoherence mechanisms of ^{209}Bi donor electron spins in isotopically pure ^{28}Si," Physical Review B **86**, 245301 (2012).

[59] E. B. Hale and T. G. Castner, "Ground-State Wave Function of Shallow Donors in Uniaxially Stressed Silicon: Piezohyperfine Constants Determined by Electron-Nuclear Double Resonance," Physical Review B **1**, 4763–4783 (1970).

[60] B. Koiller, X. Hu, and S. Das Sarma, "Strain effects on silicon donor exchange: Quantum computer architecture considerations," Physical Review B **66**, 115201 (2002).

[61] H. Huebl, A. R. Stegner, M. Stutzmann, M. S. Brandt, G. Vogg, F. Bensch, E. Rauls, and U. Gerstmann, "Phosphorus Donors in Highly Strained Silicon," Physical Review Letters **97**, 166402 (2006).

[62] M. Usman, C. D. Hill, R. Rahman, G. Klimeck, M. Y. Simmons, S. Rogge, and L. C. L. Hollenberg, "Strain and electric field control of hyperfine interactions for donor spin qubits in silicon," Physical Review B **91**, 245209 (2015).

[63] L. Dreher, T. A. Hilker, A. Brandlmaier, S. T. B. Goennenwein, H. Huebl, M. Stutzmann, and M. S. Brandt, "Electroelastic Hyperfine Tuning of Phosphorus Donors in Silicon," Physical Review Letters **106**, 037601 (2011).

[64] J. Mansir, P. Conti, Z. Zeng, J. Pla, P. Bertet, M. Swift, C. Van de Walle, M. Thewalt, B. Sklenard, Y. Niquet, and J. Morton, "Linear Hyperfine Tuning of Donor Spins in Silicon Using Hydrostatic Strain," Physical Review Letters **120**, 167701 (2018).

[65] J. Pla, A. Bienfait, G. Pica, J. Mansir, F. Mohiyaddin, Z. Zeng, Y. Niquet, A. Morello, T. Schenkel, J. Morton, and P. Bertet, "Strain-Induced Spin-Resonance Shifts in Silicon Devices," Physical Review Applied **9**, 044014 (2018).

[66] D. D. Thornton and A. Honig, "Shallow-Donor Negative Ions and Spin-Polarized Electron Transport in Silicon," Physical Review Letters **30**, 909–912 (1973).

[67] G. W. Morley, D. R. McCamey, H. A. Seipel, L.-C. Brunel, J. van Tol, and C. Boehme, "Long-Lived Spin Coherence in Silicon with an Electrical Spin Trap Readout," Physical Review Letters **101**, 207602 (2008).

[68] T. Sekiguchi, M. Steger, K. Saeedi, M. L. W. Thewalt, H. Riemann, N. V. Abrosimov, and N. Nötzel, "Hyperfine Structure and Nuclear Hyperpolarization Observed in the Bound Exciton Luminescence of Bi Donors in Natural Si," Physical Review Letters **104**, 137402 (2010).

[69] D. R. McCamey, J. van Tol, G. W. Morley, and C. Boehme, "Fast Nuclear Spin Hyperpolarization of Phosphorus in Silicon," Physical Review Letters **102**, 027601 (2009).

[70] A. Yang, M. Steger, D. Karaiskaj, M. L. W. Thewalt, M. Cardona, K. M. Itoh, H. Riemann, N. V. Abrosimov, M. F. Churbanov, A. V. Gusev, A. D. Bulanov, A. K. Kaliteevskii, O. N. Godisov, P. Becker, H.-J. Pohl, J. W. Ager, and E. E. Haller, "Optical Detection and Ionization of Donors in Specific Electronic and Nuclear Spin States," Physical Review Letters **97**, 227401 (2006).

[71] A. Yang, M. Steger, T. Sekiguchi, M. L. W. Thewalt, T. D. Ladd, K. M. Itoh, H. Riemann, N. V. Abrosimov, P. Becker, and H.-J. Pohl, "Simultaneous Subsecond Hyperpolarization of the Nuclear and Electron Spins of Phosphorus in Silicon by Optical Pumping of Exciton Transitions," Physical Review Letters **102**, 257401 (2009).

[72] M. Steger, K. Saeedi, M. L. W. Thewalt, J. J. L. Morton, H. Riemann, N. V. Abrosimov, P. Becker, and H.-J. Pohl, "Quantum Information Storage for over 180 s Using Donor Spins in a ^{28}Si "Semiconductor Vacuum"," Science **336**, 1280–1283 (2012).

[73] K. Saeedi, S. Simmons, J. Z. Salvail, P. Dluhy, H. Riemann, N. V. Abrosimov, P. Becker, H.-J. Pohl, J. J. L. Morton, and M. L. W. Thewalt, "Room-Temperature Quantum Bit Storage Exceeding 39 Minutes Using Ionized Donors in Silicon-28," Science **342**, 830–833 (2013).

[74] P. Studer, S. R. Schofield, C. F. Hirjibehedin, and N. J. Curson, "Studying atomic scale structural and electronic properties of ion implanted silicon samples using cross-sectional scanning tunneling microscopy," Applied Physics Letters **102**, 012107 (2013).

[75] C. D. Weis, C. C. Lo, V. Lang, A. M. Tyryshkin, R. E. George, K. M. Yu, J. Bokor, S. A. Lyon, J. J. L. Morton, and T. Schenkel, "Electrical activation and electron spin resonance measurements of implanted bismuth in isotopically enriched silicon-28," Applied Physics Letters **100**, 172104 (2012).

[76] Y. Manassen, R. J. Hamers, J. E. Demuth, and A. J. Castellano Jr., "Direct observation of the precession of individual paramagnetic spins on oxidized silicon surfaces," Physical Review Letters **62**, 2531 (1989).

[77] D. Rugar, C. Yannoni, and J. Sidles, "Mechanical detection of magnetic resonance," Nature **360**, 563–566 (1992).

[78] D. Rugar, R. Budakian, H. Mamin, and B. Chui, "Single spin detection by magnetic resonance force microscopy," Nature **430**, 329–332 (2004).

[79] J. M. Taylor, P. Cappellaro, L. Childress, L. Jiang, D. Budker, P. R. Hemmer, A. Yacoby, R. Walsworth, and M. D. Lukin, "High-sensitivity diamond magnetometer with nanoscale resolution," Nat Phys **4**, 810–816 (2008).

[80] A. Gruber, A. Drabenstedt, C. Tietz, L. Fleury, J. Wrachtrup, and C. v. Borczyskowski, "Scanning Confocal Optical Microscopy and Magnetic Resonance on Single Defect Centers," Science **276**, 2012–2014 (1997).

[81] C. Durkan and M. E. Welland, "Electronic spin detection in molecules using scanning-tunneling- microscopy-assisted electron-spin resonance," Applied Physics Letters **80**, 458–460 (2002).

[82] H. Malissa, D. I. Schuster, A. M. Tyryshkin, A. A. Houck, and S. A. Lyon, "Superconducting coplanar waveguide resonators for low temperature pulsed electron spin resonance spectroscopy," Review of Scientific Instruments **84**, 025116 (2013).

[83] A. J. Sigillito, H. Malissa, A. M. Tyryshkin, H. Riemann, N. V. Abrosimov, P. Becker, H.-J. Pohl, M. L. W. Thewalt, K. M. Itoh, J. J. L. Morton, A. A. Houck, D. I. Schuster, and S. A. Lyon, "Fast, low-power manipulation of spin ensembles in superconducting microresonators," Applied Physics Letters **104**, – (2014).

[84] Y. Artzi, Y. Twig, and A. Blank, "Induction-detection electron spin resonance with spin sensitivity of a few tens of spins," Applied Physics Letters **106**, 084104 (2015).

[85] N. Dayan, Y. Ishay, Y. Artzi, D. Cristea, E. Reijerse, P. Kuppusamy, and A. Blank, "Advanced surface resonators for electron spin resonance of single microcrystals," Review of Scientific Instruments **89**, 124707 (2018).

[86] O. W. B. Benningshof, H. R. Mohebbi, I. A. J. Taminiau, G. X. Miao, and D. G. Cory, "Superconducting microstrip resonator for pulsed ESR of thin films," Journal of Magnetic Resonance **230**, 84–87 (2013).

[87] A. J. Sigillito, A. M. Tyryshkin, T. Schenkel, A. A. Houck, and S. A. Lyon, "All-electric control of donor nuclear spin qubits in silicon," Nature Nanotechnology **12**, 958–962 (2017).

[88] C. Eichler, A. Sigillito, S. Lyon, and J. Petta, "Electron Spin Resonance at the Level of 10^4 Spins Using Low Impedance Superconducting Resonators," Physical Review Letters **118**, 037701 (2017).

[89] V. Ranjan, S. Probst, B. Albanese, T. Schenkel, D. Vion, D. Esteve, J. Morton, and P. Bertet, "Electron Spin Resonance spectroscopy with femtoliter detection volume," arXiv:2002.03669 [cond-mat, physics:quant-ph] (2020).

[90] A. Megrant, C. Neill, R. Barends, B. Chiaro, Y. Chen, L. Feigl, J. Kelly, E. Lucero, M. Mariantoni, P. J. J. O'Malley, D. Sank, A. Vainsencher, J. Wenner, T. C. White, Y. Yin, J. Zhao, C. J. Palmstrøm, J. M. Martinis, and A. N. Cleland, "Planar superconducting resonators with internal quality factors above one million," Applied Physics Letters **100**, 113510 (2012).

[91] C. Song, M. P. DeFeo, K. Yu, and B. L. T. Plourde, "Reducing microwave loss in superconducting resonators due to trapped vortices," Applied Physics Letters **95**, 232501 (2009).

[92] R. Barends, J. Wenner, M. Lenander, Y. Chen, R. C. Bialczak, J. Kelly, E. Lucero, P. O Malley, M. Mariantoni, D. Sank, H. Wang, T. C. White, Y. Yin, J. Zhao, A. N. Cleland, J. M. Martinis, and J. J. A. Baselmans, "Minimizing quasiparticle generation from stray infrared light in superconducting quantum circuits," Applied Physics Letters **99**, 113507 (2011).

[93] A. D. O'Connell, M. Ansmann, R. C. Bialczak, M. Hofheinz, N. Katz, E. Lucero, C. McKenney, M. Neeley, H. Wang, E. M. Weig, A. N. Cleland, and J. M. Martinis, "Microwave dielectric loss at single photon energies and millikelvin temperatures," Applied Physics Letters **92**, 112903 (2008).

[94] D. S. Wisbey, J. Gao, M. R. Vissers, F. C. S. da Silva, J. S. Kline, L. Vale, and D. P. Pappas, "Effect of metal/substrate interfaces on radio-frequency loss in

superconducting coplanar waveguides," Journal of Applied Physics **108**, 093918 (2010).

[95] A. A. Houck, J. A. Schreier, B. R. Johnson, J. M. Chow, J. Koch, J. M. Gambetta, D. I. Schuster, L. Frunzio, M. H. Devoret, S. M. Girvin, and R. J. Schoelkopf, "Controlling the Spontaneous Emission of a Superconducting Transmon Qubit," Physical Review Letters **101**, 080502 (2008).

[96] H. Paik, D. I. Schuster, L. S. Bishop, G. Kirchmair, G. Catelani, A. P. Sears, B. R. Johnson, M. J. Reagor, L. Frunzio, L. I. Glazman, S. M. Girvin, M. H. Devoret, and R. J. Schoelkopf, "Observation of High Coherence in Josephson Junction Qubits Measured in a Three-Dimensional Circuit QED Architecture," Physical Review Letters **107**, 240501 (2011).

[97] M. Reagor, H. Paik, G. Catelani, L. Sun, C. Axline, E. Holland, I. M. Pop, N. A. Masluk, T. Brecht, L. Frunzio, M. H. Devoret, L. Glazman, and R. J. Schoelkopf, "Reaching 10 ms single photon lifetimes for superconducting aluminum cavities," Applied Physics Letters **102**, 192604 (2013).

[98] A. Bruno, G. de Lange, S. Asaad, K. L. van der Enden, N. K. Langford, and L. DiCarlo, "Reducing intrinsic loss in superconducting resonators by surface treatment and deep etching of silicon substrates," Applied Physics Letters **106**, 182601 (2015).

[99] D. R. Heslinga and T. M. Klapwijk, "Schottky barrier and contact resistance at a niobium/silicon interface," Applied Physics Letters **54**, 1048–1050 (1989).

[100] T. V. Duzer and C. W. Turner, *Principles of Superconductive Devices and Circuits* (Prentice Hall, 1999).

[101] A. I. Gubin, K. S. Il'in, S. A. Vitusevich, M. Siegel, and N. Klein, "Dependence of magnetic penetration depth on the thickness of superconducting Nb thin films," Physical Review B **72**, 064503 (2005).

[102] R. H. Dicke, "Coherence in Spontaneous Radiation Processes," Physical Review **93**, 99–110 (1954).

[103] C. J. Wood and D. G. Cory, "Cavity cooling to the ground state of an ensemble quantum system," Physical Review A **93**, 023414 (2016).

[104] V. V. Temnov and U. Woggon, "Superradiance and Subradiance in an Inhomogeneously Broadened Ensemble of Two-Level Systems Coupled to a Low-Q Cavity," Physical Review Letters **95**, 243602 (2005).

[105] I. Diniz, S. Portolan, R. Ferreira, J. M. Gérard, P. Bertet, and A. Auffèves, "Strongly coupling a cavity to inhomogeneous ensembles of emitters : potential for long lived solid-state quantum memories," 1101.1842 (2011).

[106] M. Xu, X. Han, C.-L. Zou, W. Fu, Y. Xu, C. Zhong, L. Jiang, and H. X. Tang, "Radiative cooling of a superconducting resonator," arXiv:1910.01203 [quant-ph] (2019).

[107] Z. Wang, M. Xu, X. Han, W. Fu, S. Puri, S. M. Girvin, H. X. Tang, S. Shankar, and M. H. Devoret, "Quantum Microwave Radiometry with a Superconducting Qubit," arXiv:1909.12295 [quant-ph] (2019).

[108] P. K. Day, H. G. LeDuc, B. A. Mazin, A. Vayonakis, and J. Zmuidzinas, "A broadband superconducting detector suitable for use in large arrays," Nature **425**, 817–821 (2003).

[109] H. Engstrom, "Infrared reflectivity and transmissivity of boron-implanted, laser-annealed silicon," Journal of Applied Physics **51**, 5245–5249 (1980).

[110] L. A. Williamson, Y.-H. Chen, and J. J. Longdell, "Magneto-Optic Modulator with Unit Quantum Efficiency," Physical Review Letters **113**, 203601 (2014).

[111] S. K. Wong, D. A. Hutchinson, and J. K. S. Wan, "Chemically induced dynamic electron polarization. II. A general theory for radicals produced by photochemical reactions of excited triplet carbonyl compounds," The Journal of Chemical Physics **58**, 985–989 (1973).

[112] M. W. Doherty, N. B. Manson, P. Delaney, F. Jelezko, J. Wrachtrup, and L. C. L. Hollenberg, "The nitrogen-vacancy colour centre in diamond," Physics Reports The nitrogen-vacancy colour centre in diamond, **528**, 1–45 (2013).

[113] J. G. Castle and D. W. Feldman, "Resonance Modes at Defects in Crystalline Quartz," Physical Review **137**, A671–A673 (1965).

[114] J.-P. Gayda, P. Bertrand, A. Deville, C. More, G. Roger, J. F. Gibson, and R. Cammack, "Temperature dependence of the electronic spin-lattice relaxation time in a 2-iron-2-sulfur protein," Biochimica et Biophysica Acta (BBA) - Protein Structure **581**, 15–26 (1979).

[115] Y. Zhou, B. E. Bowler, G. R. Eaton, and S. S. Eaton, "Electron Spin Lattice Relaxation Rates for S = 12 Molecular Species in Glassy Matrices or Magnetically Dilute Solids at Temperatures between 10 and 300 K," Journal of Magnetic Resonance **139**, 165–174 (1999).

[116] J. Kroll, F. Borsoi, K. van der Enden, W. Uilhoorn, D. de Jong, M. Quintero-Pérez, D. van Woerkom, A. Bruno, S. Plissard, D. Car, E. Bakkers, M. Cassidy, and L. Kouwenhoven, "Magnetic-Field-Resilient Superconducting Coplanar-Waveguide Resonators for Hybrid Circuit Quantum Electrodynamics Experiments," Physical Review Applied **11**, 064053 (2019).

[117] A. Ghirri, C. Bonizzoni, D. Gerace, S. Sanna, A. Cassinese, and M. Affronte, "$YBa_2Cu_3O_7$ microwave resonators for strong collective coupling with spin ensembles," Applied Physics Letters **106**, 184101 (2015).

[118] C. Bonizzoni, A. Ghirri, and M. Affronte, "Coherent coupling of molecular spins with microwave photons in planar superconducting resonators," Advances in Physics: X **3**, 1435305 (2018).

[119] A. Abragam and M. Goldman, "Principles of dynamic nuclear polarisation," Reports on Progress in Physics **41**, 395–467 (1978).

[120] J. H. Ardenkjær-Larsen, B. Fridlund, A. Gram, G. Hansson, L. Hansson, M. H. Lerche, R. Servin, M. Thaning, and K. Golman, "Increase in signal-to-noise ratio of 10,000 times in liquid-state NMR," Proceedings of the National Academy of Sciences **100**, 10158–10163 (2003).

[121] M. F. Gely, M. Kounalakis, C. Dickel, J. Dalle, R. Vatré, B. Baker, M. D. Jenkins, and G. A. Steele, "Observation and stabilization of photonic Fock states in a hot radio-frequency resonator," Science **363**, 1072–1075 (2019).

ÉCOLE DOCTORALE

**Physique
en île-de-France
(EDPIF)**

université
PARIS-SACLAY

Titre : Refroidissement radiatif d'un ensemble de spins

Mots clés : résonance magnétique, résonance paramagnétique électrique, hyperpolarisation, circuits supraconducteurs, donneurs de bismuth, micro-ondes

Résumé : Les spins dans le solides interagissent faiblement avec leur environnement électromagnétique et atteignent presque toujours l'équilibre thermique en échangeant de l'énergie avec le réseau cristallin dans lequel ils sont insérés. Cependant, comme prédit par Purcell, des expériences récentes ont démontré que l'émission radiative peut devenir le canal de relaxation d'énergie le plus rapide pour les spins d'électron si l'échantillon est inséré dans une cavité micro-onde résonante avec petit volume de mode et de faible taux de perte. Dans ce régime, les spins devraient se thermaliser à la température des photons présents dans le mode de la cavité, indépendamment de la température de l'échantillon. Cette thèse présente la démonstration de cette idée, en montrant que les spins peuvent être refroidis en manière radiatif au-dessous de la température de l'échantillon en couplant la cavité à une source de rayonnement thermique froid. L'expérience est réalisée avec un ensemble de spins électroniques réalisés par des donneurs de bismuth dans le silicium, couplés à un résonateur supraconducteur de taille micrométrique. La température de spin est déduite en mesurant la polarisation de spin avec des techniques de résonance paramagnétique électrique pulsés. Une augmentation de polarisation par un facteur supérieur à 2 est observée lorsque le résonateur est connectée à une résistance froide, prouvant que les spins sont refroidis radiativement par rapport au cristal de silicium qui les héberge. La technique démontrée représente une méthode nouvelle et universelle pour améliorer la polarisation de spin au-delà de l'équilibre thermique, avec des applications potentielles en résonance magnétique.

Title : Radiative cooling of a spin ensemble

Keywords : magnetic resonance, electron spin resonance, hyperpolarization, superconducting circuits, bismuth donors, microwave measurements

Abstract : Spins in solids interact only weakly with their electromagnetic environment and in usual situations they reach thermal equilibrium by exchanging energy with their host lattice. However, recent experiments have demonstrated that radiative emission can become the fastest energy relaxation channel for the electron spins if the sample is inserted in a resonant microwave cavity of small mode volume and low loss rate, as predicted by Purcell. In this regime spins are then expected to thermalize to the cavity mode regardless of the lattice temperature. This thesis presents the demonstration of this idea, by showing that spins can be radiatively cooled below the sample temperature by coupling the cavity to a cold thermal radiation source. The experiment is realized with an ensemble of electron spins consisting in bismuth donors in silicon coupled to a micron-size superconducting resonator and the spin temperature is inferred by measuring the spin polarization with pulsed electron spin resonance techniques. A more than twofold increase of polarization is observed when the resonator input is connected to a cold resistive load, proving that spins are radiatively cooled with respect to their host lattice. The demonstrated technique represents a new and universal method to enhance electron spin polarization beyond thermal equilibrium, with potential applications in electron spin resonance spectroscopy.